

Technische Universität München
Institut für Energietechnik

Lehrstuhl für Thermodynamik

Reduction of Heating Loads and Interior Window Fogging in Vehicles

Manuel Lorenz

Vollständiger Abdruck der von der Fakultät für Maschinenwesen der
Technischen Universität München zur Erlangung des akademischen Grades
eines

DOKTOR – INGENIEURS

genehmigten Dissertation.

Vorsitzender:

Univ.-Prof. Dr.-Ing. Manfred Hajek

Prüfer der Dissertation:

1. Univ.-Prof. Dr.-Ing. Thomas Sattelmayer

2. Univ.-Prof. Dr. phil. Klaus Bengler

Die Dissertation wurde am 09.06.2015 bei der Technischen Universität München eingereicht
und durch die Fakultät für Maschinenwesen am 28.09.2015 angenommen.

Casus ubique valet; semper tibi pendeat hamus. Quo minime credas gurgite,
piscis erit.

Überall herrscht der Zufall. Laß deine Angel nur hängen. Wo du's am
wenigsten glaubst, sitzt im Strudel der Fisch.

Ovid, 47 BC - 18 AD

Vorwort

Dem Dichter Ovid folgend, habe auch ich meine Angel in den Ozean der Thermodynamik gehängt und beharrlich nach den Bestandteilen meiner Dissertation gefischt.

Von 2009 bis 2014 hatte ich hierzu eine Anstellung als wissenschaftlicher Mitarbeiter am Lehrstuhl für Thermodynamik der TU München. Den diversen Geldgebern welche dies ermöglicht haben, insbesondere dem BMBF, AUDI und DENSO, möchte ich meinen Dank aussprechen. Im Rahmen zweier großer Förderprojekte, "eperformance" und "Visio.M", an denen ich während meiner Zeit am Lehrstuhl arbeiten durfte, habe ich das Fundament der vorliegenden Arbeit aufgebaut.

Mein herzlicher Dank gilt meinem Doktorvater Prof. Thomas Sattelmayer für die Betreuung der Arbeit. Er hat mit seinen kritischen Einwänden und Anregungen maßgeblich zum erfolgreichen Gelingen beigetragen. Weiterhin möchte ich Prof. Klaus Bengler nicht nur für den Einsatz als Zweitprüfer danken, sondern insbesondere auch dafür, dass ich für alle in dieser Arbeit gezeigten Experimente die Klimakammer des Lehrstuhls für Ergonomie der TU München nutzen durfte. Den 22 freiwilligen Testpersonen, die in den Klimakammerversuchen 10 Minuten lang frieren mussten, gilt besondere Anerkennung.

Gedankt sei Reinhart Ubat, der durch seine ausrangierte und an mich vermachte Ringlampe entscheidend zum Erfolg dieser Arbeit beigetragen hat.

Vielen Dank auch allen die so gewissenhaft Korrektur gelesen oder mich fachlich beraten haben: Markus Spinnler, John Harvey, Alexander Kroiss, Leonhard Hörth, Veronika Lorenz, Marco Lorenz und Thomas Emmert.

Ebenso einen herzlichen Dank allen Studenten, die zum Gelingen dieser Arbeit beigetragen haben und deren Studienarbeiten am Ende dieser Arbeit aufgelistet sind.

Für die schöne Zeit am Lehrstuhl möchte ich mich stellvertretend bedanken bei Mathieu Zellhuber, Michael Hertweck, Volker Seidel, Gary Jasor, Camilo Silva, Alejandro Cardenas, meinen diversen Zimmerkollegen, der TP Gruppe, dem Fußballteam und bei allen namentlich nicht erwähnten, die sich eventuell vergessen fühlen.

Vielen Dank meinen Eltern sowie meinen Schwieger- und Bonuseltern für unermüdliches Kinderhüten und die Unterstützung während der Schreibphase.

Ich widme diese Arbeit meinen Freunden, meiner Familie, meiner Frau Veronika und meinen drei Kindern Marta, Vinzent und N. N. Ohne euch hätte ich die Angel längst ins Meer geworfen.

Abstract

The driving efficiency of electric vehicles is significantly reduced by the high necessary cabin heating power during winter operation. Promising concepts to reduce the required power are the insulation of the cabin and in particular the windows, local heating to establish passenger thermal comfort without conditioning the entire cabin and airflow recirculation. Recirculation has high potential, as approximately 50% of the necessary heating power arises from ventilation losses in steady-state operation. However, air-recirculation at cold ambient conditions quickly leads to window fogging due to vapor emission from the passengers and evaporation of accumulated water in the cabin. To predict the energy saving potential of various optimization measures, a coupled numerical cabin model is developed, including a Computational Fluid Dynamics (CFD) model of the cabin airflow, a heat transfer model of the solid cabin parts, the Fiala Physiological Comfort (FPC) model and a new model for the prediction of window fogging. Experiments are performed to validate the simulation of window fogging. A new measurement technique is established and validated to measure the contact angle of single droplets and droplet arrays from perpendicularly above during the condensation and evaporation process. This allows the local vapor mass flow rates to be quantified. For typical window fogging conditions it is shown that the dependence of the mass transfer on the droplet structure is negligible. Thus, the conclusion is that a film condensation model satisfactorily reproduces the heat and mass transfer.

Contents

Vorwort	v
Abstract	vii
List of Figures	xiii
List of Tables	xv
Nomenclature	xvii
1 Introduction	1
1.1 Technological Background	1
1.2 Cabin Optimization Measures	2
1.3 Goal of the Thesis	4
1.4 Thesis Overview	6
2 Window Fogging	9
2.1 Theory and State-of-the-Art	9
2.1.1 Molecular Approach	10
2.1.2 Macroscopic Approach	13
2.1.3 Influence of Gravitation on the Interface	14
2.1.4 Drop-Wise Condensation and Evaporation	15
2.1.4.1 Heat Transfer Rate	16
2.1.4.2 Droplet Growth Rate	17
2.1.4.3 Surface Coverage	19
2.1.5 Window Fogging in Vehicles	19
2.1.6 Simulation of Window Fogging	21
2.2 Experimental Investigations	24
2.2.1 Test Rig Setup and Experimental Parameters	24

2.2.2	Drop Shape Analysis and Contact Angle Measurement Method	30
2.2.2.1	Influence of Gravity on the Droplet Shape	32
2.2.2.2	Neglecting Gravitational Influences	34
2.2.2.3	Verification of the Contact Angle Measurement Method	37
2.2.2.4	Image Processing	38
2.2.2.4.1	Identification of Horseshoe Shape Reflections	39
2.2.2.4.2	Identification of Circular Reflection Shapes	42
2.2.2.5	Iterative Optimization of the Algorithm	44
2.2.3	Condensation and Evaporation Mass Flux Measurement	45
2.2.3.1	Measurement Error and Sensitivity Analysis	46
2.2.4	Experimental Results	50
2.2.4.1	Area-Related Measurement Parameters	50
2.2.4.2	Nucleation and Sub-Cooling	54
2.2.4.3	Contact Angles	55
2.2.5	Droplet Structure and Mass Transfer	57
2.2.5.1	Turbulence Induction by the Droplet Structure	58
2.2.5.2	Influence of the Size of the Liquid-Vapor Interface on Vapor Mass Transfer	60
2.2.5.3	Thermal Insulation of the Condensate	62
2.2.5.4	Experimental Verification of Droplet Structure Influences on Mass Transfer	63
2.3	Simulation of Window Fogging	66
2.3.1	Computational Fluid Dynamics	66
2.3.1.1	Near-Wall Modeling	66
2.3.1.2	Condensation and Evaporation Model	67
2.3.1.3	CFD Model of the Test Rig	70
2.3.2	Analytical Approach	72
2.3.3	Experimental Validation of the Fogging Model	80
2.4	Conclusion	83
3	Passenger Thermal Comfort	85
3.1	Thermal Comfort Theory	85
3.2	Thermal Comfort in Vehicles	86

3.3	Thermal Comfort Modeling	88
3.4	Fiala Physiological Comfort (FPC) Model with CFD and Heat Conduction Boundary Condition	89
3.4.1	Physiological Comfort	90
3.4.2	Clothing and Direct Contact to Vehicle Parts	93
3.5	Validation of the Comfort Model	94
3.6	Conclusion	99
4	Cabin Modeling	101
4.1	State-of-the-Art of Vehicle Cabin Modeling	101
4.2	Generic Compact Car Cabin Model	103
4.2.1	CFD Cabin Air Model	104
4.2.2	Structure Heat Transfer	107
4.2.2.1	Discretization	107
4.2.2.2	Air-filled Gaps in the Vehicle Structure	110
4.2.2.3	Boundary Conditions	112
4.3	Coupled Simulation of Sub-Models	114
4.4	Simulation Test Cases	117
4.4.1	Air Inlet Parameters and Control Algorithms	119
4.5	Saving Potential of Optimization Measures	121
4.5.1	Baseline Configuration	122
4.5.2	Glazing Options	122
4.5.3	Local Heating Measures	127
4.5.4	Optimized Configuration	129
4.6	Conclusion	133
5	Summary	135
6	Outlook	139
	Appendix	143
A	Velocity Profiles Measured by PIV	145
B	Measured Light Intensity Distribution	149
C	Contact Angle Measurement on Different Substrate Surfaces	151
D	Data and Comfort Votes of 22 Test Subjects of the Comfort Study	155

E Physical Properties of Humid Air	157
F Vehicle Parts, Assumed Material Layers and Physical Properties of the Generic Vehicle Cabin Model	161
Bibliography	163
Supervised Theses	179

List of Figures

1.1	Sub-models and coupled simulation model	5
2.1	Lennard-Jones 6-12 potential	11
2.2	Illustration of a liquid-vapor interfacial region	12
2.3	Axisymmetric droplet profile with gravitational influence	15
2.4	Window fogging model assumed by Kitada [72]	21
2.5	Window fogging test rig setup in the climate chamber	24
2.6	Schematic illustration of the experimental setup	25
2.7	Droplet pattern time series during condensation and evaporation	27
2.8	Schematic optical measurement setup	30
2.9	Ray paths of three different reflection mechanisms	31
2.10	Deviation of droplet shape due to gravitation	35
2.11	Profile shapes of a droplet with and without gravitational influence	35
2.12	Droplet captured synchronously from above and from the side .	38
2.13	Contact angle derived by two measurement techniques	39
2.14	Automatic detection of horseshoe shape reflections	41
2.15	Automatic detection of circular reflections	42
2.16	Radially averaged intensity values at a droplet image	43
2.17	Droplet condensation pattern with detected reflections	46
2.18	Contact angle as a function of the detected ratio of the reflections	47
2.19	Contact angle deviation at a reduced image resolution	48
2.20	Droplet shapes on different substrates during condensation . .	50
2.21	Measurement results of the reference condensation experiment	52
2.22	Light ray scattering for different condensation patterns	54
2.23	Droplet radius and contact angle during condensation	56
2.24	Droplet radius and contact angle distribution during evaporation	57
2.25	Interactions between droplet geometry and mass flow rate . . .	58
2.26	Constant vapor concentration lines around droplets	61
2.27	Film height on four different polycarbonate substrates	65

2.28	Boundary layer of the non-dimensional velocity	66
2.29	Energy and mass transfer in the first mesh cell	68
2.30	Boundary conditions of the 2D CFD Test rig model	71
2.31	Different analyzed mesh types	71
2.32	Condensation mass flux deviation of different meshes	72
2.33	Illustration of the simplified analytical model	73
2.34	Substrate surface temperature derived by CFD and analytically .	78
2.35	Local condensation rate derived by CFD and analytically	79
2.36	Measured and simulated condensate volume	81
2.37	Condensation rates derived by different approaches	82
2.38	Evaporation rates derived by different approaches	82
3.1	Factors influencing thermal comfort	86
3.2	FPC passive system model	90
3.3	FPC active system model	92
3.4	Setup of the experimental and simulation comfort test case . . .	95
3.5	Thermal sensation derived by experiment and simulation	97
3.6	Thermal comfort derived by experiment and simulation	98
3.7	Measured and simulated seat surface temperature	99
4.1	Options for the discretization of cabin models	102
4.3	Meshed geometry of a generic compact car with two occupants	105
4.4	Visualization of the airflow in the cabin	105
4.5	Material layers inside the vehicle body segments	108
4.6	Discretization of the multilayer structure	109
4.7	Exchange of physical variables between the various sub-models	114
4.8	Flowchart of the applied coupled simulation method	116
4.9	Control flowchart of the air inlet parameters	120
4.10	Simulation results of the baseline configuration	123
4.11	Influence of different glazing options	125
4.12	Influence of local heating measures on power and comfort . . .	128
4.13	Simulation results of the optimized configuration	131

List of Tables

2.1	Dependence between droplet growth rate and volume flow . . .	17
2.2	Overview of window fogging experimental parameters	28
2.3	Analyzed polycarbonate surfaces and measured contact angles .	64
2.4	Assumed properties and parameters for the analytical approach	77
3.1	Thermal sensation and comfort scales used in the study	92
4.1	Gap coefficient C_g for different gap orientations	112
4.2	Parameters for the coupled simulation test cases	117
4.3	Results of the baseline and the optimized configuration	130

Nomenclature

Latin Characters

A	Area	$[\text{m}^2]$
A_T	Temperature solution matrix	$[\text{s}^{-1}]$
$a_{k,i}$	Material property coefficients	$[\text{J kg}^{-1} \text{K}^{-1}]$
b_i	Material property exponent	$[-]$
b_T	Temperature solution vector	$[\text{K s}^{-1}]$
W	Width	$[\text{m}]$
C_g	Orientation coefficient for of an inclined gap	$[-]$
C_S	Vehicle part dependent coefficient	$[\text{W m}^{-2.8} \text{K}^{-1} \text{s}^{0.8}]$
C_μ	$k - \epsilon$ Model constant (= 0.09)	$[-]$
c	Specific heat capacity	$[\text{J kg}^{-1} \text{K}^{-1}]$
D	Diameter/width	$[\text{m}]$
D	Diffusion coefficient	$[\text{m}^2 \text{s}^{-1}]$
E	Empirical constant (= 9.793)	$[-]$
e	Relative Deviation	$[-]$
F	System free energy	$[\text{J}]$
F	Viewing factor	$[-]$
f	Fraction	$[-]$
f	Image scale factor	$[\%]$
g	Gravitational force	$[\text{m s}^{-2}]$
H	Height	$[\text{m}]$
h	Heat transfer coefficient	$[\text{W m}^{-2} \text{K}^{-1}]$
I	Relative image pixel intensity	$[-]$
i, k	Counter	$[-]$
k	Parameter of repulsion potential	$[-]$
k	Turbulence kinetic energy	$[\text{J kg}^{-1}]$
k_c	Mass transfer coefficient	$[\text{m s}^{-1}]$

NOMENCLATURE

L	Latent heat of condensation	$[\text{J kg}^{-1}]$
L	Length	$[\text{m}]$
\dot{m}''	Mass flux	$[\text{kg m}^{-2} \text{s}^{-1}]$
\dot{m}'''	Volumetric mass source	$[\text{kg m}^{-3} \text{s}^{-1}]$
M	Molar mass	$[\text{kg mol}^{-1}]$
m	Exponent of Lewis correlation	$[-]$
m_{th}	Area specific thermal inertia	$[\text{J K}^{-1} \text{m}^{-2}]$
N	Number	$[-]$
n	Refraction index	$[-]$
N_A	Number per unit Area	$[\text{m}^{-2}]$
\vec{n}	Surface normal vector	$[-]$
P	Power	$[\text{W}]$
p	Pressure	$[\text{Pa}]$
\dot{q}''	Heat flux	$[\text{W m}^{-2}]$
\dot{q}'''	Volumetric heat source	$[\text{W m}^{-3}]$
R	Radius/distance	$[\text{m}]$
R	Thermal resistance	$[\text{K m}^2 \text{W}^{-1}]$
R_0	Radius of curvature at droplet apex	$[\text{m}]$
R_1, R_2	Principal radii of curvature	$[\text{m}]$
S_C	Shape coefficient of circular reflection	$[-]$
s	Arc length	$[\text{m}]$
T	Temperature	$[\text{K}], [^{\circ}\text{C}]$
t	Time	$[\text{s}]$
u	Specific internal energy	$[\text{J kg}^{-1}]$
u, v	Velocity	$[\text{m s}^{-1}], [\text{km h}^{-1}]$
\dot{V}	Volume flow	$[\text{m}^3 \text{s}^{-1}]$
V	Volume	$[\text{m}^3]$
w	Mass fraction	$[-]$
w_{bl}	Blood perfusion rate	$[\text{s}^{-1}]$
x	Molar fraction	$[-]$
x, y, z	Cartesian coordinates	$[\text{m}]$
y	Wall distance	$[\text{m}]$

Greek Characters

α	Light ray angle	$[^{\circ}]$
----------	-----------------	--------------

α_{hs}	Opening angle of horseshoe reflection	[°]
α_{p}	Molecular polarizability	[C m ² V ⁻¹]
β	Energy equivalent of the blood perfusion rate	[W m ⁻³ K ⁻¹]
γ	Surface tension	[J m ⁻²]
δ_{lam}	Viscous sublayer thickness	[m]
δ	Dirac delta function	[-]
$\tilde{\delta}$	Normalized Dirac delta function	[m ⁻¹]
ϵ	Turbulence dissipation rate	[m ² s ⁻³]
ϵ_{LJ}	Parameter of Lennard-Jones 6-12 potential	[J]
ϵ_{lw}	Long-wave emissivity	[-]
θ	Contact angle	[°]
κ	Von Kármán constant (= 0.419)	[-]
λ	Hydrodynamic resistance coefficient	[-]
λ	Thermal conductivity	[W m ⁻¹ K ⁻¹]
λ_{dis}	Parameter of London dispersion potential	[J m ² V ² C ⁻²]
λ_0	Parameter of repulsion potential	[J m ^{9...15}]
μ	Dynamic viscosity	[Pa s]
μ	Growth rate exponent	[-]
ν	Kinematic viscosity	[m ² s ⁻¹]
ρ	Density	[kg m ⁻³]
Σ	Radiation exchange coefficient	[W m ⁻² K ⁻⁴]
σ	Contact line tension	[J m ⁻¹]
σ_{B}	Stefan-Boltzmann constant (= 5.67 · 10 ⁻⁸)	[W m ⁻² K ⁻⁴]
σ_{LJ}	Parameter of Lennard-Jones 6-12 potential	[m]
τ_{wall}	Wall shear stress	[Pa]
Φ	Molecular interaction potential	[J]
ϕ	Relative humidity	[-]
ϕ	Surface coverage	[-]
φ	Polar angle	[°]
Ψ, ζ	Auxiliary term	[-]
ω	Geometry factor	[-]

Subscripts

∞	Ambient
0	Set-point

NOMENCLATURE

a	Air
a, b, c, n	Counter
ar	Arterial
bl	Blood
bw	Black and white image
c	Intersection
cl	Clothing
cln	Contact line
co	Coolant
cond	Condensation
conv	Convective
cv	Finite control volume
dis	London dispersion force
duct	Conductive
east	East-side of discretization node
evap	Evaporation
film	Water film
fog	Fogged
free	Free length between droplets
g	Gap
gr	Ground
grav	Gravitational influence
h	Heated
h	Hydraulic
hs	Horseshoe type reflection shape
hy	Hypothalamus (head-core)
in	Inside
init	Initial condition
j-1	Western spatial discretization node
j	Central spatial discretization node
j+1	Eastern spatial discretization node
L	Latent
l	Liquid
lam	Laminar
light	Annular light source

LJ	Lennard-Jones 6-12
m	Mean
max	Maximum
met	Metabolism
mix	Mixture
nat	Natural convection
bw	Optimized
out	Outside
P	Mesh center node
p	At constant pressure
px	Pixel
r	Recirculation
rad	Radiative
rep	Repulsion
s	Surface/solid
sat	Saturation
sk	Skin
sky	Sky
spher	Spherical shape
st	Seat
t	Turbulent
v	Vapor
w	Water
warm	Warmer wall side
west	West-side of discretization node

Superscripts

+	Non-dimensional parameter based on wall shear stress τ_{wall}
*	Non-dimensional parameter based on turbulence kinetic energy k
→	Vector
'	Turbulence fluctuation
n, n+1	Actual and subsequent discrete time step

Non-Dimensional Numbers

Bo	Bond number	$\frac{\Delta\rho g R_0^2}{\gamma}$
----	-------------	-------------------------------------

Gr	Grashof number	$\frac{gL_g^3 T_{g2}-T_{g1} }{0.5(T_{g2}+T_{g1})\nu^2}$
Le	Lewis number	$\frac{Sc}{Pr}$
Nu	Nußelt number	$\frac{hD_h}{\lambda_a}$
Pr	Prandl number	$\frac{\mu c_p}{\lambda}$
Ra	Rayleigh number	Gr · Pr
Re	Reynolds number	$\frac{v_m D_h}{\nu}$
Sc	Schmidt number	$\frac{\nu}{D}$
Sh	Sherwood number	$\frac{k_c D_h}{D}$

Abbreviations

ADSA	Axisymmetric Drop Shape Analysis
C _{1,2,3}	Reflection types
CFD	Computational Fluid Dynamics
DTS	Dynamic Thermal Sensation
EWf	Eulerian Wall Film
FPC	Fiala Physiological Comfort
HiL	Hardware in the Loop
HVAC	Heating Ventilation and Air-Conditioning
KSU	Kansas State University
MET	Metabolic Equivalent of Task
NEDC	New European Driving Cycle
OTC	Overall Thermal Comfort
PC	Polycarbonate
PI	Proportional Integral control element
PIV	Particle Image Velocimetry
PMV	Predicted Mean Vote

PPD	Predicted Percentage of Dissatisfied
PT1	First-order lag element
RANS	Reynolds Averaged Navier-Stokes
RNG	Re-Normalisation Group
S2S	Surface to Surface
SD	Standard Deviation
SIMPLE	Semi-Implicit Method for Pressure Linked Equations
TC	Thermal Comfort
TS	Thermal Sensation
UDF	User Defined Function

1 Introduction

1.1 Technological Background

Mobility is the "ability to move or be moved freely and easily" [106] and is a major achievement of modern age. Nevertheless, this freedom is nowadays paid for by an excessive use of fossil energies – in particular mineral oil. The majority of transportation systems, such as airplanes, ships, trucks and automobiles are powered by mineral based fuels. Not only because of ever more strict regulations to avoid CO₂ driven climate change, but more significantly the decreasing availability of mineral oil, will force a transition to alternative energy sources. In 2012, the ratio of the remaining world proven crude oil reserves and actual oil production lies still at 56 years, further reservoirs are still being discovered [103] and new exploitation techniques such as fracking are developed. Although the oil price is currently falling, in the long term perspective it is predicted to rise due to the limitation of resources [104, 105].

Alternative technologies may in future become more competitive due to rising prices of fossil oil or legislative incentives. Besides alternative fuels such as bio-fuels, liquefied natural gas or hydrogen, electrical energy storages are particularly promising for providing or buffering propulsion energy to automobiles. These battery electric vehicles or hybrid electric vehicles have a significantly higher tank-to-wheel efficiency. Especially under low load driving conditions, which occur for example in urban driving cycles, combustion engines are generally over-dimensioned to be able to provide sufficient acceleration power. A side effect of the high efficiency of electric and hybrid electric vehicles is that auxiliary on-board consumers account for a bigger portion of the overall energy consumption. Furthermore, waste heat generation of an electric drive train, which can be used for cabin heating, is not as abundant as in vehicles with a low tank-to-wheel efficiency. Electrically powered heating systems thus reduce the range of electric vehicles drastically [60]. But also hybrid vehicles and highly efficient combustion powered vehicles have only

small waste heat output at low power operation or during the warm-up phase of the engine. Covering this lack of waste heat by additional heating systems has a negative effect on the overall vehicle efficiency and fuel consumption. The necessary steady-state thermal power for vehicle cabin conditioning in fresh air mode is as high as 6 kW for the heating power and 9 kW for the evaporator cooling power¹ [67]. Attempts must therefore be made to reduce this high demand by various cabin optimization measures. This would significantly enhance the suitability of such vehicles for everyday use. The identification and quantification of such measures are subjects of this thesis.

1.2 Cabin Optimization Measures

Cabin optimization measures have already been analyzed by various authors for the operation of vehicles at warm ambient conditions and high solar irradiation with the goal to reduce the auxiliary air-conditioning load. Common concepts to reduce the high soaking temperatures of parked vehicles include the reduction of the solar transmission and absorption of the glazing, solar-reflective paint and cabin ventilation powered by solar panels [91, 126].

For operation in cold environments fewer optimization concepts are proposed and they are partly differing from the measures which are advantageous in summer. Insulation of the cabin and the glazing is one of the most promising concepts to reduce the steady-state heating demand at cold ambient conditions, but this can have negative effects for summer operation at the same time. Although additional insulation reduces the thermal losses if differences between the cabin and the ambient temperature are high, the more severe problem in summer are high ambient humidity levels and solar irradiation involving high soaking temperatures of parked vehicles. Additional vehicle insulation increases this soaking temperature due to a stronger greenhouse effect [125]. However, at cold ambient conditions, soaking of the vehicle is an advantage. Insulation of the vehicle and especially the glazing leads to a reduction of the necessary heating power and enhances thermal comfort because of higher surface radiation temperatures and reduced draft [101].

¹At -20°C ambient temperature, respectively at 40°C ambient temperature, 50% relative humidity and 900 W/m^2 solar irradiance.

An even greater and easier realizable measure to reduce the thermal demand in summer and winter operation is the recirculation of cabin air instead of pure fresh-air mode. According to Großmann [67] approximately 50% of the above mentioned heating demand and even a higher fraction of the cooling demand are saved by full recirculation mode. Whereas in summer the recirculation fraction is only limited by sufficient air-quality which must be guaranteed [7], recirculation quickly leads to fogging of the windows at cold ambient conditions due to low window temperatures and water vapor emissions in the cabin.

Another effective way to reduce the power consumption of the central Heating Ventilation and Air-Conditioning unit (HVAC) as well as the overall thermal energy consumption is the application of local conditioning measures. Instead of distributing air relatively unfocused into the cabin and towards the windows or passengers, thermal conditioning can also be realized by localized targeted systems. These include state-of-the-art measures such as window, seat or driving wheel heating, but also more innovative concepts such as panel heating [21], seat belt conditioning [75] and zonal air-conditioning [79]. Several recent studies show that the thermal power is decreased significantly by such systems, whereas the thermal comfort level is maintained or even increased [16, 21, 79, 87].

There is a strong necessity in the vehicle development process to predict the effect of various cabin optimization measures in an early design stage. This is efficiently achieved by numerical simulation. Various concepts of cabin models are used in industry and have been presented in publications. These include fast computing 0D or 1D thermal models which can be easily integrated into a complete vehicle simulation [18, 134] or a "Hardware in the Loop" (HiL) simulation [54]. Such models can provide good estimations of the overall heat transfer, the airflow and the mean cabin air temperature. Models which can account for an air temperature gradient inside the cabin include zonal models [54], detailed 3D shell structural models [39, 116] and CFD models of the cabin geometry and the internal flow field [131, 132]. Nevertheless, modeling the above mentioned measures requires not only a 3D temperature and humidity distribution but also detailed sub-models of the thermal comfort perception and the evaluation of window fogging.

1.3 Goal of the Thesis

The goal of this thesis is to develop a tool for the prediction of the effects of various cabin optimization measures, such as recirculation, insulation and local heating. First, this requires a **3D CFD cabin model** to obtain the temperature and humidity distribution and evolution. To model the heat transfer between the cabin air and the environment, a transient shell layer **structural model** is used. The same model is also applied to compute the seat temperature evolution.

The state-of-the-art motivation to apply local heating or cooling measures is an enhancement of passenger thermal comfort. Nevertheless, little is known about the energy saving potential if local measures widely replace the central HVAC conditioning, which is a goal of this thesis. The effect of local measures, such as seat or panel heating, together with a reduction of the central HVAC heating power, on energy consumption and **thermal comfort** shall be analyzed. The prediction of passenger thermal comfort is realized by the established Fiala Physiological Comfort (FPC) model, as this model takes the influence of temperature and humidity gradients inside the cabin into account.

Reduced fresh air supply due to recirculation can quickly lead to window fogging at cold ambient conditions, thus the issue of **window fogging** is indirectly linked to the question of how much heating energy is saved.

The numerical model must therefore be capable of reproducing the four mentioned aspects as illustrated in figure 1.1. Various interactions between the different aspects exist, e.g. the surface temperature of the windows has an influence on window fogging, thermal comfort and cabin heat transfer. Only a model that fully integrates all aspects in one coupled model can account for such interactions.

Although there are several publications [29, 31, 40, 72, 161] and software solutions [9, 24] specifically addressing the issue of window fogging simulation in vehicles, relevant aspects seem not to be resolved unanimously. Especially the question whether or not the geometry of the condensed droplets has an influence on the heat and mass transfer from and to the window surface is discussed contrarily in different publications. In power plants the effect of "drop-wise condensation" significantly enhances the heat and mass transfer

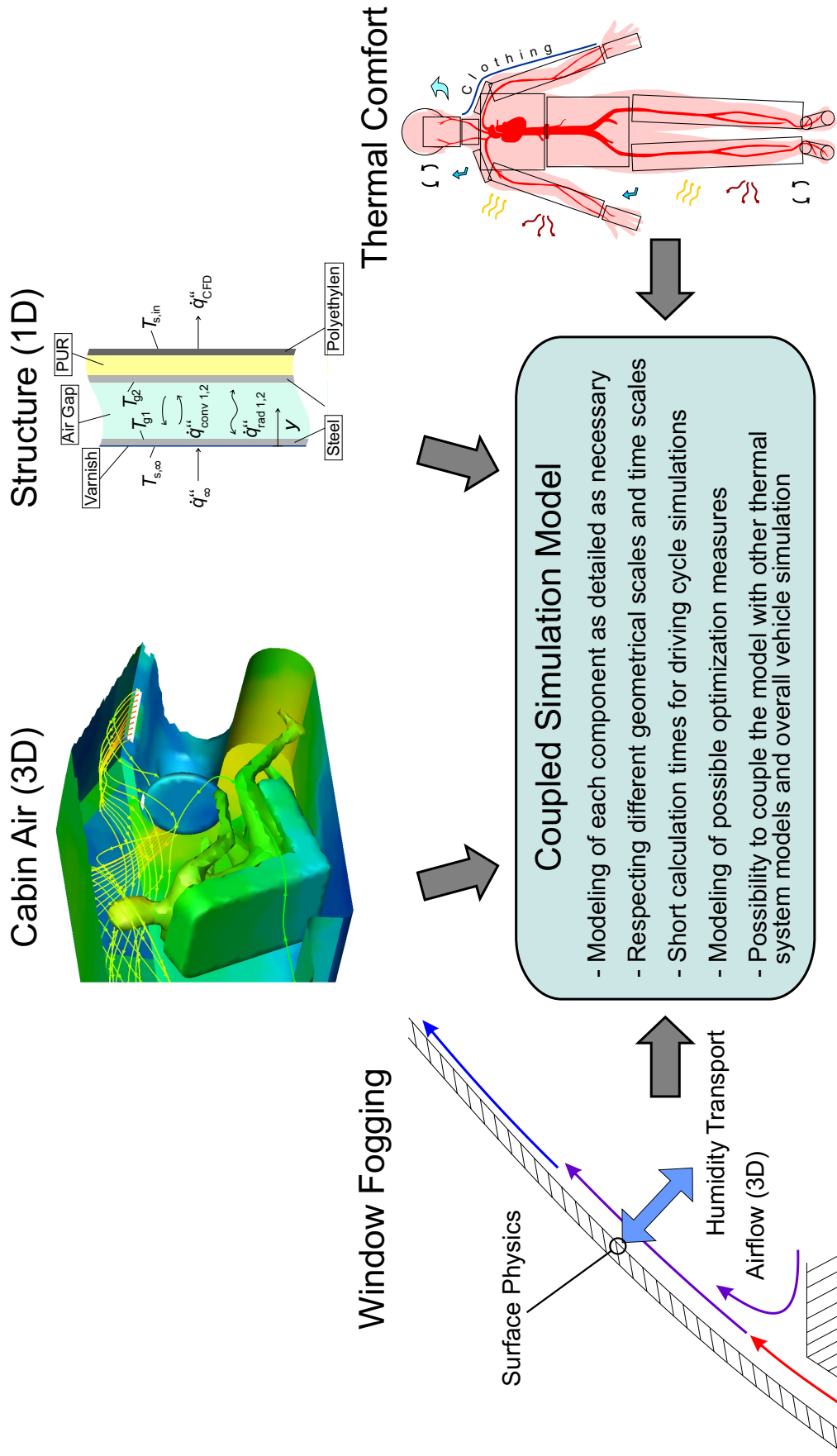


Figure 1.1: Sub-models and coupled simulation model to predict the energy saving potential of different optimization measures.

in comparison to "film condensation". However, opinions differ on whether similar effects are also relevant under typical window fogging conditions. Hydrophobic coatings or polymer glazing materials can significantly alter the resulting contact angles of droplets which has a major influence on the transparency of a fogged window as shown in a preceding study [84]. Several hypotheses, which are presented in section 2.2.5, reinforce the theory that the droplet geometry has not only an influence on optics but also on mass transfer. On the other hand, the vapor transport process is characterized by diffusion through air, leading to heat transfer rates being orders of magnitude lower than in power plants. Thus, a further goal of this thesis is to find out whether or not an interaction between heat and mass transfer and the droplet geometry exists. Based on these findings a suitable numerical window fogging model shall be developed and integrated into the coupled cabin model.

The local condensation mass flux needs to be measured to be able to validate the performance of the window fogging model. To find possible interactions between heat and mass transfer and the droplet geometry, the droplet distribution, size and shape also need to be known. Therefore a new measurement technique which detects shapes, respectively contact angles, of single droplets and droplet arrays from perpendicularly above is developed. This technique, together with an image processing algorithm, allows to measure the local condensation and evaporation mass flux optically.

1.4 Thesis Overview

As described in the previous section, one part of the thesis is a numerical cabin model to quantify the effects of different optimization measures. This entails the inclusion of different sub-models to compute cabin temperature and humidity transport, heat transfer in the vehicle structure, passenger thermal comfort and window fogging. These sub-models differ significantly in the underlying physics, appropriate modeling approaches and experimental methods for the validation. It is therefore decided to structure the thesis according to these different sub-models.

Unlike in other theses there are no global chapters for "Theory", "State-of-the-Art", "Experimental Methods" et cetera, but in each chapter (e.g. "Window Fogging") these chapters are included separately. Subsequent to the "In-

roduction", the main chapters are thus: "2 Window Fogging", "3 Passenger Thermal Comfort" and "4 Cabin Modeling". Whereas chapters 2 and 3 focus on specific single topics, chapter 4 includes the CFD modeling of the vehicle cabin, the structural heat transfer model and the coupled simulation of all sub-models. In section "4.5 Saving Potential of Optimization Measures" the effects of various cabin optimization measures are predicted.

The thesis concludes with a global summary of all topics and an outlook for possible future research and development projects.

2 Window Fogging

The prevention of window fogging is essential if heating energy is saved by the reduction of the cabin fresh air supply. Therefore, the development of a suitable and validated window fogging model as a part of the coupled vehicle cabin model is the goal of this chapter. In section 2.1 the underlying physics of droplet formation, droplet contact angles and mass transfer is discussed. An overview over the issue of window fogging in vehicles and the state-of-the-art of its numerical modeling is given. The paragraphs included in sections 2.1.1 and 2.1.2 are partly adapted from Carey [23], who gives a good overview of various droplet and liquid-vapor phase-change phenomena. In section 2.2 an experimental setup and experimental results are presented which are used to validate the performance of the window fogging model. The experiments include a new measurement technique to measure contact angles and droplet volumes. This allows to measure the local area-based condensation and evaporation rate. In section 2.3 the numerical window fogging model is presented and compared to experimental data.

2.1 Theory and State-of-the-Art

The following sections include topics related to window fogging with which readers may not be as familiar, such as molecular interactions, surface tension, contact angles, drop-wise condensation and modeling approaches for window fogging. These topics are considered essential e.g. for the understanding of a new analysis method of droplet shapes and contact angles presented in chapter 2.2.2. Nevertheless, the reader is expected to be familiar with the basics of other related and applied physical theories, such as mixing and saturation of water vapor in air or diffusive and turbulent transport mechanisms. If required, detailed information on these theories are found in various standard references (compare e.g. [10, 12]).

2.1.1 Molecular Approach

In this section an overview of molecular interactions is given for the understanding of surface tension effects of water droplets. Surface tension is responsible for the shape of droplets, the contact angle, contact angle hysteresis and coalescence. Droplet shape analysis and contact angle measurements are essential parts of the experiments presented in chapter 2.2.

Relevant physical phenomena of droplets, such as nucleation, surface tension and contact angles, can be described by molecular interactions. Between the liquid water molecules, the gas molecules and the molecules of the substrate material, different repulsive and attractive forces act in dependence of the distances of the respective molecules from each other. At a very low distance R between two molecules the repulsive forces dominate. This is explained by the so called Pauli repulsion or Pauli exclusion principle which summarizes the repulsive effects of the interferences between overlapping electron orbits of two molecules [97]. The exact mechanisms involved depend on the types of molecules, but in a simplified approach the repulsive potential function is written as:

$$\Phi_{\text{rep}} = \frac{\lambda_0}{R^k}, \quad 9 \leq k \leq 15. \quad (2.1)$$

Here, λ_0 is a constant which depends on the type of molecules. The acting force of the two molecules corresponds to the derivative of the potential function and is $-\frac{d\Phi}{dR}$.

At larger distances, acting forces include the electrostatic forces, induction forces or the London dispersion forces. Electrostatic forces arise between ionized particles or between polar molecules. The polarity of molecules can also be induced by either an ionized particle, another polar molecule or even an apolar molecule, as in the case of the London dispersion forces. For the London dispersion forces the potential function is written as :

$$\Phi_{\text{dis}} = -\frac{\lambda_{\text{dis}}\alpha_P^2}{R^6}. \quad (2.2)$$

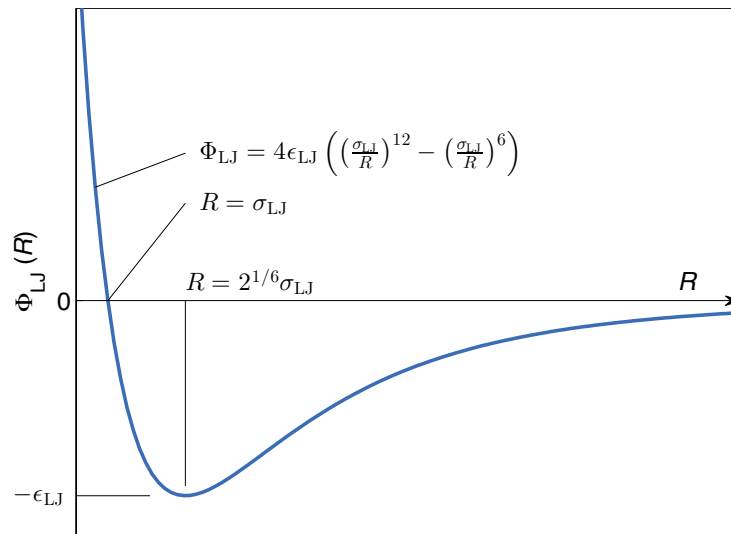


Figure 2.1: Lennard-Jones 6-12 potential (image adapted from Carey [23]).

Water molecules have a strong dipole moment. Hydrogen bonds between the molecules can provoke a strong intermolecular binding force, which is responsible for the relatively high boiling temperature of water. The weak intermolecular forces are also frequently summarized as van der Waals forces [97]. The strength of these forces depends on the dipole moment or respectively the polarizability α_P of the molecules. The associated energy potential is approximately proportional to R^{-6} . The repulsive and attractive forces are summed in a global potential function. A simplified but well-known approach of such a function is the Lennard-Jones 6-12 potential:

$$\Phi_{LJ} = 4\epsilon_{LJ} \left(\left(\frac{\sigma_{LJ}}{R} \right)^{12} - \left(\frac{\sigma_{LJ}}{R} \right)^6 \right). \quad (2.3)$$

Here, the repulsive potential is assumed to decrease by the power of -12 with rising molecule distance R . The parameters ϵ_{LJ} and σ_{LJ} depend on the type of molecule.

The right part of the minimum of this function explains the fact that energy needs to be removed when distant molecules are brought closer together (latent heat of condensation) and added when molecules are separated (latent heat of evaporation).

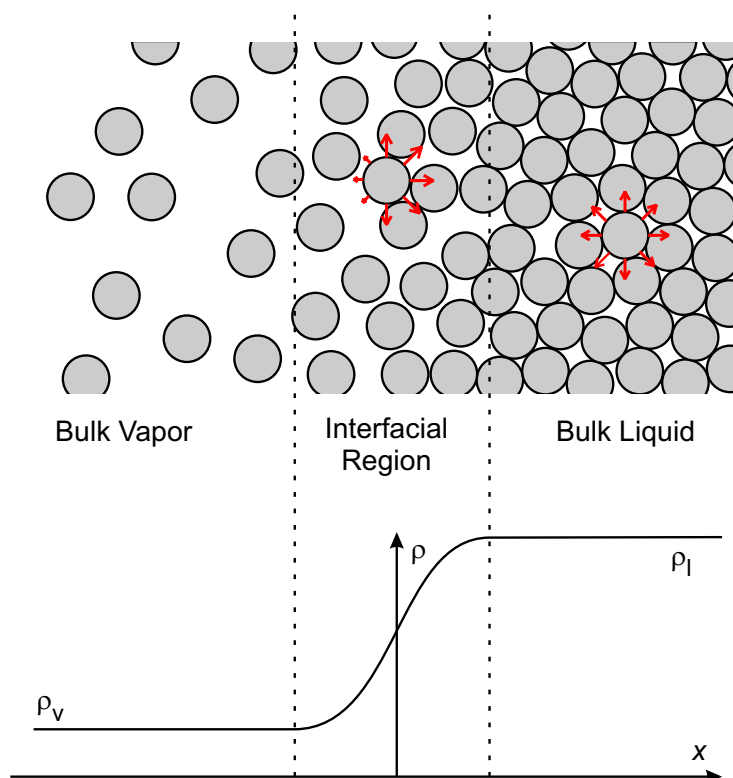


Figure 2.2: Schematic illustration of the liquid-vapor interfacial region showing a variation of the molecular density (image adapted from Carey [23] and Marchand et al. [89]). Arrows illustrate exemplarily the attractive molecular forces between droplets in the bulk liquid and in the interfacial region.

The interface region of water in touch with its vapor can be described by a molecular approach. The density in the interface region is lower than in the bulk liquid. The energy per molecule is higher in the interface region, as the inter-molecular distances become larger, which can also be seen in the potential function (see figure 2.1). Thus, an additional excess free energy per unit area needs to be supplied for the generation of the interface. At the same time, a force balance consideration of the molecules in the interface region shows that attractive forces, which have a greater range, dominate this region. Due to the density gradient, more attractive partner molecules lie on the bulk liquid side. Hence, a macroscopic force per unit length parallel to the interface becomes visible (see figure 2.2).

This interfacial force determines the geometry of the liquid-vapor interface and the contact angle θ . The molecular interactions are analogous for pure water in contact with its vapor and for water in contact with humid air, where

non-condensable gas molecules, such as N_2 and O_2 , dissolve in the liquid phase and the water density distribution is slightly different. Nevertheless, the presence of non-condensable gases has a negligible influence on surface tension, if the gas phase is saturated [109, 120, 142].

2.1.2 Macroscopic Approach

A macroscopic approach of surface tension is first developed qualitatively by Young in 1805 [152]. The Young-Laplace equation relates the difference in static pressure across an interface to the radii of curvature and the surface tension γ of the interface. It can be derived both by force balance or thermodynamic considerations from an infinitesimal interface section (compare [23]). This equation is used to mathematically describe the droplet shape of an axisymmetric droplet with and without gravitational influence in the developed drop shape analysis method (see sections 2.2.2.1 and 2.2.2.2):

$$\Delta p = \gamma \left(\frac{1}{R_1} + \frac{1}{R_2} \right). \quad (2.4)$$

The classical Young equation describes the contact angle at a three phase contact line and is derived by minimizing the excess Gibbs free energy at constant volume with respect to the contact angle (see left boxes in equations (2.5) – (2.6) and compare [150]):

$$\boxed{dF = p dV + \sum_i \gamma_i dA_i} + \boxed{\sigma dL_{\text{cln}}}. \quad (2.5)$$

The theory of the so-called contact line tension σ is first mentioned by Gibbs in 1878 [63] and is since then controversially discussed by various authors [62, 82, 111, 147]. The reported orders of magnitude of the line tension range from values as low as 10^{-11} J/m up to values as high as 10^{-5} J/m with negative as well as positive signs [147]. As the current state of science on this topic seems not yet to be completely clarified, it is not discussed in detail here. Nevertheless, the dependencies of the contact angle on droplet radius observed in section 2.2.4.3 of this thesis possibly result from line tension effects, which is the reason why this theory is mentioned here. An additional potential excess

free energy σ per unit length of the contact line leads to an additional term in equation (2.5) and yields the modified Young equation (2.6):

$$\gamma_{s,v} - \gamma_{s,l} = \gamma_{l,v} \cos \theta + \frac{\sigma}{R_{\text{cln}}}. \quad (2.6)$$

2.1.3 Influence of Gravitation on the Interface

Gravitational forces do not influence the shape of small droplets, such as those observed in the conducted condensation experiments presented in section 2.2.4. Nevertheless, for the sake of completeness, the new contact angle and drop shape analysis method presented in section 2.2.2 is derived for both, droplets with and without gravitational influences. The following paragraphs help to understand the influence of gravity on the droplet shape.

Gravitational forces can have a significant influence on the shape of the liquid-vapor interface due to the density difference $\Delta\rho$ of the two phases. This influence is expressed by the dimensionless Bond number Bo which relates gravitational forces to interfacial forces:

$$\text{Bo} = \frac{\Delta\rho g R_0^2}{\gamma}. \quad (2.7)$$

As seen in equation (2.7), the Bond number increases with the square of the radius R_0 which is used as the characteristic length scale¹. Hence, the gravitational influence can be neglected for small droplets where the local principal radii of curvature R_1 and R_2 are equal in all points ($R_0 = R_1 = R_2$). This leads to a spherical shape of the interface [23].

For large droplets with a distinctive influence of gravity, the shape of the droplet is complex but can nevertheless be generally described by the Young-

¹ Here, R_0 is the radius of curvature at the droplet apex. Although also other quantities such as the projected droplet diameter are used as a length scale in literature, using R_0 has advantages in solving the differential equation which describes the profile of an axisymmetric droplet profile with gravitational influence, and has been proposed by others as a characteristic length scale of the droplet [23, 127].

Laplace equation (2.4) extended by the height dependent influence of gravity with the pressure difference Δp_0 between the two phases at the droplet apex :

$$\gamma \left(\frac{1}{R_1} + \frac{1}{R_2} \right) = \Delta p = \Delta p_0 + \Delta \rho g z. \quad (2.8)$$

Here, the origin of the coordinate system is at the apex of the droplet and the rotationally symmetric interface is described by the coordinates x , z and φ in dependence of the arc length s measured from the origin (see figure 2.3). No analytic solution is known to equation (2.8), but it is first solved numerically by Bashfort and Adams in 1883 [11].

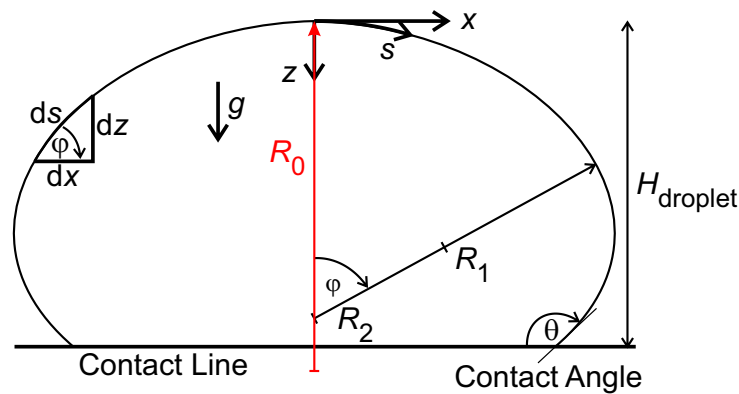


Figure 2.3: Axisymmetric droplet profile with gravitational influence and definition of the coordinate system (image adapted from Rotenberg et al. [122]).

A numerical approach to solve equation (2.8) is presented in section 2.2.2.1: The surface profile of an axisymmetric droplet is used to measure the contact angle and volume of the droplet by observed light reflections.

2.1.4 Drop-Wise Condensation and Evaporation

In fogging at window surfaces, water usually condenses by forming small droplets. The formation of droplets instead of a continuous film is called drop-wise condensation. Depending on the surface, the droplet shape can vary significantly. Some existing window fogging models (see section 2.1.6) take into account the geometry of the condensed droplets. In chapter 2.2.5 it is studied in detail, under which conditions the droplet shape and distribution has an influence on condensation and evaporation mass transfer. In the following

paragraphs the influence of drop-wise condensation and evaporation on heat and mass transfer is explained.

On hydrophobic surfaces, which form large contact angles with the condensing fluid, drop-wise condensation occurs instead of film condensation. Drop-wise condensation substantially increases heat and mass transfer in some cases. The phenomenon is studied by various authors, but the technological background of most studies is power-plant research: Here, drop-wise condensation leads to a higher heat transfer efficiency in condensers and a significant improvement of the overall plant efficiency (compare e.g. [76, 148]). The focus of such studies often lies on the maximization of the heat transfer coefficient and on sustainable promoter coatings on copper condensers to ensure drop-wise condensation. The high contact angle of water on the coating leads to the formation of droplets rather than a film. Thus, blank condenser area is partly exposed to the condensing gas. The surface temperature of the blank surfaces is significantly lower than the surface temperature of the water film or the droplets. Therefore, the heat transfer coefficient is increased by a factor of more than ten for droplet condensation in comparison to film condensation [81].

2.1.4.1 Heat Transfer Rate

Chung et al. [28] compare the actual condensation and heat transfer rates in the presence of non-condensable gases in water vapor and find experimentally that even small concentrations of air reduce the heat transfer rate significantly in drop-wise as well as film-wise condensation. Both rates become approximately equal at air concentrations of 1.6 – 6.5%, as the transport process is governed by diffusion through an air-rich layer at the surface.

Ganzevles and Geld [59] study the heat and mass transfer of a pattern of 12 hemispheres on a wall, representing droplets in a channel flow. The mass transfer rate is determined by the evaporation of naphthalene, separately from the hemispheres and from the flat parts in between. They observe an increase of the mass transfer coefficient of 100% for the hemispheres in comparison to the flat parts and a dependency of the mass flow rate on the droplet size. These results are obtained for relatively large droplets ($D_{\text{droplet}} = 3 - 8 \text{ mm}$), a limited number (12 droplets), a projected surface coverage of $\phi = 33\%$ and

Reynolds numbers between $Re = 4 \cdot 10^2$ and $Re = 9 \cdot 10^3$. Most of these conditions are nevertheless quite different from window fogging conditions and are not directly transferable: For window fogging the amount of droplets is typically very large, the surface coverage is high and the droplets are very small, at least in the beginning.

2.1.4.2 Droplet Growth Rate

Fritter et al. [58], Beysens et al. [14, 15] as well as Family and Meakin [44, 90] study in detail the different phases of drop-wise condensation, coalescence of droplets and the resulting droplet patterns and size distributions. They describe the process of coalescence to be self-similar, as the coalescence of large droplets leaves a large portion of blank substrate surface where a new generation of small droplets can form. They develop a statistical 2D numerical model for the prediction of drop-wise condensation patterns and the drop size distribution on a surface. The volume of a single droplet at this surface is described to be proportional to time due to diffusion from the bulk flow through a layer of quiet air [14]. Thus, Beysens et al. [14] give the droplet radius law of growth as:

$$R \propto t^\mu, \quad (2.9)$$

with an exponent of $\mu = 1/3$. This is equivalent to an average area-related condensation rate that is not dependent on the droplet size distribution if the number of droplets stays constant. An overview of the dependence between growth rate exponent μ and volumetric growth rate is given in table 2.1.

Table 2.1: Dependence between droplet growth rate exponent μ and volumetric growth rate. If the number of droplets at a surface is constant, the area-related volumetric growth rate dV/dt equals the condensation or evaporation volume flux and is proportional to \dot{m}''_{cond} , respectively \dot{m}''_{evap} .

μ	R	dV/dt
1/3	$R \propto t^{1/3}$	$dV/dt = \text{const.}$
1/2	$R \propto t^{1/2}$	$dV/dt \propto R$
1	$R \propto t$	$dV/dt \propto R^2$

On the other hand, Leach et al. [78] experimentally find a strong dependence of the volumetric growth rate on the size of individual droplets. They postulate the individual volumetric growth rate dV/dt to be proportional to the radius R for small drops up to a diameter of $2.5 \cdot 10^{-5}$ m to $5 \cdot 10^{-5}$ m corresponding to a growth rate exponent of $\mu = 1/2$. According to Leach et al. [78], the growth rate of large droplets is proportional to the droplet surface, which is equivalent to a growth rate exponent of $\mu = 1$. As the droplet size distribution and density can vary significantly over time due to coalescence, the growth rates of individual droplets can only be transferred to an area-averaged condensation mass flux after an integration over the entire droplet population.

The diffusive steady-state evaporation rate of a single droplet in a stationary gas volume is proportional to the radius of the droplet $\dot{m}''_{\text{evap}} \propto R$, leading to a growth rate exponent of $\mu = 1/2$. This can be shown on a theoretical base (compare [113]) and is also confirmed experimentally by Birdi et al. [17] for a single droplet resting on a solid plate.

Chandra et al. [25] study numerically and experimentally the evaporation of a single droplet on a warm surface ($60^\circ\text{C} - 110^\circ\text{C}$) as a heat transfer driven problem. Whereas the evaporation rate of the respective droplet remains constant until the droplet is almost completely evaporated, a strong dependence of the evaporation rate on the contact angle of a droplet is reported. By adding 1000 ppm of a surfactant solution to a droplet, the initial contact angle on steel is reduced from 90° to 20° and the evaporation time is reduced by 50%.

The droplet growth rates given in literature and presented above show that droplet growth, respectively condensation and evaporation rate, changes significantly depending on the factors involved. For single droplets different growth laws apply than for droplet arrays. Average growth rates of $\mu \neq 1/3$ indicate a dependence of the condensation and evaporation mass flux on the size of the droplets. Such a dependence requires a droplet model to accurately predict the condensation and evaporation mass flux. Existing models to predict window fogging in vehicles are presented in section 2.1.6 and partly include droplet models, whereas other presented models use homogeneous film models. Whether or not a droplet model is required under typical window fogging conditions is analyzed experimentally and theoretically in chapter 2.2.5.

2.1.4.3 Surface Coverage

Tanemura [138] shows by Monte Carlo simulation that the surface coverage ϕ of a random packing by uniform disks on a 2D surface is $\phi = 55\%$. With a non-uniform distribution of disk sizes, higher surface coverage values are possible. Fritter et al. [58] find a surface coverage of 57% for a statistical simulation of a condensation process assuming spherical droplets.

Prior to the onset of coalescence, Leach et al. [78] experimentally find a surface coverage close to 55%. As condensation proceeds, they report a significant dependence of the surface coverage from the contact angle with an increasing value of ϕ for smaller contact angles. On silanized glass with a contact angle of $\theta = 100^\circ$, a coverage of 60% is observed, whereas on a polyvinylidene chloride (PVDC) surface with a contact angle of $\theta = 60^\circ$ the surface coverage ϕ rises to 75 – 80%. Zhao and Beysens [160] analyze the surface coverage for a broad variation of the contact angle on a silicon wafer and find values of $\phi = 95\%$ for small contact angles of $\theta = 10^\circ$, and ϕ close to 55% for a contact angle of $\theta = 90^\circ$. They identify the rising influence of contact angle hysteresis to be responsible for this difference.

2.1.5 Window Fogging in Vehicles

Interior window fogging in vehicles and the parameters involved are investigated analytically by Peters already in 1972 [110]. For a long time, the interest in this subject is motivated from a driving safety perspective. Window fogging and defogging and the related issue of exterior window icing and deicing are therefore subject of several regulations and standardized test procedures in different countries [8, 43, 117, 141]. Typically, the HVAC system of a vehicle must be capable of deicing and demisting a certain area fraction of the windscreen during a defined period of time. This is the reason why the HVAC system and the air nozzles are mainly designed for a powerful defrost operation instead of an energy efficient and sustainable prevention of window fogging. Possible improvements to the **defrost nozzles design** are summarized by Nasr and AbdulNour [96]. Promising measures are analyzed by Sakamoto et al. [128] and include the reduction of turbulence and airflow attenuation and the optimization of the size, position and relative angle between the windshield and the nozzles.

Aceves and Smith [1] identify the humidity production by the passengers to be responsible for the high heating loads in vehicles because of the necessary defogging operation and high fresh air volume flow. They propose a desiccant **dehumidification system** for electric vehicles.

An HVAC design patented by DENSO [100] and presented by Shikata et al. [133] describes a **two-layer flow** system. In the upper part of the vehicle dry ambient air is conducted to the windows, whereas in the lower part of the vehicle, air is recirculated, which helps to reduce the ventilation losses during heating operation.

Algorithms and **sensors** to avoid interior window fogging and to control the recirculation and fresh airflow have become state-of-the-art in some vehicles [69, 70, 140, 146]. Nevertheless, sensors are mostly placed at the front window and thus can only roughly estimate the window fogging affinity of the other windows.

Electrical window heating is an efficient way to reduce the window fogging although the electrical energy input is considerable. Just for the rear window heating system, the typically applied electrical power lies between 200 – 300 W [67]. Wire based systems are state-of-the-art for front and rear windows and progress is made with transparent heatable coatings or films [67, 136]. An important advantage of electrical window heating is the possibility to easily control the window surface temperature according to the local fogging affinity.

There are a number of **coatings** to reduce window or spectacle fogging, respectively to improve the visibility through a fogged surface. These coatings consist of a hydrophilic layer [80, 98, 102] or a layer which is able to absorb a certain amount of water [80]. Thus, although the condensation mass flux is not influenced, the condensed film or absorbed water generates less light scattering than droplets. Nevertheless, the buffering capacity of such coatings is limited, and they are still too expensive and damageable for standard automotive applications.

Thermal insulation of the vehicle and notably the windows is a means to reduce the fogging affinity and to enhance thermal comfort. Norin [101] proposes double pane glazing to significantly raise the inner surface temperature of the glazing above the cabin dew point temperature and thus avoid window fogging and enhance thermal comfort at the same time. Polycarbonate as a

glazing material is proposed by Gasworth and Tankala [61] to reduce the heating and air-conditioning load as the thermal conductivity of polycarbonate is reduced by 80% in comparison to glass. An advantageous fogging behavior of polycarbonate due to the higher inner surface temperature and a better transparency of the fogged surface are reported in two earlier studies by Lorenz et al. [84, 88].

2.1.6 Simulation of Window Fogging

Several publications focus specifically on the numerical simulation of window fogging and defogging. In this section existing models for the simulation of window fogging in vehicles are presented. It is shown that some authors [29–32, 46, 72] apply droplet models which take an influence of the droplet pattern and the droplet geometry on heat and mass transfer into account. Other authors [22, 40, 161] use thin film models and neglect any influence of the real condensate structure. One goal of this thesis is to find out whether such an influence is relevant for window fogging in vehicles. The overview of existing models is thus presented as the base for the developed window fogging model, which is presented in section 2.3.1.2.

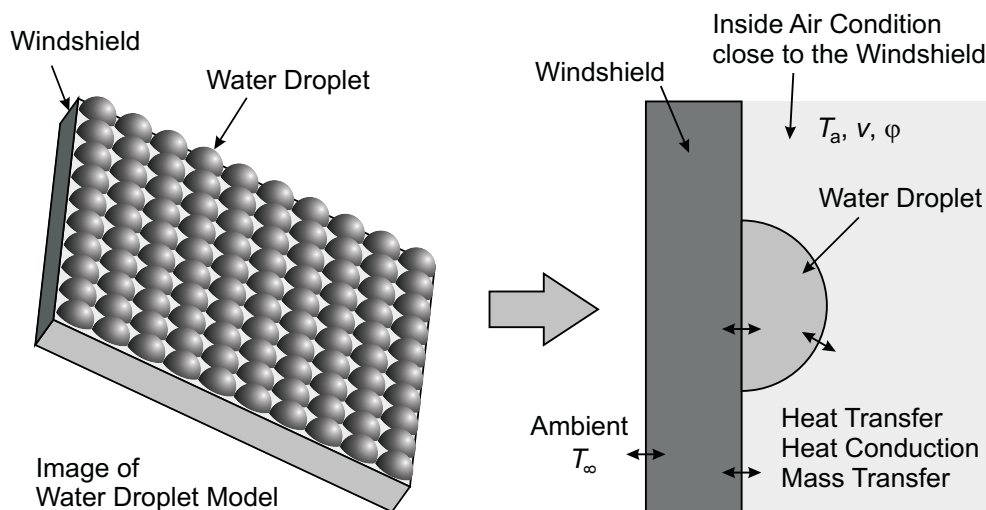


Figure 2.4: Droplet window fogging model assumed by Kitada for the evaluation of the evaporation mass flow (image adapted from Kitada et al. [72]).

Kitada et al. [72] propose an analytical droplet model, coupled with a CFD simulation of the cabin to calculate the defogging speed of automobile windshields (see figure 2.4). The vapor mass flux and the heat flux are expressed

as functions of the temperatures of the bulk flow and the droplets, the corresponding vapor pressures and the size of the hemispherical droplet vapor interface. During evaporation, the rate of change of the droplet radius dR/dt is assumed to be independent of time and droplet size, which is equivalent to a radius growth rate coefficient of $\mu = 1$. The droplet radius change rate during condensation is assumed proportional to R^{-1} , corresponding to a growth rate coefficient of $\mu = 0.5$.

Croce et al. [29–31] and Candido and Croce [32] apply a condensation and evaporation model similar to the evaporation model of Kitada et al. [72], which considers the droplet distribution and geometry. In analogy to the classical "Messinger" model [92], which is used to predict the icing of airfoils, a heat transfer balance is conducted at the liquid-vapor and solid-vapor interfaces including the latent heat production to determine the temperature of the interface and the droplets. The diffusive mass flow rate per unit area is assumed to be proportional to the liquid-vapor interface area of the droplet, corresponding again to a radius growth rate coefficient of $\mu = 1$ at a constant droplet number.

Fayazbakhsh and Bahrami [46] develop an analytical model for mist condensation by natural convection. This model is based on the works of Croce et al. [29–31] by describing the heat and mass transfer balances at the liquid-vapor interface and the liquid-solid interface of the droplet. A constant surface coverage of 55% is assumed. The vapor side heat and mass transfer is solved via an empirical Nusselt, respectively Sherwood correlation. The interface temperature is assumed to be equal for the liquid-vapor and the liquid-solid interface. Thus, the resulting interface temperature at a specific position is solved by iteration.

Thiago et al. [161] use a built-in defogging model of the CD-ADAPCO STAR-CCM+ CFD software [24] to model the fogging and defogging process of an automobile windshield. This defogging model is a thin film model. For computing the diffusion mass flux inside a cell, an adjustable empirical constant to determine the mass transfer coefficient k_c is applied.

Doroudian [40] and Brunberg and Aspelin [22] use the Defogging Module² of FLUENT Version 6.3, built-in via User Defined Functions (UDF) based on the c-programming language. Here, fogging and defogging is modeled by a con-

tinuous film model. Individual droplets are not regarded and the film is assumed to be thin and stationary. The mass transfer between the first highly resolved prism mesh node ($y^+ = 1$) and the water film surface is calculated by a diffusion law.

In section 2.2.5 of this study, it is shown that the influence of the droplet structure on heat and mass transfer is negligible for typical flow conditions and droplet sizes. A film model is thus found to adequately represent the relevant physical phenomena. As it is shown later the concept which is followed for the window fogging model is in parts based on the code of the Defogging Module of FLUENT version 6.3 provided by ANSYS [93]. For this thesis the Defogging Module is extended and used as a window fogging model, which is presented in section 2.3.1.2.

²The Defogging Module is not included in later versions of ANSYS FLUENT. The used version of ANSYS FLUENT is 14.5 and includes a so-called Eulerian Wall Film model (EWF), which is also suitable for modeling moving wall-films or a diffusion controlled thin water film [4, 5]. Nevertheless, no published studies applying this new model are available and the source and physics of the applied equations cannot be reconstructed.

2.2 Experimental Investigations

2.2.1 Test Rig Setup and Experimental Parameters

A simple experimental setup is used to derive suitable data for the development and validation of a condensation and evaporation model to simulate window fogging (see figures 2.5 and 2.6). Consisting of a rectangular channel [1 x 0.05 x 0.06 m], the geometrical setup of the test rig deviates fundamentally from the geometry of a vehicle cabin. Nevertheless, it is designed this way to provide an ideal measurement accessibility, a defined airflow over the fogged surface and an adjustable surface temperature. Consequently, the derived data is well suited to validate the CFD model without the uncertainty of local temperature and flow variations occurring in more complex geometries.

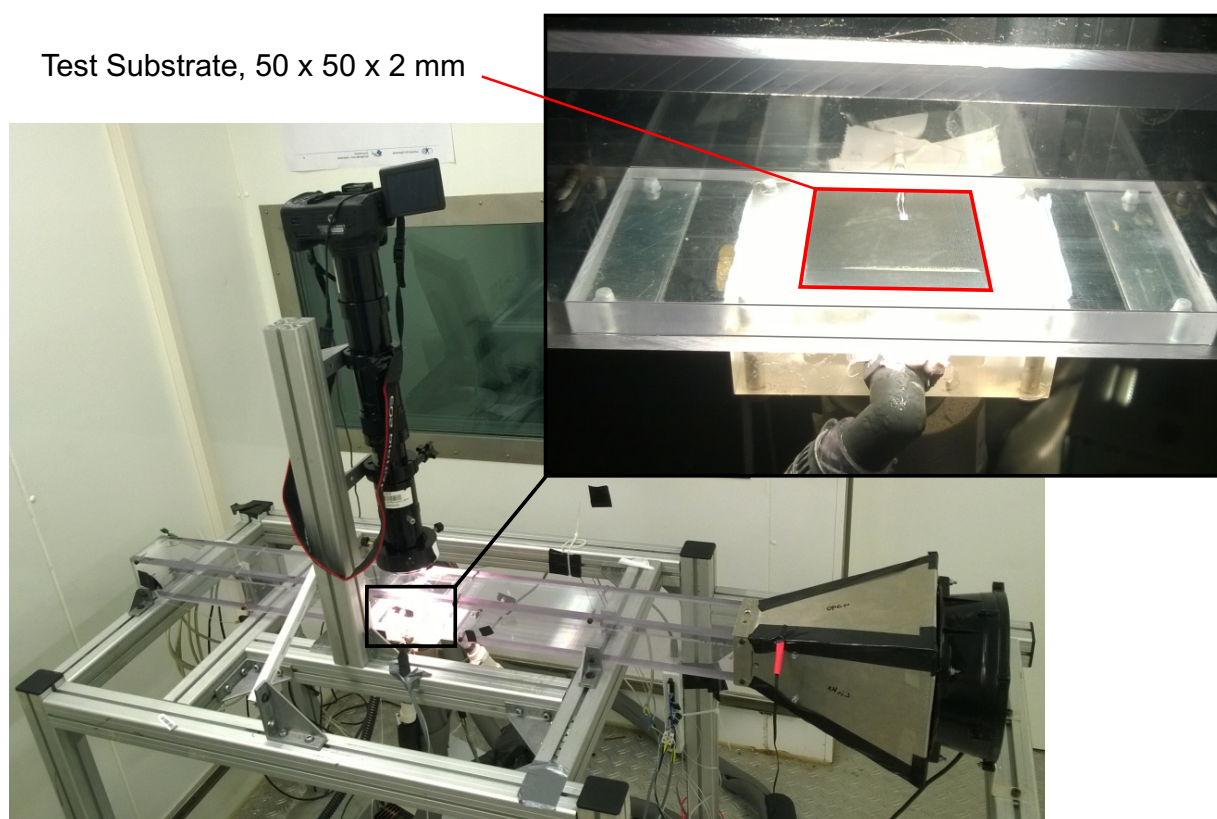


Figure 2.5: Window fogging test rig setup in the climate chamber.

The test section is located in the bottom center of a rectangular polycarbonate channel. A test substrate (50 x 50 x 2 mm) is embedded into the wall and

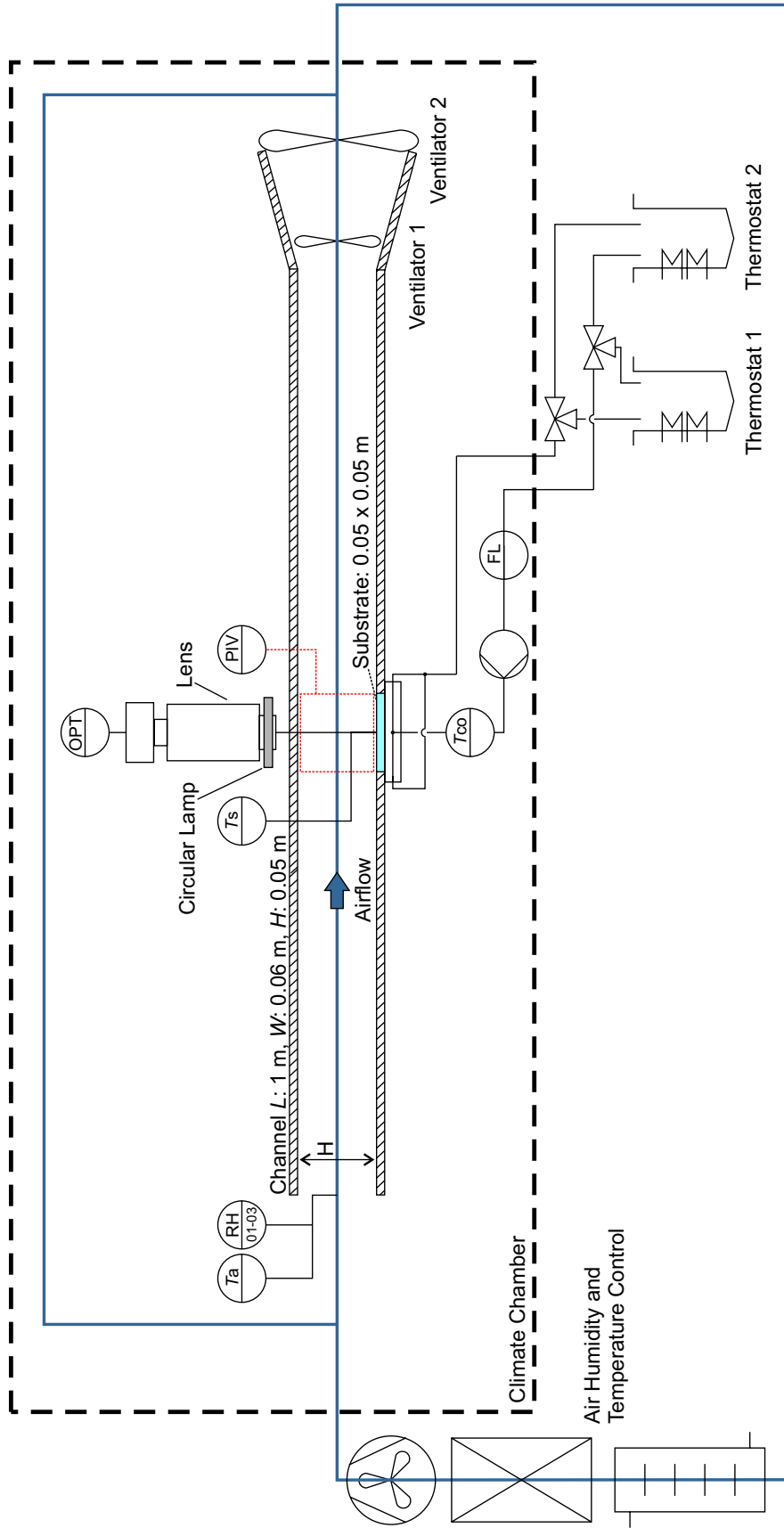


Figure 2.6: Schematic illustration of the experimental setup in the climate chamber with the following sensors: OPT – Digital camera, PIV – Particle Image Velocimetry, T_a – Air temperature, RH – Relative humidity, T_s – Surface Temperature, T_{co} – Coolant temperature, FL – Volume flow meter.

cooled by liquid from the bottom side to achieve condensation on the top side. Air is sucked through the channel by two ventilators in the rear part of the channel to generate an adjustable air flow velocity v_a in the channel. To provide a constant air temperature and humidity of the inflow air, the whole setup is placed into a climate chamber. The cooling of the substrate is realized by two switchable thermostats at different temperature levels and a water-ethanol 60%-40% mixture as a coolant. The lower temperature level $T_{co,0} = -5^\circ\text{C}$ is applied for the condensation phase, whereas the higher temperature level $T_{co,0} = 15^\circ\text{C}$ is subsequently used for evaporation of the condensed water on the substrate surface. In this way, the temperature of the substrate is kept almost constant during one test phase, but is changed almost instantaneously when switching from the condensation phase to the evaporation phase (compare figure 2.21).

During the two phases the condensed droplet pattern at the substrate center is observed with an optical measurement setup which is explained more in detail in section 2.2.2. A time series of this droplet pattern is illustrated in figure 2.7.

Conventional measurement instrumentation is used to capture the temperature T_a and humidity ϕ_a of the air and the temperature T_{co} and volume flow \dot{V}_{co} of the coolant. The actual absolute air pressure p_a is taken from a nearby meteorological station for each experimental run [83]. Particle Image Velocimetry (PIV) measurements are performed in a 50 x 50 mm cross section centrally above the substrate (see figure 2.6). The obtained two-dimensional transient flow fields allow the derivation of the mean velocity distribution as well as velocity fluctuations along the channel height. These parameters are imposed as inlet boundary conditions on the CFD simulation as described in section 2.3.1.3. The PIV measurements are performed in advance of the actual condensation and evaporation tests for an isothermal flow of 20°C at various velocities. The velocity and turbulence parameters derived from the PIV measurements are found in appendix A.

Experiments are conducted for a considerable range of different temperatures, humidity levels, airflow velocities and substrate types. The parameter variation presented in this study is limited to the variation of the airflow velocity and the substrate surface properties. The experimental parameters are listed in table 2.2. Four different airflow velocities are analyzed, which allows

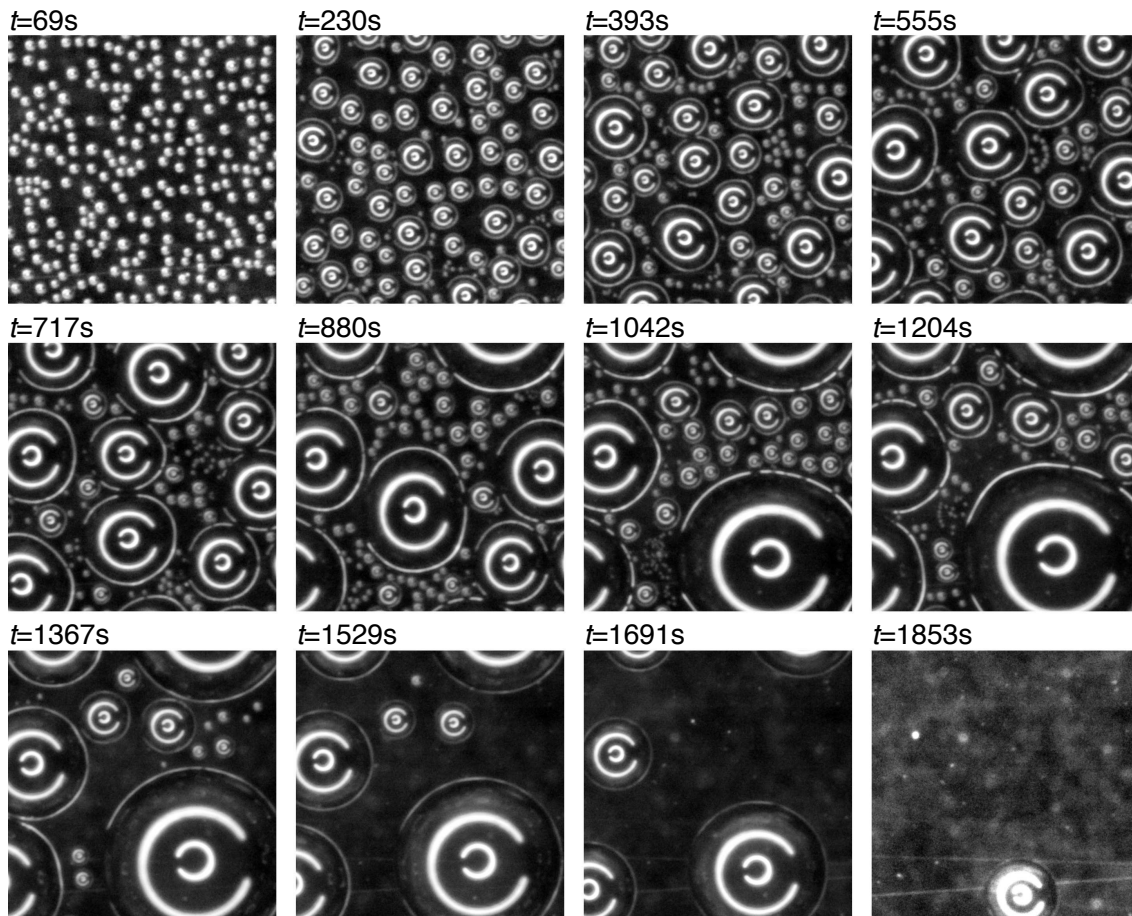


Figure 2.7: Droplet pattern time series during the condensation phase condensation ($t = 0 - 1200$ s) and the evaporation phase ($t = 1200 - 1840$ s) on a central 1×1 mm section of the untreated polycarbonate substrate at $Re = 2.9 \cdot 10^4$. The visible horseshoe-shaped reflections originate from an annular light source which is covered in one sector. This helps to differentiate between different reflections.

the analysis of laminar, transitional and turbulent flow regimes with Reynolds numbers between $1.2 \cdot 10^3$ and $4.9 \cdot 10^4$. These velocities are attained by different set-points of the two ventilators and range from the lowest mean air velocity of $v_{a,m} = 0.364$ m/s up to 14.3 m/s. A velocity of $v_{a,m} = 8.37$ m/s serves as a reference and is used as an example to illustrate various measurement parameters and for a mesh study of the corresponding CFD case (see chapter 2.3.1.2). This velocity level is sufficiently high to account for possible turbulence effects. The highest velocity level of 14.3 m/s is more sensitive to deviations and errors as the temperature difference between the surface tempera-

Table 2.2: Overview of the window fogging experimental parameters. Reference case parameters are underlined.

Parameter	Values
$v_{a,m}$	0.364/ 1.94/ <u>8.37</u> / 14.3 $\frac{m}{s}$
Surface Treatment	Hydrophobe Coating/ <u>Untreated</u> / Mechanical Abrasion 1/ Mechanical Abrasion 2
$T_{co,0}$	-5, 15 °C
\dot{V}_{co}	5 l/min
$T_{a,m}$	20.5 °C
$\phi_{a,m}$	49%
$p_{a,m}$	$96.2 \cdot 10^3$ Pa

ture and the saturation temperature of the air is only approximately 2 K at the substrate center (compare figure 2.34).

To analyze the interactions between the droplet geometry and the condensation and evaporation mass flux, a parameter variation with four different treatments of the substrate surface is carried out:

- The untreated polycarbonate surface serves as reference and is used for most measurements.
- This surface is coated by a hydrophobic coating (NANO CONCEPT NTV 100) to achieve larger contact angles of the droplets.
- To achieve smaller contact angles, a slight mechanical abrasion of the untreated polycarbonate surface is achieved by gently rubbing with a tissue generating micro-scratches at the surface.
- The rubbing is repeated to achieve a further abrasion and even smaller contact angles.

All surface treatments analyzed in the measurements consist of a polycarbonate substrate to assure equal heat transfer characteristics. Differences of the radiative heat transfer due to these surface treatments are neglected. The contact angles and experimental results of the different surface treatments are found in section 2.2.5.4. Measurements on other substrate materials such as

glass or different coatings are only used for qualitative measurements of the surface coverage and contact angle measurements of single droplets (see figure 2.20 and appendix C).

The climate chamber temperature at the inlet of the channel is measured on average $T_{a,m} = 20.5\text{ °C}$ with a standard deviation due to oscillations of $SD \pm 0.2\text{ K}$. The measured relative humidity at this position is $\phi_{a,m} = 49\%$ on average with a standard deviation due to oscillations of $SD \pm 0.3\%$. Both, air temperature and water vapor content, are oscillating slightly with a cycle duration of approximately 400 s due to the climate chamber control. The volume flow of the coolant is approximately $\dot{V}_{co} = 5\text{ l/min}$, and the coolant system is thermally insulated, so temperature differences in the coolant system are small. The coolant temperature T_{co} stays almost perfectly constant, at -5 °C during the condensation phase and 15 °C during the evaporation phase, with deviations due to settling after the coolant reservoirs are switched.

An annular light source is mounted around the lens of the camera, 85 mm away from the substrate surface. The light source uses fiberglass to transport the shortwave light from the light bulb to the ring, thus as little heat as possible is introduced. Nevertheless, the evaluation of the experiments shows a measurable influence of the radiation heat \dot{q}''_{light} absorbed in the substrate. Thus, the intensity distribution of the light source at a distance of 85 mm is measured by a thermal absorption sensor. The measured distribution of \dot{q}''_{light} is illustrated in appendix B and is used as heat source in the simulation models of the test rig in section 2.3.

As stated before, the geometrical setup of the test rig deviates from the geometry of vehicle cabins. Concerning the flow parameters, the conditions tested in the experiment nevertheless fully cover, or even are in excess of, typical conditions encountered in vehicles. Typical cabin flow velocities in vicinity of the front window lie between 2 – 7 m/s during defrost operation [40, 67, 161]. In the rear part of the cabin the velocity is strongly influenced by natural convection and is generally lower. The boundary layers at the windows can develop along the entire length of the window ($\approx 1\text{ m}$) and are in general significantly thicker than those of the experiment. Doroudian [40] gives a typical boundary layer thickness of 17 mm at the front window. On the other hand, droplets become significantly larger in vehicles, if fogging is not prevented, and dripping of the droplets at a size of several millimeters becomes relevant. Yet, such con-

ditions are not analyzed in the experiments as the goal of vehicle operation is to prevent window fogging or to remove fog.

2.2.2 Drop Shape Analysis and Contact Angle Measurement Method

To analyze the shape and volume of the condensate droplets, a new measurement technique is developed. The contact angle between each droplet and the substrate surface, as well as the droplet volume are derived by observed light reflections in the droplet. These reflections are detected by an automatic algorithm for each frame captured by the optical sensor of a camera. The image resolution of the camera is 5184x3456 px. The scale of the captured images is 1370 px/mm and is determined by a calibration slide which is placed on the substrate before the experiment. The size of the droplets and observed reflections is obtained using this scale. The optical measurement setup to capture the droplets and to quantify the condensate volume is illustrated in figure 2.8.

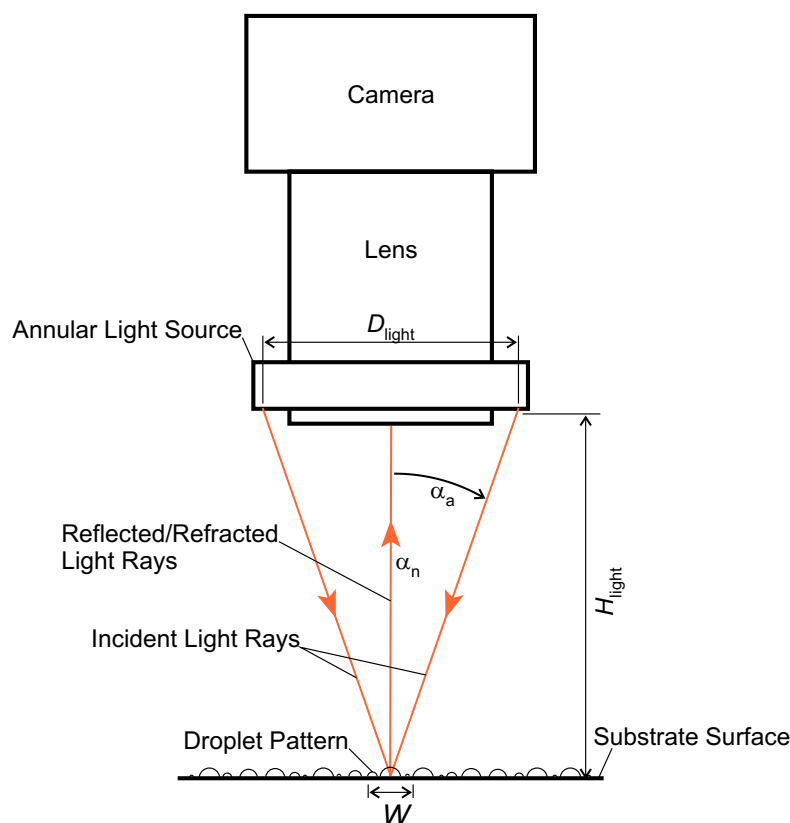


Figure 2.8: Schematic illustration of the optical measurement setup of the developed contact angle and drop shape analysis method.

The observed reflections originate from a thin annular, respectively horseshoe-shaped, light source of the diameter D_{light} , which is surrounding the optical axis. The amount of observable reflections appearing at a single droplet depends on the incident light angle, on the contact angle of the droplet and on the reflectivity of the substrate. The light ray paths of three different types of reflections are illustrated in figure 2.9. In the conducted experiments on polycarbonate two reflections C_1 and C_2 are in general well observable. A third reflection C_3 is only visible for larger contact angles (here $\theta \geq 80.5^\circ$) and its intensity is lower. Therefore, C_3 is not used for the evaluations.

Reflection C_2 appears flipped in comparison to the other two reflections. As seen in figure 2.9, although the incident rays come from the same side for all reflections, the exiting ray of reflection C_2 is visible at the opposite side of the droplet. This effect is used in the condensation experiments with many droplets to distinguish different reflection types. One sector of approximately 30° of the annular light source is covered, resulting in a horseshoe shape.

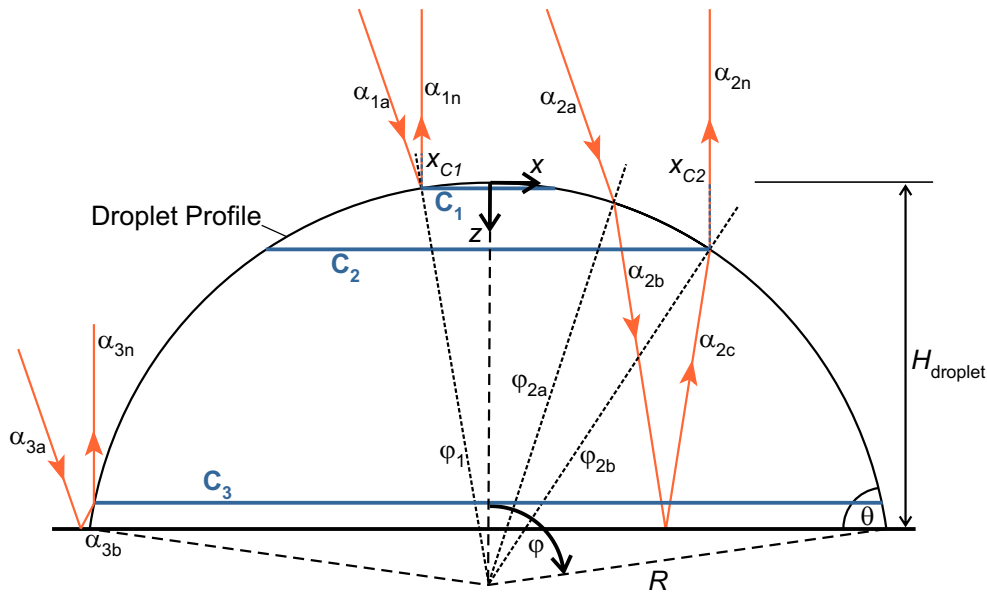


Figure 2.9: Ray paths of three different possible reflection mechanisms C_1 , C_2 and C_3 at a droplet. For a better clarity, only one parallel beam of rays from the light source is illustrated here. For an annular light source all ray paths exist also mirrored.

The optical setup is placed perpendicularly above the area of interest at a defined distance H_{light} between the light source and the substrate. The rays of the light source meet the droplets in the substrate center at an incident angle $\alpha_a = 19^\circ$, which is defined by the distance H_{light} and the diameter D_{light} .

To prevent significant variations of this angle, all observed droplets must be located within a small region W around the optical axis of the measurement setup. This is achieved by a small angle of view and a large focal length of the long-distance lens used. With the lens used, a focal length of approximately 0.5 m, a viewing angle of 6° and a magnification ratio of 6:1 is realized.

A small aperture diameter (here 6 mm) ensures that the light rays reflected in the droplets reach the optical system at an angle α_n close to 0° . This angle serves as an assumption for the light ray path calculation at each droplet. The small aperture opening also ensures a relatively large depth of field which allows an acceptably sharp capture of different types of reflections with shifted virtual object distances. Assuming these generalized global ray angles, the local ray path is expressed as a function of the droplet geometry. This geometry can be complex due to contact angle hysteresis and gravitational influences but in many cases the droplet shape can be approximated by a spherical cap, or at least rotational symmetry can be assumed.

For the evaluation, the two reflections of the annular light source C_1 and C_2 are used. C_1 results from reflection of the incident ray in the curved droplet surface. C_2 results from light rays which are refracted when passing the liquid-gas interface, subsequently reflected in the substrate and finally refracted when passing the liquid-gas interface again. Reflection C_3 results from a reflection in both, the substrate and the interface surface, and is visible for large contact angles and incident angles α_a , but is not used for the evaluation in this study. The light ray path evaluation and drop shape analysis is presented first for the general case including gravitational influences (section 2.2.2.1) and is subsequently derived for the simplified case of a spherical droplet geometry (section 2.2.2.2).

2.2.2.1 Influence of Gravity on the Droplet Shape

Although gravitational influences are neglected in most cases, because interfacial forces exceed gravitational forces, a generally valid method for all axisymmetric droplets is derived. For large droplets the droplet profile is described by the Young-Laplace equation (2.8), presented in section 2.1.3. A solution following Rotenberg et al. [122] is developed for the description of the droplet profile, which is used for the computation of the light ray paths.

At the apex ($z = 0$), it is assumed that all radii of curvature are equal $R_1 = R_2 = R_0$ due to the rotational symmetry. Inserted in equation (2.8), the pressure difference Δp_0 is replaced by:

$$\Delta p_0 = \frac{2\gamma}{R_0}. \quad (2.10)$$

By definition, the principal radius of curvature R_1 in the illustrated plane is:

$$R_1 = \frac{ds}{d\varphi}. \quad (2.11)$$

Furthermore, geometrical considerations at the axisymmetric droplet profile of figure 2.3 reveal that the principal radius of curvature R_2 in a plane perpendicularly to the illustrated plane is expressed by:

$$R_2 = \frac{x}{\sin \varphi}. \quad (2.12)$$

By inserting equations (2.10) – (2.12), equation (2.8) is rewritten as:

$$\frac{d\varphi}{ds} = \frac{2}{R_0} + \frac{\Delta\rho g z}{\gamma} - \frac{\sin \varphi}{x}. \quad (2.13)$$

Considerations at an infinitesimal element of the droplet profile in figure 2.3 reveal:

$$\frac{dx}{ds} = \cos \varphi, \quad (2.14)$$

$$\frac{dz}{ds} = \sin \varphi. \quad (2.15)$$

The three equations (2.13) – (2.15) form a set of first-order differential equations. These equations are integrated numerically for a presumed value of R_0 to derive the droplet profile, starting at the origin where:

$$\begin{aligned}x(s = 0) &= 0 \\z(s = 0) &= 0 \\ \varphi(s = 0) &= 0\end{aligned}\tag{2.16}$$

The MATLAB built-in equation solver *ode45* is used to find discrete points of the droplet profile. To evaluate the shape of the droplet as a function of the apparent reflections, the laws for reflection and refraction are used in combination with the set of differential equations which describe the droplet profile. With the above mentioned assumptions for the light ray paths, it is assumed for reflection C_1 :

$$\varphi_1(x = x_{C1}) = \frac{\alpha_{1a} + \alpha_{1n}}{2}.\tag{2.17}$$

Nevertheless, the numerical integration of equations (2.13) – (2.15) needs to be started at the origin of the coordinate system with a presumed value of R_0 . The correct value of R_0 is thus found in an iterative process to meet condition (2.17) defined by reflection C_1 . Once the value of R_0 and the corresponding droplet profile are known, reflection C_2 is used to find the contact line of the droplet, which then also defines the remaining geometry parameters, such as the contact angle and the droplet volume. The apparent x -position of the reflection C_2 is a function of the laws of refraction and reflection in the droplet and the substrate surface and is iteratively correlated with the droplet height H_{droplet} .

2.2.2.2 Neglecting Gravitational Influences

For small droplet sizes ($Bo < 1$) and small contact angles, the influence of gravity on the droplet shape is below 10% as seen in figure 2.10 and 2.11. In the conducted condensation experiments shown in section 4.5, the radius of the largest droplets is approximately $R_0 = 0.6$ mm, corresponding to a Bond number of $Bo = 0.05$. Therefore, gravitational forces are neglected and a more simple calculation process is applied. On an ideally flat and homogeneous substrate surface, axisymmetric conditions are assumed. The Young-Laplace equation (2.4) reveals that the droplet radius of curvature is thus equal at all

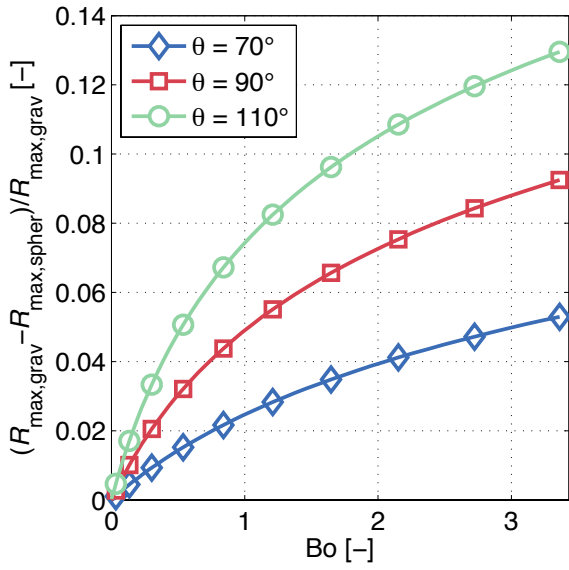


Figure 2.10: Deviation of the shape, respectively the projected droplet radius, due to the gravitational influence depending on Bond number and contact angle.

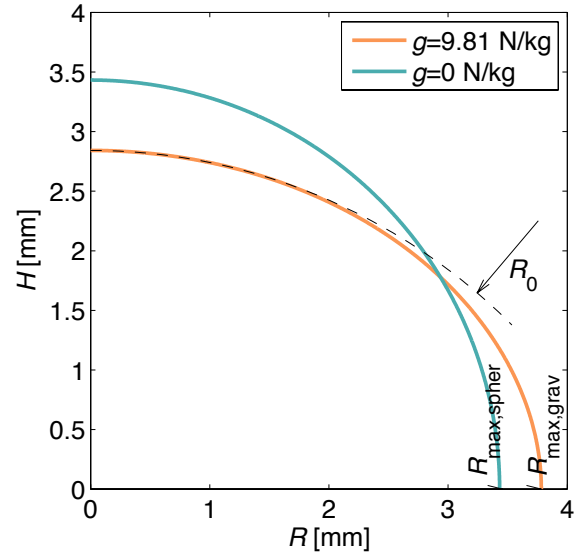


Figure 2.11: Profile shapes of a droplet of identical volume and $\theta = 90^\circ$ with and without gravitational influence ($g = 9.81 \text{ N/kg} \rightarrow \text{Bo} = 3.3$).

points $R_1 = R_2 = R$. The shape of the droplet is therefore described by a spherical cap and depends only on the contact angle between the substrate and the liquid-vapor interface.

The following equations are derived by geometrical considerations from the simplified light ray paths leading to the reflections C_1 and C_2 illustrated in figure 2.9. The droplet geometry is expressed as a function of the light ray angles α_i and the angular positions φ_i of the respective refraction and reflection points as well as the apparent positions of the reflections x_{C_1} and x_{C_2} .

With equation (2.17) the droplet radius of curvature R is derived from the size of reflection C_1 :

$$R = \frac{x_{C_1}}{|\sin \varphi_1|}. \quad (2.18)$$

The apparent size of reflection C_2 gives the angular position φ_{2b} of the liquid-vapor interface point where the light ray of C_2 exits the droplet:

$$\varphi_{2b} = \sin^{-1} \left(\frac{x_{C_2}}{R} \right). \quad (2.19)$$

The law of refraction at this point gives a relation between the light ray angles α_{2c} and α_{2n} :

$$\alpha_{2c} = \varphi_{2b} - \sin^{-1} \left[\frac{\sin(\varphi_{2b} - \alpha_{2n}) n_a}{n_w} \right]. \quad (2.20)$$

The relation between the light ray angles α_{2b} and α_{2c} is given by the law of reflection at the substrate surface:

$$\alpha_{2b} = -\alpha_{2c}. \quad (2.21)$$

The law of refraction at the liquid-vapor interface point, where the light ray of C_2 enters the droplet, gives a relation which needs to be solved implicitly for the angle φ_{2a} :

$$\sin(\varphi_{2a} - \alpha_{2a}) n_a = \sin(\varphi_{2a} - \alpha_{2b}) n_w. \quad (2.22)$$

By the above described dependencies, the droplet height H_{droplet} is expressed as a function of the droplet radius and the obtained light ray angles:

$$H_{\text{droplet}} = \frac{R}{2} \left[2 - (\cos \varphi_{2a} + \cos \varphi_{2b} + \cot \alpha_{2c} (\sin \varphi_{2a} - \sin \varphi_{2b})) \right]. \quad (2.23)$$

The contact angle θ is only a function of the obtained angles:

$$\theta = \cos^{-1} \left[(\cos \varphi_{2a} + \cos \varphi_{2b} + \cot \alpha_{2c} (\sin \varphi_{2a} - \sin \varphi_{2b})) \right]. \quad (2.24)$$

The droplet volume V_{droplet} is written as a function of the droplet height H_{droplet} and the contact angle θ :

$$V_{\text{droplet}} = \pi H_{\text{droplet}}^2 \left(R - \frac{H_{\text{droplet}}}{3} \right). \quad (2.25)$$

The measurement method described above is a fundamentally new method to detect contact angles. An application for a patent was filed [86]. As shown

below, the method is automatized and used, not only for the measurement of contact angles, but also for the approximation of the condensed droplet volume on a surface. The apparent radii of the reflections x_{C1} and x_{C2} are detected by an automatic algorithm from the image of a single droplet or a droplet array. With the above described relations the complete shape and position of the droplets is approximated. Besides the geometrical setup, which defines the incident and reflected light ray angles, and besides the measured radii of the reflections, the only additional input to the simplified set of equations (2.17) – (2.25) is the ratio of the refraction indices of water and air, which is assumed to be constant at $n_w/n_a = 1.33$.

2.2.2.3 Verification of the Contact Angle Measurement Method

To demonstrate the validity and accuracy of the method, an additional experimental investigation is conducted. In these experiments a single droplet is gently placed on a substrate and captured simultaneously by the described system from perpendicularly above and by an additional camera from the side. Thus, the new measurement method is directly compared with an established conventional method. The applied conventional method is based on the Axisymmetric Drop Shape Analysis (ADSA) and is described e.g. by Rotenberg et al. [122]: In the experiments of the present study 15 points along the projected profile of the liquid-vapor interface and two points of the projected liquid-solid interface (baseline) are detected graphically (see figure 2.12). The drop profile described by equation (2.8) which fits these points best is computed. The average of the two contact angles at the intersections of the droplet profile and the baseline is calculated. The accuracy of this method depends very much on the optical quality of the image, the rotational symmetry of the droplet and the user who marks the interface points. From the performed measurements it is estimated that the uncertainty of the conventional method is approximately 1° . A weak point of the conventional method is the viewing perspective from the side, as seen in figure 2.12. A correct detection of the baseline is in some cases difficult, especially for droplets with a contact angle close to 90° . Additionally, only two intersection points are visible, but due to inhomogeneities and contact angle hysteresis the contact angle sometimes varies significantly along the circumference.

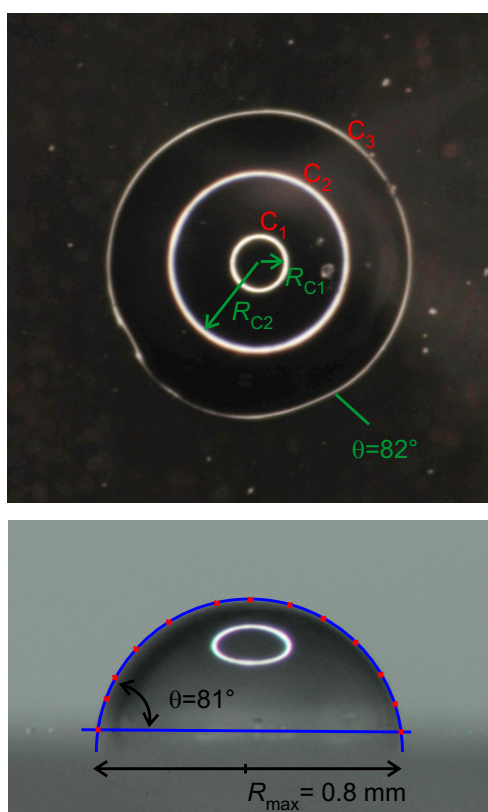


Figure 2.12: Single droplet on a polycarbonate surface captured synchronously from perpendicularly above (upper image) with reflections C_1 , C_2 and C_3 and viewed from the side (lower image). The droplet size in this figure corresponds to a Bond number of $Bo = 0.09$.

The simultaneous comparison of the two measurement techniques shows that the average deviation between the two methods is 0.6° and thus lower than the expected measurement accuracy of the conventional method (see figure 2.13). Further verification experiments on hydrophobic substrate materials (see figures C.2 and C.3), on hydrophilic substrate materials (see figures C.4 and C.5) and measurements with a large droplet (see figures C.6 and C.7) confirm the good agreement of the two methods and are presented in appendix C.

2.2.2.4 Image Processing

An algorithm is developed in MATLAB to automatically post-process the images of the droplet condensation experiments. This algorithm is based on the assumption of axisymmetric droplets and works well as long as the droplet

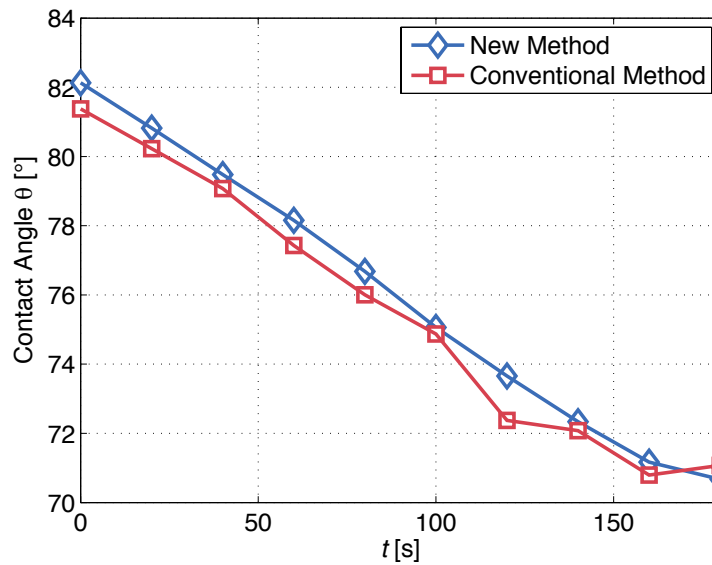


Figure 2.13: Contact angle of the two measurement techniques derived simultaneously for a single evaporating droplet on a polycarbonate substrate, $Bo(t = 0) = 0.09$. A corresponding picture time series of the evaporating droplet is depicted in figure C.1.

shape is approximately axisymmetric. The reflections of the circular lamp, visible in each droplet, are used to identify the droplet and to assess its geometry. To identify and differentiate reflections C_1 , C_2 and C_3 a horseshoe shape light source is used. As seen in the images of the droplets (see figure 2.14) and in the illustration of the ray paths (see figure 2.9), reflection C_2 appears mirrored compared to the reflections C_1 and C_3 . Therefore, the C_2 -type reflection is easily identified by the orientation of the horseshoe shape.

For large droplets reflections C_1 and C_2 are clearly visible and an algorithm is designed to detect these reflections, which is presented in the following section 2.2.2.4.1. With the detected size of both reflections, the geometry of the droplet is calculated according to equations (2.17) – (2.25). To account also for small droplets which are not detectable by this algorithm, a second algorithm is developed and explained in section 2.2.2.4.2.

2.2.2.4.1 Identification of Horseshoe Shape Reflections

The sequence of the algorithm is illustrated in figure 2.14 for a section of the original image containing a large droplet. First, the original image inten-

sity is adjusted to increase the overall contrast and image noise is reduced by a Gaussian filter (see figure 2.14 [a] and [b]). The image is then binarized by the MATLAB built-in function *im2bw* at a certain intensity level I_{bw} (see figure 2.14 [c]). This level has a significant influence on the obtained shape of the reflections and is therefore iteratively optimized as explained in section 2.2.2.5. The binary image is then analyzed by the MATLAB built-in function *bwboundaries* to locate the boundaries between black and white pixels (see black profile in figure 2.14 [d]). A loop is performed over all detected boundaries to differentiate between characteristic, valid reflections and incomplete or invalid shapes. The criterion for valid reflections is the similarity of the detected shape to the expected horseshoe shape as described mathematically by equations (2.26) – (2.29).

For this evaluation the center of the points which describe the horseshoe reflection is calculated. The two endpoints of the horseshoe shape determine the opening angle of the horseshoe shape α_{hs} (see figure 2.14 [d]). At these points a differentiation between the inner contour and the outer contour is done and the respective mean radii $R_{in,m}$ and $R_{out,m}$ are calculated (see figure 2.14 [e]). Four criteria for the validity of the shape are defined:

The normalized and averaged deviations of the local radii $R_{in,i}$ and $R_{out,i}$ from the respective mean values,

$$\frac{\sum_{i=1}^{N_{px,in}} |R_{in,i} - R_{in,m}|}{N_{px,in} \cdot R_{in,m}} < 0.167, \quad (2.26)$$

and,

$$\frac{\sum_{i=1}^{N_{px,out}} |R_{out,i} - R_{out,m}|}{N_{px,out} \cdot R_{out,m}} < 0.25, \quad (2.27)$$

the ratio of the mean radii $R_{in,m}$ and $R_{out,m}$,

$$\frac{R_{out,m}}{R_{in,m}} < 4, \quad (2.28)$$

and the opening angle,

$$\alpha_{hs} < 90^\circ. \quad (2.29)$$

The limiting values given here for the different criteria are found to work well for the measurements of this study. However, they may need to be adjusted for other measurements.

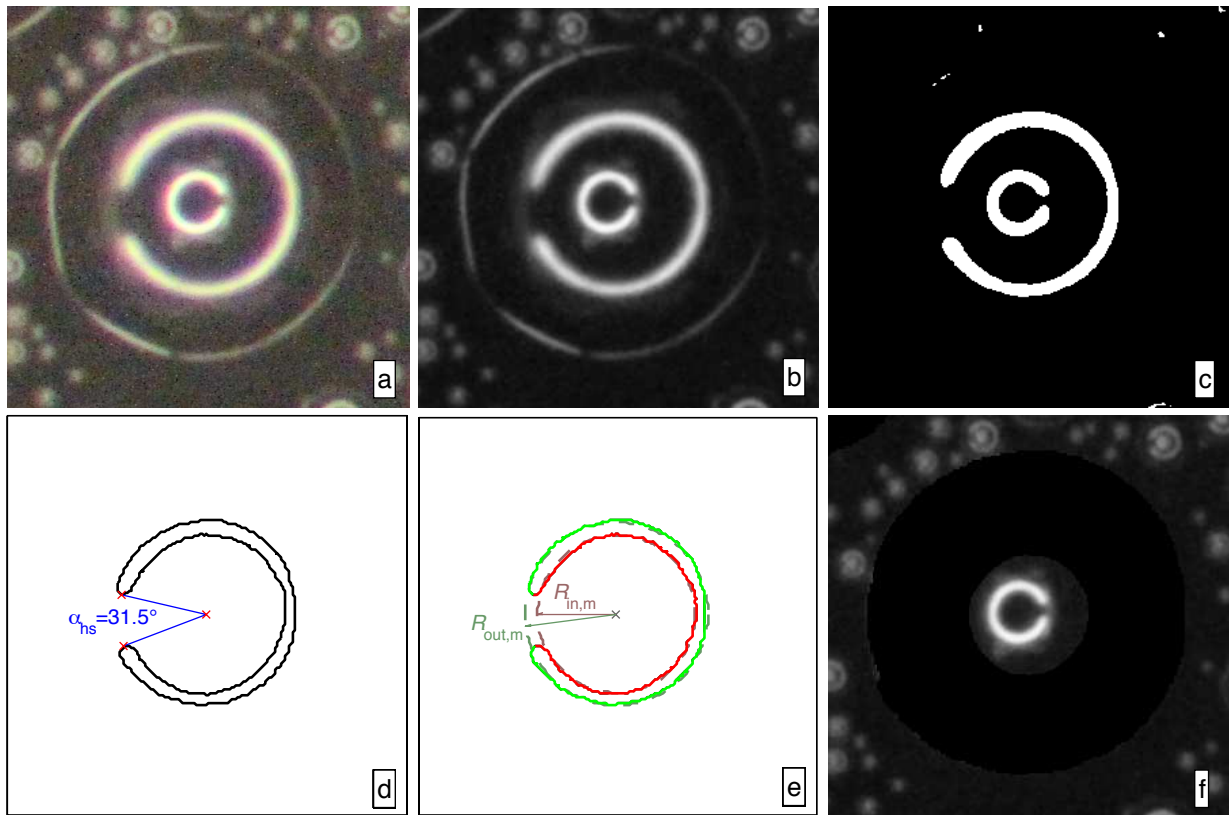


Figure 2.14: Automatic detection of horseshoe shape reflections: [a] original image detail; [b] resolution, color and noise adaption; [c] binarization (here $I_{bw} = 50\%$); [d] detected boundary of reflection C_2 with detected opening angle α_{hs} ; [e] inner and outer contours of horseshoe reflection with mean radii $R_{in,m}$ and $R_{out,m}$; [f] masked image after horseshoe detection for further processing.

The radius associated with a reflection, respectively the apparent position $x_{C1/C2}$, is needed for the contact angle evaluation and is assumed as the average of the inner and the outer mean radii $R_{in,m}$ and $R_{out,m}$. This ensures the obtained value of the droplet radius to be almost independent of the binariza-

tion level I_{bw} , as the "line-width" of the horseshoe shape significantly depends on this level.

For large droplets, constituting the major part of the overall droplet volume in most measurement points, reflections C_1 and C_2 are in general easy to identify.

2.2.2.4.2 Identification of Circular Reflection Shapes

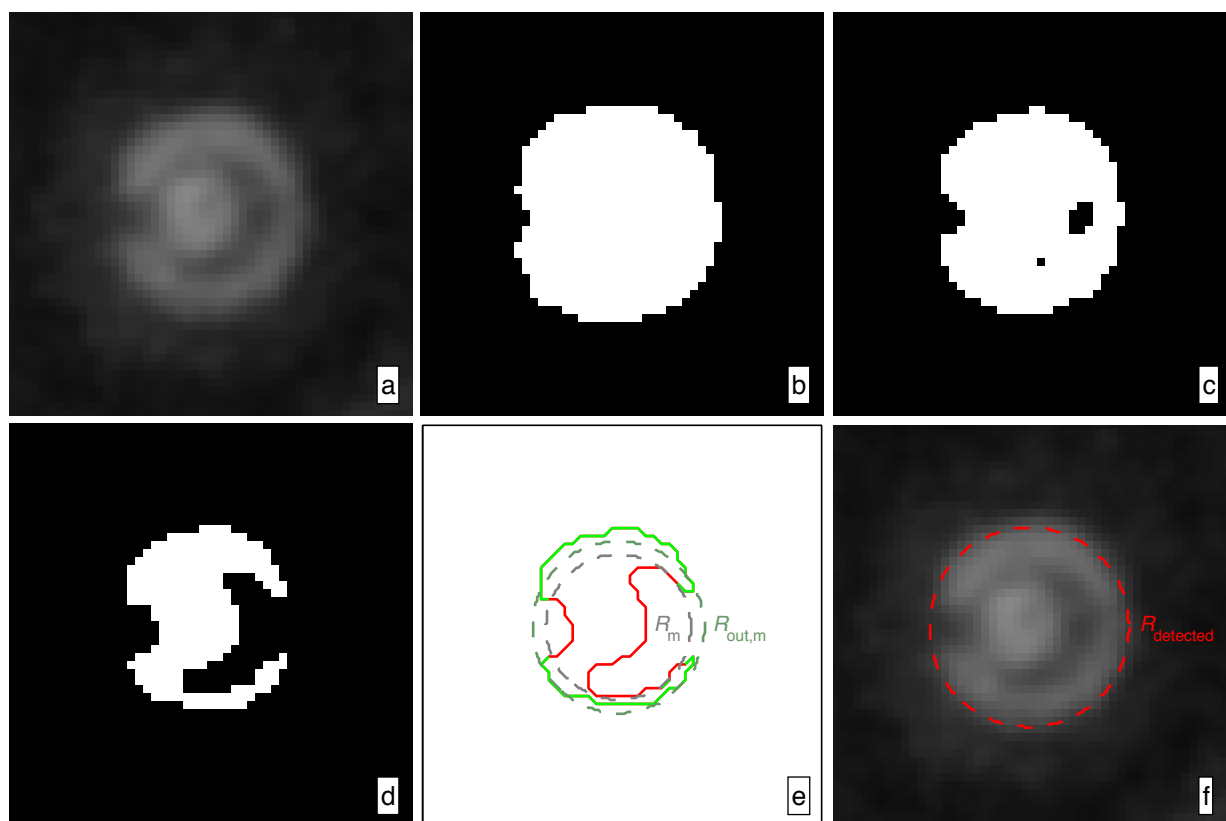


Figure 2.15: Automatic detection of circularly shaped reflections: [a] adapted image (corresponding to figure 2.14b); [b] binarization at $I_{bw} = 20\%$; [c] binarization at $I_{bw} = 27.5\%$; [d] binarization at $I_{bw} = 35\%$; [e] detected contour and radii; [f] detected radius independent of I_{bw} (see also figure 2.16).

The reflections of smaller droplets are, on the other hand, not identifiable as horseshoe-shaped C_1 or C_2 reflections, but rather as single bright spots due to the finite resolution of the camera and optical aberrations. To estimate the volume of these smaller droplets, a second algorithm is developed, identifying small bright objects in the image with an approximately circular shape. This

second detection algorithm also analyzes the adapted and binarized images (see figure 2.14 [a], [b] and [c]). But here, I_{bw} not only influences the detected shape of the reflection but also its size, which is seen in figure 2.15 [b – d]. Although the outer contour of a detected shape is circular, the inside contour is still irregular, e.g. due to an overlapping with the inner reflection C_1 (see figure 2.15 [d]). Therefore, an algorithm is developed which is widely independent of I_{bw} .

Similarly to equation (2.26) and (2.27), the criterion for a valid reflection shape is based on the difference of the local and the mean radius of the detected boundary. Here, only points outside of the mean radius R_m are considered (see figure 2.15 [e]) to define the criterion:

$$S_c = \frac{N_{px,out} \cdot R_{out,m}}{\sum_{i=1}^{N_{px,out}} |R_{out,i} - R_{out,m}|} > 13. \quad (2.30)$$

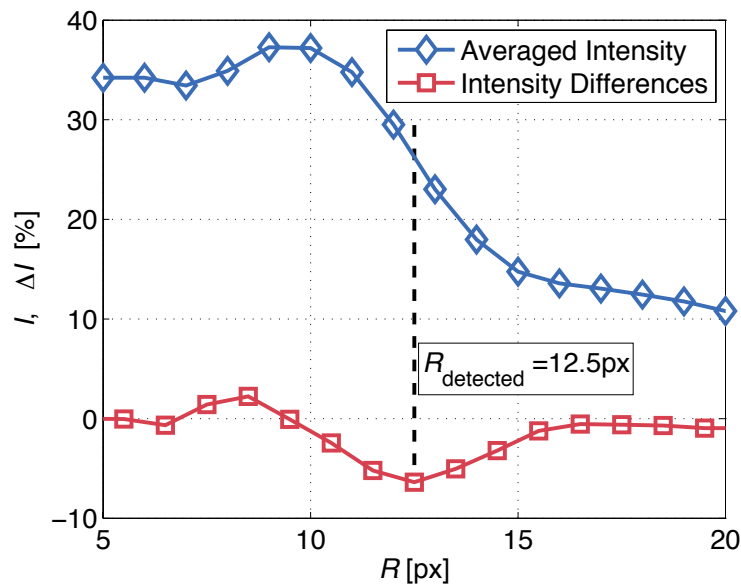


Figure 2.16: Radially averaged intensity values and intensity differences between neighboring pixels to determine a characteristic radius at the location of the maximum negative intensity gradient.

To assure the radius detection to be almost independent of I_{bw} , the final radius determination is based again on the grayscale image 2.15 [a]. As seen in figure 2.16, the radius detection is designed to detect the radius location with the maximum negative intensity gradient. The intensities of the pixels corre-

sponding to concentric circles³ around the center of the detected boundary are averaged. The detected radius is assumed to correspond to the abscissa of the minimum value of the deviation of this intensity curve (see figure 2.16). This radius is assumed to correspond to reflection C_1 , if a further concentric reflection is detected outside of this reflection, otherwise it is assumed to correspond to reflection C_2 .

2.2.2.5 Iterative Optimization of the Algorithm

The above described criteria for the detection of reflections are formulated conservatively. It is preferred to rather detect only few reflections at a specific binarization level than detecting a wrong contour as a valid reflection. The number of correctly detected reflections strongly depends on the local intensity level of the reflections, which varies with image position, size of the droplets and type of reflection (C_1 or C_2). Therefore, both algorithms described in 2.2.2.4 are repeated several times at different binarization levels I_{bw} to identify as many valid reflections as possible. To avoid multiple detections of the identical reflection and to reduce the computing effort, each correctly identified reflection is masked black before proceeding to the next binarization level (see figure 2.14 [f]). To reduce computing time, the optimum levels of I_{bw} are searched iteratively in a smaller section of each image. For the first algorithm, the optimum value of I_{bw} is searched iteratively so that the sum of all detected radii of the C_1 and C_2 -type reflections is maximized. Thus, as many reflections as possible are detected and a stronger weighting of big droplets is realized.

$$I_{bw,opt} = \max_{I_{bw}} \left(\sum^{N_{C1/C2}} R_m^{0.5} \right). \quad (2.31)$$

The criterion of the optimum intensity level I_{bw} for the second algorithm, identifying circular objects, is to maximize the sum of the shape coefficients

³ Pixels corresponding to a specific radius are selected using an algorithm first presented by Bresenham [20].

S_c of all detected droplets defined by equation (2.30). Thus, the maximum number of circular reflections is detected at this intensity level:

$$I_{bw,opt} = \max_{I_{bw}} \left(\sum^N S_C \right). \quad (2.32)$$

The optimum intensity level I_{bw} of each evaluation is detected by the MATLAB built-in function *fminbnd*.

2.2.3 Condensation and Evaporation Mass Flux Measurement

After running the two detection algorithms at different binarization levels, a post-processing algorithm is used to correlate the corresponding reflections and droplets. As seen in figure 2.17, the majority of droplets and reflections is detected correctly. For large droplets both reflections, C_1 and C_2 , are detected and assigned correctly and an evaluation of the contact angle as well as the volume are performed as described in section 2.2.2.2. For small droplets, the corresponding reflections are not detected with sufficient accuracy or only one of the reflections is detected. Thus the contact angle is approximated by the mean contact angle found in the current test series. This allows to roughly estimate the volume of the small droplets.

To measure the rate of condensation and evaporation per unit area in the center of the polycarbonate test substrate, the condensate volume of sequential images is correlated with the frame rate of the camera which is 0.1 fps. A density of $\rho_w = 1000 \text{ kg/m}^3$ is assumed for the condensed water to estimate the corresponding mass flux. To eliminate errors originating from the edge of the image where some droplets are only partly visible, a border region of the maximum observed droplet size is omitted for the evaluation (see frame in figure 2.17). Droplets cut by the frame line of this reference section are proportionally included in the volume computation.

From the size and contact angle distribution of all detected droplets, secondary values such as the wetted area, liquid-gas interface and fluid volume per unit substrate area are calculated.

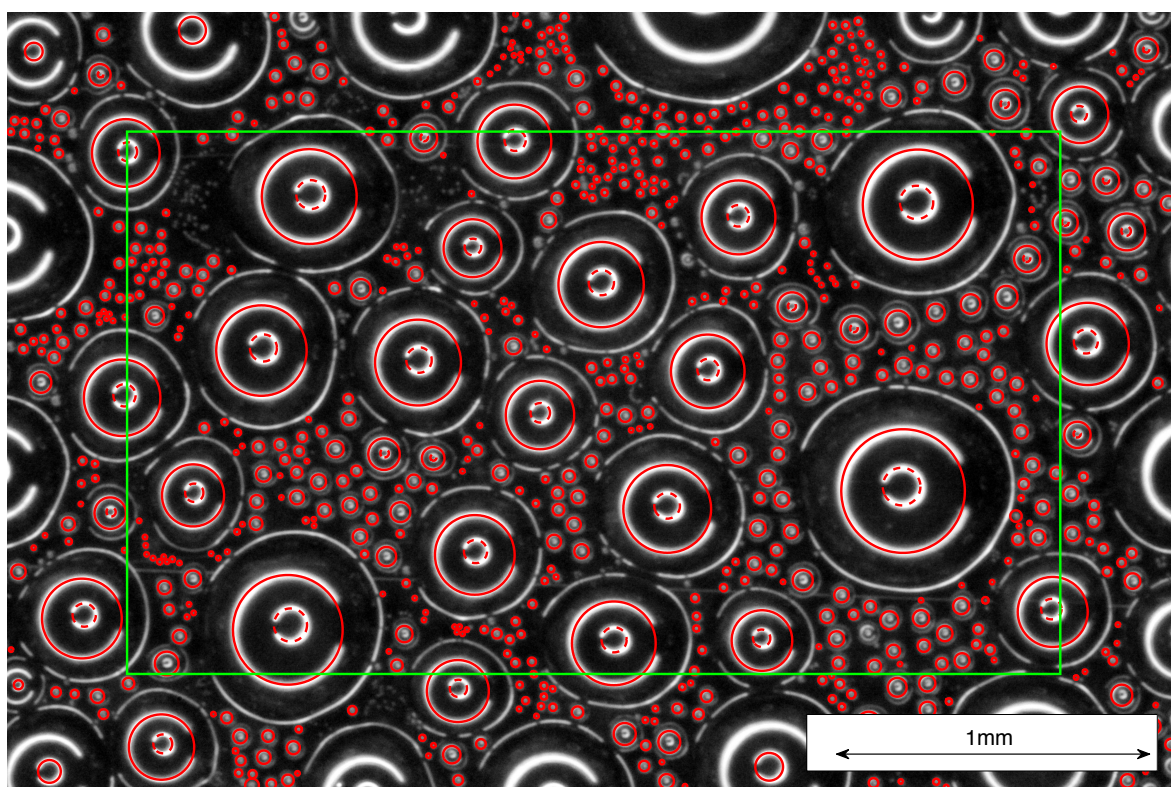


Figure 2.17: Droplet condensation pattern with detected C_2 (solid circles) and C_1 reflections (dashed circles) as well as the reference section (green rectangle) used for the evaluation of droplet volume per unit substrate area. The image is from a condensation experiment on untreated polycarbonate at $Re = 2.9 \cdot 10^4$ and $t = 1020$ s.

2.2.3.1 Measurement Error and Sensitivity Analysis

The new measurement method has various influencing factors and some of them are difficult to quantify. Therefore, it is not possible to specify an overall measurement error of the method. Nevertheless, some influencing factors are estimated separately.

The geometrical setup of the **light source** determines the global incident light ray angle and is therefore one of the measured input parameters of the method. In the conducted experiments, the distance of the light ring to the substrate plane is 85 mm and the light ring diameter is 60 mm, resulting in an incident light angle of $\alpha_{1a} = 19^\circ$. An error of 1° by measuring this incident angle leads to a deviation of the obtained contact angle of 2° for a contact angle of 90° and slightly bigger deviations for very small and large contact angles.

For spherical droplets, the evaluation is based on the **radius detection** of the apparent reflections C_2 and C_1 . The correct determination of these radii by the automatic algorithm is therefore essential. Although the geometrical extension of the real glass fiber light ring is very thin (~ 0.5 mm), the reflections of the light ring appear significantly thicker in the image. This is partly due to scattering of the light and overexposure of the image in these regions. Furthermore, each droplets acts like an additional lens in the light path and causes a shift of the focus depending on the geometry of the droplet and varying for reflection C_1 and C_2 . A small aperture of the lens helps to overcome this problem but leads to longer exposure times. The radius of the respective reflections is approximated by averaging the inner and outer visible reflection radius at a certain intensity level I_{dw} . Although this procedure delivers good results, the method is sensitive to a wrongly detected radius ratio as seen in figure 2.18. For a contact angle of 90° , an error of one of the detected radii by 1% leads to a deviation of the calculated contact angle of 1.5° .

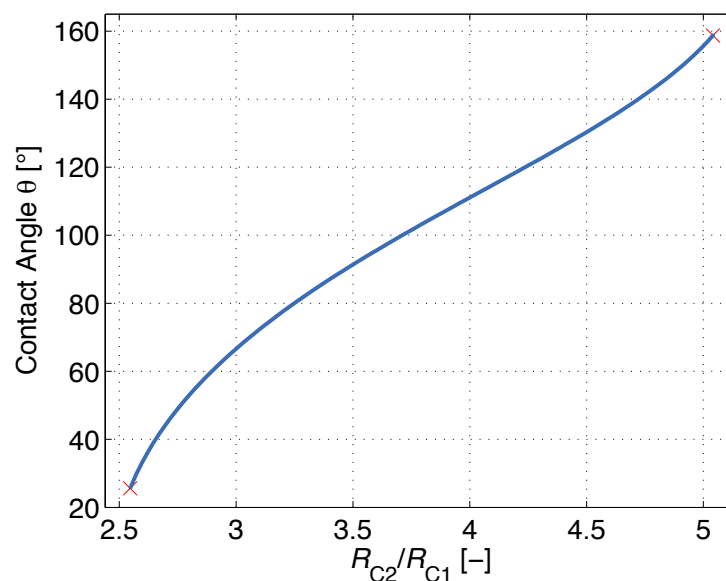


Figure 2.18: Contact angle as a function of the detected ratio of the reflections C_2 and C_1 for a spherical droplet and an incident angle of $\alpha_{1a} = 19^\circ$. The two crosses mark the limits (here 26° and 159°) where reflection C_2 is not anymore observable due to geometrical restrictions.

For relatively large droplets ($R \cong 1$ mm), the experimental comparison with an established contact angle measurement method shows that the error range is within a few degrees at maximum (see section 2.13). In the experiments some of the detected droplets are significantly smaller but for small droplets a

verification is not possible due the quick evaporation of single small droplets. In the following it is tried to estimate the contact angle measurement error for small droplets resulting from a reduced **image resolution**.

The detected contact angle is a function of the incident light ray angle α_{1a} and the detected radius ratio of the reflections R_{C2}/R_{C1} . The incident angle is assumed to be approximately constant for all droplets. The ratio of the detected radii varies slightly due to the shift in focus and due to the limited resolution of the optical system. To quantify the effect of the limited resolution, a study with the identical input image of figure 2.17 at varying resolutions is performed. The detected contact angles of specific drops of this image are compared at a gradually decreased image resolution. As the smallest droplets cannot be resolved anymore at the lowest resolution, only the 14 largest droplets detectable at all resolutions are compared. Whereas one of the large droplets ($R \cong 0.3 \text{ mm}$) is resolved by approximately 800×800 pixels in the original image ($f = 100\%$), an image scale factor $f = 5\%$ results in a resolution of only 40×40 pixel for the same droplet. The resolution reduction is calculated by a cubic interpolation scheme integrated in MATLAB (built-in function: *imresize*).

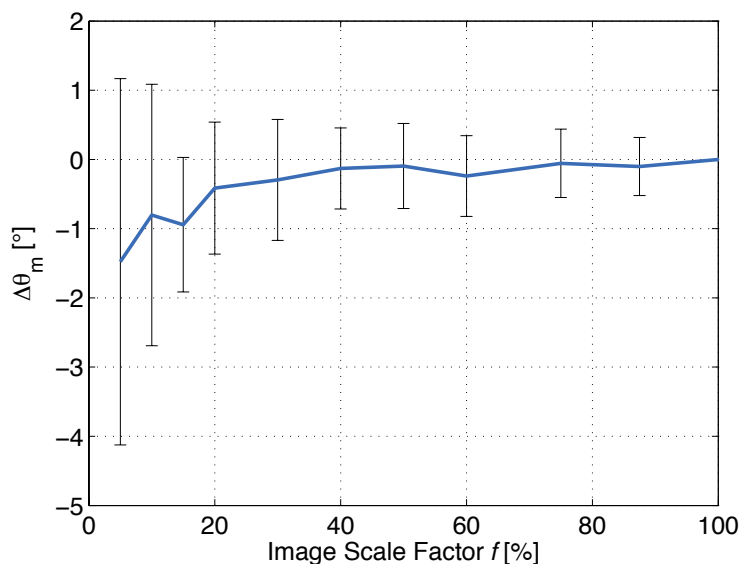


Figure 2.19: Average contact angle deviation of the 14 largest droplets of figure 2.17 at an artificially reduced image resolution.

It is seen in figure 2.19 that between 40% and 88% of the original resolution the mean error is close to 0° . Here, the standard deviation of approximately $\pm 0.5^\circ$

illustrates a statistical variance of the result. At resolutions lower than 40% of the original resolution, the standard deviation increases to a value of $\pm 2.6^\circ$ and the average error becomes slightly negative. Neglecting possible effects of the limited image sharpness, this result is transferred to a size dependence of the measurement error: Thus, the contact angle of a 20 times smaller droplet ($R = 0.3 \text{ mm} \rightarrow R = 0.015 \text{ mm}$) would involve the contact angle being detected 1.4° smaller on average than the contact angle of a large droplet including a standard deviation of the measurement result of $\pm 2.6^\circ$.

In addition to the above mentioned measurement uncertainties, there are others which are more difficult to quantify. One of them is the **deviation from an axisymmetric shape** of the droplets. Reasons for this deviation are inhomogeneities and the roughness of the substrate surface leading to a hysteresis of the contact angle. The visible effect of the hysteresis on the droplet shape is the larger, the smaller the nominal contact angle is. Validation measurements are also performed for a single droplet with a small contact angle ($30^\circ < \theta < 45^\circ$) and show a good agreement between the conventional method and the method developed for this thesis (see appendix C.5). Nevertheless, successful image detection of the condensation experiments is only feasible down to an average contact angle of 79° , even though experiments are always performed on smooth and clean surfaces. Qualitative condensation experiments on more hydrophilic surfaces (low- ϵ coated glass $\theta \cong 65^\circ$) deliver partly asymmetric droplet shapes, which can no longer be evaluated by the algorithm (see figure 2.20 [b]). Similar tests on uncoated float glass ($\theta \leq 26^\circ$) show that the shapes of the droplets become even more irregular (see figure 2.20 [c]). During the condensation phase, the contact line of the droplets is pinning to the substrate surface. This means that although two droplets coalesce, significant parts of the droplet contact lines remain at their position due to contact angle hysteresis. This leads to an irregular shape of the contact line. Zhao et al. [160] find that pinning is substantially more distinct for small contact angles, which is confirmed qualitatively in this study.

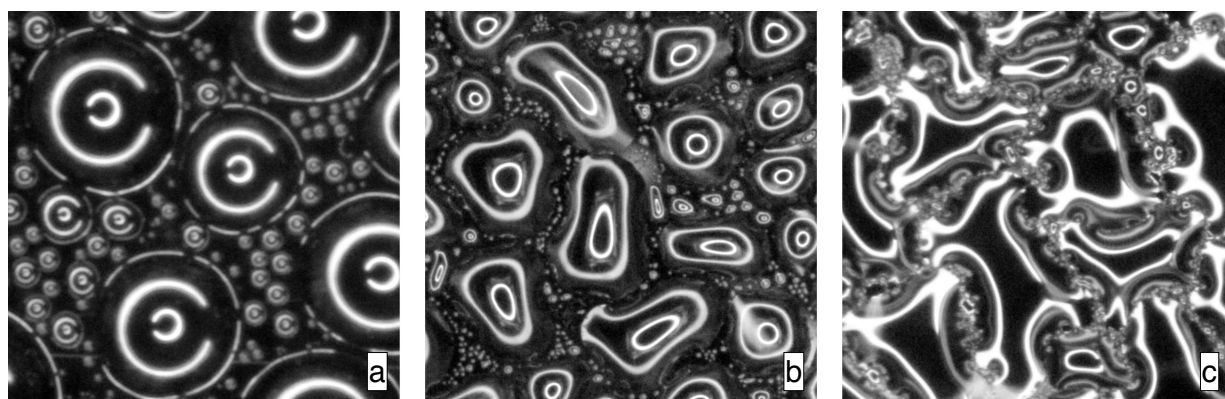


Figure 2.20: Droplet shapes during condensation on: [a] polycarbonate ($\theta \cong 90^\circ$); [b] low-e coated glass ($\theta \cong 65^\circ$); [c] float glass ($\theta \leq 26^\circ$). On float glass the contact angles are so small that only reflection C_1 is visible.

2.2.4 Experimental Results

One goal of this thesis is the appropriate modeling of window fogging, which includes also verifying experimentally, whether or not the condensate structure has an influence on mass transfer. This verification is presented in section 2.2.5. Beside the mass flux, also other measurement results, such as the number of droplets and the size of the liquid-vapor interface, are found in section 2.2.4.1. An interesting dependence between the contact angle and the droplet size is observed by applying the above described contact angle measurement method during the condensation and evaporation experiments. This dependence is explained in section 2.2.4.3. In the following sections results are only presented for the reference Reynolds number of $Re = 2.9 \cdot 10^4$. In section 2.3.3 experimental and simulation results are also presented for other airflow velocities.

2.2.4.1 Area-Related Measurement Parameters

As explained in section 2.2.1, the experiments are conducted in two phases. During the 1200 s condensation phase, the substrate is cooled by thermostat 1 with a temperature of -5°C , and water is accumulating on the substrate surface. Subsequently, the water supply is switched to thermostat 2 with a higher temperature of 15°C until the accumulated water is completely evaporated. The **coolant temperature** T_{co} of 15°C during the evaporation phase is below

the air temperature of 20 °C. Thus, the direction of the heat flux is not changed during the experiment. Evaporation is nevertheless realized by a surface temperature above the saturation temperature of the humid air. This is relevant for the theoretical considerations in section 2.2.5. The coolant temperature measured just before reaching the rear side of the substrate is shown in figure 2.21. The sudden change of coolant temperature illustrates the condensation phase ($t < 1200$ s) and the evaporation phase ($t > 1200$ s).

The two different phases and the switching point are clearly visible in the measured droplet **volume per unit area** or mean film height H_m (see figure 2.21), which is derived by a summation of all measured and estimated droplet volumes inside the reference section illustrated in figure 2.17. The film height increases, reaches its maximum at approximately 1200 s and decreases again. The droplet volume is in good approximation linear in time during the condensation and evaporation phase, besides small non-linearities at the beginning, the switching point and the end of the experiment.

The evaluation of the contact angles and the correct detection of the droplet volume V_{measured} is only possible for larger droplets, as reflections C_1 and C_2 are both needed to be clearly detectable. Therefore, at the beginning of the condensation phase, when all droplets are still very small, the volume is only estimated ($V_{\text{estimated}}$). This is done by an approximate detection of the droplet radii as explained in section 2.2.2.4 and an estimation of the respective contact angles. By growing of the droplets, more and more contact angles become detectable. As the large droplets constitute the main part of the overall droplet volume, the **fraction of measured droplet volume** to overall droplet volume f_{measured} quickly rises to a value of over 95%. After the evaporation of the very small droplets at the beginning of the evaporation phase, almost all droplets and contact angles are detected correctly, as only larger droplets remain (compare also lowest row in figure 2.7). The fraction of the measured volume f_{measured} reaches nearly 100% as seen in figure 2.21.

Whereas the droplet volume in figure 2.21 is approximately linear, another characteristic of the droplet distribution is the **number of droplets per unit area** N_A , which is highly non-linear. Starting at a value of zero, this parameter jumps to its maximum at the beginning of the condensation phase with a value as high as $7 \cdot 10^8$ droplets per square meter. As very small droplets are difficult to capture, the real value of this parameter is possibly even a little

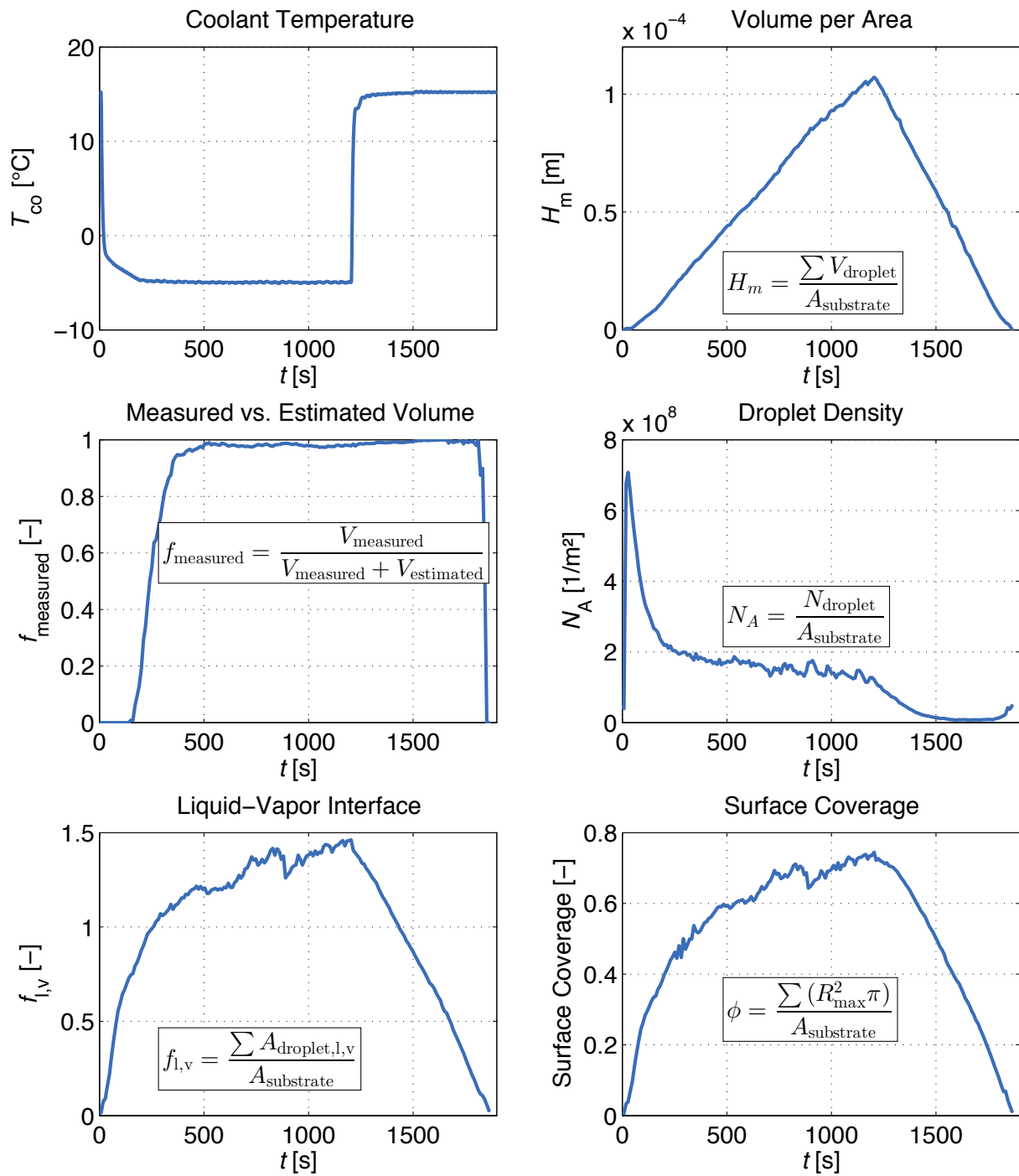


Figure 2.21: Coolant temperature and various area related measurement results of the reference condensation experiment with an untreated polycarbonate surface and $Re = 2.9 \cdot 10^4$.

higher. When droplet coalescence starts to dominate the droplet distribution, the number of droplets drops significantly and reaches an almost constant

value of approximately $1.5 \cdot 10^8$ droplets per square meter. When the evaporation phase starts, the number of droplets reduces again drastically and finally approaches a value of zero⁴.

The integral value of the **liquid-vapor interface** of all detected droplets exceeds the value of the corresponding substrate area, yielding a fraction of up to $f_{l,v} = 1.3$ (see figure 2.21). As explained in section 2.1.4 the condensation and evaporation mass flux is in some cases dependent on the size of the liquid-vapor interface. The experimentally observed dependence of the mass flow rate on the droplet geometry is discussed in section 2.2.5.

Another interesting parameter is the fraction of substrate area covered by droplets, the **surface coverage** ϕ . Qualitatively, the evolution of this parameter is similar to the area of the liquid-vapor interface. In the conducted experiments on polycarbonate, ϕ rises to a maximum value of approximately 70% (see figure 2.21). The value is higher than the theoretically constant surface coverage of 57%, obtained by a 2D simulation of the droplet pattern [58]. As soon as contact angle hysteresis is involved, the surface coverage is significantly higher as is also explained in section 2.2.3.1 and seen in figure 2.20: For the glass surface with distinct contact angle hysteresis, the surface coverage reaches values close to 100%. The irregular shape of the droplets covers almost the entire space between the droplets. On the other hand, the circular droplet shapes on polycarbonate allow significant parts of the substrate to remain uncovered.

In figure 2.22 it is schematically shown that the visibility through a fogged window depends significantly on the surface coverage and on the droplet shape. Even for relatively small contact angles, the majority of light passing through a curved droplet is diffracted in a way that the perceived image is blurred significantly. On the other hand, a sharp image (with a reduced intensity and contrast) is perceived if at least a part of the light passes through the nonwetted surface fraction. Another way not to diffract the light is achieved if significant parts of the liquid-vapor interface are parallel to the substrate surface. Hydrophilic anti-fogging coatings take advantage of this effect by forming a smooth water film instead of single droplets as explained in section 2.1.5.

⁴The slight increase of the droplet number at the end of the evaporation phase is due to an erroneous detection of impurities at the almost dry substrate surface.

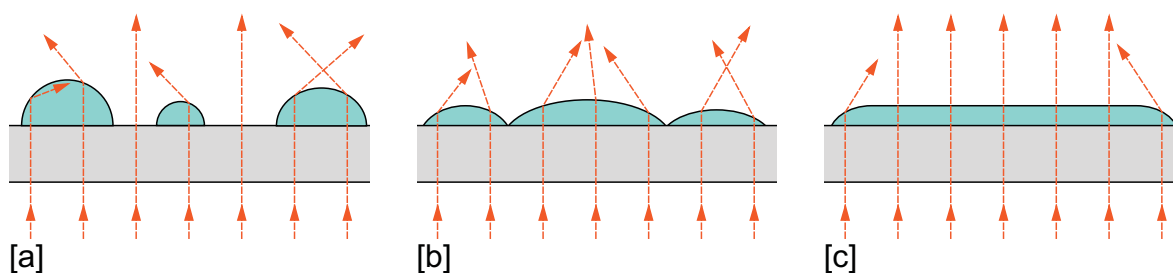


Figure 2.22: Parallel light rays passing through a fogged substrate with different surface properties. The light portion which is not significantly diffracted from the original direction depends on the surface coverage and on the geometry of the droplet, respectively the surface film: [a] surface with a significant part of uncovered substrate area; [b] surface with no uncovered substrate area; [c] surface with a homogenous liquid film (e.g. anti-fogging coating).

2.2.4.2 Nucleation and Sub-Cooling

During the experiments it is observed that droplets start growing predominantly in substrate locations with micro-scratches or impurities. Therefore, droplet nucleation and sub-cooling phenomena are studied in a separate experiment. The coolant temperature is reduced slowly until the beginning of droplet nucleation is observed in the substrate center. Subsequently, the temperature is raised slightly again to find out at which temperature the droplets evaporate again. Within the measurement reproducibility of approximately 0.5 K no significant hysteresis between the coolant temperature at which nucleation starts and the temperature at which droplets begin to evaporate again is observed. It is thus concluded that, although the surface of the polycarbonate substrate is very smooth, sub-cooling plays only a little role during the nucleation of droplets. The surface temperature at which condensation begins is thus assumed to be the vapor saturation temperature.

Another observed phenomena is the sub-cooling of liquid water prior to the formation of frost. Although the surface temperature of the substrate is below 0°C in some experiments, the droplets remain liquid in all conducted experiments. Only several Kelvin below the nominal freezing point, droplets start to freeze and desublimation is observed instead of condensation. Thus, the saturation pressure over liquids is applied for the computation of diffusion mass fluxes, whereas the saturation pressure over ice surfaces would need to

be applied if desublimation were studied (see equations (E.1) and (E.2) in appendix E).

2.2.4.3 Contact Angles

The observed macroscopic contact angle of water droplets on a substrate varies quite significantly although it is, in theory, determined by the surface excess free energy which is a material property (compare section 2.1.2, and Carey [23]). On real surfaces a wide variation of contact angles and strong deviation from the theoretical value is observed due to contact angle hysteresis. In the validation measurements with single droplets it is shown that the contact angle of evaporating droplets reduces after they are gently placed on a substrate surface (compare figure 2.13). A theoretical minimum value of this dropping contact angle is called the receding contact angle in contrast to the advancing contact angle which is the maximum contact angle of a growing droplet [153]. Both limits define the possible range of contact angle hysteresis. In a drop-wise condensation process, the size distribution and geometry of the droplets is determined by nucleation, growth by condensation and by coalescence of the droplets. When the interfaces of two droplets approach each other, they suddenly coalesce and form a single new droplet. The interfacial forces shape this droplet again into an axisymmetric geometry. Nevertheless, the contact line faces a certain resistance (pinning) due to contact angle hysteresis when traveling over the surface. This leads to a variation of the contact angle along the perimeter of the droplet and to droplets deviating from the axisymmetric shape (compare figure 2.20). The difference between advancing and receding contact angles can be large, which explains also the wide variation of contact angles measured during the condensation phase (see figure 2.23).

Besides the variation of the contact angle of individual droplets, figure 2.23 also reveals a dependence between the droplet radius and the contact angle. The measurement error is possibly larger for small droplets (compare section 2.2.3.1) but the detected contact angles are on average clearly larger for small droplets. A dependence between the contact angle and the droplet size is reported by several authors (compare [2, 41, 62, 82, 111, 147]). The phenomenon is explained by the existence of a line tension, which is an energy per unit length of the contact line, analogous to the surface tension (compare sec-

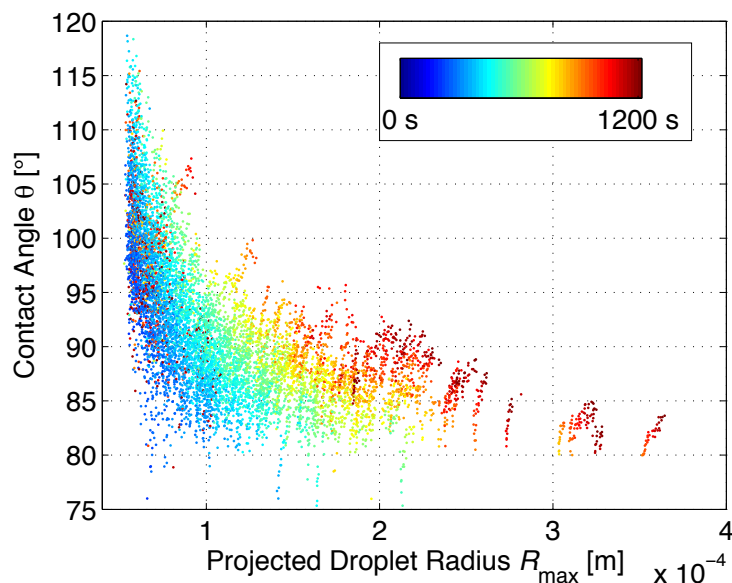


Figure 2.23: Droplet radius and contact angle distribution during the condensation phase on untreated polycarbonate and $Re = 2.9 \cdot 10^4$.

tion 2.1.2). A positive value of the line tension of approximately $\sigma = 2 \cdot 10^{-6}$ J/m found by regression analysis from equation (2.6) possibly explains the rising contact angles for small droplets observed in the experiments on polycarbonate.

As soon as the evaporation phase starts, droplet coalescence comes to an end and the droplet size distribution and evolution is determined only by evaporative mass transfer. This phase is comparable to the evaporation of a single droplet (compare figure 2.13). Due to the small ratio of droplet volume to droplet surface, small droplets evaporate more quickly and expose a significant part of the substrate area. The blank substrate area has a positive influence on the transparency as illustrated schematically in figure 2.22. For larger droplets, characteristic trajectories of the droplet radius and the contact angle are shown in figure 2.24. First, the contact angle drops at an almost constant projected radius which is equivalent to the radius of the contact line for contact angles $\theta < 90^\circ$. Subsequently, the radius drops at an almost constant contact angle, which is approximately 75° , here.

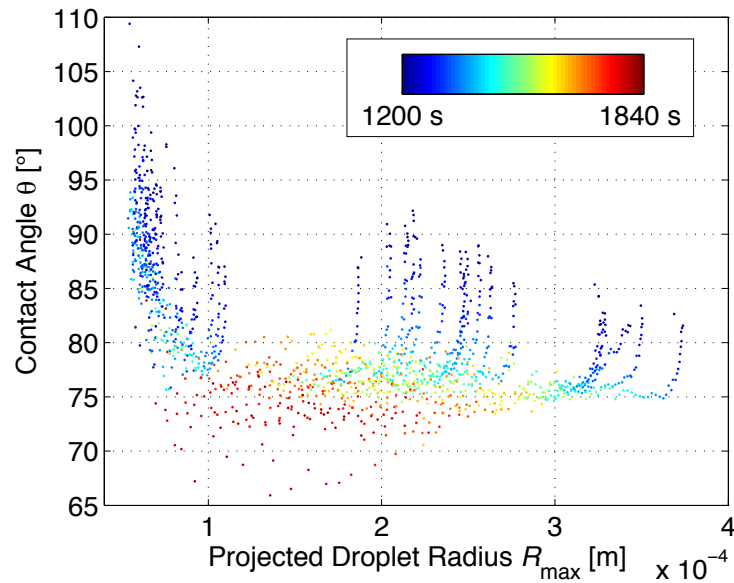


Figure 2.24: Detected droplet radius and contact angle distribution and evolution during the evaporation phase on untreated polycarbonate and $Re = 2.9 \cdot 10^4$.

2.2.5 Droplet Structure and Mass Transfer

The phenomenon of drop-wise condensation, where heat and mass transfer in a condenser is significantly higher than in a film-wise condensation regime, is known from power plant research and is explained in section 2.1.4. Here, the heat and mass transfer is significantly impacted by the surface structure of the condensed liquid. On the other hand, drop-wise condensation is proven to be less effective in the presence of a non-condensable gas [28]. A dependence of the droplet geometry on mass transfer under window fogging conditions is also assumed by various authors [29–32, 46, 72] (compare section 2.1.5). Three identified hypotheses for such a dependence are schematically illustrated in figure 2.25 and comprise:

1. Turbulence induction by the droplet structure ("surface roughness")
2. Size of the liquid-vapor interface
3. Thermal insulation of the condensate

The estimations, presented in the following sections, are made to analyze whether these hypotheses are relevant under typically encountered window fogging conditions and the conditions of the performed experiments.

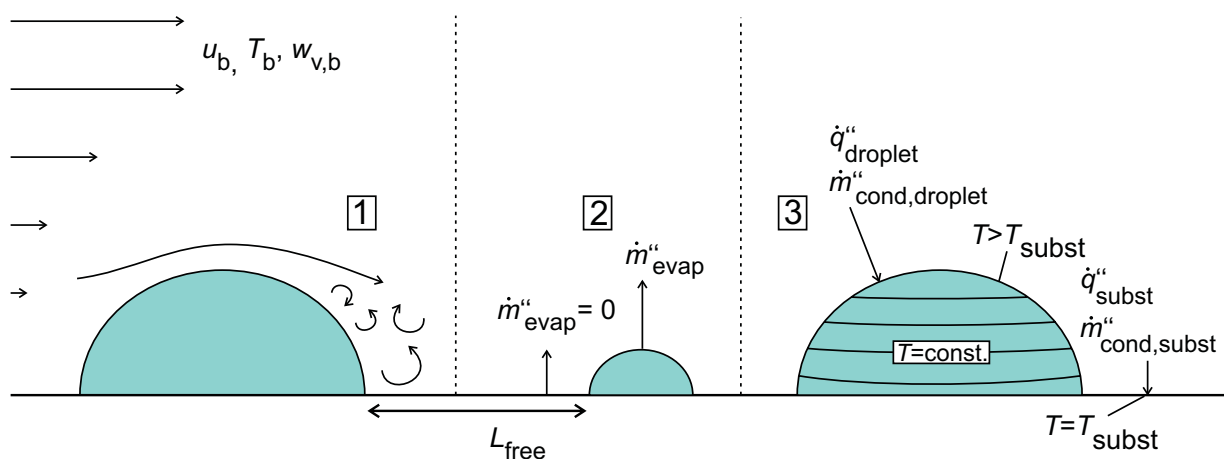


Figure 2.25: Schematic illustration of three possible interaction mechanisms between the droplet structure and the condensation and evaporation mass flow rate: [1] turbulence induction by the droplet; [2] size of the liquid-vapor interface; [3] thermal insulation of the condensate.

2.2.5.1 Turbulence Induction by the Droplet Structure

If turbulence were induced by the droplets in the conducted experiments, the additional turbulent transport would enhance heat transfer during the condensation phase and the evaporation phase which would lead to a higher surface temperature in both cases in comparison to a smooth surface. Hence, the level of supersaturation would be reduced during the condensation phase and enhanced during the evaporation phase. At the same time also the mass transfer coefficient would be enhanced due to the additional turbulent transport. During condensation both effects possibly neutralize each other, whereas during evaporation a higher mass flux would be obtained with larger droplets.

A rough wall surface enhances the production of turbulence in the boundary layer if the roughness peaks are sufficiently high. This leads to a higher pressure loss in channels in comparison to smooth walls. At the same time all other transport processes are enhanced due to turbulent transport. However, it is assumed that the structure and in particular the roughness of a surface has no influence on the flow if it is smaller than the laminar sublayer of the

turbulent boundary layer (compare e.g. Schlichting et al. [129]). This laminar sublayer extends approximately to a non-dimensional wall distance of:

$$y^+ = \frac{y \sqrt{\frac{\tau_{\text{wall}}}{\rho}}}{\nu} \leq 5. \quad (2.33)$$

Only if peaks of the surface profile emerge from the laminar sublayer, an effect of the flow on turbulence, pressure drop and transport processes is observed.

To estimate the minimum thickness of the laminar sublayer at the substrate center during the experiments, the wall shear stress τ_{wall} is calculated for the highest occurring Reynolds number of $4.9 \cdot 10^4$ at $\nu_m = 14.3$ m/s as follows:

$$\tau_{\text{wall}} = \frac{\lambda}{4} \rho \frac{\nu_m}{2}, \quad (2.34)$$

with the resistance coefficient for a hydraulically smooth pipe [115]:

$$\frac{1}{\sqrt{\lambda}} = 2 \log_{10} (\text{Re} \sqrt{\lambda}) - 0.8. \quad (2.35)$$

At the maximum investigated Reynolds number, $\lambda = 0.021$ is obtained and yields $\tau_{\text{wall}} = 0.61$ Pa, including the assumption of a fully developed turbulent channel flow at the substrate center. A CFD analysis of the experimental setup reveals a similar wall shear stress of $\tau_{\text{wall}} = 0.51$ Pa at the substrate center. Applying equation (2.33), the viscous sublayer thickness δ_{lam} extends approximately to a wall distance of $y = 1.1 \cdot 10^{-4}$ m at the substrate center. During all performed test series the maximum measured elevation of the droplets is $H_{\text{droplet}} = 3.8 \cdot 10^{-4}$ m, whereas the maximum mean elevation (mean film height) is $1.2 \cdot 10^{-4}$ m. It is therefore concluded that some of the droplets emerge from the laminar sublayer, possibly contributing to turbulence production. However, the majority of measurement points are obtained at lower Reynolds numbers and include smaller droplets. A clear influence of a "surface roughness" effect on the flow is therefore not confirmed by this estimation.

2.2.5.2 Influence of the Size of the Liquid-Vapor Interface on Vapor Mass Transfer

If the mass flux were proportional to the liquid-vapor interface or the droplet radius, the mass flux would be significantly lower at the beginning of the condensation phase and at the end of the evaporation phase in the experiment. In the middle part of the experiment, the liquid-vapor interface is significantly larger than the substrate area surface (see figure 2.21). Hence, the mass flux would then be larger than for a flat film. Large contact angles at hydrophobic surfaces enlarge the liquid-vapor interface, and higher condensation and evaporation mass fluxes would be observable.

The evaporation mass flow rate of single droplets is a function of the droplet radius, respectively the size of the liquid-gas interface (compare [113]). Amongst other authors Croce et al. [30] introduce a fogging model where the heat and mass transfer depends on the area ratio of the liquid-vapor interface and the solid-vapor interface (compare section 2.1.5).

As illustrated in the following, the influence of the size of the liquid-vapor interface is related to the issue of turbulence induction by the droplets. Additionally, also other effects may become relevant. For example, when the distances between individual droplets are very large, local variations of the water vapor content arise which reduce the evaporation mass flux in comparison to a continuous film.

Similarity considerations between the momentum transport at a rough wall (see section 2.2.5.1) and the water transport at a "rough" liquid-vapor interface lead to the assumption that similar principles apply. Lorenz⁵ [85] formulates a corresponding analogy for momentum transport and heat transport. Here, the heat transfer at a rough surface is also not enhanced as long as the roughness height lies within the laminar sublayer. On the other hand, if in a turbulent flow the surface is sufficiently rough, heat transfer is enhanced by up to 120% in comparison to a smooth wall. In this case the thermal conductivity of the substrate starts to play an important role.

In a laminar flow or boundary layer the inhomogeneities of the water content present in proximity of the droplet surfaces dissipate quickly (see figure 2.26).

⁵ Lorenz, Marco is not the author of this study.

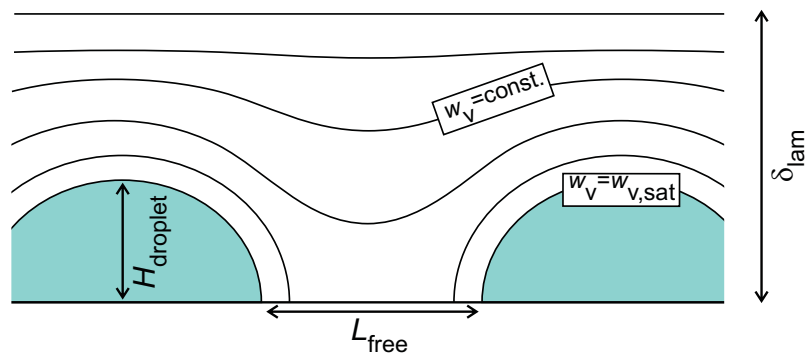


Figure 2.26: Schematic illustration of lines of constant vapor concentration around two evaporating droplets inside the viscous sublayer.

The vapor mass flow rate depends on the level of humidity supersaturation and is not dependent on the structure of the liquid-vapor interface. In the same manner, the analogy between momentum and mass transport must apply for turbulent flows with a laminar sublayer. Therefore, an array of droplets reveals approximately the same condensation or evaporation mass flow rate as a water film, as long as the droplets lie within the viscous sublayer thickness δ_{lam} of the droplet.

Although the droplet height might not have an influence on mass transfer, consideration of single evaporating droplets shows that in special cases the mass transfer must be a function of the droplet size and the droplet distribution. In section 2.1.4 it is shown that the evaporation rate of a single droplet in a laminar environment is proportional to the droplet radius. In a droplet array, if the spacings between the droplets L_{free} become very large, the mass transfer to the bulk flow is reduced in comparison to a smooth film or a dense droplet array. The reason for this is that differences in humidity concentration cannot dissipate before reaching the turbulent region (see figure 2.26). It is assumed that the structure of a droplet array has a negligible influence on the mass transport if:

$$H_{\text{droplet}} < \delta_{\text{lam}} \text{ and } L_{\text{free}} < \delta_{\text{lam}}. \quad (2.36)$$

The first condition is equal to the consideration in section 2.2.5.1. The second condition becomes in some cases relevant during the end of the evapora-

tion phase. Here, the small droplets disappear at first and only the very large droplets remain. The distances between those droplets are consequently relatively large (compare figure 2.7). Due to coalescence during the condensation phase, the distances between the largest droplets are in the same order of magnitude as the projected droplet diameter of the largest droplet generation.

2.2.5.3 Thermal Insulation of the Condensate

If the thermal insulation of the film or the droplets were relevant in the conducted experiments, the liquid-vapor interface temperature would be higher than the vapor-solid surface temperature. Hence, the condensation mass flux would be lower than if the liquid-vapor interface were equally cool. The condensation mass flux would also become smaller with growing of the film. An additional surface coverage or film formation involved e.g. by a lower contact angle would further reduce the condensation mass flux. During the evaporation phase the mass flux would be enhanced by the higher liquid-vapor interface temperature, as the coolant temperature is at 15 °C still below the air-temperature of 20 °C

The negative effect of the thermal insulation of a condensate film is the main reason why droplet condensation is preferred to film condensation in power plant technology: Here, the surface temperature of a blank surface is significantly lower than the surface temperature of the liquid-vapor interface. Nevertheless, heat transfer rates in power plant condensers are orders of magnitude higher than for window fogging conditions.

The maximum heat transfer rate which occurs in the experiments is estimated using a correlation for hydrodynamically developed, turbulent pipe flow. The local turbulent Nußelt number is computed according to equation (2.46) by Gnielinski [65] (see section 2.3.2 for details). It is estimated that the thermal resistance of the liquid boundary layer at the coolant side is negligible in comparison to the thermal resistance of the substrate. The heat flux occurs essentially perpendicularly to the wall, so the local heat flux is approximated as:

$$\dot{q}''(x) = \frac{T_a - T_{co}}{\frac{D_h}{Nu_x \lambda_a} + \frac{H_{PC}}{\lambda_{PC}}}. \quad (2.37)$$

For the highest occurring Reynolds number of $4.9 \cdot 10^4$ and the experimental parameters as described in section 2.2.1, the local heat flux from the bulk flow to the coolant in the test rig center is $1.1 \cdot 10^3 \text{ W/m}^2$ during the condensation phase. This is in good agreement with the corresponding CFD analysis, which reveals $1.2 \cdot 10^3 \text{ W/m}^2$ (see section 2.3.1.2).

The additional thermal resistance R_{film} of a thin homogeneous water film, which is assumed to correspond to the average droplet volume per unit area and is measured $1.2 \cdot 10^{-4} \text{ m}$ at maximum, is approximated as:

$$R_{\text{film}} = \frac{H_{\text{film}}}{\lambda_w}. \quad (2.38)$$

This additional resistance then leads to an increase in liquid-vapor interface temperature of $T_s = 0.13 \text{ K}$. The condensation mass flux is assumed proportional to the supersaturation of the water content:

$$\dot{m}''_{\text{cond}} \propto \Delta w_v = w_{v,b} - w_{v,\text{sat}}(T_s). \quad (2.39)$$

Here, a level of supersaturation of $\Delta w_v = 1.38 \text{ g}_v/\text{kg}_a$ is obtained for the lower interface temperature versus $\Delta w_v = 1.32 \text{ g}_v/\text{kg}_a$ for the higher interface temperature including the additional thermal resistance of the water film. This deviation is below 5% and illustrates that the effect can be neglected in good approximation. The reason is that under window fogging conditions typically encountered in vehicles, heat fluxes are relatively low and the film is relatively thin or at least is desired to be thin in comparison to power plant applications.

2.2.5.4 Experimental Verification of Droplet Structure Influences on Mass Transfer

The results obtained from the preceding estimations and theoretical considerations indicate that the conditions found in the experiment are at the limit of significance for all three hypotheses. Additionally, most test cases are performed at lower Reynolds numbers than $4.9 \cdot 10^4$ and most droplets are significantly smaller than the maximum assumed droplet radius.

To verify the theoretical considerations, an experimental parameter study is performed to check whether a dependence is seen in the experiments. A first indicator for no dependence is the linearity of the condensed volume over time which is already seen in figure 2.21. The condensation and evaporation rates depend significantly on the Reynolds number and the resulting surface temperature but remain in good approximation constant during one operation point instead of changing significantly with growing or reducing droplet sizes. This is observed in various tests at different Reynolds numbers (compare section 2.3.3, figure 2.36). A further test series with a variation of the hydro-affinity and thus different contact angles is performed to check if a dependence between droplet shapes and mass fluxes exists. Four different surface treatments as explained in section 2.2.1 lead to a variation of the contact angle:

Table 2.3: Overview of analyzed polycarbonate surfaces and measured mean contact angles.

No.	Surface treatment on PC substrate	Contact angle θ_m [°]
1	Hydrophobic coating	96.5
2	Untreated	90.3
3	Mechanical abrasion (level 1)	81.6
4	Mechanical abrasion (level 2)	79.3

Although the geometry of the droplets, i.e. the droplet radii, the heights and the contact angles, change significantly for the four different samples, no significant influence on the area-averaged accumulated water volume is observed in figure 2.27.

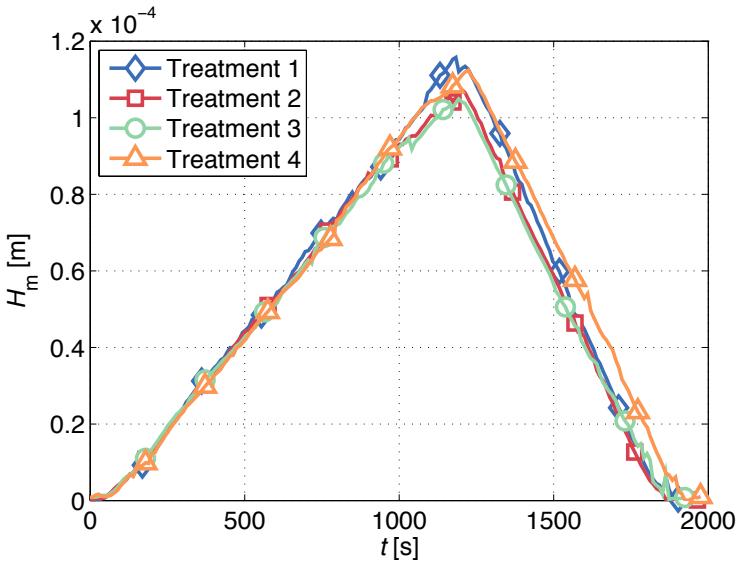


Figure 2.27: Experimentally determined mean film height on polycarbonate substrates with four different surface properties and varying contact angles.

The conditions in the test rig differ from window fogging conditions in vehicles due to different geometries as explained in section 2.2.1. Possible influences of the droplet structure on mass transfer are shown to be stronger for high Reynolds numbers, thin boundary layers, large droplet sizes and high heat transfer rates. Therefore, influences of the droplet structure on mass transfer are expected to be even lower in vehicle cabins, because the boundary layers at the windows are in general thicker and the heat fluxes lower than in the conducted experiments.

2.3 Simulation of Window Fogging

2.3.1 Computational Fluid Dynamics

2.3.1.1 Near-Wall Modeling

Window fogging is a phenomenon occurring at gas-solid interfaces. An accurate modeling of the transport processes at this wall is essential to achieve correct estimations of the wall temperature and the condensation and evaporation mass flux. Temperature and humidity transport in laminar flow is based on diffusive mechanisms. In turbulent flows both quantities are also transported convectively by turbulent diffusion. In fully turbulent flows, turbulent transport exceeds the laminar diffusion by orders of magnitude. Near to the wall, on the other hand, viscous damping reduces the tangential velocity fluctuations and kinematic restrictions reduce fluctuations normal to the wall.

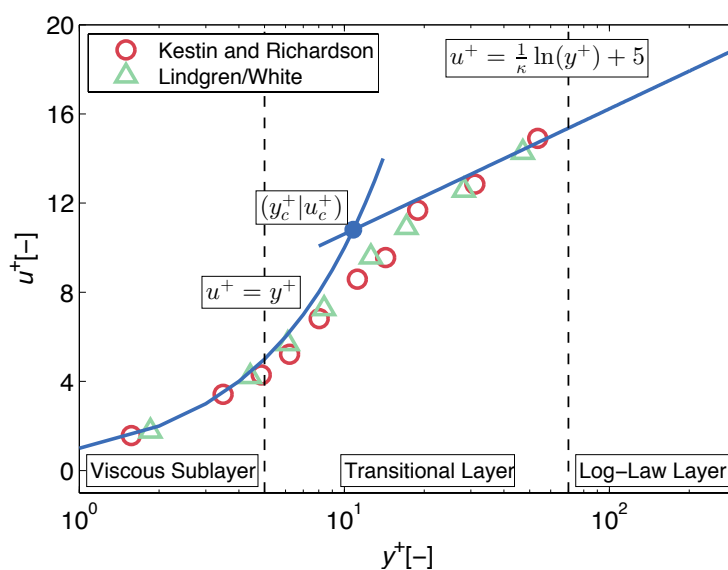


Figure 2.28: Boundary layer of the non-dimensional velocity u^+ at the wall with asymptotic approach to the linear law in the viscous sublayer and the logarithmic law away from the wall (image adapted from Schlichting et al. [129] with experimental data from Kestin and Richardson [71] and Lindgren/White [149]).

The region of the boundary layer which is dominated by laminar diffusion is called viscous sublayer. It is followed by a transitional layer where molecular viscosity and turbulence are both significant and a fully-turbulent layer where

transport processes are dominated by turbulence (see figure 2.28 and compare e.g. Schlichting et al. [129]).

The modeling of the near-wall region is challenging because strong gradients in all solution variables can coexist, as e.g. in the case of window fogging. Common Computational Fluid Dynamics (CFD) solutions principally offer two different approaches to model the near-wall region: The first option is to completely resolve the boundary layer, including the viscous sublayer by a sufficient number of computational nodes. As all gradients are orders of magnitude higher normal to the wall than in wall direction and the flow propagates almost parallel to the wall, the mesh needs to be refined only perpendicularly to the wall. In unstructured meshes the application of prism layers is essential to correctly model the wall region.

For the computational accuracy, it is in general favorable to completely resolve the boundary layer. If the boundary layer cannot be resolved, e.g. due to computational capacity restrictions, another option is the application of so-called wall functions. Here, the transport between the wall and the first near-wall mesh node is modeled by a simplified function, taking into account the transport variables at this node. A common type of function are Standard Wall Functions, where the velocity profile is approximated by a logarithmic function. This is in good agreement with measured velocity profiles in the turbulent boundary layer region (see figure 2.28). In the viscous boundary layer the velocity distribution is well reproduced by a linear function. In ANSYS FLUENT, Standard Wall Functions are implemented such that if the non-dimensional distance of the first near-wall node is larger than the respective value of the intersection point of the two curves, the logarithmic function is taken, and the laminar function if the value is smaller (see equation (2.40) and compare figure 2.28).

2.3.1.2 Condensation and Evaporation Model

As shown in section 2.2.5, the dependence of the area-averaged condensation and evaporation mass flux on the droplet structure is negligible for most window fogging conditions. The dependence becomes only relevant in conditions with high turbulence levels, large droplets or high heat transfer rates. Nevertheless, such conditions are not characteristic for window fogging in au-

tomobiles. Therefore, the condensation and evaporation is modeled merely as a function of the thermodynamic condition at the substrate surface and the adjacent flow field. The model does not account for the droplet distribution or the contact angle.

Several CFD-tools are equipped with a film condensation and evaporation model [5, 24]. One relevant application for such models is the vapor condensation in power plants. Therefore, such models can be coupled with two phase flow simulations and include the movement of the liquid film and effects such as film separation. Such effects are not considered relevant for the simulation of window fogging in this thesis, as the goal of the analyzed cabin optimization measures of section 4.5 is to keep the fog layer as thin as possible, to remove it or to avoid it completely. One of the latest versions of ANSYS FLUENT (version 14.5) includes an Eulerian Wall Film (EWF) model, capable to reproduce diffusive condensation and evaporation rates. Nevertheless, there is little documentation about the applied equations and coefficients. Modeling approaches such as wall functions are not built-in (compare [4, 5]). Therefore, the underlying equations of a diffusive condensation and evaporation model are integrated in FLUENT via a User Defined Function (UDF). The Defogging Module UDF, provided by ANSYS [93] from an old version (FLUENT 6.3), serves as basis for the coding of this function. The condensation or evaporation mass flux is modeled as explained in the following.

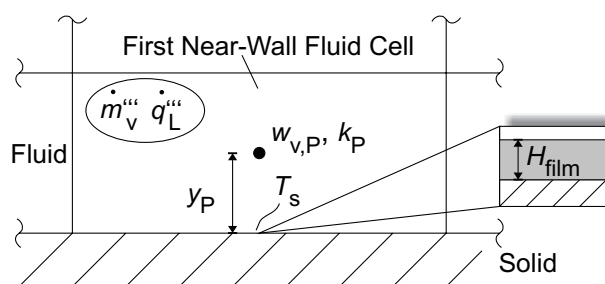


Figure 2.29: Illustration of the energy and mass transfer in the first CFD cell of the fluid domain.

The temperature at a given wall interface is T_s . The water film at this interface is assumed to be very thin. Thus, temperature differences between the solid wall surface and the liquid-air interface are neglected, which is a valid simplification as shown in chapter 2.2.5. At the liquid-air interface, the

gas-side of the interface is assumed to be saturated and the water content is $w_{v,\text{sat}} = f(T_s, p)$. The water content $w_{v,P}$ in vicinity of the wall, at the first cell node P , may be higher or lower than at the wall, yielding the driving force of vapor diffusion. Close to the wall all gradients parallel to the wall are negligible and it is therefore assumed that the mass transfer is only a function of the variables at point P and the corresponding wall interface (see figure 2.29).

Applying Standard Wall Functions leads to a rising error for fine meshes, respectively low y^*/y^+ values⁶. Therefore, it is recommended to either fully resolve the boundary layer, the first node lying in the viscous sublayer, or to apply a coarser mesh with the first node lying in the logarithmic region. To minimize the error for fine meshes, the logarithmic approach is replaced by the linear approach at the intersection y_c^* of both profiles if the first mesh node is closer to the wall than the intersection (compare figure 2.28) [4]. The non-dimensional water content is thus written as:

$$w^* = \frac{(w_{v,\text{sat}} - w_{v,P}) \rho C_\mu^{1/4} k_P^{1/2}}{\dot{m}''_{\text{cond}}} = \begin{cases} \text{Sc} \cdot y_P^* & \text{if } y_P^* < y_c^*, \\ \text{Sc}_t \left[\frac{1}{\kappa} \ln(E \cdot y_P^*) + f(\text{Pr}) \right] & \text{if } y_P^* \geq y_c^*, \end{cases} \quad (2.40)$$

with the non-dimensional wall distance y_P^* at the near-wall node:

$$y_P^* = \frac{y_P \rho C_\mu^{1/4} k_P^{1/2}}{\mu}. \quad (2.41)$$

For condensation conditions, \dot{m}''_{cond} is defined to be positive and for conditions leading to evaporation \dot{m}''_{cond} is negative.

From equation (2.40) the condensation or evaporation mass flux is calculated during the CFD iteration process as a function of the transport variables $w_{v,P}$, k_P , T_s and the local pressure p for every wall face. The film height H_{film} of the condensed water is calculated as follows:

$$\frac{dH_{\text{film}}}{dt} = \rho_w \dot{m}''_{\text{cond}}. \quad (2.42)$$

⁶In ANSYS FLUENT wall functions are formulated based on the non-dimensional wall distance y^* rather than y^+ [4].

At $H_{\text{film}} = 0$ and negative obtained values of $\dot{m}''_{\text{cond}} < 0$, i.e. an evaporation condition, the mass flux \dot{m}''_{cond} is set to zero, as obviously no water evaporates without the surface being wetted. For each wall cell of the fluid domain, a water vapor source term and a latent heat source term are added to conserve the energy and water balances:

$$\dot{m}'''_{\text{v}} = \frac{-\dot{m}''_{\text{cond}} A_{\text{s,cell}}}{V_{\text{cell}}}, \quad (2.43)$$

$$\dot{q}'''_{\text{L}} = \frac{L \cdot \dot{m}''_{\text{cond}} A_{\text{s,cell}}}{V_{\text{cell}}}. \quad (2.44)$$

2.3.1.3 CFD Model of the Test Rig

The experiments described in section 2.2 are designed to develop and validate the numerical window fogging model. The geometry of the described test rig is therefore partly incorporated into a 2D CFD mesh. The polycarbonate walls of the channel and the substrate are modeled as solid CFD domains including only conductive heat transfer.

To achieve the best possible matching of measurement and simulation, measured quantities, i.e. coolant temperature, air temperature, humidity, pressure, velocity, turbulence and light heat source are imposed as boundary conditions and source terms to the numerical domain as illustrated in figure 2.30. The coolant temperature is imposed to the domain as a measured time series, whereas all other quantities are taken as time-averaged results from the corresponding measurement. The actual area of interest, i.e. the section above the cooled substrate, is extended upstream and downstream to an overall length of the domain of 150 mm, to cover diffusive and conductive transport in vicinity of the substrate.

Different RANS turbulence models are tested but it is found that differences between the respective models are small. The RNG $k - \epsilon$ model is recommended for indoor turbulent flows in literature [26, 159]. Therefore, this tur-

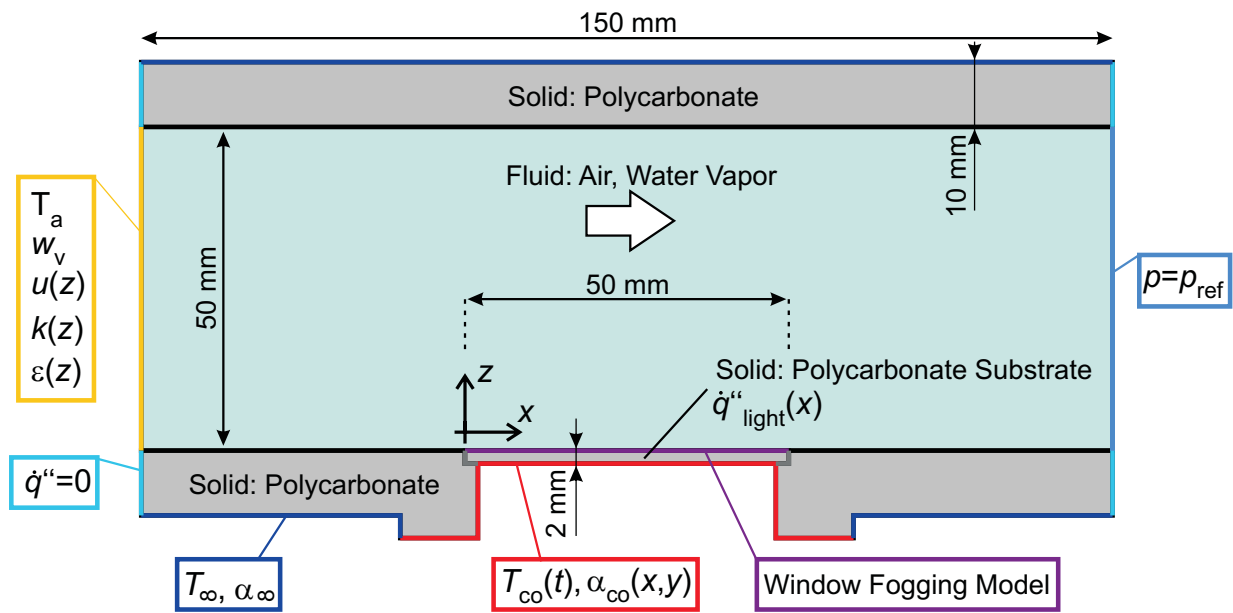


Figure 2.30: Numerical 2D domains for the validation of the fogging model with imposed boundary conditions from measurements.

bulence model is used for the CFD validation cases and for the following cabin simulation in section 4.2.1.

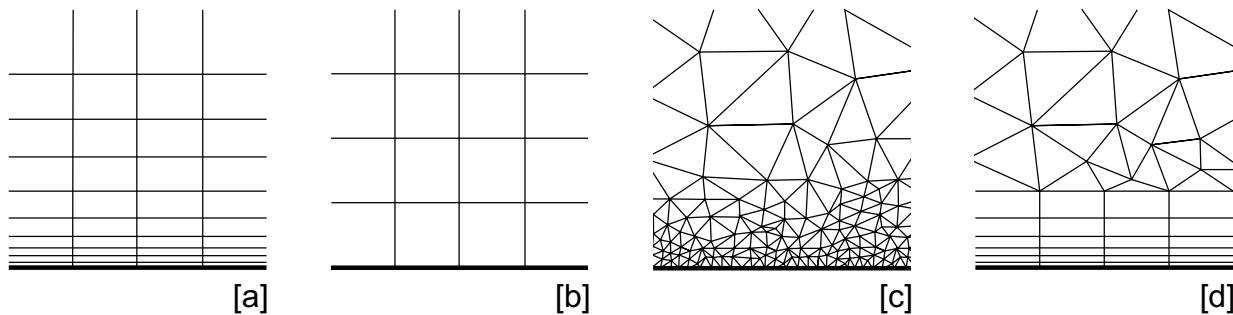


Figure 2.31: Schematic illustration of different mesh types analyzed to verify the influence of the mesh on the simulation results: [a] structured mesh with wall refinement; [b] structured mesh uniform mesh size; [c] unstructured mesh with wall refinement; [d] unstructured mesh with prism layers.

A mesh study is performed to analyze the dependency of the result on different mesh resolutions and the structure of the mesh. In figure 2.32 computation results of four different types of meshes, as illustrated in figure 2.31, are compared. It is assumed that the most detailed structured mesh with wall refinement, corresponding to mesh type [a] of figure 2.31, delivers the most accurate results. This mesh is taken as reference (Ref.) for the comparison with

the other meshes. The variable of interest is the condensation and evaporation mass flux rate in the center of the substrate which is compared to the experimental data in section 2.3.3.

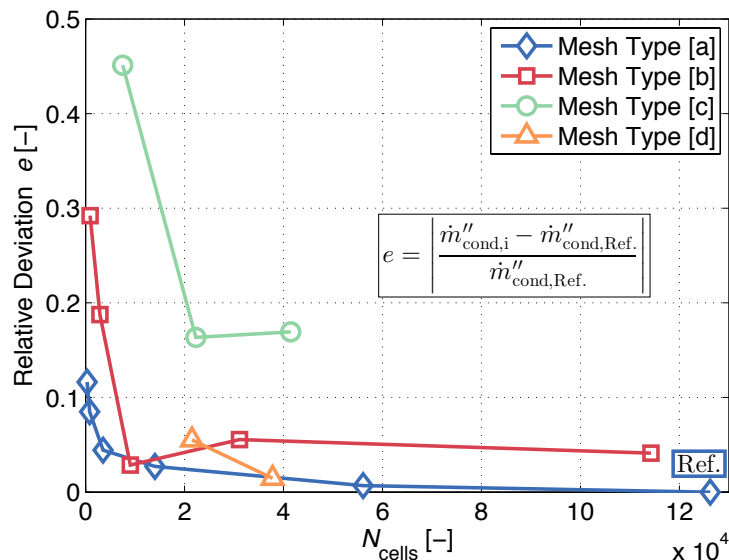


Figure 2.32: Relative deviation e of the center point condensation mass flux from the reference mesh solution (finest structured mesh) at $Re = 2.9 \cdot 10^4$ for different mesh types and resolutions.

The mesh sensitivity analysis shows that by increasing the mesh resolution all solutions approach the solution of the reference mesh. A fine wall mesh resolution and parallel cells at the wall are essential to obtain reliable results. Thus, either a structured mesh with wall refinement [a] or an unstructured mesh with prism layers [d] can be used to obtain a solution with reasonable computational effort and good accuracy.

2.3.2 Analytical Approach

The simple geometry of the test rig also allows an analytical approach to estimate the condensation and evaporation rates. Although an analytical window fogging model is not suitable for vehicle cabins, there are simpler configurations where such a model is applicable. Analytical results are compared to the CFD simulation and the experimental data.

The approach is based on a similar analytical model of natural convection and condensation presented by Fayazbakhsh and Bahrami [46] although dif-

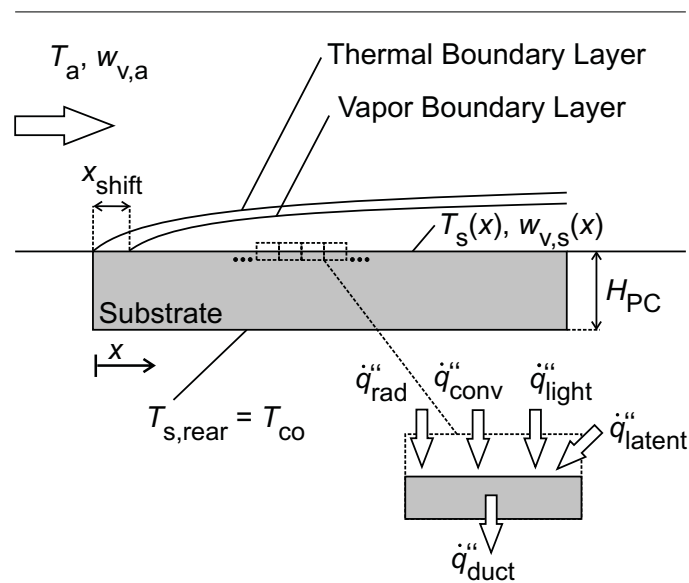


Figure 2.33: Schematic illustration of the simplified model for the analytical approach.

ferent correlations and assumptions are applied in the model of the present study. Some simplifying assumptions are necessary to solve the temperature and mass flux distribution at the surface analytically:

- The problem is assumed to be steady-state and one-dimensional, so a constant coolant temperature T_{co} is assumed during the condensation and evaporation phase and thermal inertia is neglected.
- A Nußelt correlation for fully developed pipe flow is used for the approach. The entrance flow length $L_h = L_{pipe}/D_h$ which is necessary for hydrodynamically fully developed flow depends on the Reynolds number and ranges between 10 and 60 for turbulent flows and up to $\cong 130$ for laminar flows [113]. Such lengths are not realizable for the test rig, but the velocity profiles (see appendix A) show that the flow field can be assumed to be approximately fully developed at the substrate surface, although the flow length in the current test rig design is only $L_h \cong 9$.
- Another assumption, analogous to the CFD model, is that the thickness and structure of the condensate has no influence on the flow, the surface temperature and the mass flux rates (see section 2.2.5).

At the upstream edge of the cooled substrate surface, the thermal boundary layer starts to develop. The development of the thermal boundary layer in a

fully developed laminar pipe flow at constant wall temperature is known as the Graetz-Nußelt problem, and a solution can only be obtained numerically [66]. The local Nußelt number is given by an approximation derived from the numerical solution [65]:

$$\text{Nu}_{x,\text{lam}} = \sqrt[3]{3.66^3 + 0.7^3 + \left(1.077 \sqrt[3]{\text{Re} \cdot \text{Pr} \frac{D_h}{x}} - 0.7\right)^3}. \quad (2.45)$$

For turbulent flow in the same configuration the local Nußelt number is approximated as follows [65]:

$$\text{Nu}_{x,t} = \frac{(\zeta/8) \text{Re} \text{Pr}}{1 + 12.7 (\zeta/8)^{0.5} (\text{Pr}^{2/3} - 1)} \left[1 + \frac{1}{3} \left(\frac{D_h}{x}\right)^{2/3}\right], \quad (2.46)$$

with:

$$\zeta = (1.8 \log_{10}(\text{Re}) - 1.5)^{-2}. \quad (2.47)$$

For Reynolds numbers in the laminar-turbulent transition regime $2300 < \text{Re} < 10000$, the Nußelt number is derived by interpolation from equation (2.45) at $\text{Re} = 2300$ and equation (2.46) at $\text{Re} = 10000$, as proposed for a similar case by Gnielinski [65]:

$$\text{Nu}_{x,\text{lam},t} = (1 - \Psi) \text{Nu}_{x,\text{lam},2300} + \Psi \cdot \text{Nu}_{x,t,10000}, \quad (2.48)$$

with:

$$\Psi = \frac{\text{Re} - 2300}{10000 - 2300}. \quad (2.49)$$

These applied Nußelt correlations are defined for constant wall temperature. On the rear side of the substrate, the heat transfer rate is very high so that $T_{s,\text{rear}} = T_{\text{co}}$ is assumed. Nevertheless, the thermal resistance of the substrate is not negligible and leads to a variation of T_s . The temperature gradient in the

first part of the substrate is high, whereas it is significantly lower in the second part (see figure 2.34). Therefore, it is assumed that the error made by applying equations (2.45) – (2.49) is acceptable. The local convective heat flux to the substrate is thus calculated as:

$$\dot{q}_{\text{conv}}'' = \text{Nu}_x \frac{\lambda_a}{D_h} (T_a - T_s). \quad (2.50)$$

The heat flux by long-wave radiation⁷ is approximated by assuming that the surrounding surfaces are much larger than the substrate surface and have a uniform temperature equal to the air temperature T_a :

$$\dot{q}_{\text{rad}}'' = \sigma_B \cdot \epsilon_{\text{lw}} (T_a^4 - T_s^4). \quad (2.51)$$

Assuming the temperature of the rear side of the substrate uniformly as $T_{\text{s,rear}} = T_{\text{co}}$, the conductive heat transfer from the substrate surface to the coolant is written as:

$$\dot{q}_{\text{duct}}'' = \frac{\lambda_{\text{PC}}}{H_{\text{PC}}} (T_s - T_{\text{co}}). \quad (2.52)$$

Finally, the latent heat flux of condensation or evaporation depends on the corresponding local mass flux rates. With \dot{m}_{cond}'' defined to be positive for condensation and negative for evaporation it results:

$$\dot{q}_{\text{L}}'' = L \cdot \dot{m}_{\text{cond}}''. \quad (2.53)$$

Analogously to equation (2.50), where the heat transfer is calculated by the Nußelt number, $\dot{m}_{\text{cond}}''(x)$ is calculated by the dimensionless Sherwood num-

⁷The gray-body emissivity of the substrate for the analytical approach and the CFD case of the test rig is assumed to be $\epsilon_{\text{lw}} = 0.95$. This corresponds to the emissivity of water, as it is assumed that the substrate surface is predominantly covered with droplets. The change of the surface gray-body emissivity ϵ_{lw} due to the actual condensate surface coverage is neglected.

ber Sh defining the dimensionless mass transfer between the surface and the bulk phase:

$$\dot{m}''_{\text{cond}} = Sh \frac{\rho D}{D_h} (w_{v,a} - w_{v,s}). \quad (2.54)$$

Here, $w_{v,a}$ is the vapor content in the bulk phase and $w_{v,s}$ is the vapor content at the wall surface. If the wall surface is wetted, it is assumed that $w_{v,s} = w_{v,\text{sat}} = f(p, T_s)$.

Detailed documentation about Sherwood number correlations for different flow configurations is not available in literature. Nevertheless, the analogy between heat and mass transfer is applicable. This analogy relates the Nusselt number of a certain flow configuration to the respective Sherwood number of the same configuration by the Lewis number with an exponent $m = 1/3$ for water vapor in air [10]:

$$\frac{Sh}{Nu} = Le^m. \quad (2.55)$$

Accordingly, the same equations (2.45) – (2.49) to derive the Nusselt number are also used to derive the Sherwood number. Here, again an approximation is made because $w_{v,s}$ is not constant but depends on the surface temperature and therefore varies along x . The position $x = 0$ in equations (2.45) – (2.49) is where the thermal boundary layer development starts. For the temperature boundary layer, this position is assumed to be the front edge of the substrate plate. For the vapor content, this position shifts downstream in the case of a varying surface temperature because condensation only begins as soon as the surface temperature drops below the saturation temperature of the bulk vapor content $w_{v,a}$. This temperature dependent shift x_{shift} is taken into account in the calculation of the mass flux, starting where the surface temperature T_s begins to fall below the saturation temperature T_{sat} :

$$T_s(x = x_{\text{shift}}) = T_{\text{sat}}(w_v = w_{v,a}). \quad (2.56)$$

The position x in equations (2.45) – (2.49) is replaced by $x - x_{\text{shift}}$ and the flow rate \dot{m}''_{cond} is set to zero for negative values of x .

For the evaporation case, the surface temperature of the substrate is higher than the saturation temperature over the whole substrate length. Thus, water evaporates wherever the surface is wetted. Nevertheless, in the experiment water evaporates only where it condensed before. Accordingly, the shift length x_{shift} , which is calculated for the condensation phase is also applied for the respective evaporation phase.

The foregoing equations (2.50) – (2.53) and the light source \dot{q}''_{light} (see appendix B) describe the heat fluxes from and to the substrate surface at a certain x -position. A heat flux balance is done for the substrate surface as illustrated in figure 2.33 and delivers:

$$\dot{q}''_{\text{conv}} + \dot{q}''_{\text{L}} + \dot{q}''_{\text{rad}} + \dot{q}''_{\text{light}} - \dot{q}''_{\text{duct}} = 0. \quad (2.57)$$

Substituting all terms of equation (2.57) by the above described relations, the only unknown is the local surface temperature of the substrate T_s . For each position x this temperature is evaluated iteratively. Here, the MATLAB built-in function *fzero* is used. Knowing the local surface temperature, the local condensation or evaporation rate is calculated by equation (2.54).

Table 2.4: List of assumed properties and parameters for the analytical approach.

Property	Value	Property	Value
$\nu_{a,m}$	0.364, 1.94, 18.37, 114.3 m/s	T_{co}	-5, 15 °C
Re	1.2E3, 16.6E3, 12.9E4, 14.9E4	ρ_a	96.2 · 10 ³ Pa
T_a	20.5 °C	$w_{v,a}$	8.03 · 10 ⁻³ kg _v /kg _a
D_h	5.45 · 10 ⁻² m	H_{PC}	2 · 10 ⁻³ m
λ_{PC}	0.2 W/(m K)	ρ_a	1.14 kg/m ³
μ_a	1.82 · 10 ⁻⁵ Pa s	$c_{p,a}$	1.02 · 10 ³ J/(kg K)
λ_a	2.75 · 10 ⁻² W/(m K)	$D_{v,a}$	2.61 · 10 ⁻⁵ m ² s
L	2.45 · 10 ⁶ J/kg	ν	1.60 · 10 ⁻⁵ m ² s
m	$\frac{1}{3}$	ϵ_{lw}	0.95
\dot{q}''_{light}	see appendix B		

The evaluation of the above described equations delivers the surface temperature and the condensation and evaporation mass flux at the substrate surface. These steady-state 1D results are compared with the results obtained from the CFD simulation. As the CFD simulation is a transient calculation with coolant temperatures varying over time according to the experimental data, the condensation rate is compared at $t = 1195$ s shortly before switching to the higher coolant temperature and the evaporation phase.

The general distribution of the surface temperature and the condensation mass flux rate are similar in the CFD analysis and the analytical solution (see figure 2.34 and 2.35). Nevertheless, small differences are visible: The tempera-

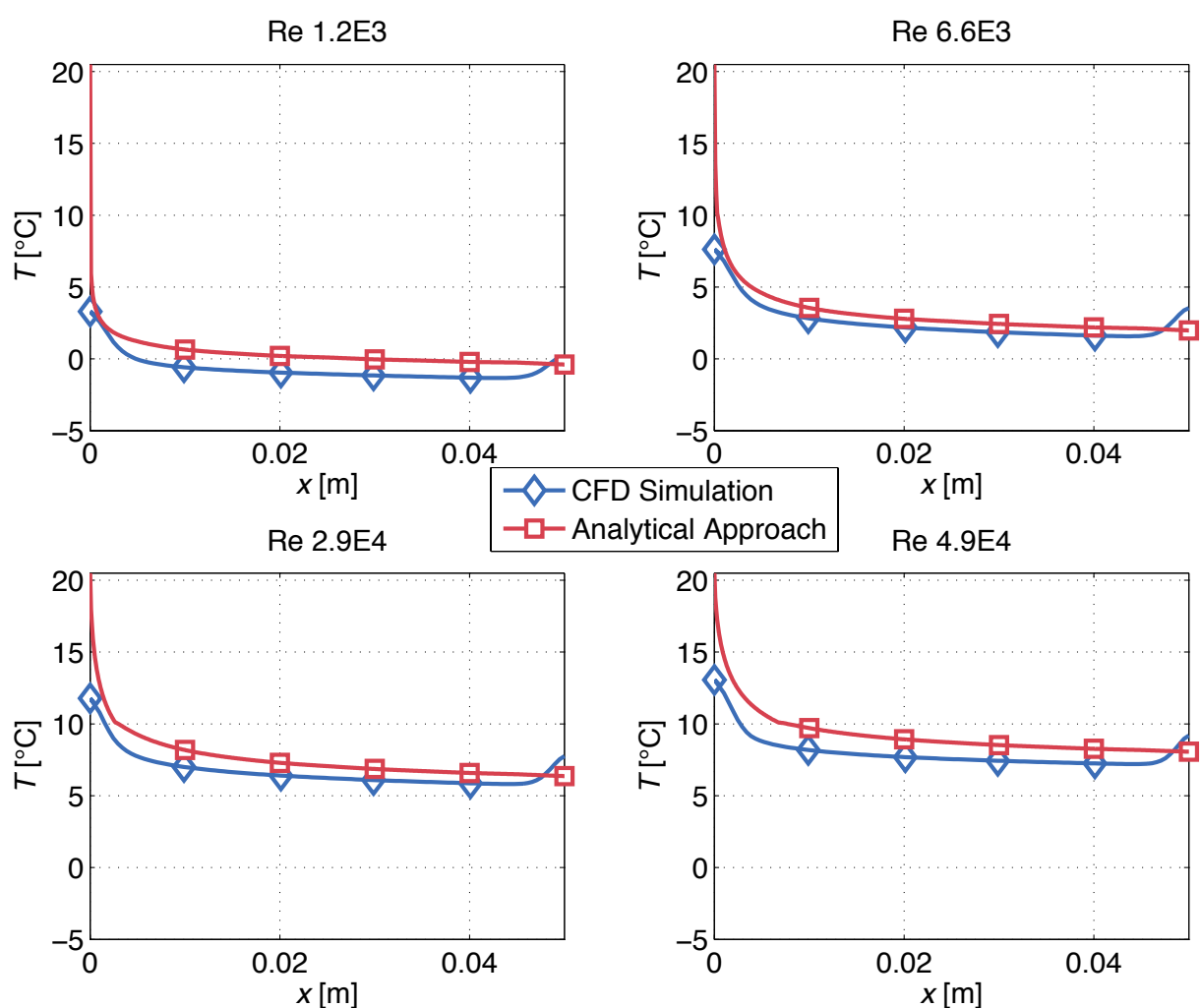


Figure 2.34: Comparison of the local surface temperature derived by CFD simulation (at $t=1195$ s) and by the analytical approach during the condensation phase.

ture distributions of the CFD simulation show that the surface temperature drops less rapidly than in the analytical analysis. The CFD model shows that in the rear part of the substrate the surface temperature rises again and the condensation rate drops. The reason for the differences in the two modeling approaches is mainly that transport processes in flow direction are not modeled in the analytical approach. As the cooled substrate is in thermal contact with the channel structure, temperature perturbations travel upstream in the solid phase and also diffusive processes lead to temperature and vapor transport upstream and downstream. This is also the reason why a larger section than the 50 mm section above the substrate is considered in the CFD analysis (see figure 2.30).

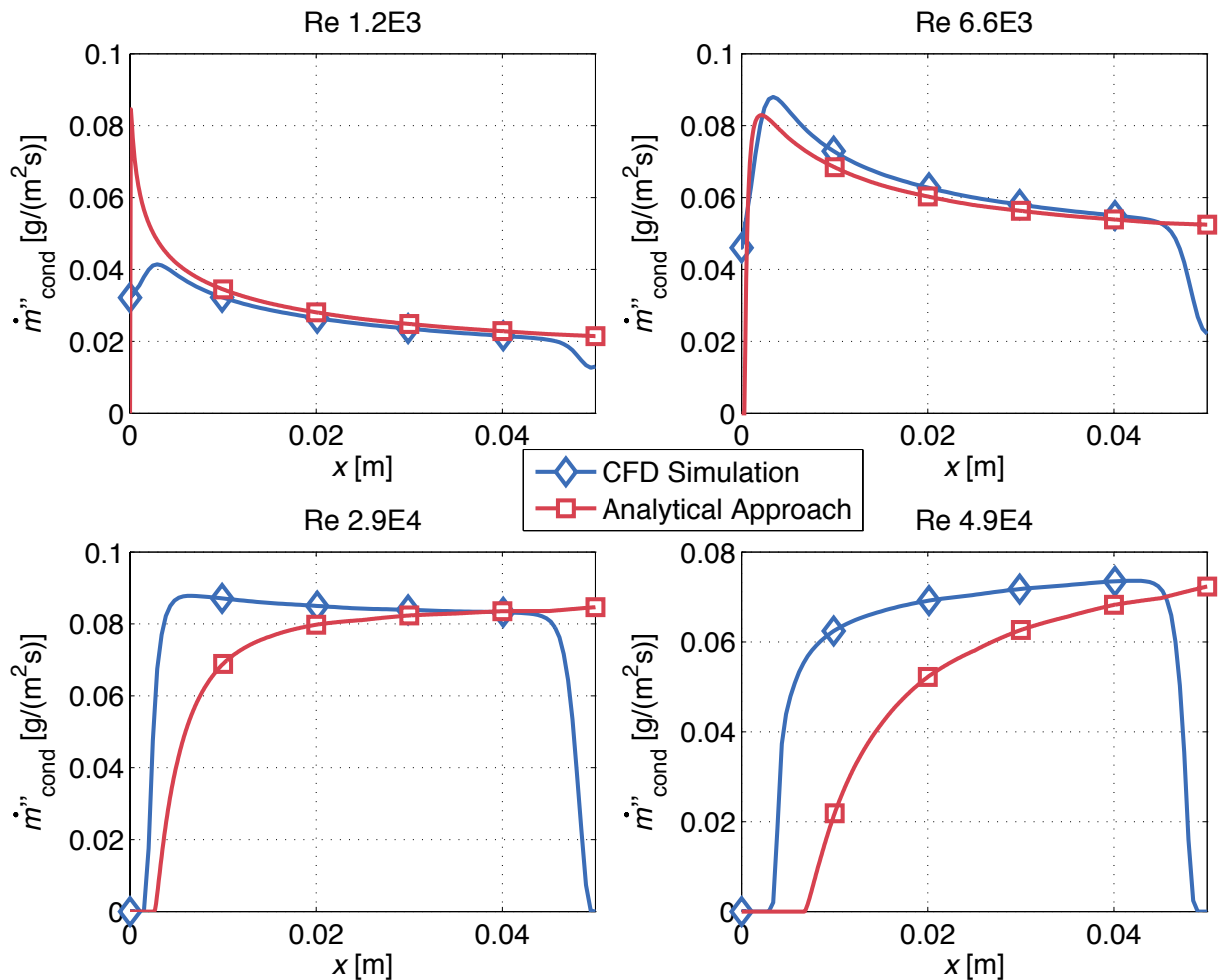


Figure 2.35: Comparison of the local condensation rate derived by CFD simulation (at $t=1195$ s) and by the analytical approach during the condensation phase.

The surface temperature shows similar distributions for all air speeds, whereas the distribution of the condensation rate is quite different for the analyzed Reynolds numbers. The reason for this effect is that the surface temperature depends almost only on the development of the thermal boundary layer, whereas the condensation rate depends on the development of the thermal as well as the vapor boundary layer. Condensation occurs only below the saturation temperature and depends on the local level of subcooling which varies significantly along the substrate. For low air speeds the condensation rate reaches its maximum right after the substrate edge. The maximum is shifted downstream for higher air speed values. Also the substrate length x_{shift} where no condensation occurs, becomes larger with rising Reynolds numbers.

2.3.3 Experimental Validation of the Fogging Model

Before the CFD fogging model is integrated in the overall vehicle model, its performance is validated against experimental data at different Reynolds numbers. The lowest Reynolds number is with $Re = 1.2 \cdot 10^3$ in the laminar flow regime, whereas the higher Reynolds numbers up to $Re = 4.9 \cdot 10^4$ are clearly turbulent.

For all flow velocities, the differences between experiment and transient CFD simulation are small, as seen in figure 2.36. It is also seen from figure 2.36 that the condensate volume is approximately linear for all velocities, so the rates of condensation and evaporation are constant.

To obtain and compare these rates, the condensate volume is linearized and differentiated separately for the condensation phase and the evaporation phase. Transition times of 120 s before and after the three transition points (start, thermostat switch and end of each test) are omitted for this evaluation. It is seen in figure 2.37 that the condensation rate rises up to a Reynolds number of $Re = 2.9 \cdot 10^4$ after which it reduces again. The absolute value of the evaporation rate on the other hand rises continuously with an increasing Reynolds number (see figure 2.38). This behavior is due to two effects influencing mass transport: Firstly, the rising flow rate and turbulence level enhance the mass transport and the vapor gradient at the wall leading to higher rates. Secondly, flow rate and turbulence also influence heat transfer, leading to a higher surface temperature at higher Reynolds numbers and thus, higher

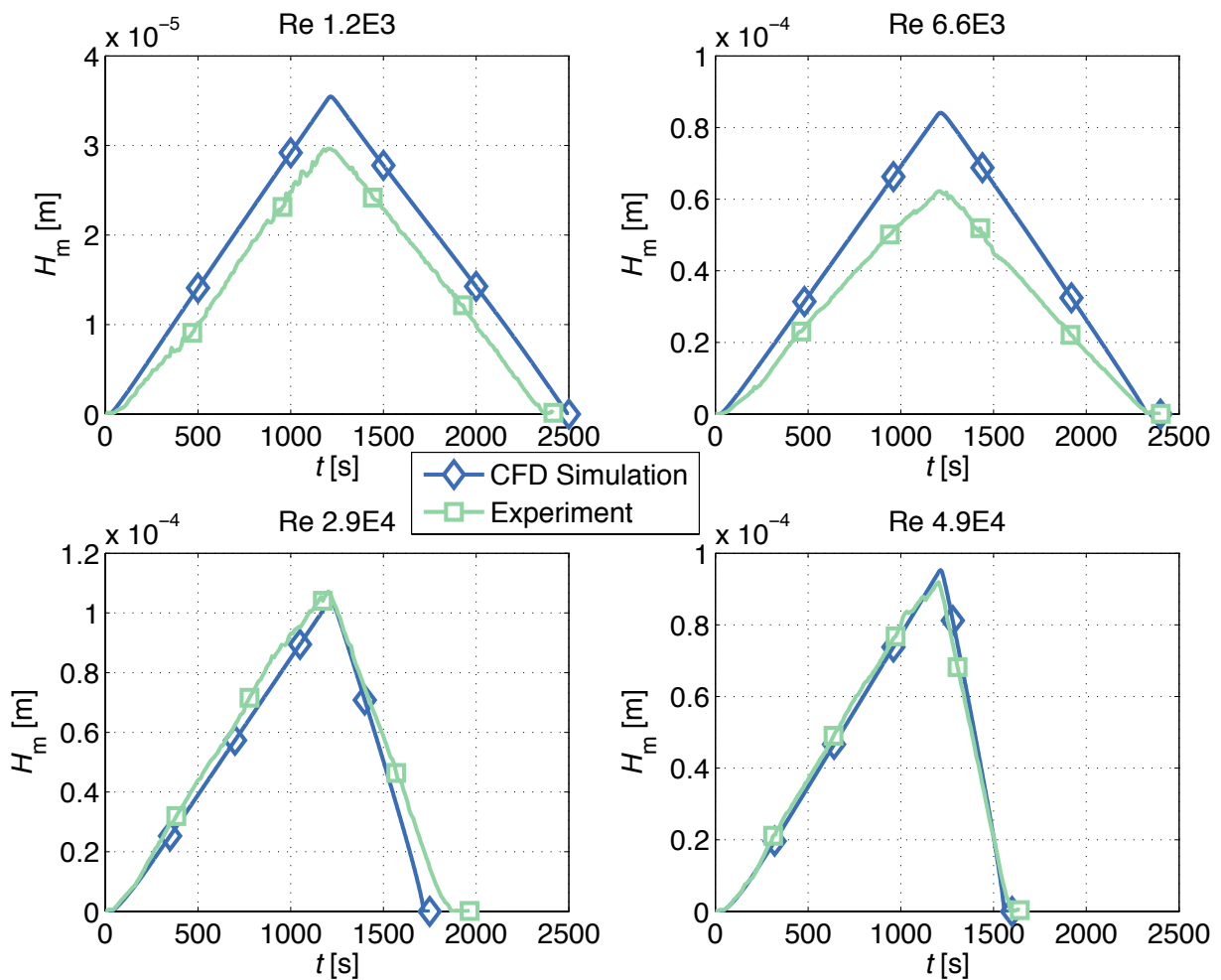


Figure 2.36: Comparison of the condensate volume derived by measurement and CFD simulation for different flow velocities as a function of time.

saturation water content at the wall. This second effect leads to a reduction of the vapor gradient during the condensation phase and an increase of the gradient during the evaporation phase. All three data sets, i.e. experiment, analytical approach and simulation, reproduce the two effects correctly. The comparison reveals a maximum deviation of approximately 30% of the condensation and evaporation rates between the CFD-simulation, the analytical approach and the experiment.

It is thus concluded that the CFD-simulation as well as the analytical model predict the condensation and evaporation mass flux at the substrate center reasonably well. A model including the influence of the droplet geometry, the droplet distribution or the mean condensate film thickness is not necessary under these conditions. The analytical model on the other hand can only be

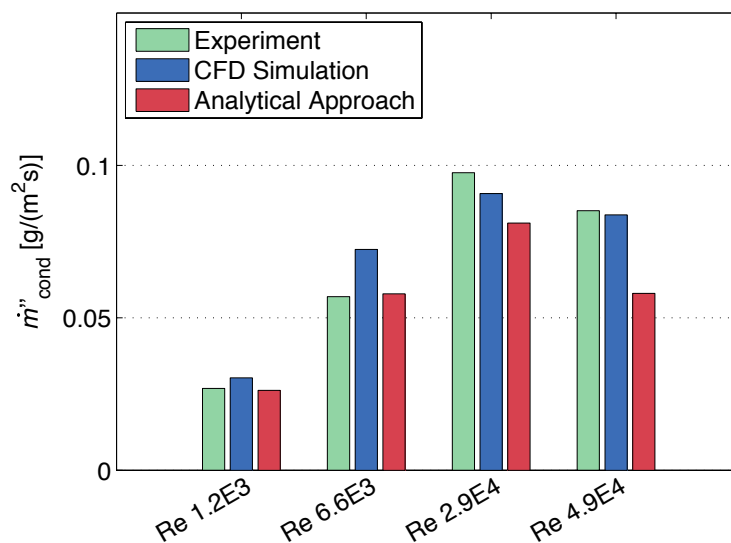


Figure 2.37: Comparison of the mass flux during the condensation phase derived by measurement, CFD simulation and analytical approach for different flow velocities.

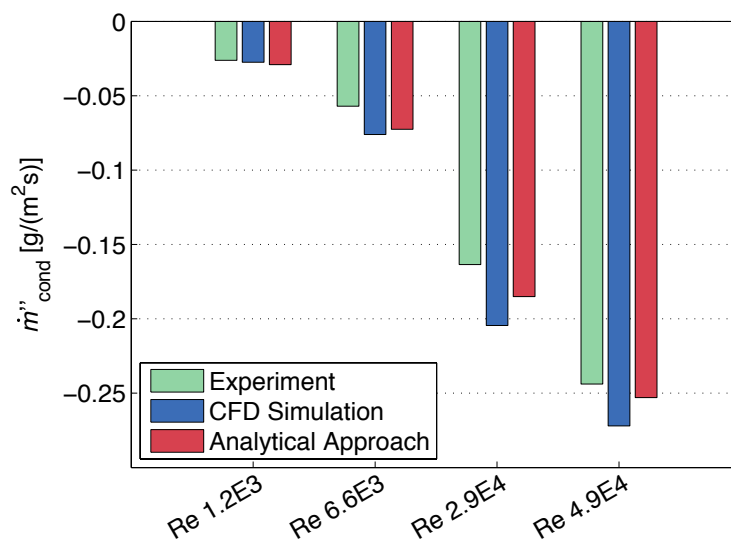


Figure 2.38: Comparison of the mass flux during the evaporation phase derived by measurement, CFD simulation and analytical approach for different flow velocities.

applied due to the simplicity of the test rig geometry and shows e.g. significant differences at the boundaries of the domain. In a real cabin geometry only the CFD model is assumed to reproduce the temperature distribution and fogging mass fluxes adequately.

2.4 Conclusion

The analysis of various published modeling approaches and theories for window fogging and drop-wise condensation and evaporation reveals different approaches. Some window fogging models include influences of the droplet structure on the mass transfer rate by using a droplet model, whereas others neglect them by using a film model. A relevant dependence between the structure of the condensate and the mass transfer rate is known from drop-wise versus film-wise condensation in power plant technology. On the other hand, already a small fraction of non-condensable gases reduces the difference between film-wise and drop-wise condensation significantly. One goal of this thesis is to find out if this difference is relevant under typical window fogging conditions in vehicles.

A measurement technique developed in this study allows to measure the contact angle and volume of droplets during the condensation and evaporation. Thus, an area-averaged local mass flux of a basic condensation and evaporation experiment is obtained. Three different hypothetical mechanisms for a dependence of mass transfer on droplet structure are estimated theoretically and compared to the experimental results. It is found that a dependence exists only for high Reynolds numbers, thin boundary layers, large droplet sizes and high heat transfer rates. Such conditions are in most cases not typical for window fogging in vehicles and are not reproduced in the experiments. The conducted experiments at various droplet sizes, contact angles and different air velocities confirm that no dependence is observable under the analyzed conditions.

It is thus concluded that a film model reproduces the condensation and evaporation mass transfer rate sufficiently well. A suitable CFD window fogging model is implemented in ANSYS FLUENT. This model includes wall mass transfer by a Standard Wall Function approach, but neglects influences of the droplet structure and the amount of condensate. A 2D mesh of the test rig geometry is generated, and boundary conditions obtained from the experiment are applied. This allows a quantitative evaluation of the window fogging model. The simple test rig setup also allows an analytical estimation of the mass transfer rate. The CFD model as well as the analytical model show good

agreement with the experimental data for various airflow velocities with maximum deviations of the mass flux of approximately 30%.

The window fogging model introduced above, is integrated in the vehicle cabin model presented in chapter 4. It is used to quantify the window area fraction where fog occurs during the simulated driving cycle. This is important to evaluate the influences of different glazing materials and cabin air recirculation not only on the energy saving potential but also on window fogging and thus driving safety.

3 Passenger Thermal Comfort

Besides security aspects, such as the deicing and defogging of the windows, the main task of the Heating Ventilation and Air-Conditioning (HVAC) system in vehicles is the generation of a comfortable condition for the passengers. Consequently, optimization measures must not only need to be evaluated according to their HVAC power reduction potential but also according to their influence on passenger thermal comfort. General influences on thermal comfort and specifically on thermal comfort in vehicles are summarized in section 3.1 and 3.2. Different state-of-the-art modeling approaches to predict thermal comfort are presented in section 3.3. The adapted Fiala Physiological Comfort (FPC) model, which is integrated into the cabin coupled simulation model, is explained in section 3.4. An experimental comfort study with 22 test subjects is presented in section 3.5. This study is designed to validate the adapted and integrated FPC model and to analyze the influences of local heating measures on thermal comfort and sensation.

3.1 Thermal Comfort Theory

Thermal Comfort is defined as "that condition of mind that expresses satisfaction with the thermal environment and is assessed by subjective evaluation" [3]. Thermal sensation on the other hand is understood as the perception of a certain temperature level as hot, cold or neutral. Both parameters can be accessed in experiments by the evaluation of votes of individuals with the help of adequate scales (see table 3.1). Although a coupling between thermal comfort and sensation exists, hot or cold local sensations do not automatically lead to an uncomfortable state. A warm hand for example is perceived comfortable if the overall sensation is cold, and vice versa [155].

There are various factors influencing the human thermal perception of the environment. These are grouped into physical, intermediate and physiological factors [57]. Whereas the physical conditions can be reproduced quite well

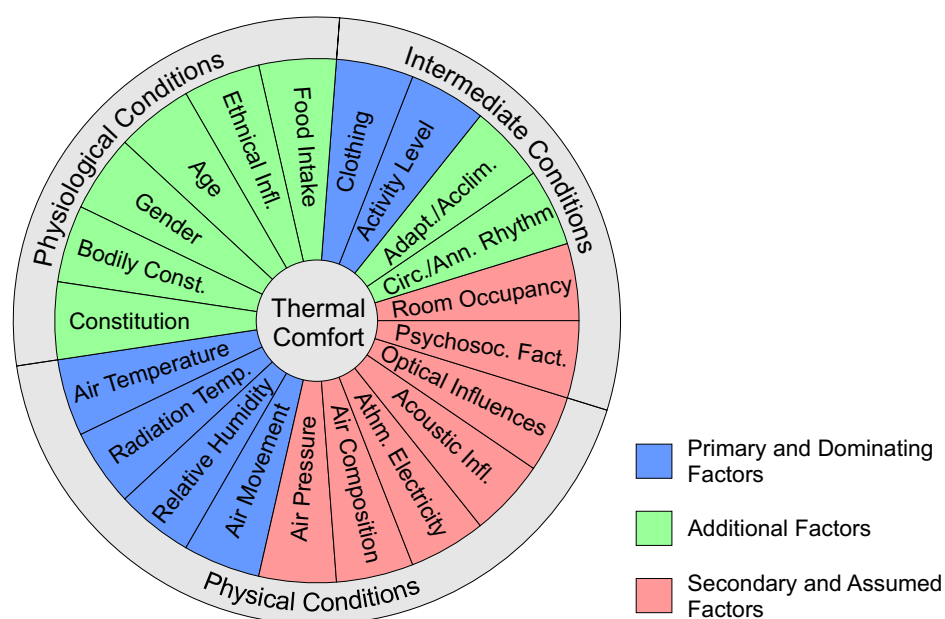


Figure 3.1: Factors influencing thermal comfort (image adapted from Frank [57]).

in experimental setups, this is more difficult for the intermediate conditions such as the activity level and the clothing. Finally, the physiological factors are varying for each individual and lead to a large statistical dispersion of the obtained comfort and sensation votes. Therefore, objective and reproducible results for thermal comfort and sensation can only be derived by averaging experimental data of a sufficiently large number of subjects.

3.2 Thermal Comfort in Vehicles

Thermal comfort in vehicles is not exclusively an issue of passenger satisfaction but may also be an issue of driving safety. Yet, due to scarcely available data, Temming [139] does not identify a clear evidence between the number of accidents and the interior cabin climate. Nevertheless, general test data about effects of the climate on the health state and performance of humans indicate that such a dependence may exist [139]. The HVAC system and the interior climate of vehicles is, however, the topic of several standards and official guidelines [36, 37, 144]: The German Standard DIN 1946-3 [36] states fundamental differences between the optimum climate in buildings and in vehi-

cles and describes the mean cabin air temperature, leading to a comfortable climate in vehicles, as a function of the ambient temperature: At an ambient temperature of $-20\text{ }^{\circ}\text{C}$, the recommended mean cabin temperature is as high as $28\text{ }^{\circ}\text{C}$, taking into account the low radiation temperature of the surrounding surfaces, whereas at moderate ambient temperatures of $20\text{ }^{\circ}\text{C}$ a cabin temperature of $22\text{ }^{\circ}\text{C}$ is sufficient. Another recommendation is that the temperature stratification is supposed to be perceived comfortable if the footwell air temperature is around 2 K to 12 K higher than in the head region [36].

Zonal air-conditioning is state-of-the-art in many vehicles and provides each passenger with a customized temperature level, but requires more complex HVAC designs. Such systems are also used to save energy, because not the entire cabin is conditioned but only the actually required areas, and air exchange between individual zones is minimized [79].

Besides the conditioning of the air, thermal comfort can also be achieved or improved by heating or cooling local elements of the vehicle cabin. This is efficiently achieved by systems which are in thermal contact with the passenger such as the state-of-the-art seat and the steering wheel heating. Supporting or improving thermal comfort by seat heating or cooling is the topic of numerous publications (compare e.g. [16, 95, 108, 130]). Nevertheless, little is known about the efficiency and the influence on thermal comfort or discomfort, for cases where such systems widely replace the central HVAC systems to save energy. A preceding study by Lorenz et al. [87], which is explained in detail in section 3.5, shows that an acceptable comfort level is achieved by heating the seat at a reduced air temperature, and saving a significant part of the thermal energy at the same time.

The application of a peltier-powered seat heating and cooling system, combined with an optimized control algorithm to save energy for the central HVAC power, in a prototype electric vehicle is described by Präbst et al. [114]. Other innovative concepts include panel heating [21, 118], heating of various vehicle parts surrounding the passengers, or the seat belt as an additional vehicle part which is in direct contact with the passenger [75].

3.3 Thermal Comfort Modeling

Given the large amount of factors influencing thermal comfort, it is a challenging task to accurately predict the average perceived comfort level or to even obtain reproducible experimental results. Extensive investigations taking into account many of the above mentioned factors are performed by Fanger [45]. Fanger derives the Predicted Mean Vote (PMV) and the Predicted Percentage of Dissatisfied (PPD) based on the obtained statistical distributions of many individual votes, taking into account the primary factors, i.e. air temperature, humidity, radiation temperature, clothing, activity level and air movement (compare figure 3.1). These experiments are, however, conducted in a homogenous and steady-state environment, and the Fanger model is designed accordingly. The model derives the skin temperature by a steady-state heat balance of the metabolic heat production, the convective, evaporative and radiative heat transfer from the body to the environment and the respiratory heat exchange. The experiments conducted by Fanger [45] show a linear dependence between the skin temperature and the perception of thermal neutrality at different activity levels. Assuming the skin temperature obtained by this linear correlation, the difference between the internal heat production and the body heat loss to the environment is calculated. This difference delivers the PMV and PPD value of the Fanger model. The model is equation based and provides good and quick estimates of the thermal sensation in moderate, homogeneous and steady-state environments. Being well established, it has been integrated in international standards [3, 35].

The indoor climate conditions of a vehicle cabin, however, are frequently highly asymmetric and transient. Models for assessing such conditions have been developed recently by Fiala [48], Tanabe et al. [137] or Yokoyama et al. [151]. In these models the human body is subdivided into different parts where heat transfer and tissue temperature are computed. Nevertheless, statistical correlations derived from experiments with human test subjects are indispensable to derive comfort parameters from the obtained temperature values.

Zhang [155] and Zhang et al. [156–158] investigate thermal sensation and comfort in non-uniform and transient environments. Individual body parts are exposed to a different temperature level than the rest of the body. They ob-

serve and quantify significant differences in the temperature perception depending on the body part and on the overall thermal sensation of the subjects. Immediately after a specific body part is exposed to the cool or hot environment, a stronger negative or positive sensation is obtained than after acclimatization at this temperature level. The thermal sensation level for individual body parts is found by regression analysis from experiments and consists of a dynamic component and a steady-state component. Local comfort of individual body parts is described as a function of the overall thermal sensation and the sensation of the respective body part. The above described effect of cooling or heating of a body part, leading to local comfort while the overall thermal sensation is warm, respectively cool, is found to be stronger for some body parts than for others. The Overall Thermal Comfort (OTC) level, including the identified influences, is finally computed as the average of the two minimum local comfort values and the maximum local comfort values [158].

3.4 Fiala Physiological Comfort (FPC) Model with CFD and Heat Conduction Boundary Condition

A widely used physiological model of the human body for the prediction of thermal comfort is the Fiala Model [48]. The comfort model applied in the present thesis is also based on the original Fiala Model, first presented by Fiala in 1998 [48]. In the following years, the model is extended, further developed, subjected to international validation studies and used in various industrial and research applications [49, 53]. Currently, several versions of the Fiala Model are in use, adopted by various companies, research institutes and laboratories. For use in a previously presented study by Lorenz et al. [87], a new flexible interface for dynamic coupling and data exchange with other simulation applications is developed.

The FPC model simulates the human heat transfer process inside the body and predicts the distribution of body tissue and skin temperatures as well as the associated physiological regulation responses. The FPC model also incorporates various models for predicting the overall and local thermal sensation and comfort responses. Detailed information about the software version of the FPC model used for this thesis is found in the corresponding user guide [42].

3.4.1 Physiological Comfort

The FPC model divides the human body into 20 parts, each of them being subdivided into 1–4 angular sectors. This results in a total of 63 body segments illustrated schematically in figure 3.2.

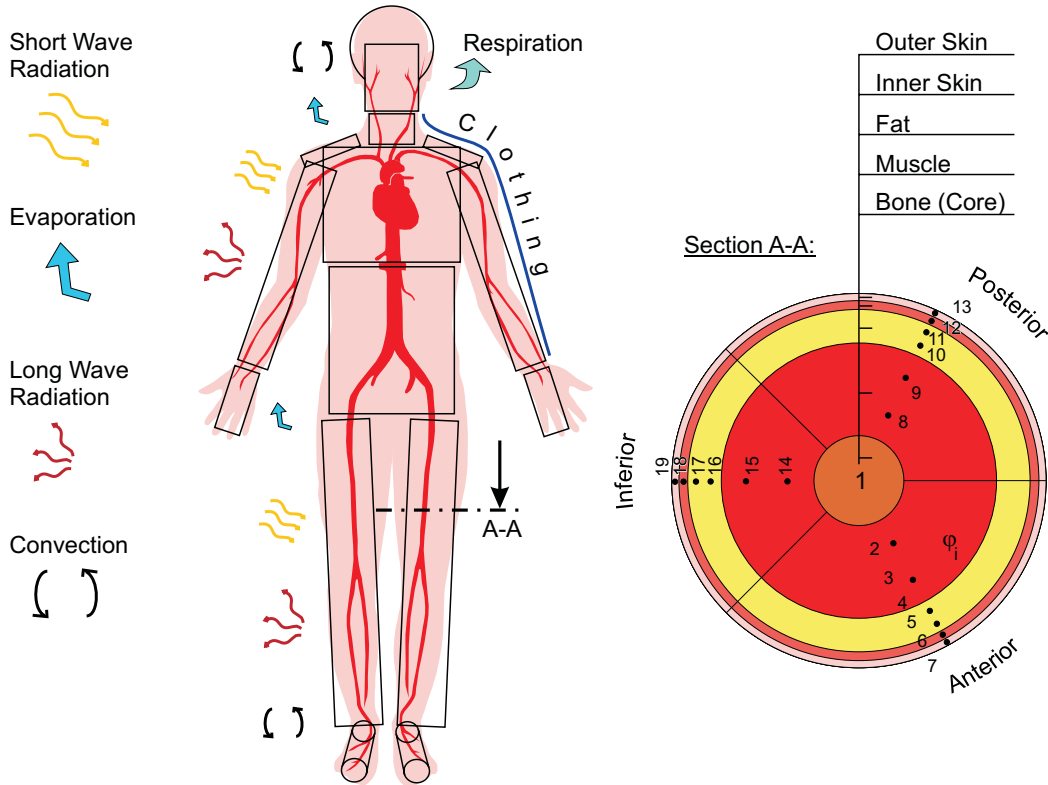


Figure 3.2: Schematic illustration of the FPC passive system model (image adapted from Fiala [48]).

In each body segment, the physiological tissue composition is modeled as individual layers with constant physical and variable physiological properties. The 1D spatial discretization normal to the body segment surface results in a total of 366 tissue nodes. At each tissue node, the dynamic heat transport is modeled, based on the Bio-Heat Transfer Equation (3.1) [50]. In this equation the geometry factor ω allows a formulation which is valid for two different coordinate systems. Whereas the head is approximated by a sphere ($\omega = 2$), all other body parts are represented by cylinders ($\omega = 1$):

$$\rho c \frac{\partial T}{\partial t} = \lambda \left(\frac{\partial^2 T}{\partial R^2} + \frac{\omega}{R} \frac{\partial T}{\partial R} \right) + \dot{q}_{\text{met}}''' + w_{\text{bl}} \rho_{\text{bl}} c_{\text{bl}} (T_{\text{bl,ar}} - T). \quad (3.1)$$

The above equation, combined with equations for the blood flow and the blood temperature, represents the passive system of the FPC model (see figure 3.2).

The following human thermoregulatory mechanisms are modeled in the active system and are included as statistically derived functions of the head core and mean skin temperature deviations from the thermo-neutral condition (see figure 3.3):

- Shivering
- Skin blood flow constriction
- Skin blood flow dilatation
- Sweating

Analogously to the thermoregulatory mechanisms, the Dynamic Thermal Sensation (DTS) and the Thermal Sensation (TS) are based on the predicted mean skin and head core (hypothalamus) temperature as physiological "signals" using the 7-point thermal sensation scale [52]. Whereas TS contains only static components, DTS contains both, static and dynamic components to account for temporal changes of environmental and personal conditions. The Overall Thermal Comfort (OTC), incorporated also in the FPC model, is predicted, based on the obtained body temperatures according to the works of Zhang et al. [156–158], using a 9-point comfort scale (see table 3.1 and compare section 3.1).

The reason why two different scales are used, is to find differences in the perception of thermal sensation and thermal comfort. These differences occur predominantly under asymmetric conditions. As explained above, the overall thermal sensation, may be neutral if one part of the body is hot and another part of the body is cold. At the same time such a condition can cause discomfort due to the asymmetry. The 7-point thermal sensation scale and the 9-point thermal comfort scale are used in the experiments, as explained in section 3.5, to be able to directly compare the results with the DTS value and the OTC value being both output by the FPC model.

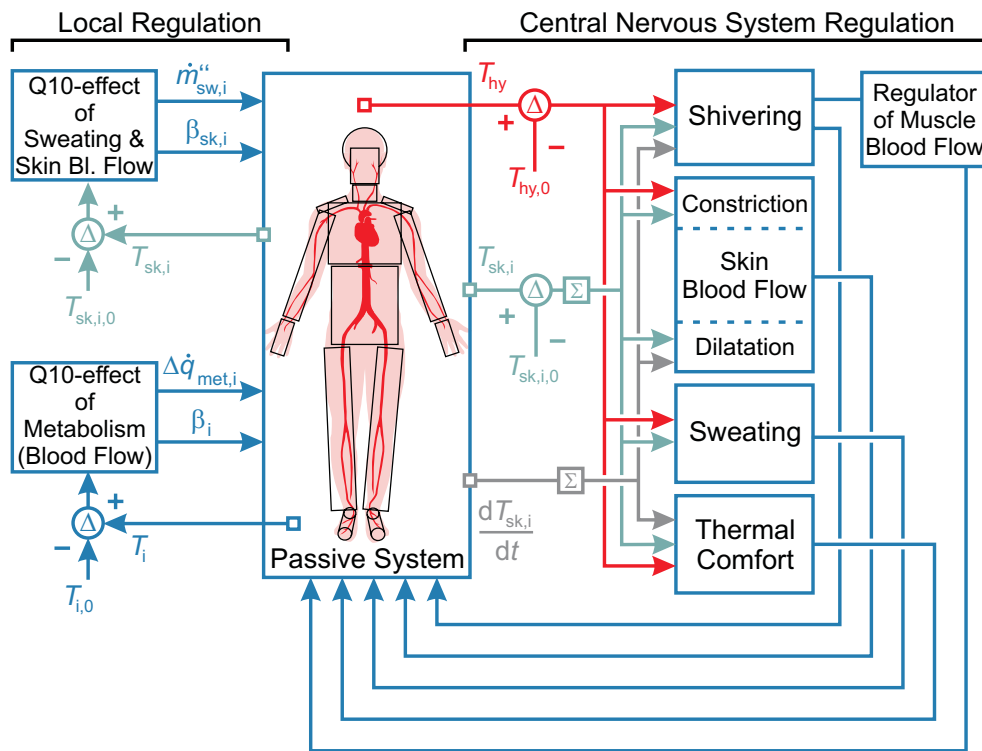


Figure 3.3: Block diagram of the active system of the FPC model with the central nervous system regulation mechanisms and the local regulation due to the Q10-effect (image adapted from Fiala [42]). The Q10-effect arises due to a dependence of biochemical reactions on local tissue temperature and a modification of the local nodal sweat rate and skin blood flow according to the skin temperature [48].

Table 3.1: Thermal sensation and comfort scales used in the study.

7-Point thermal sensation scale (TS/DTS)		9-Point thermal comfort scale (OTC)	
		+4	Very comfortable
3	Hot	+3	
2	Warm	+2	Comfortable
1	Slightly warm	+1	
0	Neutral	-/+0	Just uncomfortable/comfortable
-1	Slightly cool	-1	
-2	Cool	-2	Uncomfortable
-3	Cold	-3	
		-4	Very uncomfortable

The output data of the FPC model which is used by the other sub-models comprises: the local skin temperatures, sweat/skin moisture production rates, va-

por pressure in the outer cutaneous layer, respiratory heat losses and expired moisture mass rate. The coupling of the comfort model with the cabin model and the coupled simulation algorithm are explained in section 4.3.

In the present study the evaluation of the physiological and comfort states is performed just for one person, i.e. the driver (see mannequin in figure 4.3 and 4.4). The assumed Metabolic Equivalent of Task $MET^1=1.3$ corresponds to a driving activity and is slightly lower for a passive passenger. All variables predicted for the driver, such as surface temperatures and moisture emissions, are nevertheless applied also to the second passenger mannequin in the CFD model, as it is assumed that the thermal conditions are similar for both passengers.

3.4.2 Clothing and Direct Contact to Vehicle Parts

Transport processes inside the clothing of the passengers are not included in the used version of the FPC model. These processes are therefore calculated by a FLUENT User Defined Function (UDF) in the CFD cabin model (see section 4.2.1) yielding the surface temperature of the clothing, which is a function of the local air temperature, the clothing insulation R_{cl} and the skin temperature. Analogously, the water vapor emission through the skin and the clothing is calculated in the UDF as a function of the vapor pressure in the outer cutaneous layer, the diffusion resistance of the skin and the clothing and the local vapor pressure of the cabin air. The assumed clothing configuration corresponds to a light wintery clothing assembly with an average thermal resistance of $R_{cl,m} = 0.26 \text{ m}^2\text{K/W}$. This clothing configuration is applied for all CFD cases and is designed to represent also the clothing configuration of the test subjects in the comfort experiments in section 3.5.

For coupling the FPC model with the other described sub-models, a heat flux boundary condition is imposed on all body segments of the FPC model. This heat flux is determined in the CFD cabin model for individual body segments in contact with the air. For body parts in contact with the seat surface, the heat

¹ The MET rate describes the activity level of a person and is defined as the ratio between the metabolic energy rate of a person performing a certain activity and the reference activity. The reference activity, 1 MET, is defined as 58.2 W/m^2 , corresponding to the energy consumption per unit skin area (approx. 1.8 m^2) and equals approximately the activity level of a seated person at rest. $MET=1.3$ corresponds to a driving activity between light and heavy traffic [45].

flux $\dot{q}''_{sk,cl}$ from the skin to the clothing and $\dot{q}''_{cl,st}$ from the clothing to the seat surface are approximated by equation (3.2) and (3.3):

$$\dot{q}''_{sk,cl} = \frac{T_{sk,st,m} - T_{cl,st}}{0.5 \cdot R_{cl,st,m}}, \quad (3.2)$$

$$\dot{q}''_{cl,st} = \frac{T_{cl,st} - T_{s,st,m}}{0.5 \cdot R_{cl,st,m}}. \quad (3.3)$$

Here, $T_{sk,st,m}$ is the area-weighted skin temperature of the body parts in contact with the seat: the posterior parts of the upper legs, buttocks and the back. $T_{s,st,m}$ is the area-weighted temperature of the front side surface of the seat in contact with the passenger and $T_{cl,st}$ is the temperature of an additional thermal inertia node of the clothing in contact with the seat surface. $R_{cl,st,m}$ is the area-weighted local clothing thermal resistance of the multi-layered clothing between the passenger and the seat surface with a factor of 0.5 for an equal distance of the clothing thermal node to the skin and to the seat surface. The resistance $R_{cl,st,m}$ is estimated 30% of the original local clothing thermal resistance $R_{cl,i}$ reduced by the contact pressure.

These heat fluxes are imposed as a boundary condition on the structure model seat surface, as well as on the respective FPC passenger model body segments. The temporal evolution of the clothing layer temperature between the passenger and the seat surface is calculated as:

$$\frac{dT_{cl,st}}{dt} = \frac{\dot{q}''_{sk,cl} - \dot{q}''_{cl,st}}{m_{th,cl,st}}. \quad (3.4)$$

with the area-averaged thermal inertia $m_{th,cl,st}$ of the clothing between the passenger and the seat surface which is estimated to $990 \text{ J}/(\text{K m}^2)$.

3.5 Validation of the Comfort Model

The FPC comfort model presented above, including the coupling with the CFD environment and a thermal model of a vehicle seat, is validated using data from a thermal comfort experiment, originally designed and conducted by

Lorenz et al. [87] for purposes of a previous study. The study involves 22 (9 female and 13 male) test subjects featuring the following average characteristics²: age 29 years SD ± 7 years, body height 1.75 m SD ± 0.08 m, and weight 69 kg SD ± 11 kg. The clothing of the subjects is standardized as far as possible and includes normal underwear, t-shirt, jeans, shoes, fleece gloves and a fleece jacket. The clothing insulation of these garments is estimated by a modification of the widely used Kansas State University KSU-uniform. The estimated and averaged overall clothing insulation of the here applied configuration is $R_{cl,m}=0.26$ (m²K)/W. The measured temperatures and comfort levels are compared to the numerical simulation results of this setup. To achieve reproducible boundary conditions for all subjects, the experiments are conducted in a climate chamber.

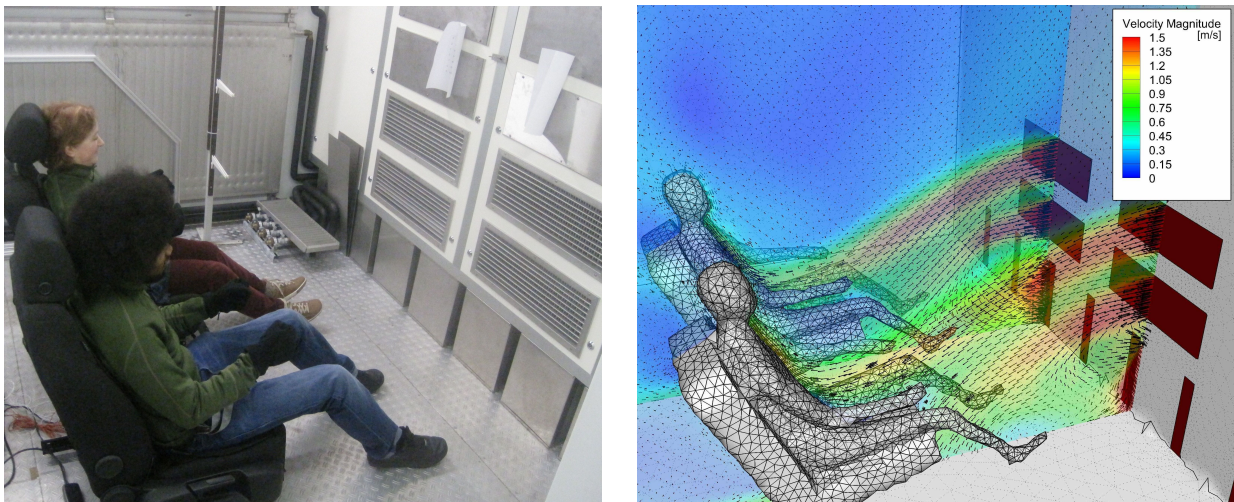


Figure 3.4: Comparison of the geometrical setup of the experimental and CFD simulation test case. The four air inlet openings in the front wall and the air outlets underneath are visible in both images.

The geometrical setup of the experiment and the corresponding geometry of the numerical model are shown in figure 3.4. In the experiment the subjects are seated pairwise on two car seats in a symmetric configuration. There is a constant airflow speed of 1.5 m/s towards the passengers from two air inlets on each side. Each inlet valve is 0.2 x 0.6 m in size and at a distance of 1.6 m from the faces of the subjects. The air temperature and the relative humidity in the chamber are kept constant at 5 °C and 50%. The chamber itself and the seats are preconditioned at this air-state before each exposure. The subjects are approximately at thermal neutrality when starting the measurement and

² See appendix D for detailed information.

sitting down on the seats. Each measurement lasts 20 minutes. After 10 minutes seat heating with a constant electrical input of 35 W per seat is switched on.

On each seat four temperature sensors are placed to record the mean seat contact temperature. In specified intervals of 1–2 minutes, the subjects are asked to report their overall thermal sensation and their overall thermal comfort according to two different scales as illustrated in table 3.1. Thermal sensation is measured by the 7-point thermal sensation scale and thermal comfort by the 9-point comfort scale. The averaged results of these measurements are illustrated in figure 3.5 and 3.6, and individual results are found in appendix D.

The geometry and the boundary conditions of this comfort experiment are designed to be well suited for an efficient validation of the numerical model and to represent conditions similar to those in a vehicle at the same time. With two step responses, the static response as well as the dynamic behavior of the coupled system are subjected to validation. The first step response occurs when entering the cold climate chamber coming from a thermally neutral state and the second one occurs after 600 s when the seat heating is switched on.

The results of this experimental study are compared with the corresponding numerical simulation results of the same geometrical setup. The settings of the CFD model described in this chapter correspond to the settings of the CFD vehicle cabin model described in section 4.2.1. The seat heating power is assumed to be distributed homogeneously over the seat surface and is modeled as a 100 W/m^2 constant heat source in the numerical model.

In analogy to other comfort experiments, there are relatively large inter-individual variations in the thermal sensation and comfort votes. The corresponding standard deviations are between 0.4 and 1.5 for the thermal sensation (Experiment: TS) and between 1.0 and 1.4 for the thermal comfort (Experiment: TC) votes. The thermal sensations, thermal comfort votes, and seat contact temperatures observed in the experiment are plotted as average values of the 22 subjects with the respective variations $\pm\text{SD}$ as error bars (see figures 3.5, 3.6 and 3.7).

Both, the experimental and the numerical results clearly indicate cold overall thermal sensations during the first part of the experiment with values between -2 (cool) and -3 (cold). Coming from a thermally neutral environment this

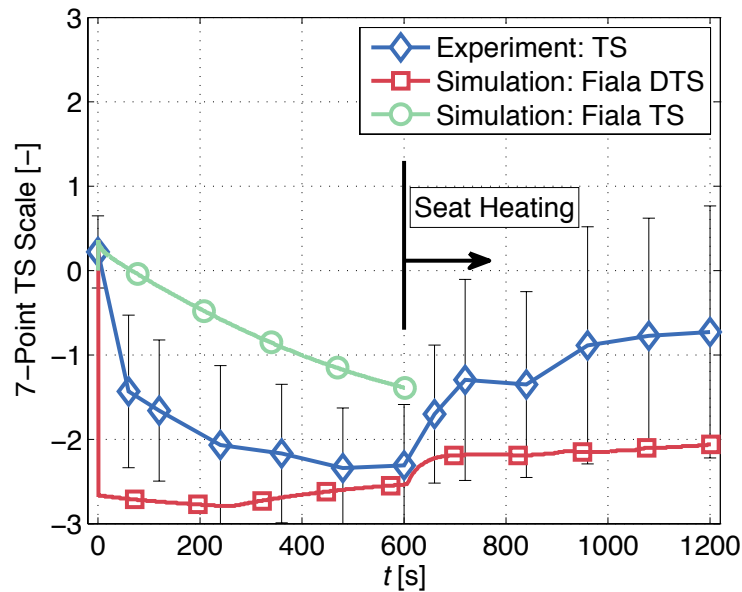


Figure 3.5: Comparison between the averaged thermal sensation vote of the experiments (Experiment: TS) and the DTS and TS value output by the FPC model explained in section 3.4.

value decreases on average less rapidly in the experiment than the Fiala DTS signal in the simulation (see figure 3.5). The simulated DTS value shows a sudden drop when applying the heat flux boundary condition obtained in the cooler environment. This immediate drop is not observed as a group-average response in the experiment although several individuals report such a perception of their thermal sensation (see appendix D).

According to other studies (see e.g. Fiala et al. [52] for reference) there is a characteristic drop and recovery in the human sensation of temperature, following a sudden change in environmental conditions towards cold, which is not observed in this experiment. These temporal cold-sensation "overshoots" typically occur about 5 minutes after the sudden drop in ambient temperature. The DTS index is designed to reproduce this dynamic response [52] using simulation time step lengths between 1–5 minutes. The FPC model in the coupled simulation, which uses simulation time steps < 2 s, does not show this behavior. An analysis reveals that the dynamic component of DTS, associated with the simulation time steps used, dominates DTS during the first 600 s. Thus, in figure 3.5 the effect is not visible for the Fiala TS signal, which only accounts for static influences (compare section 3.4).

After switching on the seat heating, a distinct rise in thermal sensation is observed in the experiment and in the DTS value of the simulation. Nevertheless, the DTS value seems to underpredict the balancing effect of the seat heating in this scenario. As DTS is originally developed to predict dynamic sensation responses in homogenous environments [48], it may underestimate the impact of pronounced local stimuli on the overall response in asymmetric exposure scenarios.

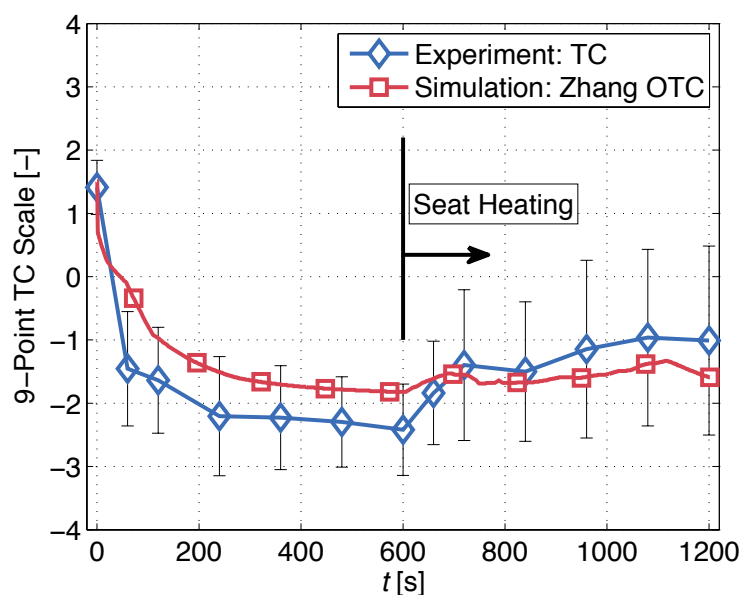


Figure 3.6: Comparison between the averaged thermal comfort (TC) vote of the experiments and the OTC value by Zhang et al. [156–158] output by the FPC model.

The OTC values according to the model of Zhang (see section 3.3) are also calculated and output by the FPC model and are in good agreement with the average thermal comfort values found in the experiment (see figure 3.6): Thermal comfort is measured positive in the beginning of the experiment. Subsequently, the value decreases to approximately -2 (uncomfortable) and rises again up to -1 (slightly uncomfortable) after the seat heating is switched on. Nevertheless, the balancing effect of the seat heating is also observed to be stronger in the experiment than in the simulation.

The averaged seat contact temperatures of the experiment show a mean standard deviation between the tests of 0.85 K and are in good general agreement with predicted temperatures (see figure 3.7). The deviations in the dynamic behavior of the temperatures are explained by the thermal inertia of the sensors which is not accounted for in the simulation. The temperature reaches

approximately 30 °C after 10 minutes and rises up to almost 40 °C after switching on the seat heating. Most subjects do not yet sense this temperature as too warm due to their overall cold sensation (see appendix D).

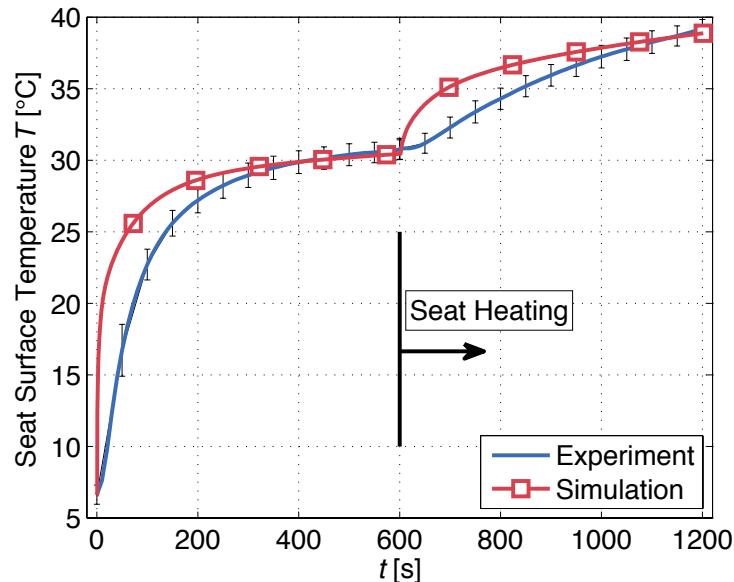


Figure 3.7: Comparison of the averaged measured seat surface temperature and the area-weighted simulated temperature of the seat front side surface derived by equations (3.3) and (3.2).

The comfort model presented in this chapter is capable of reproducing the thermal perception of the test subjects during the experiments and reproduces also the effect of local conditioning measures. Nevertheless, the positive effect of local measures may in real applications be stronger than predicted by the model. Seat heating proves to be a suitable measure to efficiently generate an acceptable comfort level for passengers in a cold vehicle cabin, at least for a limited period of time.

3.6 Conclusion

Various factors influence the thermal comfort and sensation of a person. The inhomogeneous and transient conditions in a vehicle require a more sophisticated model than the well-established model of Fanger [45]. The FPC model resolves the human body in 366 tissue nodes and accounts also for blood flow, respiration heat transfer and thermoregulatory mechanisms. The integration of this model into a CFD and 1D heat transfer environment and the valida-

tion of the model is presented already in a preceding study by Lorenz et al. [87] and is summarized in the present thesis. The validation experiments with 22 test subjects show that seat heating significantly raises thermal sensation and improves thermal comfort in a cold environment with little energy input. The integrated and adapted FPC model is capable of approximately predicting the thermal comfort and sensation. The positive effect of seat heating on the thermal sensation and comfort in a cold environment is nevertheless underestimated in the conducted experiment. Thus, future adaptations to the FPC model are necessary to better account for transient and local effects. The following predictions of seat heating and other cabin optimization measures presented chapter 4.5, using the FPC model, possibly underestimate positive local effects on thermal comfort and sensation.

4 Cabin Modeling

A suitable thermal model of the vehicle cabin is essential to predict cabin temperatures and the necessary conditioning power. In section 4.1 state-of-the-art modeling approaches for vehicle cabins are presented. The applied generic vehicle cabin model consists of a CFD model to predict the cabin air-flow, the temperature and species distribution and a 1D structure model to account for the heat transfer in the adjacent solid parts. These two parts of the model are explained in section 4.2. In section 4.3 the used coupled simulation method is explained, which integrates the window fogging and the comfort model explained in chapters 2 and 3 and the two components of the cabin model explained in section 4.2. A winter climate simulation scenario is explained in section 4.4 to finally compare in section 4.5 different simulation test cases including various cabin optimization measures in comparison to a baseline configuration.

4.1 State-of-the-Art of Vehicle Cabin Modeling

Modeling of passenger cabins has become an important part of automotive development. Detailed CFD cabin models are used to predict the distribution of the inflow air, passenger thermal comfort and defogging capabilities of HVAC systems (compare e.g. [124, 131, 132]). One-dimensional and analytical heat transfer models estimate the solar load and the necessary thermal heating and cooling power (compare e.g. [6, 47, 56, 99, 134]).

Recent developments attempt to integrate models of many different vehicle components into a "virtual vehicle" model [13, 112]. With such a holistic model, complex interactions between different components can be described. Important interactions of a passenger cabin model with other components include not only the thermal management components of a vehicle, such as the HVAC and the coolant cycle, but also the vehicle speed dependent exterior heat transfer or even coupling between thermal comfort, driving behavior

and driving safety. The different relevant time scales of components and the claim to perform long-time driving cycle simulations often require a reduced modeling depth of components. Concerning the cabin model, the heat and mass transfer inside the cabin is frequently reduced to a one-zone model with a single thermal inertia node (see figure 4.1). In this case the heat transfer to the surrounding structure is expressed by one or several flow dependent heat transfer coefficients [18, 134]. The computational effort of such a model is very low, but gradients inside the cabin, which are important e.g. for the comfort and window fogging evaluation, need to be neglected. So-called zonal cabin models, as described e.g. by Flieger et al. [54, 55] or Mora et al. [94], with several computation nodes to model the air volume overcome this problem. Besides the size of the zones, respectively cells, the main difference from zonal models to CFD models is that the mass flow between the zones is tabulated for a set of chosen parameters, such as air-inlet speed or recirculation fraction. In CFD models on the other hand, the air exchange between the cells is calculated by solving the physical flow equations. Thus, for zonal models the air-flow exchange between neighboring zones needs to be characterized by either experiments or CFD simulations for a wide range of operating points. These input parameters have a large influence on the obtained results and lead to significant deviations between simulation and experimental results [54].

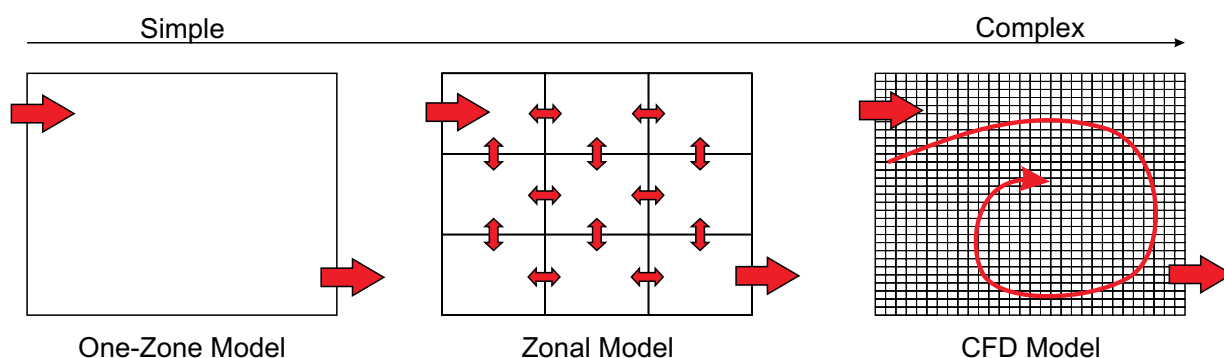


Figure 4.1: Options for the level of detail of the cabin model discretization (image adapted from Flieger [54]).

The surrounding structure of the cabin, such as the doors, the roof or the windows, determine the heat transfer between the cabin air and the environment as well as the thermal inertia of the cabin. The most detailed modeling option is a conjugate heat transfer model, including a detailed 3D mesh of the solid parts to account for the heat transfer. As heat transfer occurs predominantly perpendicularly to the surrounding cabin surfaces, frequently a 1D

shell model, consisting of different material layers, is used. A solution for this kind of cabin model is offered e.g. by THESEUS FE [116].

4.2 Generic Compact Car Cabin Model

A generic compact car cabin model with two occupant mannequins is developed for this study (see figure 4.2). The main goal of this model is to evaluate the energy saving potential of different measures, such as insulated glazing, recirculation or local heating measures. A generic geometry is chosen to obtain predictions independent of a specific car manufacturer. Additionally, the geometry details of a realistic cabin are secondary for the prediction of general tendencies, which are supposed to be valid for a variety of different vehicles. Heat and mass transport inside the cabin air is calculated in a 3D CFD cabin air model described in section 4.2.1. Heat transfer in the solid parts of the vehicle is calculated in a 1D shell structure model which is described in section 4.2.2.

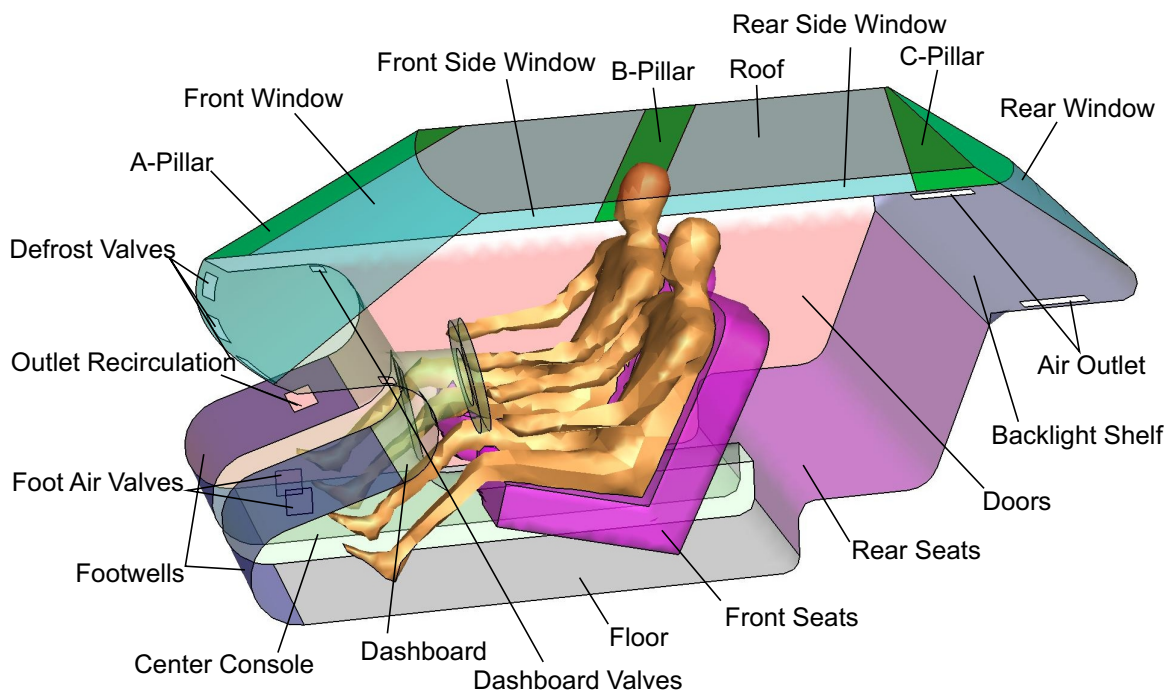


Figure 4.2: Generic compact car cabin with two passengers and the considered vehicle parts. The assumed material composition of each part is found in appendix F.

Several air valves in the dashboard, in the footwell walls and close to the front window are integrated as CFD velocity inlets for passenger and defrost air supply (see figure 4.4). Two air outlets are integrated as pressure outlets symmetrically at the rear shelf for the cabin exhaust air and in the passenger footwell area for the recirculation airflow. The mannequins in the 3D CFD model serve as an interface to calculate the heat and mass exchange between the cabin and the passengers. Physiological parameters and the predicted comfort sensation are calculated in the comfort model described in section 3.4.

4.2.1 CFD Cabin Air Model

The geometry and the meshing of the CFD cabin model are depicted in figure 4.3. The geometry of the vehicle is converted into an unstructured tetrahedron mesh with 5 parallel prism cell layers at all walls. The first prism layer height is between 2 mm and 5 mm. The mesh being parallel and finer close to the walls allows to model the transport processes to and from the walls more accurately. A typical boundary layer thickness near the windshield is approximately 17 mm [40]. A finer resolution of the wall mesh and up to 20 prism layers would be favorable to accurately resolve the boundary layer. Nevertheless, the coarser mesh is chosen due to advantages in calculation time, meshing effort and convergence behavior. Also the bulk mesh of the CFD model is defined to be relatively coarse with a maximum cell width of 0.1 m leading to a total of $4.6 \cdot 10^5$ tetrahedron and prism cells. The aim of the CFD model is to reproduce the main temperature gradients inside the cabin and to approximate the surface heat and mass transfer. This is mainly achieved by the wall refinement with prism layers. A mesh study of the cabin with one coarser mesh ($2.4 \cdot 10^5$ cells) and one finer mesh ($1.1 \cdot 10^6$ cells) reveals a maximum integral heat transfer deviation of 5%. It is therefore assumed that the chosen mesh is a good compromise between achievable accuracy and computational effort.

ANSYS FLUENT 14.5 is used as a solver for the 3D flow equations and the heat and mass transfer from and to the surfaces. For the coupled simulation it is essential to ensure a robust and well converging computational behavior of all models, in particular the CFD model, at various boundary conditions. The RNG $k-\epsilon$ turbulence model is found to perform well and it is reported by different authors that its accuracy for moderate buoyant indoor airflow is good,

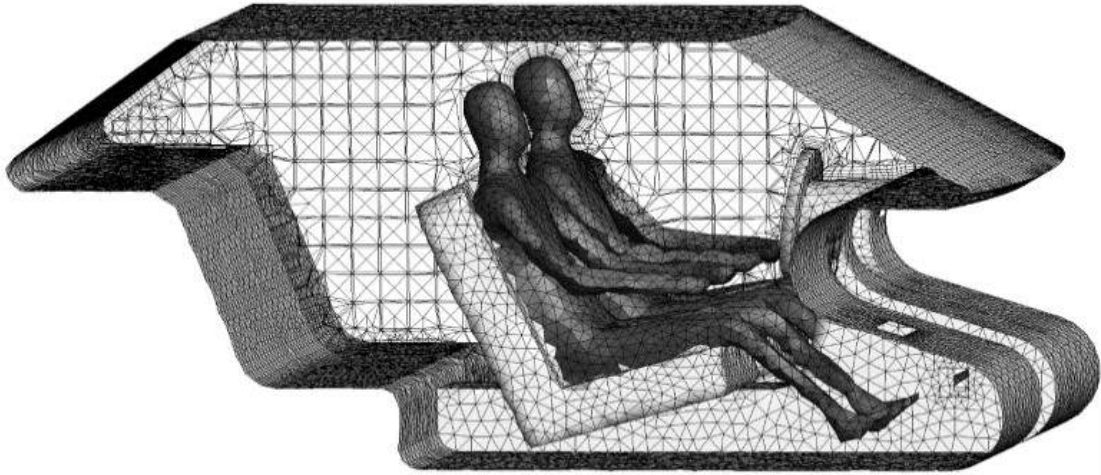


Figure 4.3: 3D meshed geometry of a generic compact car with two occupants. The geometry model is used for the CFD simulation and for the definition of interfaces to the structure model and the FPC passenger comfort model.

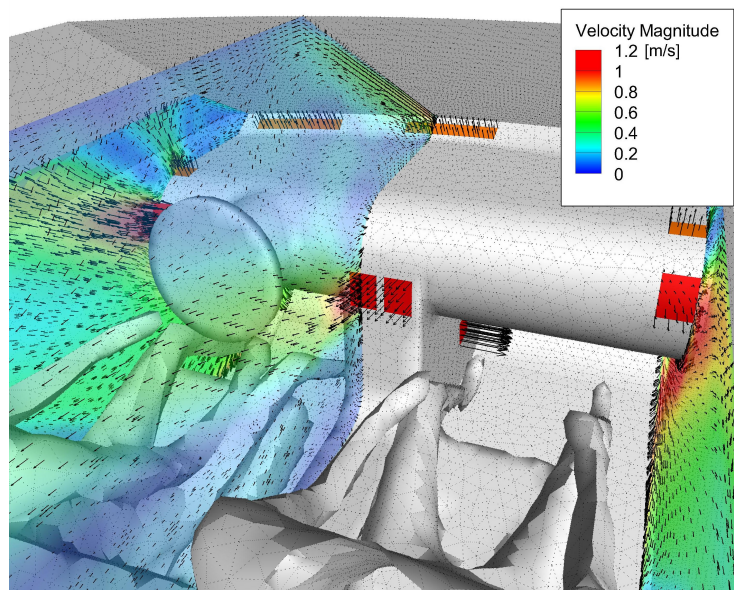


Figure 4.4: Visualization of the airflow in the cabin with dashboard, defrost and foot air valves.

along with a high computational efficiency [26, 159], and it is also used for similar applications e.g. by Roy et al. [123].

As explained in section 2.3.1.1, the application of Standard Wall Functions yields the best results at a specific wall mesh resolution depending on the local flow condition. For a complex geometry as a vehicle cabin and varying

flow rates, it is nevertheless challenging to generate a wall mesh with a homogeneously distributed non-dimensional wall distance y^+ , respectively y^* . The near wall treatment with Enhanced Wall Treatment equations, offered in ANSYS FLUENT, uses a blending method between the linear (laminar) and the logarithmic (turbulent) law of the wall and is therefore applicable to a greater range of wall mesh resolutions than Standard Wall Functions [4]. The presented simulation test cases shows y^+ values between approximately 1 and 40 and hereby fulfills the recommendations for Enhanced Wall Treatment [4].

The transport equations for momentum, energy, and species, i.e. water vapor, are solved in the CFD cabin air domain. To obtain the temporal evolution of the flow field, the pressure-based transient double precision solver of ANSYS FLUENT is used. Local temperature dependent densities are computed by the incompressible ideal-gas law. This allows the consideration of buoyancy effects by adding a gravity term to the momentum equation. Temperature dependencies of all other physical properties of humid air are defined in UDF and are found in appendix E. Second order upwind discretization schemes are used for momentum, energy, and species transport equations. The pressure-velocity-coupling is modeled using the Semi-Implicit Method for Pressure Linked Equations (SIMPLE). Gradients are calculated using the least-square-cell-based method. All settings are in good agreement with the approach for similar cases suggested in the ANSYS FLUENT User Guide [5]. Further information on the associated equations of these settings are found in the ANSYS FLUENT Theory Guide [4].

Long wave radiation is modeled using the Surface to Surface (S2S) model, included in the ANSYS FLUENT solver [5], to account for the direct long-wave radiative heat exchange between surfaces of different temperatures. Therefore, view factors between all wall faces are calculated in ANSYS FLUENT, after clustering neighboring faces to clusters of 10 face elements. Hereby, the radiative heat exchange between structure elements and passenger body parts of different surface temperature is considered, which has an important effect on thermal comfort. Radiative heat exchange with the environment is modeled in the structure heat transfer model and is explained in section 4.2.2.3.

All boundary conditions involved in the coupled simulation process of the CFD model are defined using UDF. Whereas the window fogging model is fully integrated in the CFD application and evaluated for each wall face, the struc-

ture and comfort model are coupled with the CFD model as described in section 4.3. Particularly, the various cabin wall surface temperatures $T_{s,i}$ are used as an input to the CFD model and are applied as temperature boundary conditions for the bounding walls. In the UDF the coupling parameters are read in from text files for each boundary zone. As the surface discretization is higher in the CFD model than in the 1D models, output values of the surface wall heat flux \dot{q}''_{CFD} are area-weighted for each structure segment and passenger body part and written to text files.

The coupling interface variables between the CFD model and the thermal comfort model are skin surface heat fluxes and skin temperatures. The transport process within the clothing is calculated in a UDF. This comprises the local heat transfer and skin evaporation mass flux as functions of the clothing thermal and evaporative resistances and an additional thermal mass node for the thermal inertia of the local clothing layers.

4.2.2 Structure Heat Transfer

The 1D structure heat transfer model is implemented in MATLAB and accounts for all solid parts of the vehicle cabin which are in direct contact with the interior airflow and the passengers. Each part, such as the windscreen, door or seat, is modeled as a parallel shell layer composition of different characteristic materials. The assumed material composition for each part of the generic vehicle, illustrated in figure 4.2, is found in appendix F.

4.2.2.1 Discretization

To refine the surface temperature distribution, the vehicle parts are further subdivided into segments of a maximum spatial extension of 0.1 m, corresponding to automatically assigned and clustered wall face elements of the 3D CFD surface mesh. Each segment is then 1D spatially discretized normal to the shell surface using 5 material nodes per layer. This results in a total of 19505 material nodes for 900 subdivision segments of the vehicle body.

Inside the solid material layers, physical properties are assumed constant and the dynamic heat transfer equation only accounts for heat conduction. The assumed properties for each material are listed in appendix F. To model

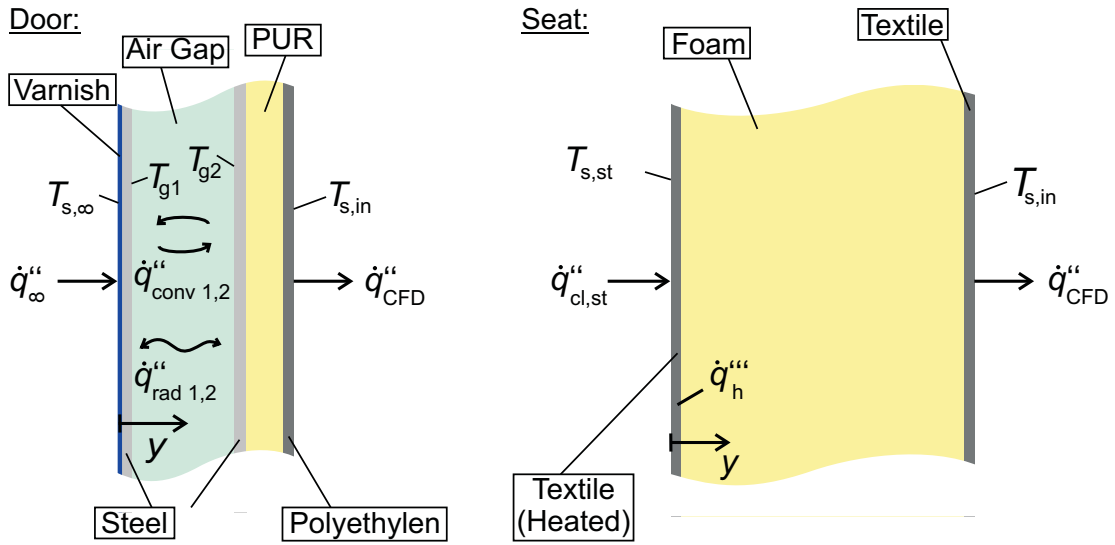


Figure 4.5: Schematic illustration of the material layers inside the vehicle body segments of the doors and the seats with the considered heat fluxes. The detailed layer composition and respective layer thicknesses of the generic vehicle cabin are listed in appendix F

heated material layers, such as electrical seat or panel heating, a heat source term \dot{q}'''_h is included, depending on the actual heating power. The dynamic heat transfer equation is formulated as follows (compare to equation (3.1) with $\omega = 0$ for Cartesian coordinates):

$$\rho c \frac{\partial T}{\partial t} = \lambda \frac{\partial^2 T}{\partial y^2} + \dot{q}'''_h + \dot{q}''_{\text{rad},g1} \tilde{\delta}(y - y_{g1}) + \dot{q}''_{\text{rad},g2} \tilde{\delta}(y - y_{g2}). \quad (4.1)$$

Here, $\tilde{\delta}(y - y_{g1/g2})$ is the Dirac delta function normalized by its integral value over the y -domain, assuring that the long-wave radiation terms are zero, except for the positions y_{g1} and y_{g2} of the walls of enclosed gaps (see section 4.2.2.2):

$$\tilde{\delta}(y) = \frac{\delta(y)}{\int_{-\infty}^{+\infty} \delta(y) dy}, \quad (4.2)$$

and $\delta(y)$ is the Dirac delta function.

The partial differential equation (4.1) is solved, using an implicit Finite-Volume method derived by an energy balance for each volume node which is explained in the following:

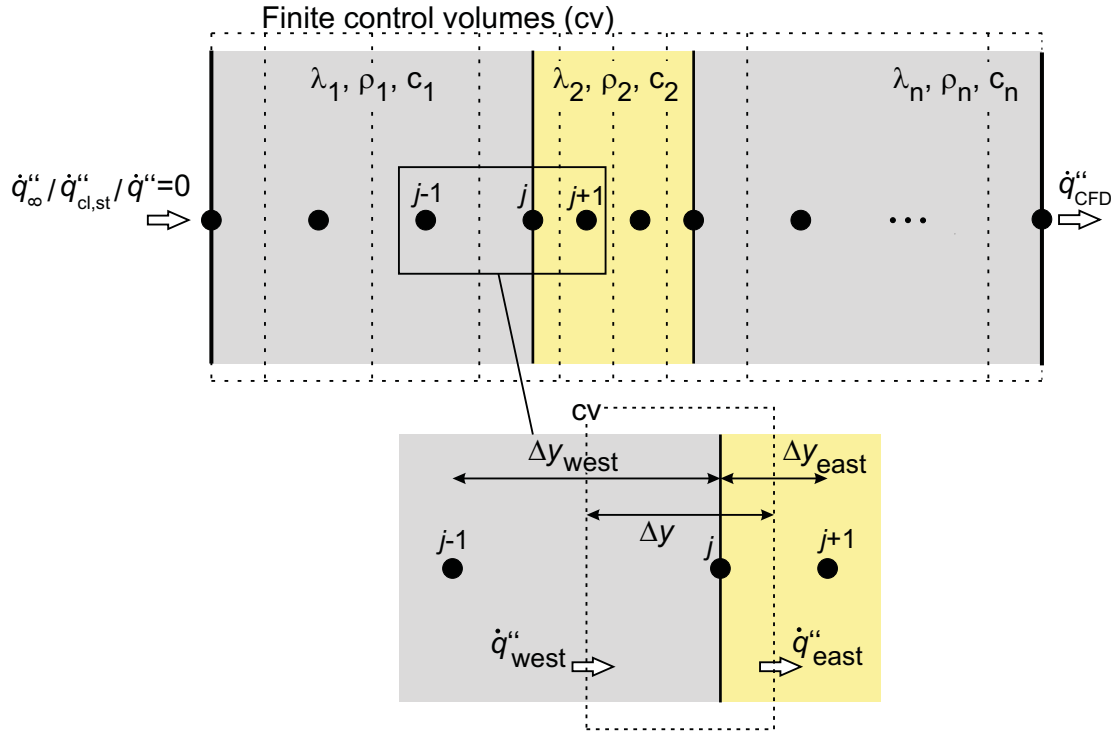


Figure 4.6: Schematic illustration of the discretization of an exemplary 1D multilayer structure and the energy balance at each control volume (cv).

For all internal nodes, which are either at the boundary of two material layers or inside a material layer, equation (4.1) is discretized as:

$$\begin{aligned}
 \frac{du}{dt} \rho \Delta y &= \dot{q}''_{west} - \dot{q}''_{east} + \dot{q}''' \Delta y + \dot{q}''_{rad} \\
 \frac{T_j^{n+1} - T_j^n}{\Delta t} m_{th,cv} &= \frac{T_{j-1}^{n+1} \lambda_{west}}{\Delta y_{west}} - \frac{T_j^{n+1} \lambda_{west}}{\Delta y_{west}} - \frac{T_j^{n+1} \lambda_{east}}{\Delta y_{east}} + \frac{T_{j+1}^{n+1} \lambda_{east}}{\Delta y_{east}} + \dot{q}''' \Delta y + \dot{q}''_{rad} \\
 \boxed{-\frac{T_j^n}{\Delta t} - \frac{\dot{q}''' \Delta y - \dot{q}''_{rad}}{m_{th,cv}}} &= \boxed{\left(\frac{\lambda_{west}}{\Delta y_{west} m_{th,cv}} \right)} \boxed{T_{j-1}^{n+1}} + \\
 &+ \boxed{\left(-\frac{\lambda_{east}}{\Delta y_{east} m_{th,cv}} - \frac{\lambda_{west}}{\Delta y_{west} m_{th,cv}} - \frac{1}{\Delta t} \right)} \boxed{T_j^{n+1}} + \\
 &+ \boxed{\left(\frac{\lambda_{east}}{\Delta y_{east} m_{th,cv}} \right)} \boxed{T_{j+1}^{n+1}},
 \end{aligned} \tag{4.3}$$

with the thermal inertia of the respective control volume:

$$m_{\text{th,cv}} = \rho_{\text{west}} c_{\text{west}} \frac{\Delta y_{\text{west}}}{2} + \rho_{\text{east}} c_{\text{east}} \frac{\Delta y_{\text{east}}}{2}, \quad (4.4)$$

and the width of the control volume:

$$\Delta y = \frac{\Delta y_{\text{west}}}{2} + \frac{\Delta y_{\text{east}}}{2}. \quad (4.5)$$

For the boundary nodes, the width of the control volume is reduced accordingly and \dot{q}''_{west} , respectively \dot{q}''_{east} are replaced by the corresponding boundary heat fluxes \dot{q}''_{∞} , \dot{q}''_{CFD} and $\dot{q}''_{\text{cl,st}}$ (see figure 4.6).

After an evaluation for all nodes, equation (4.3) is written as a linear set of equations, respectively as a matrix equation of the following form, with T^{n+1} as the array of unknown temperatures of the subsequent time step $n + 1$:

$$\boxed{b_{\text{T}}} = \boxed{A_{\text{T}}} \cdot \boxed{T^{n+1}}. \quad (4.6)$$

For forced convection heat transfer, the boundary heat flux is proportional to the surface temperature and is integrated implicitly as a function of T_j^{n+1} . For radiative and buoyant heat transfer, the term is non-linear, so it is added explicitly as a function of the already known temperature T_j^n . Thus, the linearity of the equation system is preserved.

This results in a linear set of equations for each segment which is sparse and of a maximum dimension of approximately 30 (depending on the number of layers of the respective structure segment) and is solved directly by Gaussian elimination in a built-in MATLAB routine.

4.2.2.2 Air-filled Gaps in the Vehicle Structure

Air-filled gaps inside the vehicle structure are considered e.g. for doors or double pane windows. In these gaps radiative and convective heat transfer is calculated as functions of the surface temperatures of the neighboring solid walls (gap walls).

The radiation term \dot{q}''_{rad} of equation (4.3) is zero for all nodes except the nodes corresponding to the walls of a gap. For example for the volume node of the left gap wall, i.e. wall 2 in figure 4.5 with the surface temperature T_{g2} , the term is:

$$\dot{q}''_{\text{rad},g2} = \Sigma_{g1,g2} \left(T_{g1}^4 - T_{g2}^4 \right), \quad (4.7)$$

with the exchange coefficient for parallel plates [113]:

$$\Sigma_{g1,g2} = \frac{\sigma_B}{\frac{1}{\epsilon_{lw,g1}} + \frac{1}{\epsilon_{lw,g2}} - 1}, \quad (4.8)$$

and:

$$\dot{q}''_{\text{rad},g1} = -\dot{q}''_{\text{rad},g2}. \quad (4.9)$$

Convective heat transport inside the gaps is included indirectly in the heat transfer equation (4.1): Here, the thermal conductivity λ is assumed variable and an apparent conductivity according to Klan [74] is calculated, taking into account convective and conductive heat transfer in the gap as a function of geometry, orientation and wall surface temperatures:

$$\lambda_g = \text{Nu} \cdot \lambda. \quad (4.10)$$

The molecular thermal conductivity λ of the gas and the Nusselt number is given by Klan [74] for different gap orientations [74]:

$$\text{Nu} = \begin{cases} C_g \text{Ra}^{0.33} \text{Pr}^{0.074} & \text{for } \leq 0^\circ \varphi \leq 90^\circ \\ 1 + \frac{0.025 \text{Ra}^{1.36}}{\text{Ra} + 1.3 \cdot 10^4} & \text{for } \varphi = 135^\circ \quad \text{for } 1.5 \cdot 10^5 < \text{Ra} < 10^8, \\ 1 & \text{for } \varphi = 180^\circ \end{cases} \quad (4.11)$$

with C_g according to table 4.1 and φ defined as the polar angle between the surface normal of the warmer side \vec{n}_{warm} and the vertical axis, respectively the opposite direction of the gravitational force vector \vec{g} :

$$\varphi = \arccos \left(\frac{\vec{n}_{\text{warm}} \cdot (-\vec{g})}{|\vec{n}_{\text{warm}}| \cdot |\vec{g}|} \right). \quad (4.12)$$

Table 4.1: Values of the gap coefficient C_g in equation (4.11) for different gap orientations [74].

φ	0°	30°	45°	60°	90°
C_g	0.069	0.065	0.059	0.057	0.049

Although the correlations in equation (4.11) are summarized by Klan [74] from different authors and are only valid for discrete surface orientation angles φ , a universal correlation for arbitrary surface orientations, gap widths and wall temperatures is derived. This is done by interpolating between the individual correlations and angles.

4.2.2.3 Boundary Conditions

The segment's boundary condition on the cabin air facing side of the structure is a heat flux boundary condition using \dot{q}''_{CFD} , which is calculated within the 3D CFD cabin model and which already contains radiative, convective and latent heat transfer. The second structure surface boundary condition depends on the type of vehicle part: For all vehicle body segments in contact with the ambient air, the boundary heat flux \dot{q}''_{∞} is calculated by (4.13) as a function of the exterior surface temperature of the preceding time step T_1^n :

$$\dot{q}''_{\infty} = h_{\infty}(T_{a,\infty} - T_1^n) + \sigma_B \epsilon_{\text{lw,s}} \left(F_{\text{s,sky}} \left(T_{\text{sky}}^4 - (T_1^n)^4 \right) + F_{\text{s,gr}} \left(T_{\text{gr}}^4 - (T_1^n)^4 \right) \right). \quad (4.13)$$

The viewing factors $F_{\text{s,sky}}$ and $F_{\text{s,gr}}$ are determined by the inclination angle of the specific vehicle parts, assuming the upper sky hemisphere with the uni-

form temperature T_{sky} and the lower ground hemisphere with the uniform temperature T_{gr} .

The exterior heat transfer coefficient h_{∞} depends on the vehicle part and the vehicle velocity. Here, the experimentally derived correlations by Shimizu et al. [134] for different vehicle parts are applied:

$$h_{\infty} = C_S \cdot v_{\text{car}}^{0.8} \left[\frac{\text{W}}{\text{m}^2 \text{K}} \right]. \quad (4.14)$$

with the empirical coefficient C_S given for the front window, the side windows, the rear window and roof/doors ($C_S = 3.79/7.21/4.65/4.41$) with v_{car} in [km/h] [134]. Other vehicle parts are not mentioned explicitly by Shimizu et al. [134] and are thus approximated by an average coefficient of $C_S = 5.02$.

The natural convection exterior heat transfer coefficient is in general significantly smaller than the forced convection coefficient: According to Klan [73], $h_{\infty, \text{nat}}$ equals for example $3.4 \text{ W}/(\text{m}^2 \text{K})$ at a vertical surface with a reference length of 1 m, a surface temperature of $T_{s, \infty} = 0^\circ \text{C}$ and an air temperature of $T_{a, \infty} = -10^\circ \text{C}$. The same value is reached due to forced convection already at a vehicle speed of 2.6 km/h, according to the correlation given by Shimizu et al. [134] for the side window. Heat transfer due to natural convection is therefore only relevant at high temperature differences and very low driving, respectively wind velocities. For the analyzed cases, driving speeds are significantly higher and natural convection effects at the vehicle exterior are neglected.

For the seat segments, the boundary heat flux at the passenger facing side is calculated in dependence of the passenger skin temperature and the clothing insulation as described in section 3.4. For vehicle body parts, such as the steering wheel¹ and the center console, only the thermal inertia and no heat flux to the environment is included. On one side of these parts the calculated heat flux of the CFD model \dot{q}''_{CFD} is applied and the other side is assumed adiabatic $\dot{q}'' = 0$. This is equivalent to a symmetry boundary condition at the center of the respective part. Thus, only one half of the real thickness of these parts is modeled.

¹ Direct contact between the steering wheel and the hands of the driver is not considered in this study, although a heated steering wheel is an effective measure to enhance thermal comfort.

4.3 Coupled Simulation of Sub-Models

The heat transfer between the cabin air, the cabin structure and the FPC model is fundamentally a conjugate heat transfer problem, including additionally humidity and radiative heat transport. Modeling all processes, including thermal comfort and the structure model, by using one 3D CFD model would result in a very complex system: For example the blood flow in the comfort model or the convection in air gaps in the structure would need to be considered (see sections 3.4 and 4.2.2). Therefore, the different simplified subsystems are simulated separately in a coupled model, instead of solving the whole domain at a time. The exchanged data and the coupled simulation process are depicted in figures 4.7 and 4.8. A similar coupled simulation approach, where the specific focus lies on the passenger cabin of a small bus, is described by Schmidt et al. [131]. In the present thesis a different type of vehicle class, i.e. a compact car geometry, is used where temperature gradients are in general larger.

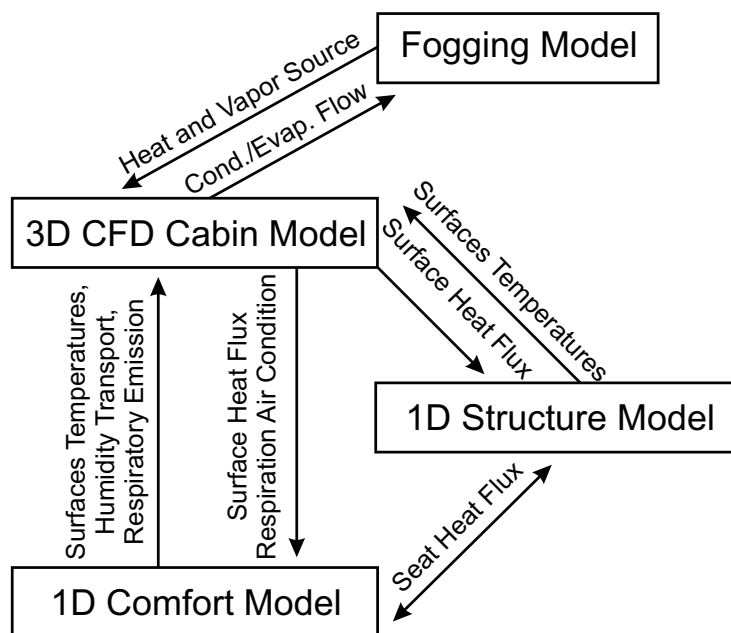


Figure 4.7: Exchange of physical variables between the various sub-models.

An effective quasi-dynamic coupled simulation method for CFD and structure heat transfer simulations is reported by Zhai et al. [154]: The computational effort is reduced significantly by modeling the air temperature distribution in a room by a 3D CFD model and by using a 1D energy simulation tool for the

prediction of wall temperatures and heat exchange with the environment. The CFD model is only used to obtain a steady-state flow field and temperature distribution at specified times. The energy simulation on the other hand uses large time steps to make predictions for cooling and heating loads which are obtained on an hourly or sub-hourly basis for a period of time ranging from a design day to a reference year. This coupled simulation method promises to significantly reduce the calculation effort as the transient CFD model requires small time steps. At the same time the method is reported to improve the prediction accuracy in comparison to conventional low-order energy simulation methods which assume a one-zone air volume and empirically derived correlations for the natural convection heat transfer.

Nevertheless, the above described method by Zhai et al. [154] becomes unstable when applied in the present study: Assuming a constant heat flux obtained from the CFD-model for the energy simulation for a period of time ends up with a diverging (e.g. too high) surface temperature just before the next coupling interval. This in turn results in a wrong (i.e. too low) heat flux obtained from CFD for the next period, leading to a conversely diverging (i.e. too low) surface temperature. In summary, surface temperatures oscillate significantly as soon as the coupling intervals become too large. Thus, applying the quasi-dynamic coupled simulation shows no computational advantage over a dynamic CFD simulation and full coupling at small time steps. The reason why the method is successfully applied by Zhai et al. [154] but fails in this study is possibly the lower temporal temperature gradient in buildings in comparison to vehicles and a lower spatial resolution of the wall thickness leading to a more inert and stable system regarding quick temperature changes.

The applied fully dynamic coupled simulation method is shown in figure 4.8. Here, solid surface temperatures are solved in the respective 1D domains of the passenger comfort model and the structure model. These temperatures are set as boundary conditions for the 3D CFD cabin model. In the CFD model, the wall heat and moisture fluxes are calculated, as they depend strongly on the local air state. This includes also the condensation and evaporation mass fluxes at cool surfaces and the associated latent heat. Subsequently, the wall heat fluxes are returned to the 1D models and used as boundary conditions to calculate the relevant processes in these domains again. The coupling data is exchanged at each time step.

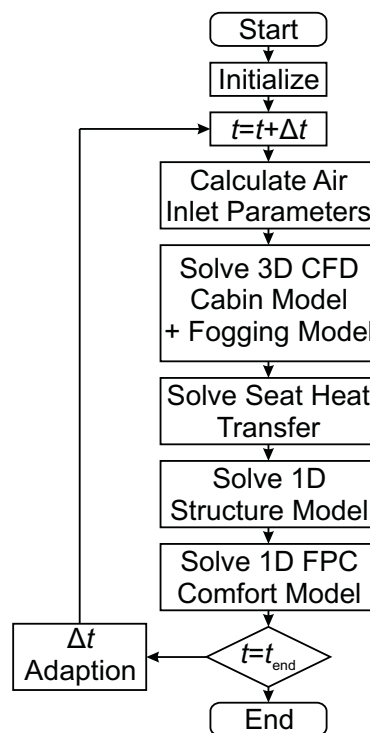


Figure 4.8: Flowchart of the applied coupled simulation method calling the various sub-models.

As variations from one time step to the next are generally small, iterations between two coupling steps until all interface variables converge, as described by Zhai et al. [154], are not applied. Adaptive time stepping is used, starting with a time step of 0.2 s at steep temporal gradients at start and adapted up to 1 s at flattening gradients towards the end of the simulation. The computation time for a 1200 s driving cycle with the coupled simulation model is approximately 19 CPU-hours at 3.4 GHz clock rate. Approximately 70% of this time is spent on the computation of the CFD flow field and the remaining 30% for the structure heat transfer, the comfort model and the coupled simulation routine itself.

The coupled simulation routine is first presented by Lorenz et al. in 2014 including the CFD model of the cabin, the FPC model and the structure model [87]. Since then, the model has been further developed especially by the inclusion of the window fogging model described in section 2.3.1.2. As the window fogging model is fully integrated in the CFD model, the coupled simulation managed by MATLAB is only responsible for the coupling of three indepen-

dent subsystems. The MATLAB routine launches directly the individual external software platforms of the sub-models: For the 3D CFD calculation this is ANSYS FLUENT 14.5. The FPC model is an independent software and further development of the original published Fiala Model [50–52]. The used FPC model version includes a mode for direct bi-directional coupling with other thermal simulation tools (see [42, 53] for more information). The signals for initiation and termination of the calculation are communicated via text files between the MATLAB routine and the external sub-models. In the same manner, physical parameters such as time stepping, heat fluxes, humidity mass flow, surface temperatures or additional boundary parameters such as the air inlet state are exchanged between the MATLAB routine and the sub-models. The 1D structure sub-model is implemented in MATLAB and therefore directly exchanges data with the coupled simulation routine.

4.4 Simulation Test Cases

The above described coupled simulation model is used to predict the saving effect of various cabin optimization measures (see section 4.5). For this purpose a test scenario equal for all test cases is designed and illustrated in table 4.2, defining the boundary conditions of the model.

The boundary conditions include environmental parameters such as the ambient air state and the radiation temperature of the environment. The initial temperatures are assumed equal to the ambient air temperature. This is a simplification as in reality higher or lower structure temperatures may occur.

Table 4.2: List of constant parameters and boundary conditions for the coupled simulation test cases.

Parameter	Value	Parameter	Value
$T_{a,\infty}$	-10°C	$\phi_{a,\infty}$	70%
Solar Load	$0\text{W}/\text{m}^2$	$p_{a,\infty}$	101,325 Pa
T_{sky}	-20°C	T_{gr}	-10°C
T_{init}	-10°C	v_{car}	32 km/h
$f_{\dot{V},\text{defrost}}$	30%	$f_{\dot{V},\text{footwell}}$	70%
$N_{\text{passengers}}$	2	$R_{\text{cl},\text{m}}$	$0.26\text{m}^2\text{K}/\text{W}$

The vehicle parts facing the cooler sky radiation temperature cool down significantly below the ambient air temperature, which aggravates the window fogging and the window icing issue. Higher structure temperatures occur due to the high thermal inertia of some components which are still slightly warm from the previous journey or due to solar irradiation.

Solar irradiation is omitted for the present study as the scenario is a severe winter climate. Various measures leading to a reduction of air-conditioning cooling power in hot climates including solar irradiation are described by other authors [27, 107, 125, 126, 145]. As the operation of the refrigeration cycle requires additional energy also in conventional vehicles, this issue is relevant for the fuel economy already for a long period of time. Only the lack of available waste heat from the drive train nowadays leads to the necessity to save heating power in electrical, hybrid and economic conventional vehicles. Therefore, the reduction of necessary heating power is a new field of interest with different possible solutions than for the reduction of cooling power.

The input parameters concerning the passengers include the number of passengers, their clothing and their assumed activity. Details for these assumptions are described in section 3.4. The overall humidity emission by each passenger calculated by the FPC model and the humidity transport model of the clothing as described in chapter 3.4 is approximately 30 g/h. Significantly higher values from 65 g/h up to 108 g/h are partly found and applied in literature for the average vapor emission per passenger [1, 8, 77, 110]. Nevertheless, in the clothing model described in section 3.4.2 the transport is limited by the diffusion resistance of the assumed winter clothing, and the passengers do not sweat. Recknagel et al. [119] and Großmann [67] give values of approximately 30 g/h of water vapor per passengers if no sweating occurs, which is in good agreement with the values computed in this study. In many cases additional humidity emissions come either from water accumulation in the HVAC [19], wet carpets or clothing of the passengers. To obtain a more realistic scenario for the test cases, the floor (carpets) of the vehicle is assumed to be continuously wetted. Water transport from the floor surfaces is calculated in analogy to the window fogging model with the evaporation rate of water as a function of the local surface temperature, humidity and flow parameters (compare chapter 2.3.1.2).

The vehicle speed, which influences the exterior convective heat transfer, is assumed constant at 32 km/h. This corresponds to a characteristic speed level of the urban part of the New European Driving Cycle (NEDC) and approximately to the average velocity of the combined cycle ($v_{m,NEDC} = 33.6$ km/h). The length of the simulated scenarios is 1200 s, which also corresponds approximately to the length of the NEDC (1180 s) and is characteristic at the same time for typical short distance drives of electric vehicles. If the vehicle is not preconditioned, the heating or air-conditioning load is significantly larger at start than at steady-state operation, due to the thermal mass of the cabin structure. In this study all initial cabin temperatures are assumed to be equal to the ambient air temperature, resulting in a high heating demand for the first 1200 s. Most of the values presented in section 4.5 are time-averaged over the 1200 s driving cycle to derive comparable values of different configurations.

4.4.1 Air Inlet Parameters and Control Algorithms

The coupled model does not contain details of the HVAC system. Nevertheless, a MATLAB or SIMULINK model of the HVAC can be easily integrated as the coupled simulation routine is also managed by MATLAB. To approximate the thermal inertia of the HVAC system and the ducts, they are modeled by approximating the air inlet temperature by a 1st-order lag element (PT1) with a time constant of 60 s and a maximum value of 55 °C (see figure 4.9). The air volume flow is coupled directly to the actual inlet air temperature: Below a minimum air inlet temperature of 0 °C, the volume flow is set to 0.02 m³/s to provide a minimum air supply. Above that temperature, the volume flow is increased linearly with the inlet air temperature, up to a maximum of 0.14 m³/s. Then this airflow is distributed to the different air inlet valves as seen in figure 4.4 and table 4.2. From the inlet air temperature and volume flow the thermal power P_{th} of the inlet airflow is calculated.

From the cabin optimization point of view, the comparison of different test cases at an equal cabin air temperature is more essential than a realistic HVAC behavior. To achieve a constant and comparable cabin air temperature in the test cases, the inlet air temperature and volume flow are controlled by an ideal PI controller with the volume-weighted cabin air temperature as a control variable (see figure 4.9). Assuming a high available thermal HVAC power of up to 10 kW allows the set-point temperature to be reached after a short period

of time, otherwise the lack of heating power would reduce the theoretical energy saving potential. Such a controller is not realizable in a real vehicle, e.g. because the volume-averaged air temperature, here obtained from the CFD model, cannot be measured. This approach nevertheless, allows an energetic comparison of different measures such as thermal insulation or recirculation, not only on a steady-state but as well on a transient basis, at the same cabin air temperature.

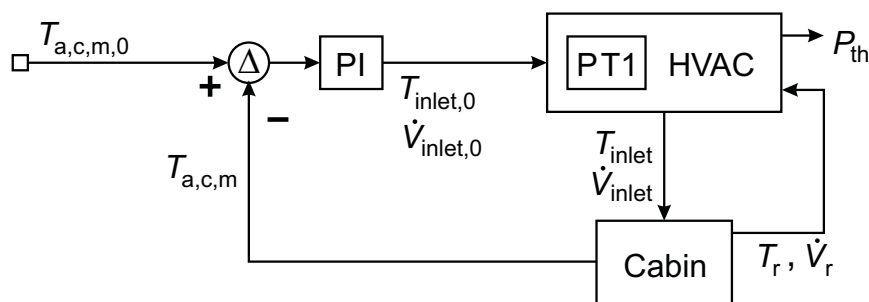


Figure 4.9: Control flowchart of the air inlet parameters and calculation of the necessary thermal HVAC power.

To model the influence of air-recirculation, different pressure outlets for fresh air and recirculated air are used in the CFD model. For pressure outlets, FLUENT offers a parameter called "Target Mass Flow Rate". The actual air state of the recirculation outlet obtained from the CFD model is used to calculate the necessary heating power and water content of the inlet airflow. Although dehumidification of the inlet air sometimes solves the issue of window fogging, this option is not considered for two reasons. First, dehumidification requires in general additional energy: The inlet air is usually cooled down by operating the refrigeration cycle, water condenses at the evaporator surface and the inlet air is reheated. In a vehicle with a heat pump refrigeration cycle, this reheat is done by the condenser in the HVAC unit, which reduces the necessary energy significantly [18, 68]. If no heat pump functionality is included, the reheating needs to be done by waste heat or electrical heating. The second reason is that typically the refrigeration cycle cannot be used for dehumidification below an ambient air temperature of approximately 5°C because of the risk of frost formation at the evaporator surface [64].

4.5 Saving Potential of Optimization Measures

A variety of possible measures to reduce the heating and cooling demand of the vehicle cabin and to maintain passenger thermal comfort exists and can be evaluated by the described model. Additionally, combinations of measures are partly advantageous: Recirculation of cabin air for example has a high energy saving potential and insulation of the windows reduces the arising fogging affinity at the same time. Within the scope of this study only a limited choice of promising measures and combinations is analyzed and compared to a baseline case.

The analyzed optimization measures include:

1. Air recirculation
2. Glazing options
 - Double pane insulation glass
 - Polycarbonate
 - Low- ϵ coated glass
 - Window heating
3. Local heating measures
 - Seat heating
 - Panel heating
4. Reduction of the cabin air temperature

The baseline case, described in section 4.5.1, consists of a configuration with standard float glass, fresh-air mode, no additional local heating measures and a set-point cabin temperature of 25.5 °C. The effect of each optimization measure on energy consumption, thermal comfort and fogging affinity is analyzed separately, setting off the baseline configuration. The various glazing options, presented in section 4.5.2, are evaluated for different recirculation fractions to analyze also the respective effects on window fogging. Measures to optimize local comfort are analyzed in section 4.5.3 at reduced cabin temperatures to quantify the energy saving at a comparable comfort level.

From the results of the separately analyzed measures, an optimized configuration of a combination of measures is derived. Nevertheless, a real optimum strongly depends on the definition of various conflicting objectives, such as thermal comfort, allowable fogging level, energy consumption, cost and weight, as well as the boundary conditions and the driving cycle. The optimized configuration presented in section 4.5.4 is thus only exemplary and has limited general significance.

4.5.1 Baseline Configuration

In figure 4.10 the temporal evolution of various simulation results is illustrated for the baseline configuration. As explained in section 4.4.1, a high available thermal power is modeled to allow a comparison of various test cases at the same mean air temperature. The inlet air temperature and the air heating power therefore reach the maximum value relatively quickly and reduce steadily as the cabin air temperature approaches its set-point of 25.5 °C. Due to this high heating power, 7.9 kW on average, a mean cabin air temperature of 20 °C is reached already after 170 s. Nevertheless, the inside mean window temperature and especially the temperature of all other inside structure surfaces takes significantly longer to reach a steady value. At full fresh air mode ($f_r = 0$), the windows fog slightly at the beginning of the simulation test case but remain subsequently free from fog due to the very high fresh-air flow which is necessary to maintain the mean cabin air temperature. At higher recirculation rates, significant parts of the windows start to fog again, as soon as the cabin humidity level rises. The predicted Dynamic Thermal Sensation (DTS) is clearly cold in the beginning of the test case and approaches a neutral sensation after 1200 s. In comparison to the air temperature, this evolution is significantly delayed due to the influence of the seat and the radiation temperature. Overall Thermal Comfort (OTC) shows a similar evolution as the thermal sensation: It starts with a clearly uncomfortable value and ends at a slightly uncomfortable value of approximately -0.5 after 1200 s.

4.5.2 Glazing Options

The glazing material has a significant influence on heat transfer and surface temperatures. A higher surface temperature leads to a lower fogging affin-

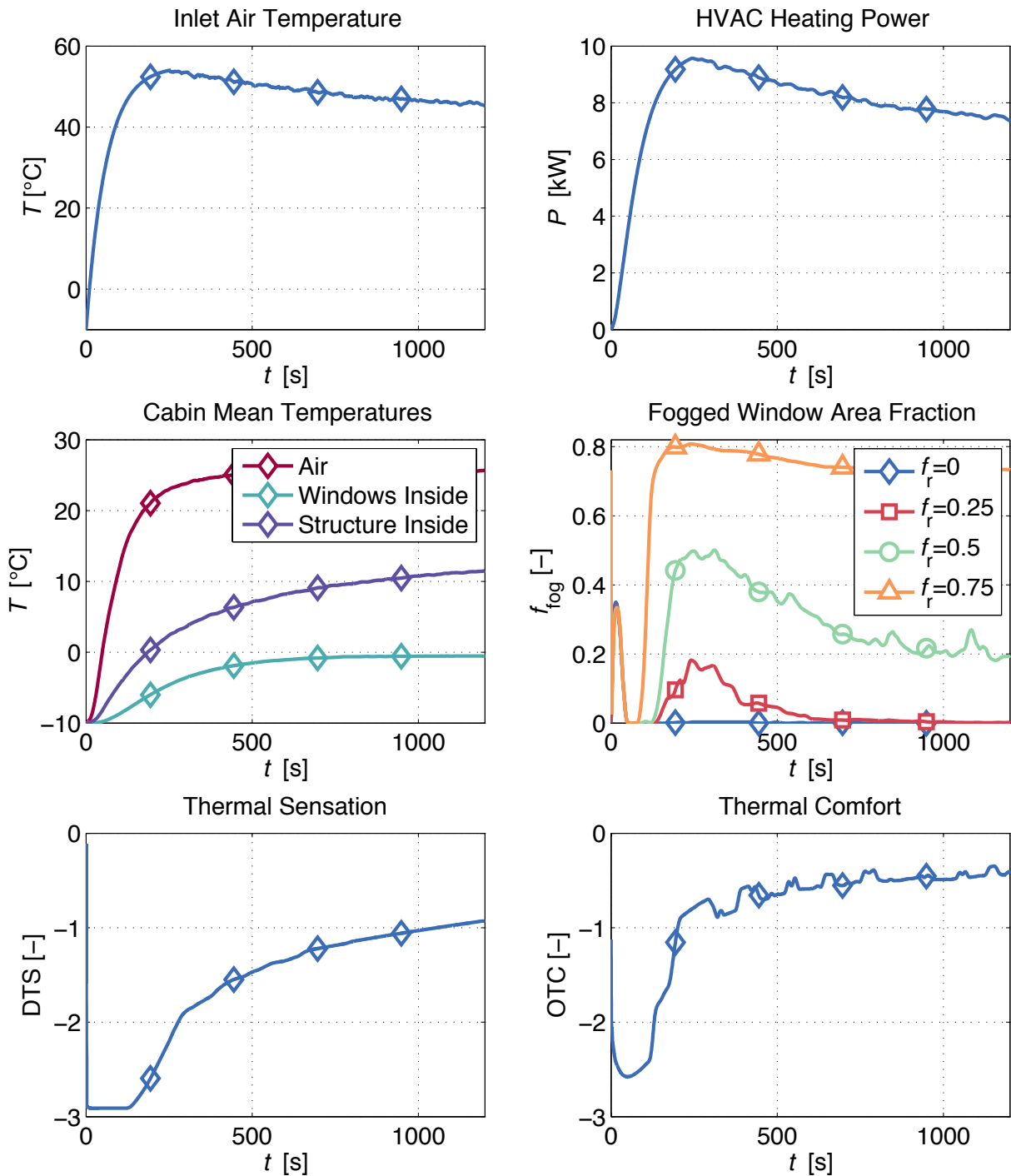


Figure 4.10: Temporal evolution of various simulation results of the baseline configuration with standard float glass, no recirculation, no additional local heating measures and a set-point air cabin temperature of 25.5 °C.

ity and in general in winter also to a higher thermal comfort perception due to reduced radiation losses. The heat transfer characteristic of the individual

glazing materials is calculated as described in chapter 4.2.2 and depends also on the orientation of the windows, and the inside and outside convective and radiative heat transfer. In vehicles there is no standardized U-value such as known from building technology because the heat transfer varies significantly with the position of the windows, the driving speed and the ventilator settings. For the purpose of comparability, U-values of the applied glazing options are nevertheless calculated according to the standard DIN EN 673 [38]. According to this standard, an exterior heat transfer coefficient of $25 \text{ W}/(\text{m K})$, an interior coefficient of $7.7 \text{ W}/(\text{m K})$ and a standardized algorithm for the air gap is applied. This results in a U-value of $5.8 \text{ W}/(\text{m K})$ for the 3 mm standard float glass and low- ϵ coated glass, $2.8 \text{ W}/(\text{m K})$ for the double pane insulation glass (3/5/3 mm) and $5.4 \text{ W}/(\text{m K})$ for the 3 mm polycarbonate glazing.

For the heated window cases, the control set-point of the window surface temperature is adjusted according to the actual fogging affinity. Thus, with a rising recirculation fraction f_r (0/ 0.25/ 0.5/ 0.75), the window surface temperature is also raised ($-4 \text{ }^\circ\text{C}/ -2 \text{ }^\circ\text{C}/ 0 \text{ }^\circ\text{C}/ 3 \text{ }^\circ\text{C}$). This avoids unnecessary electrical energy input when the fogging affinity is low or the window surface is warm anyway due to convective heating.

To evaluate the influence of different glazing options, time-averaged values over the 1200 s driving cycle are computed. The influence of different glazing options on temperature, fogging affinity, heating power and thermal comfort are evaluated and compared as a function of the recirculation fraction. The structural composition and the assumed material properties of the glazing options are listed in appendix F.

In figure 4.11 it is seen that the glazing material has a significant influence on the interior surface temperature. The time and area-averaged temperature of the insulation glass is approximately 7 K higher than of the standard float glass. The low- ϵ coating leads to a slightly lower surface temperature than float glass because of the reduced radiative heat transport to the windows. Polycarbonate on the other hand, raises the average inner surface temperature by about 2 K. The fivefold reduced thermal conductivity of polycarbonate in comparison to glass enhances the overall thermal resistance, but a significant part of the resistance is caused by the inside air boundary layer in both cases. A slight dependence of all temperatures on the recirculation fraction is seen.

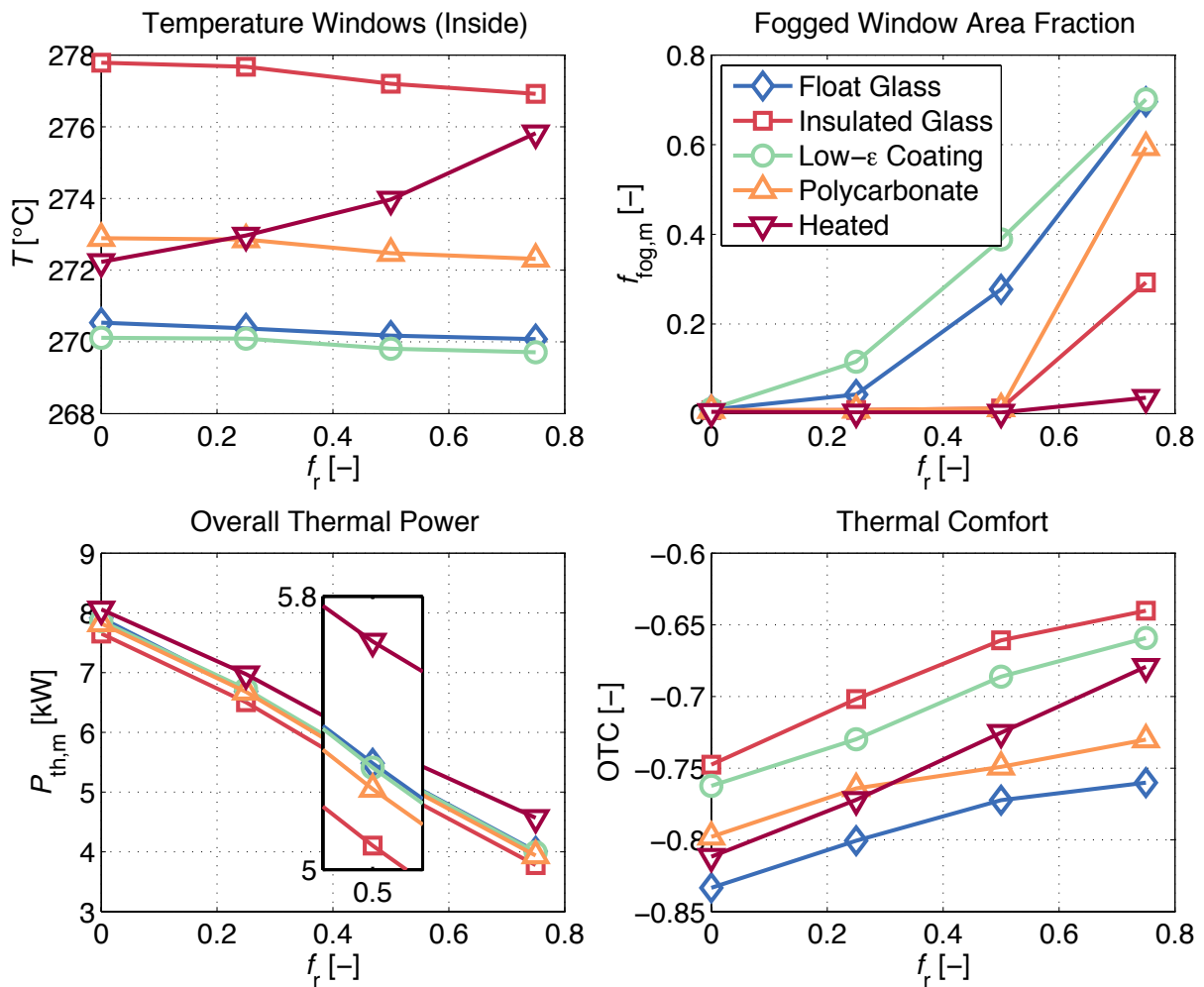


Figure 4.11: Influence of different glazing options on the time and area-averaged inside window temperature, fogged window fraction, power consumption and thermal comfort as a function of the recirculation fraction.

The average fogging affinity of all glazing options is almost zero in fresh air mode due to the high air volume flow. By raising the recirculation fraction to 50%, severe fogging is observed: More than 50% of the window area is fogged in the standard float glass and the low- ϵ coating cases. When the recirculation fraction is raised to 75%, the polycarbonate glazing also shows a high fogging affinity at large parts of the windows, but only a 30% fraction of the window area starts to fog for the double pane glazing. For the heated windows, the removal of fogging is a pure matter of sufficient energy input. With the above mentioned set-points for the inside window temperature, window fogging is avoided almost completely for all recirculation fractions.

Although the visibility cannot be predicted with the actual fogging model, it is expected to be significantly better for polycarbonate than for fogged glass (compare figure 2.20 and 2.22).

A strong and approximately linear reduction of the necessary heating power is achieved by raising the recirculation fraction. 50% recirculation instead of pure fresh air mode leads to an energy saving during the first 1200 s of more than 30% for all glazing options. An influence of the glazing material on the average necessary heating power is also seen in figure 4.11, although the differences are smaller than the differences due to recirculation. As expected, the double pane glazing requires the least energy to reach and maintain the cabin set-point temperature, and the power is reduced by 5% in comparison to the float glass cases. Polycarbonate yields a reduction of 1–2% at the same recirculation fraction. As mentioned above, the low- ϵ coating leads to reduced heat transfer, although the inner surface temperature is lower than the uncoated option. The necessary heating power is, nevertheless, only marginally reduced in comparison to float glass. Keeping in mind the respective fogging affinities, it becomes clear that only the insulation glass and polycarbonate option can passively use the additional saving potential by recirculation.

Window heating requires more overall thermal (and especially electrical) power than all other options. Nevertheless, an enhanced window surface temperature allows a higher recirculation fraction without the window to be fogged. In the analyzed simulation cases, heating of windows leads to an overall energy saving, if applied economically. This means that the windows must be heated only slightly above the vapor saturation temperature of the cabin air.

The recirculation fraction has also an influence on the predicted thermal comfort due to a different temperature distribution in the cabin and a higher humidity level in recirculation mode. The influence of the different glazing options on the predicted Overall Thermal Comfort (OTC) level is visible, although not eminent. Here, the effect is mainly driven by the reduced radiation heat losses at higher surface temperatures of the surrounding structure. This leads to a reduced asymmetry of the perceived thermal sensation at the body and thus higher OTC values. Nevertheless, the seat surface temperature is still low without seat heating and thus a certain asymmetry of the body temperature distribution is maintained. Additionally, not only the windows lead to

high radiation body heat losses but also the other surrounding cold cabin surfaces. The difference of the OTC value between the double pane glazing and the float glass is thus only 0.1. The low- ϵ coating effectively reduces the radiation losses and yields almost the same effect on the OTC value as the double pane glazing.

4.5.3 Local Heating Measures

A wide range of different local heating measures are possible and partly state-of-the-art in vehicles. In this study, the effect of seat heating and surface (panel) heating of the surrounding surfaces, i.e. the roof, the footwell and the door surfaces close to the passengers, is analyzed. The heated surfaces comprise an overall area of 3.7 m². The local heating systems are integrated in the simulation cases as heat sources inside the first cabin-facing material layer of the respective parts, as described in section 4.2.2. PI controllers are designed to reach and maintain the set-point temperatures of the individual surfaces by adjusting the necessary electrical power. The set-points are 35 °C for both seats and 50 °C for the panel heating. These values are found to have a positive effect on thermal comfort at a reasonable power input. The temperature control variables are calculated as an area-averaged value of the respective surface and serve as an input for the PI-control, similarly to the control illustrated in figure 4.9.

Local heating systems influence directly the thermal contact temperature or the radiation temperature seen by the passengers. An influence on thermal sensation and comfort is obvious. An advantageous effect of electrical heating systems on the overall power consumption is only possible if the cabin air temperature is reduced at the same time. Therefore, simulations are performed and evaluated for different cabin air temperatures (5 °C/ 12 °C/ 19 °C/ 25.5 °C). Three configurations, "no additional heating measures", "panel heating", and "seat heating" are analyzed separately to distinguish the respective effects. The results are illustrated in figure 4.12.

The necessary heating power for the comparison in figure 4.12 is separated into thermal power for the HVAC system and thermal power for the additional heating systems, i.e. seat heating and panel heating. The electrical power input of the panel heating is significantly higher than for the seat heating. As

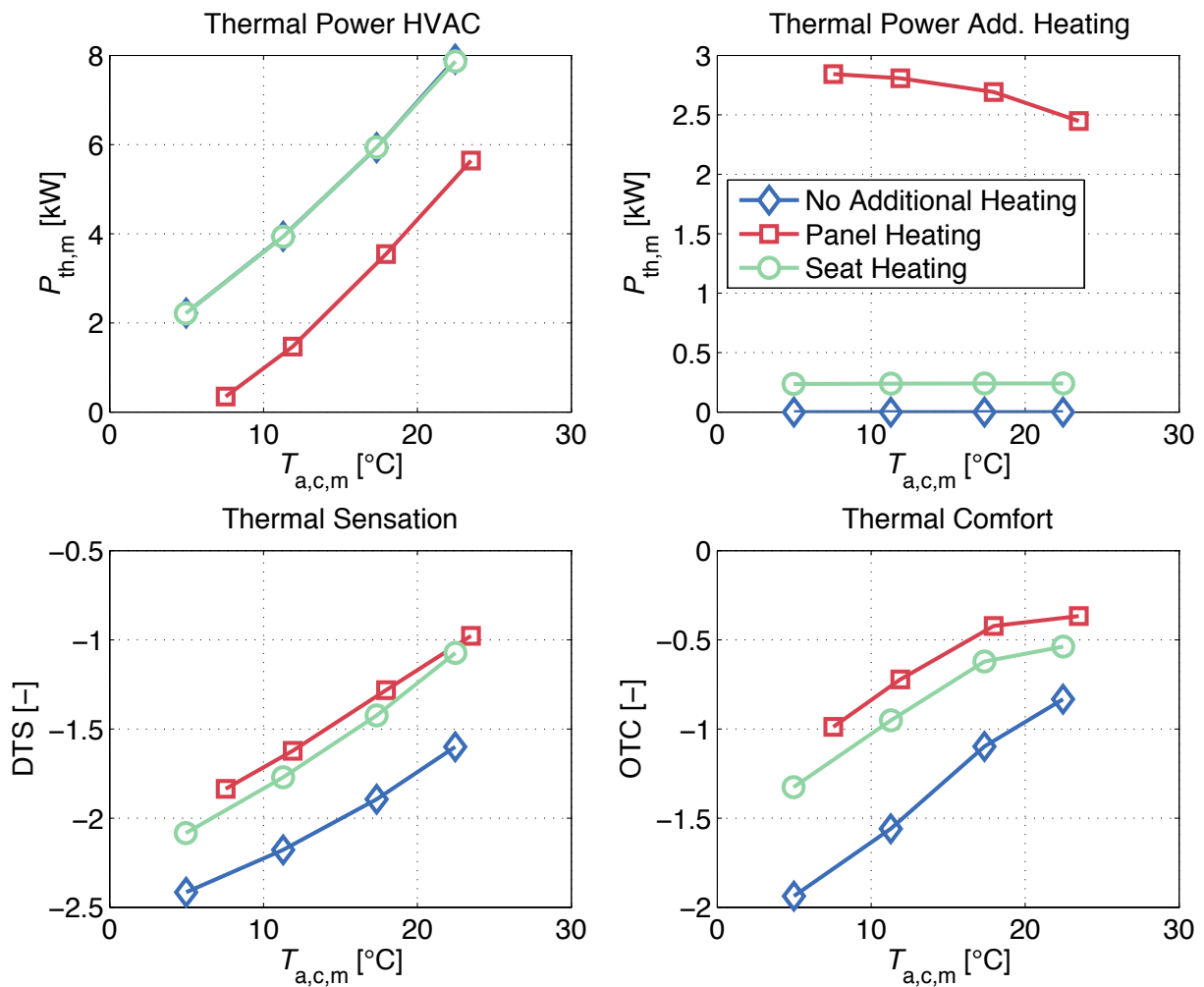


Figure 4.12: Influence of local heating measures on HVAC and additional heating power and on thermal sensation and comfort in dependence of the time and volume averaged cabin temperatures.

the cabin temperature is fixed by the control, panel heating helps to reduce the necessary HVAC heating power by almost the amount of electrical power which is necessary to heat the panels. On the other hand, the HVAC power demand of the seat heating cases and the cases without additional heating is approximately equal. The power demand of the seat heating is also independent of the air temperature. The reason for this is that the seat heating is not in direct contact with the cabin air and the required power is low in comparison to HVAC and panel heating power.

Both additional heating measures lead to a thermal sensation of approximately 0.5 DTS units higher than without additional heating at the same aver-

age air temperature. The time-averaged sensation of the first 1200 s remains still slightly cool. The average thermal comfort value is raised significantly by approximately 1.0 OTC units by seat as well as panel heating. At a reduced air temperature set-point of 12 °C, the OTC levels of the seat heating and panel heating case reach approximately the same average value as the baseline configuration at a set-point of 25.5 °C. Panel heating, as described above, has a slightly more positive influence on thermal comfort and sensation than seat heating. Keeping in mind the underprediction of local heating measures in a cold environment determined in section 3.5, their positive effect is in reality possibly stronger than found in the simulation cases presented in this thesis.

The reduction of the air temperature leads to a significantly lower heating power demand. A reduction of the time and volume averaged cabin temperature from 22 °C to 12 °C at a comparable comfort level leads to a reduction of 50% of the necessary thermal power if seat heating is applied and a reduction of 46% if panel heating is applied.

4.5.4 Optimized Configuration

As mentioned above, a real optimum of all possible configurations and parameters strongly depends on defined goals (e.g. thermal comfort vs. consumed power) as well as ambient and driving conditions. Additional important factors not investigated in detail are e.g. durability, crash performance, weight and cost of various measures. Taking into account such factors, measures such as polycarbonate glazing possibly becomes favorable over double pane glazing due to a significant weight reduction, although from a thermal and energy point of view double pane glazing is better in cold climates.

The optimized configuration presented in this chapter, is therefore only exemplary, nevertheless, yielding a significant saving potential in comparison to the baseline configuration. From the above analyzed measures, the presented optimized configuration includes:

1. Recirculation fraction of 50%
2. Double pane insulation glass
3. Inside window heating (set-point 0 °C)

4. Seat heating
5. Panel heating
6. Reduced cabin air temperature (set-point 12 °C)

The results of the optimized configuration are illustrated in figure 4.13. It is seen that the reduced cabin air temperature of 12 °C is reached quickly. After 700 s the air heating is switched off completely and only the minimum air supply of 0.02 m³/s is provided to the cabin. Then cabin heating is achieved only by the thermal power input of the panels. The inside temperature of the insulated window surface reaches quickly values above 0 °C due to the insulation and the additional window heating. Window heating is only necessary during the first 250 s of the driving cycle. The fogging affinity is very low during the entire driving cycle due to the combination of window heating and insulation. Thermal sensation (DTS) and thermal comfort (OTC) show similar temporal evolutions as in the baseline case but reach slightly higher, approximately neutral (0) values despite the significantly reduced air temperature. The combined effect of the various measures of the optimized configuration leads to the fact that better results are obtained for almost all parameters in

Table 4.3: Comparison of the time-averaged results of the baseline case and the optimized configuration.

	Baseline	Optimized	
Cabin air temperature	22.5 °C	13.1 °C	
Inlet air temperature	47.0 °C	7.1 °C	
Overall air volume flow	0.12 m ³ /s	0.04 m ³ /s	
HVAC power supply	7.9 kW	0.49 kW	} $\Sigma = 3.62$ kW
Seat power supply	-	0.24 kW	
Panel power supply	-	2.7 kW	
Window power supply	-	0.19 kW	
Mean window temperature	-2.6 °C	5,0 °C	
Mean structure temperature	6.0 °C	12.7 °C	
Fogged window fraction	0.9%	0.3%	
Dynamic Thermal Sensation (DTS)	-1.6	-1.0	
Overall Thermal Comfort (OTC)	-0.8	-0.3	

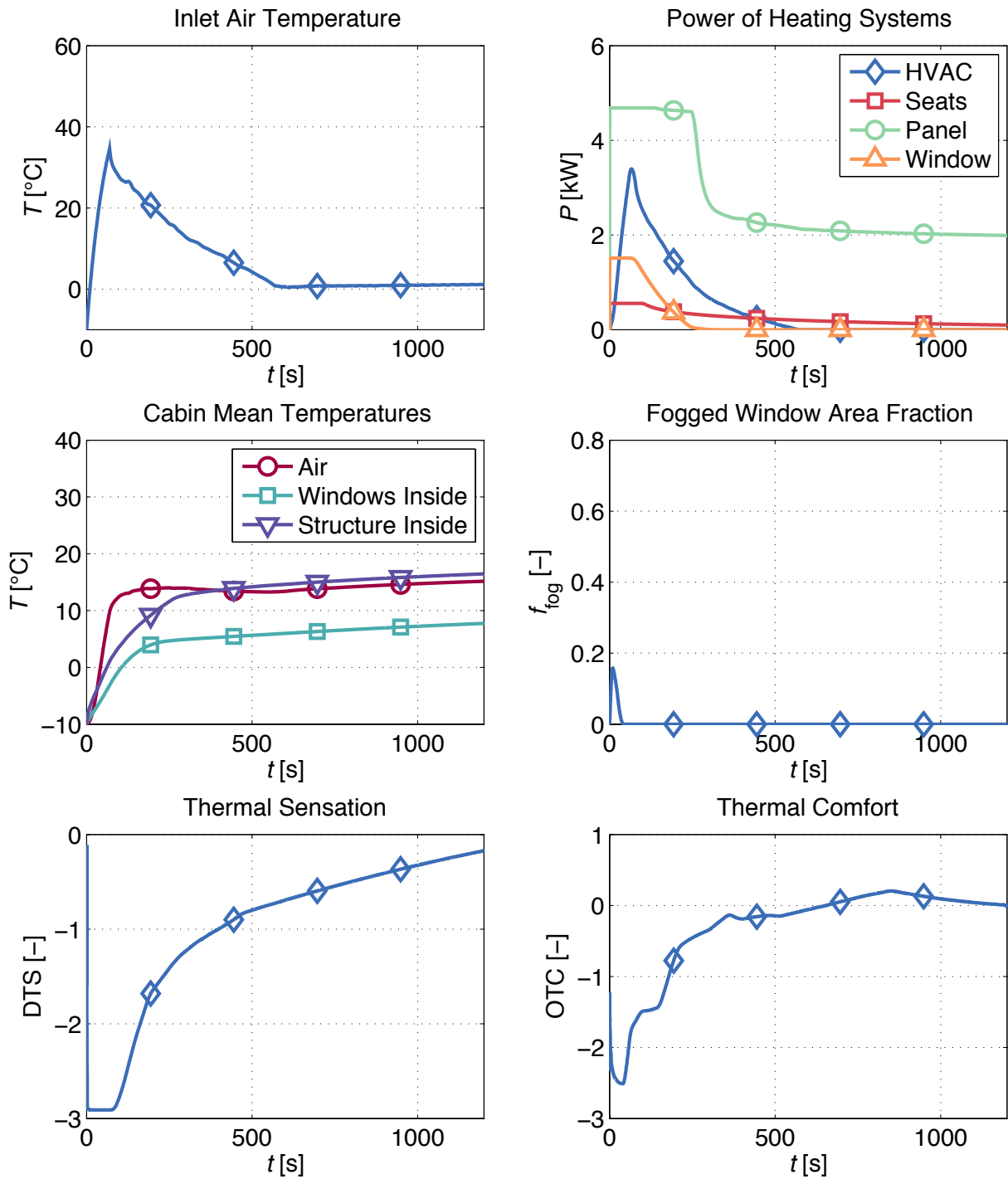


Figure 4.13: Temporal evolution of various simulation parameters of the optimized configuration with double pane glazing, 50% recirculation, seat and panel heating and a reduced cabin temperature of 12 °C.

comparison to the baseline case (see table 4.3). The largest advantage is obtained for the required thermal power. The optimized configuration requires a

mean thermal power supply of 3.6 kW, for air, panel, window and seat heating, whereas the baseline configuration requires 7.9 kW for the air heating only. This corresponds to a thermal power saving of 57% during the 1200 s driving cycle.

The seat, panel and window heating, which account for the largest part of the power demand of the optimized configuration, require in general electric heating. The HVAC air heating can, on the other hand, also be realized more effectively by a refrigeration cycle heat pump system. To provide 7.9 kW of thermal power for the reference case, a COP of 2.3 is required to reach the same saving as with the proposed optimized configuration. This value is slightly higher than the value of 1.8 predicted by Hörth et al. [68] for a realistic automotive heat pump system at -10°C . Additionally, a heat pump system is also costly, heavy and leads to new challenges such as a suitable refrigerant or the problem of frost formation at the front-end evaporator if an air-to-air heat pump is used.

4.6 Conclusion

An analysis of state-of-the-art modeling approaches for vehicle cabins reveals different levels of detail, ranging from one-zone models to detailed CFD models. Depending on the goal of the simulation and the available computational resources, a detailed or a simplified cabin model may be best-suited. Promising cabin optimization measures include airflow recirculation and local heating and cooling measures. Modeling these measures and the linked phenomena of window fogging adequately, requires a detailed distribution of temperature and humidity in the cabin.

A relatively coarse CFD model of the cabin is chosen as a compromise between computational effort and achievable accuracy of the result. Together with a 1D heat transfer model of the adjacent cabin parts, all variables of interest are resolved both temporally and spatially. A MATLAB algorithm manages the coupled simulation of the CFD cabin model, the 1D heat transfer model, the window fogging model and the comfort model, as these sub-models are partly running on different software platforms.

The simulation scenario to compare various cabin optimization measures is a winter climate at an ambient air temperature of $-10\text{ }^{\circ}\text{C}$ and a moderate vehicle speed of 32 km/h. As the transient heating power at the beginning of a driving cycle is significantly higher than the steady-state heating power, a simulation time of 1200 s is chosen. PI controllers for the different heating systems are used to allow an analysis of the necessary heating power at comparable temperature levels.

In comparison to a baseline case with no recirculation, enhancing the recirculation fraction leads to a significant reduction of the heating power. An airflow recirculation of 50% reduces the power by more than 30%. To make use of this saving potential without severe fogging of the windows, recirculation can only be applied with additional measures such as double pane insulation glass, polycarbonate glazing or window heating. Insulating the windows by double pane glazing leads to an additional reduction of the necessary heating power of up to 5%. But a higher window temperature also has a measurable, positive effect on the perceived thermal comfort. Although window heating requires an additional electrical energy input, an overall energy saving is achieved, if window heating is controlled according to the actual fogging affinity.

Analyzed measures which directly influence thermal comfort include seat and panel heating. In order to achieve an overall energy saving instead of an additional power input for the local heating systems, the configurations are evaluated at stepwise reduced cabin temperature set-points. According to the comfort model, an approximately equivalent level of thermal comfort is achieved by the application of either seat or panel heating at a 10 K reduced average cabin temperature. This leads to a reduction of the necessary thermal power of almost 50% for seat as well as panel heating. On the other hand, the additional heating systems, especially the panel heating require significant amounts of electrical energy.

Finally, an optimized configuration is presented which consists of a recirculation fraction of 50%, double pane insulation glass, inside window heating, seat heating, panel heating and a reduced cabin air temperature of 12 °C. With these applications a significant improvement is achieved in comparison to the baseline configuration. The overall necessary thermal power for the 1200 s driving cycle is reduced by 57%.

5 Summary

In this study, a **coupled simulation model** is developed to predict the saving potential of various optimization measures which reduce the thermal demand of vehicle cabin heating. Although the background of this study is about improving the performance of electric vehicles, results are also transferable to other types of vehicles. The analyzed measures include various glazing options, such as double pane glazing, polycarbonate or window heating as well as local heating measures, such as seat or panel heating, and the enhancement of air recirculation. The cabin coupled simulation model includes sub-models to quantify the heat and mass transfer in the cabin and in the cabin structure, the thermal comfort of the passengers and the fogging of the windows.

The first described sub-model of the coupled simulation model is a **window fogging model**. This model is necessary to account for condensation, resulting from humidity emissions in the cabin, too high recirculation fraction and a too low inside window temperature. For the development of the model, condensation and evaporation experiments are conducted and a new measurement technique to measure the contact angle and volume of a droplet is developed. This measurement technique allows to capture droplets from perpendicularly above and to calculate contact angles and the integral droplet volume per unit surface area, using the observed reflections of a light source. An image processing algorithm is developed to automatically detect and evaluate large numbers of droplets. Thus, local condensation and evaporation mass fluxes are quantified.

Influences of the droplet shape on the heat and mass transfer are known from drop-wise condensation in power plant technology. Several authors describe models for window fogging and partly include dependencies of the mass flux on the droplet shape. This study identifies three hypotheses of how different mechanisms can lead to a dependency. However, theoretical estimations and experimental results show that influences of the droplet shape can

be neglected if the droplets are small, the turbulence level and the heat flux are low and the fraction of non-condensable gases is high. This is the case in all analyzed window fogging conditions of this study and no significant dependence between mass flow rate and droplet structure is observed. From the experimental conditions it is estimated that any dependence is also negligible under most window fogging conditions found in vehicle cabins. Therefore, a diffusion based condensation and evaporation film model is assumed capable of representing the relevant effects. This model is developed, subsequently implemented with ANSYS FLUENT User Defined Functions (UDF) and finally validated against the experimental data.

The **quantification of thermal comfort** is the task of a second sub-model of the coupled simulation model. This is achieved by including the Fiala Physiological Comfort model (FPC). The model allows to account for temperature inhomogeneities and transient conditions, which are characteristic for vehicle operation. Hereby, the effect of various measures such as seat heating, panel heating or reducing the cabin air temperature on thermal comfort and sensation is predicted. In an experimental setup with 22 human test subjects, the effect of seat heating in a cold environment is investigated experimentally and compared to corresponding simulation results. It is found that the simulation reproduces the qualitative effect of seat heating but underestimates the positive effect of seat heating which balances discomfort resulting from a too low air temperature.

A coarsely meshed ANSYS FLUENT CFD **model of a generic vehicle cabin** is used to describe the heat and mass transfer inside the cabin. Heat fluxes and vapor condensation and evaporation mass fluxes are calculated as functions of the actual surface temperatures. The surface temperatures of the vehicle structure are calculated dynamically in a MATLAB 1D shell layer structure model, including different material layers, air gaps and a model for the heat transfer to the environment. All models are dynamically coupled, exchanging interface variables at each time step. The coupled simulation is managed by a routine developed in MATLAB.

It is shown in sample test case simulations that especially the insulation of the windows leads to a reduction of thermal losses, enhances thermal comfort and especially **reduces the window fogging affinity**. Thus, a higher recirculation fraction can be realized. But also heating of the windows, if applied with

a suitable temperature and humidity control, leads to overall energy saving by realizing a higher recirculation fraction at the same time.

Another effective way to reduce the necessary thermal power is the application of **local heating measures**. These measures are investigated in a second parameter study in dependence of the cabin air temperature. Seat heating and panel heating both prove to be effective ways to enhance thermal comfort and to reduce the necessary heating power of the central HVAC system.

In an **optimized configuration** several measures are combined to demonstrate the overall thermal power saving potential without reducing the thermal comfort level. These measures include double pane insulation glass, an enhanced recirculation fraction, seat, panel and window heating and a reduced cabin air temperature. A heating power saving potential of 57% is predicted, and fogging affinity and discomfort are at the same time reduced in comparison to the baseline configuration.

6 Outlook

In chapter 4, a new cabin model is presented and it is used to quantify the saving potential of various cabin optimization measures. The used cabin and composition of the cabin structure is a virtual generic geometry. Although the general results and conclusions might not change, simulations need to be repeated with real geometries and validated with test data of the respective vehicle geometry. New subsystem models, i.e. the window fogging model and the Fiala Physiological Comfort (FPC) model with CFD and structure boundary conditions are verified experimentally in this thesis. Suitable validation data for a complete vehicle cabin was on the other hand not available for this thesis. A further **validation of the cabin model** including all subsystems is therefore an important task for future works on this topic.

The experimental comfort study in a cold climate chamber in section 3.5 shows a significant improvement of the perceived comfort level when the seat heating is applied. Both outputs of the FPC model underpredict this effect: the Overall Thermal Comfort (OTC) model by Zhang [158], which is computed by the two minimum local comfort votes and the maximum local comfort vote, and the Fiala Dynamic Thermal Sensation (DTS) model, taking into account the dynamic signal of the area-averaged skin temperature. Additionally, the DTS signal shows a sudden drop of the thermal sensation when the environment changes from thermal neutrality to the cold environment. In the experiments it takes several minutes until the minimum thermal sensation votes are reached. Keeping in mind the saving potential of local heating (and cooling) measures predicted in this study, it is recommended to investigate such effects more in detail and **adapt the comfort models** accordingly.

In section 4.5 the saving potential of some promising cabin optimization measures is quantified. One of the most promising measures is the use of air recirculation, combined with the prevention of window fogging. In a real vehicle this will be primarily a challenge for the **window fogging detection and the control algorithms**. With the state-of-the-art vehicle sensors it is already chal-

lenging to measure the relative humidity, surface temperature or condensed water at one point instead of the entire cabin: There are quick changes of the fogged surface area if e.g. humidity is accumulated in the HVAC (so called flash-fogging), but also large reaction times arise if e.g. a thick layer of water is accumulated at a window surface. Additionally, there are unsolved questions from the legislative and customer perspectives about an eventual acceptance of fractionally fogged window areas and fogging of the rear and side windows.

An energy efficient way to prevent window fogging is to enhance thermal **insulation of the windows**. At low ambient temperatures the insulation has a positive effect on interior window fogging, thermal comfort and heat losses. Nevertheless, thermal insulation of windows can also lead to new problems: The greenhouse effect is stronger for insulated windows than for standard glass, leading to higher cabin temperatures in summer. Under winter conditions the outside window surfaces are colder and more difficult to defrost if windows are insulated. Electrical heating might be required to deice the outside pane of an insulated window and to fulfill the prescribed regulations [8, 43, 117, 141]. Positive and negative effects of thermal window insulation should thus be analyzed and compared more in detail in a future study.

The new **contact angle measurement** technique which is presented in 2.2.2 allows the measurement of the condensation and evaporation mass flux and the development of a suitable window fogging model. This technique can be **transferred to other technical fields**, for example to quantify the condensation mass flux in power plants or the fogging of spectacles. A further development of the method would also allow the geometry of non-spherical droplets, e.g. pending droplets at walls, to be quantified. Such droplet shapes can be described by the Young-Laplace equation (2.8) in section 2.2.2.1 but require more complex solving algorithms than if the assumption of rotational symmetry is included.

An issue which is mentioned in chapter 2.2.4.1 is the **prediction of visibility** through fogged windows. Being based on spherical drop shapes, even a detailed drop-wise condensation model is only suitable for hydrophobic surfaces. Here, the theoretical surface coverage is 57% and constant in the self-similar condensation regime. The visibility is dominated by the uncovered area fraction and can thus be calculated accordingly. Even the light ray scattering distribution can be calculated relatively easily for spherical droplets. On

the other hand, as soon as contact angle hysteresis is dominant, it becomes challenging to predict the surface coverage and the light scattering numerically, due to complex droplet shapes. For very hydrophilic surfaces the visibility improves again because of the light that passes the droplets or the film without being scattered significantly. For a known droplet distribution and droplet geometry, the visibility can theoretically always be calculated by ray-tracing algorithms. To **determine such complex distributions and droplet shapes**, both numerically and experimentally, remains a task for future works.

Additionally, the new measurement technique allows to study effects, such as the **contact angle hysteresis** during condensation and evaporation, as well as the **relation between droplet size and contact angle**. These topics are only briefly discussed in chapter 2.2.4.3 but can be the basis for new interesting research activities.

The thesis shows that a detailed drop-wise condensation model, including individual droplets, droplet populations, and contact angles has no significant benefit over a simple film condensation model under typical window fogging conditions, as the dependency of the mass transfer on the droplet geometry is negligible. Nevertheless, there are other conditions with very large droplets, a small fraction of non-condensable gases, high heat transfer rates or large flow velocities where a **droplet condensation model** is indispensable. Obviously, power plant technology, where a tenfold heat transfer coefficient between film condensation and drop-wise condensation is achieved, is such an application. Here, the new measurement technique can help to better quantify drop size and volume distributions and can be used to validate a detailed drop-wise condensation model.

Appendix

A Velocity Profiles Measured by PIV

The velocity values obtained by PIV are averaged over time and over the 50 mm length of the observed section above the substrate. The obtained axial velocity, turbulent kinetic energy and turbulent dissipation rate serve as boundary conditions for the CFD validation of the window fogging test rig (compare figure 2.30).

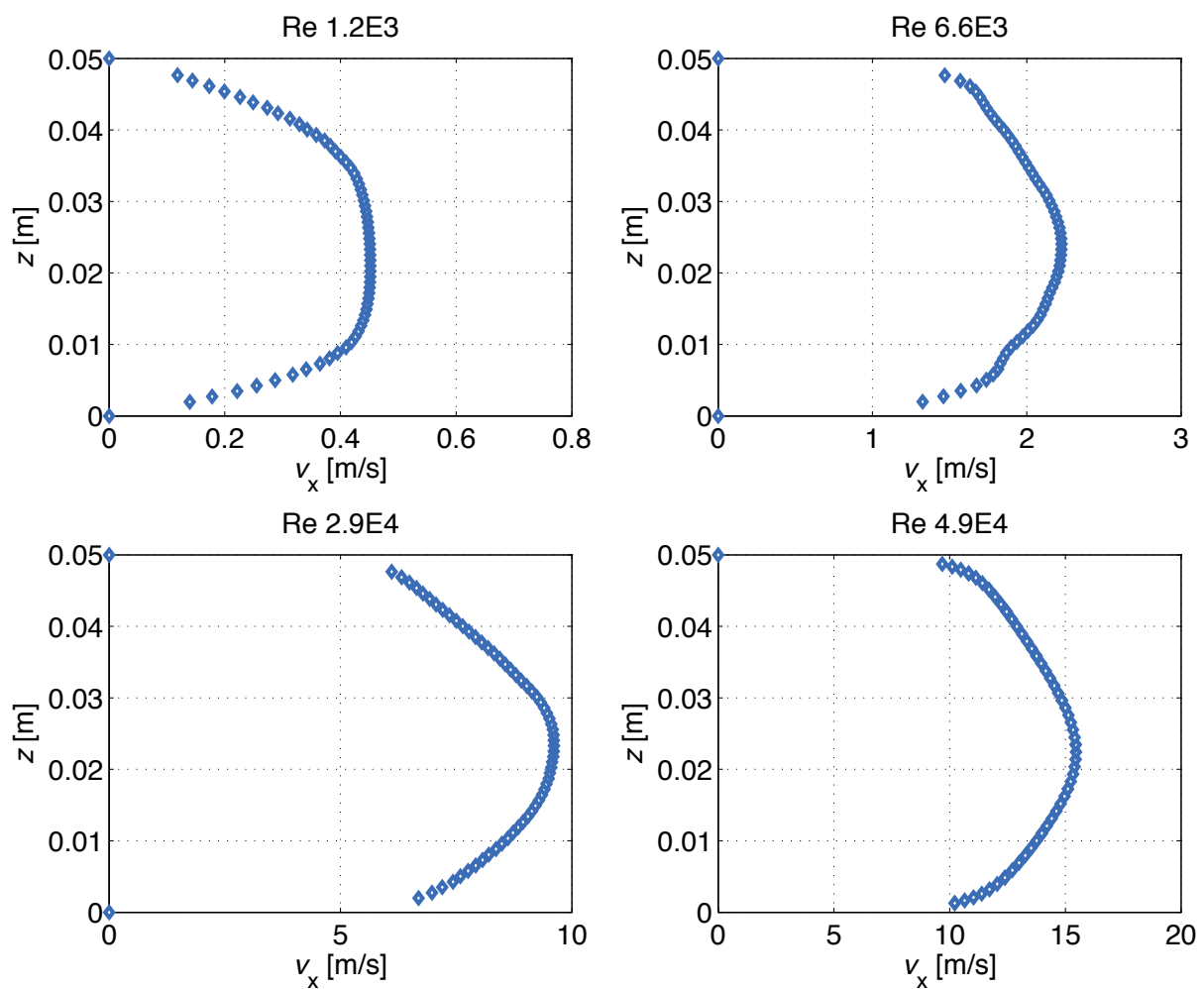


Figure A.1: Time and length averaged axial velocity profiles measured by PIV.

The turbulence kinetic energy k is defined by the velocity fluctuations:

$$k = \frac{1}{2} \left(v_x'^2 + v_y'^2 + v_z'^2 \right). \quad (\text{A.1})$$

As the velocity component in y -direction is not measured, it is approximated by:

$$v_y'^2 = \frac{1}{2} v_x'^2 + \frac{1}{2} v_z'^2. \quad (\text{A.2})$$

The turbulent dissipation rate is approximated by an equation derived for 2D PIV data by Delafosse et al. [33]:

$$\epsilon = \nu \left(2 \frac{\partial v_x'^2}{\partial x} + 2 \frac{\partial v_z'^2}{\partial z} + 3 \frac{\partial v_x'^2}{\partial z} + 3 \frac{\partial v_z'^2}{\partial x} + 2 \frac{\partial v_z'}{\partial x} \frac{\partial v_x'}{\partial z} \right). \quad (\text{A.3})$$

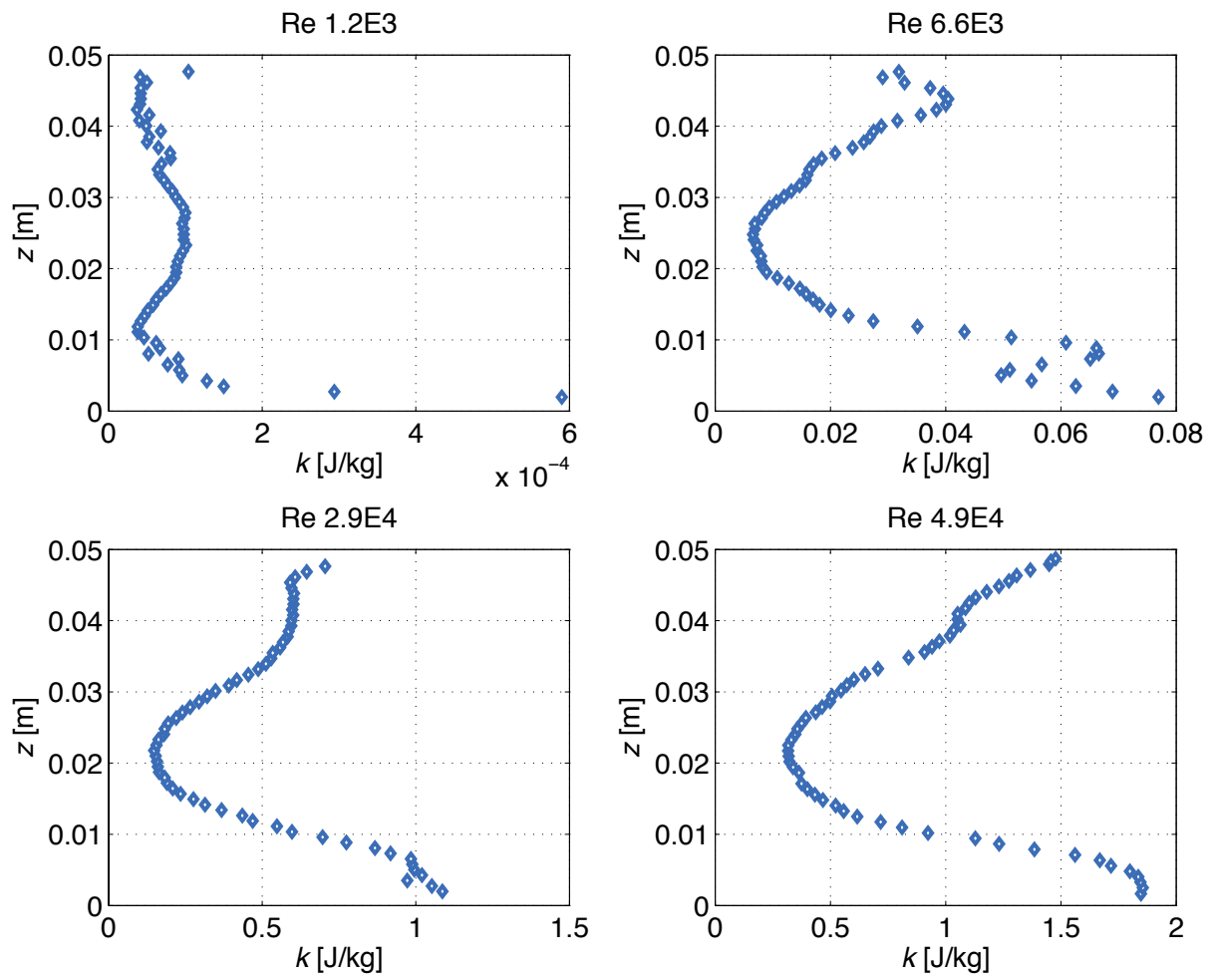


Figure A.2: Time and length averaged turbulent kinetic energy profiles measured by PIV and computed by equation (A.1) and (A.2).

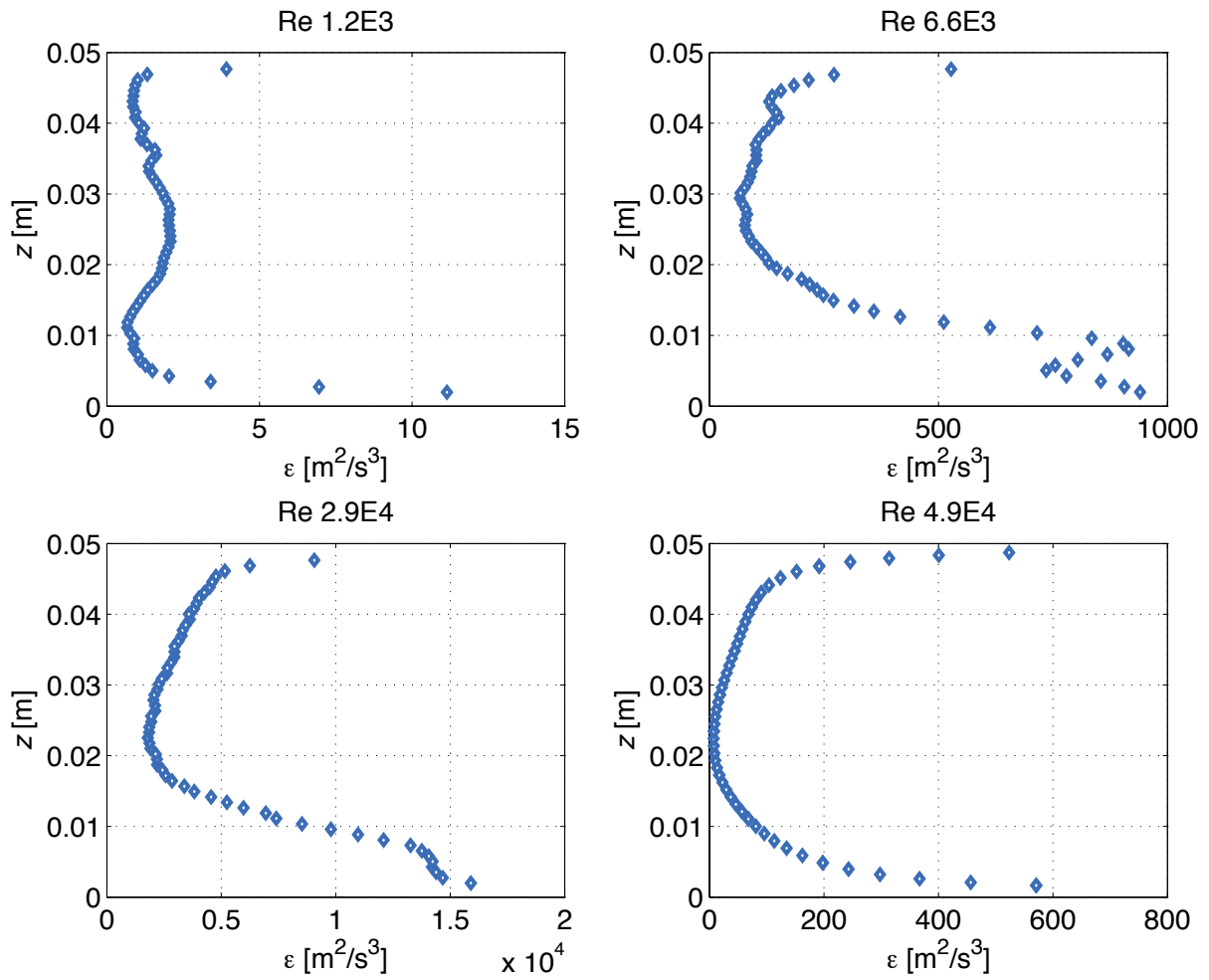


Figure A.3: Time and length averaged turbulent dissipation rate profiles measured by PIV and computed by equation (A.3).

B Measured Light Intensity Distribution

The intensity distribution of the ring lamp, used for the droplet shape and contact angle detection, is measured by a thermal sensor in a plane 85 mm away from the lamp. The broadband absorber thermal sensor (50(150)A-BB-26) from OPHIR OPTONICS with an aperture of 26 mm is used for this measurement. Here the R -coordinate is the radius from the central axis of the ring lamp. As the lamp is positioned perpendicularly above the center of the substrate, the radius of $R = 0$ corresponds to the center of the substrate. The intensity at the substrate is thus almost constant and about 250 W/m^2 . This heat source is assumed to be absorbed with an absorption coefficient of 0.83 and is included as a heat source in the substrate.

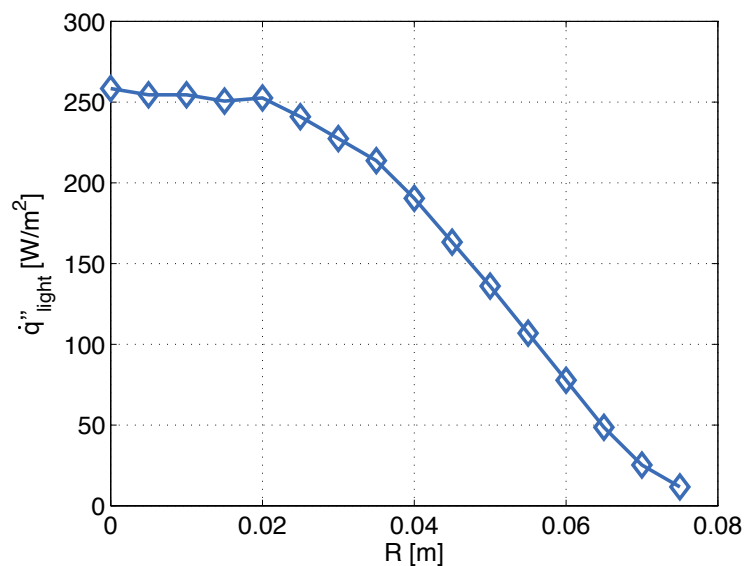


Figure B.1: Measured intensity distribution of the light ring lamp at a plane 85 mm away from the lamp.

C Contact Angle Measurement on Different Substrate Surfaces

In section 2.2.2.3 the described new contact angle measurement method is compared to a conventional method. Both techniques are applied simultaneously, by capturing a single droplet from the side and from perpendicularly above. As the droplet is evaporating slowly, a time series shows the reduction of the contact angle due to contact angle hysteresis. Measurements are performed on a polycarbonate surface (see figure 2.13) on a hydrophobic substrate material (see figures C.2, C.3, C.6 and C.7) and on a hydrophilic substrate material (see figures C.4 and C.5). All measurements confirm a good agreement of the two methods.

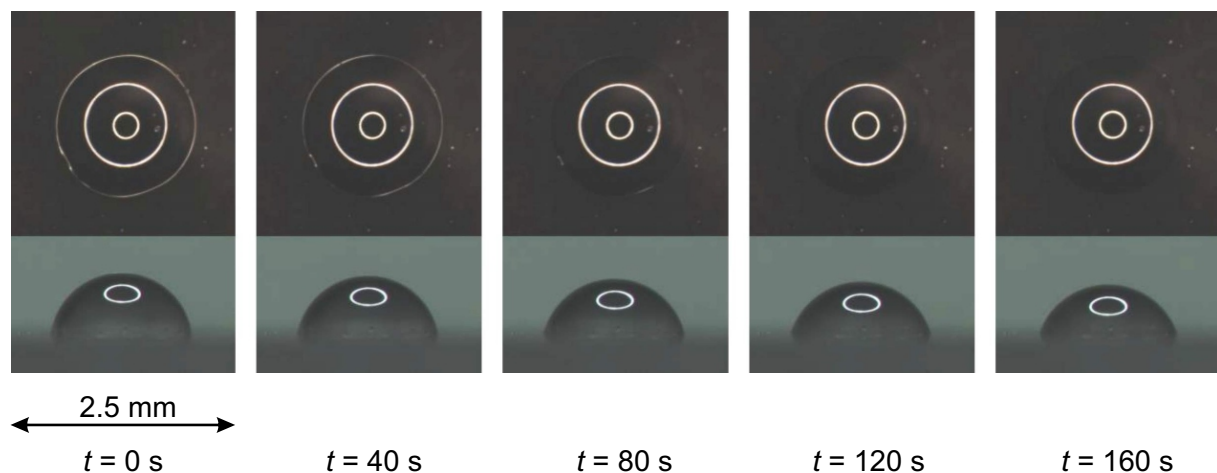


Figure C.1: Single evaporating droplet on a polycarbonate surface viewed from perpendicularly above (upper row) with reflections C_1 , C_2 and partly C_3 and viewed from the side (lower row), $Bo(t = 0) = 0.09$. The corresponding measurement values are depicted in figure 2.13.

In sections 2.2.2.1 and 2.2.2.2, the exact solution algorithm for axisymmetric droplets and the simplified solution algorithm, neglecting gravitational influences, are presented. As most of the investigated droplets are small, ($Bo < 1$),

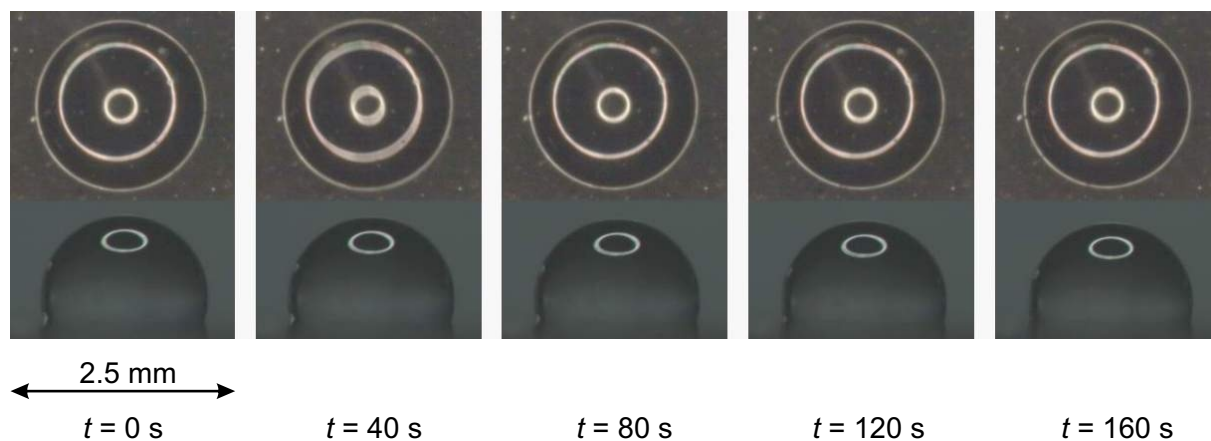


Figure C.2: Single evaporating droplet on a hydrophobic surface viewed from perpendicularly above (upper row) with reflections C_1 , C_2 and C_3 and viewed from the side (lower row), $Bo(t = 0) = 0.12$.

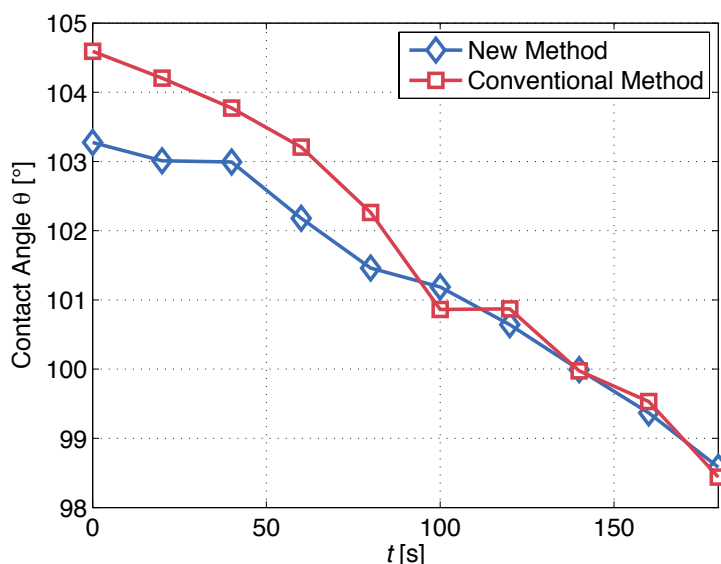


Figure C.3: Contact angle of two simultaneously applied measurement techniques of a droplet on a hydrophobic surface, $Bo(t = 0) = 0.12$.

the drop profile is assumed to be spherical and the simplified equations (2.17) -(2.25) are applied to calculate the drop shape.

For a larger droplet ($Bo \cong 1.7$) with significant influence of gravity, the exact equation (2.8) is solved numerically to determine the shape of the droplet profile as described in section 2.2.2.1. The new contact angle measurement method as well as the conventional method use this droplet profile to find the

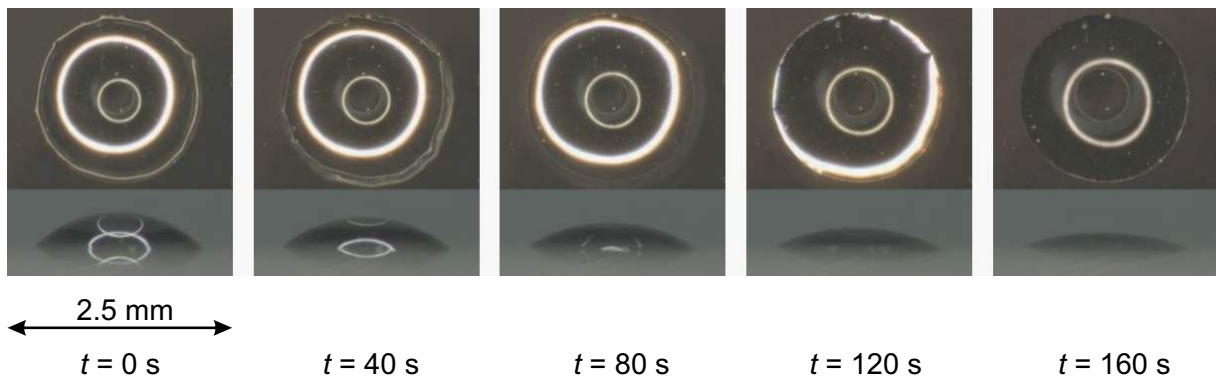


Figure C.4: Single evaporating droplet on a hydrophilic surface viewed from perpendicularly above (upper row) with reflections C_1 and partly C_2 and viewed from the side (lower row), $Bo(t = 0) = 0.25$.

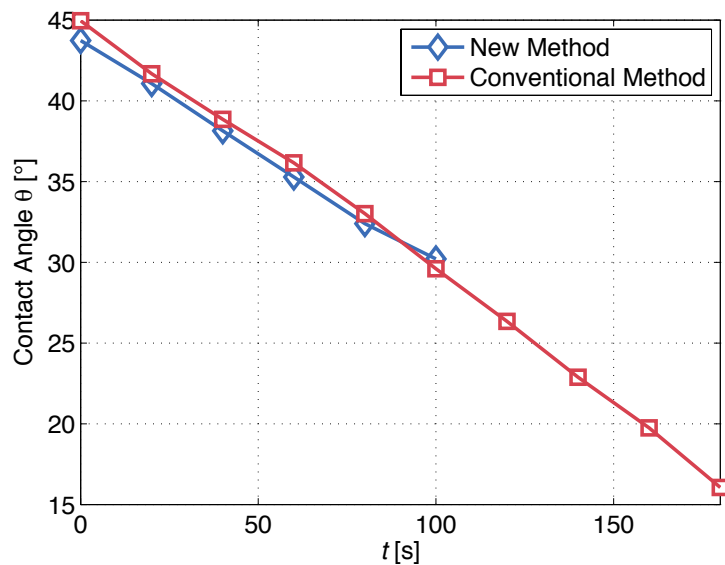


Figure C.5: Contact angle of two simultaneously applied measurement techniques of a droplet on a hydrophilic surface, $Bo(t = 0) = 0.25$. After 100 s, the contact angle is not measurable by the new method, because reflection C_2 is not entirely detectable anymore.

contact angle. As seen in figure C.7, a good agreement between both measurement methods is obtained as well.

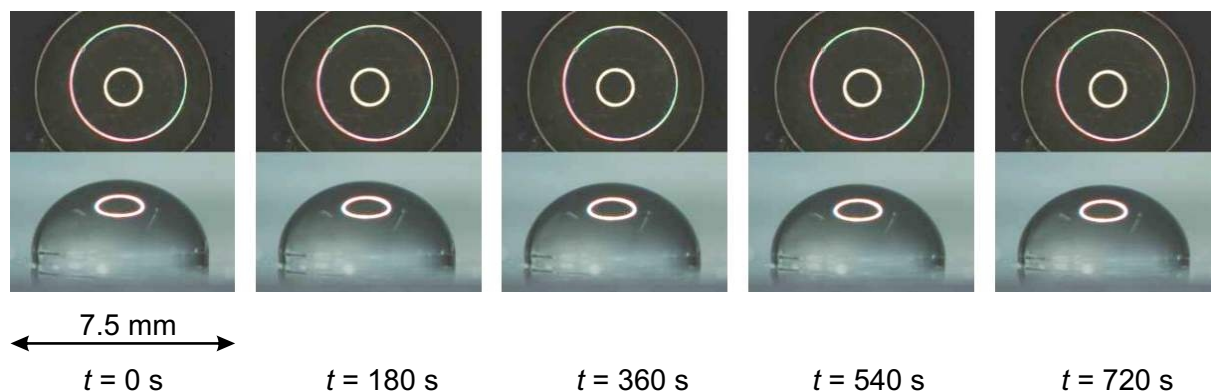


Figure C.6: Large single evaporating droplet on a hydrophobic surface viewed from perpendicularly above (upper row) with reflections C_1 , C_2 and C_3 and viewed from the side (lower row), $Bo(t = 0) = 1.7$.

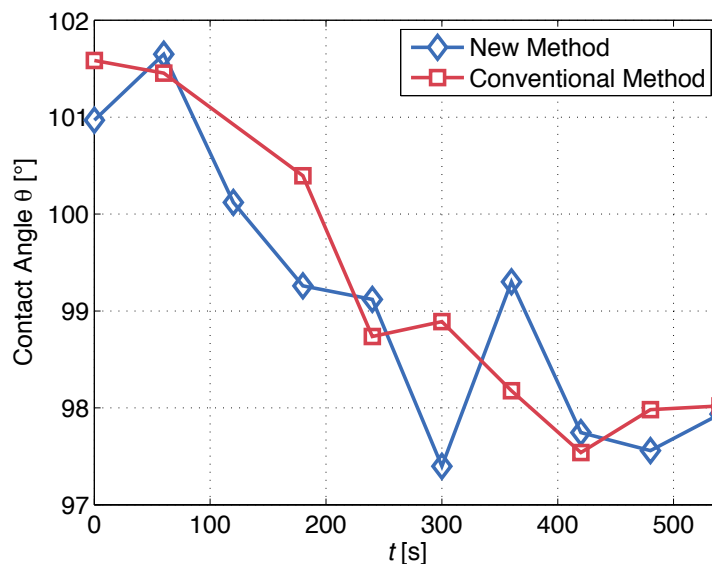


Figure C.7: Contact angle of two simultaneously applied measurement techniques of a droplet on a hydrophobic surface, $Bo(t = 0) = 1.7$.

D Data and Comfort Votes of 22 Test Subjects of the Comfort Study

E Physical Properties of Humid Air

The values applied in the models for the physical properties of humid air are derived from literature-based, temperature dependent correlations. The saturation pressure of water vapor over a liquid water surface is calculated as [135]:

$$p_{v,\text{sat}} = 611.2 \text{ Pa} \cdot e^{\left(\frac{17.62 \cdot T}{(243.12^\circ\text{C} + T)}\right)}, \quad (\text{E.1})$$

and the sublimation pressure of water vapor over an ice surface [135]:

$$p_{v,\text{sat}} = 611.2 \text{ Pa} \cdot e^{\left(\frac{22.46 \cdot T}{(272.62^\circ\text{C} + T)}\right)}. \quad (\text{E.2})$$

The diffusion coefficient of water vapor in air [12]:

$$D_{v,a} = 21.8 \cdot 10^{-6} \frac{101325 \text{ Pa}}{p} \left(\frac{T}{273.15 \text{ K}}\right)^{1.75}. \quad (\text{E.3})$$

The specific heat capacity of the k-th component air [143]:

$$c_{p,k} = \frac{1}{M_k} \sum_{i=1}^{10} a_{k,i} \left(\frac{T}{273.15 \text{ K}}\right)^{b_i}, \quad (\text{E.4})$$

with the coefficients $a_{k,i}$ and b_i defined in table E.1.

Table E.1: Coefficients $a_{k,i}$ and b_i of equation (E.4) [143].

i	$a_{\text{nitrogen},i}$	$a_{\text{oxygen},i}$	$a_{\text{argon},i}$	$a_{\text{water},i}$	b_i
1	2.475830346E6	6.408242565E5	2.078618000E1	-4.747782033E6	0
2	-2.815239891E4	-1.599937045E3	0	4.799919289E4	-1.5
3	1.116401165E5	9.984801256E3	0	-1.931588954E5	-1.25
4	-8.147644187E5	-1.280873444E5	0	1.460728340E6	-0.75
5	2.185120405E6	4.186599156E5	0	-4.000075762E6	-0.5
6	-2.978031305E6	-6.720142804E5	0	5.576209858E6	-0.25
7	-1.308008001E6	-3.799977202E5	0	2.570488297E6	0.25
8	4.305948510E5	1.378691801E5	0	-8.670521019E5	0.5
9	-8.082302563E4	-2.806954185E4	0	1.666429390E5	0.75
10	6.622545214E3	2.459943097E3	0	-1.396634620E4	1

The specific heat capacity of the mixture [143]:

$$c_{p,\text{mix}} = \frac{\sum_{k=1}^N x_k c_{p,k} M_k}{\sum_{k=1}^N x_k M_k}, \quad (\text{E.5})$$

with the molar fractions of the three main components of dry air assumed constant according to DIN ISO 2533 [34] and neglecting other components: $x_{\text{nitrogen}} = 0.781109$, $x_{\text{oxygen}} = 0.209548$ and $x_{\text{argon}} = 0.009343$. And a variable fraction of water vapor x_{water} for the computation of $c_{p,\text{mix}}$ for humid air.

The latent heat of condensation of water [121]:

$$L = \left(2500.8 \frac{\text{kJ}}{\text{kg}} - 2.36 \frac{\text{kJ}}{^\circ\text{C kg}} T + 0.0016 \frac{\text{kJ}}{^\circ\text{C}^2 \text{kg}} T^2 - 0.00006 \frac{\text{kJ}}{^\circ\text{C}^3 \text{kg}} T^3 \right). \quad (\text{E.6})$$

The conductivity of humid air [12]:

$$\lambda_{a,\text{humid}} = \lambda_{a,\text{dry}} \left(1 - \left(1 - 0.706 \frac{1}{\text{K}^{0.4}} T^{0.4} \right) \frac{p_v}{p} \right). \quad (\text{E.7})$$

with the conductivity of dry air [12]:

$$\lambda_{a,dry} = 0.02418 \frac{\text{W}}{\text{mK}} \left(1 + \frac{T}{232^\circ\text{C}} \right)^{0.727}. \quad (\text{E.8})$$

The dynamic viscosity of humid air [12]:

$$\mu_{a,humid} = \mu_{a,dry} \frac{1 - 0.568 \frac{p_v}{p}}{1 - 0.211 \frac{p_v}{p}}, \quad (\text{E.9})$$

with the dynamic viscosity of dry air [12]:

$$\mu_{a,dry} = 17.24 \cdot 10^{-6} \text{ Pa s} \left(1 + \frac{T}{209^\circ\text{C}} \right)^{0.617}. \quad (\text{E.10})$$

F Vehicle Parts, Assumed Material Layers and Physical Properties of the Generic Vehicle Cabin Model

	Textile	Steel	Polyethylen	Foam	PUR	Varnish	Glass	Low-e coating	Polycarbonate
λ [W/(mK)]	0,059	14,65	0,35	0,03	0,03	0,35	1,16	1,16	0,2
c [J/kgK]	1260	502	2300	1670	1500	2300	800	800	1170
ρ [kg/m ³]	81	7800	920	80	50	920	2480	2480	1200
ε [-]	0,9	0,26	0,9	0,9	0,8	0,95	0,88	0,3	0,9

Figure F.1: Assumed constant material properties of the cabin structure layers.

F Vehicle Parts, Assumed Material Layers and Physical Properties of the Generic Vehicle Cabin Model

Vehicle Part	Area [m ²]	# Layers	Material 1	H 1 [mm]	Material 2	H 2 [mm]	Material 3	H 3 [mm]	Material 4	H 4 [mm]	Material 5	H 5 [mm]	Material 6	H 6 [mm]
Front seats left/right	0.9/0.9	3	Textile	2	Foam	152	Textile	1						
dashboard & center console	2.4	1	Polyethylen	50										
Rear Seats	1.4	6	Varnish	0.1	Steel	0.6	Air gap	300	Steel	0.6	Foam	150	Textile	1
Backlight shelf	0.7	5	Varnish	0.1	Steel	0.6	Air gap	300	Polyethylen	5	Textile	1		
footwell left right	0.5/0.5	6	Varnish	0.1	Steel	0.6	Air gap	100	PUR	10	Foam	5	Textile	1
Roof	1.6	5	Varnish	0.1	Steel	0.6	Air gap	10	Foam	5	Textile	1		
Floor	1.8	4	Varnish	0.1	Steel	1	Polyethylen	10	Textile	5				
Door left/right	1.3/1.3	6	Varnish	0.1	Steel	0.6	Air gap	80	Steel	0.6	PUR	15	Polyethylen	3
A-pillar left right	0.06/0.06	6	Varnish	0.1	Steel	0.6	Air gap	30	Steel	0.6	Foam	5	Textile	1
B-pillar left right	0.07/0.07	6	Varnish	0.1	Steel	0.6	Air gap	30	Steel	0.6	Foam	5	Textile	1
C-pillar left right	0.09/0.09	6	Varnish	0.1	Steel	0.6	Air gap	30	Steel	0.6	Foam	5	Textile	1
Float glazing														
Front window	1.0	1	Glass	4										
Front side window left/right	0.4/0.4	1	Glass	3										
Rear side window left/right	0.3/0.3	1	Glass	3										
Rear window	0.6	1	Glass	3										
Insulated glazing														
Front window	1.0	3	Glass	4	Air gap	5	Glass	3						
Front side window left/right	0.4/0.4	3	Glass	3	Air gap	5	Glass	3						
Rear side window left/right	0.3/0.3	3	Glass	3	Air gap	5	Glass	3						
Rear window	0.6	3	Glass	3	Air gap	5	Glass	3						
Low-e coating														
Front window	1.0	2	Glass	3.9	Low-e	0.1								
Front side window left/right	0.4/0.4	2	Glass	2.9	Low-e	0.1								
Rear side window left/right	0.3/0.3	2	Glass	2.9	Low-e	0.1								
Rear window	0.6	2	Glass	2.9	Low-e	0.1								
PC glazing														
Front window	1.0	1	PC	4										
Front side window left/right	0.4/0.4	1	PC	3										
Rear side window left/right	0.3/0.3	1	PC	3										
Rear window	0.6	1	PC	3										

Figure F2: Parts of the generic vehicle model and assumed material layers including the different glazing options.

Bibliography

- [1] Aceves, S. M., and Smith, J. R., 1998. “A Desiccant Dehumidifier for Electric Vehicle Heating”. *Journal of Energy Resources Technology*, 120(2), pp. 131–136. doi: 10.1115/1.2795023.
- [2] Amirfazli, A., Kwok, D., Gaydos, J., and Neumann, A., 1998. “Line Tension Measurements through Drop Size Dependence of Contact Angle”. *Journal of Colloid and Interface Science*, 205(1), pp. 1–11. doi: 10.1006/jcis.1998.5562.
- [3] ANSI/ASHRAE, 2013. Thermal Environmental Conditions for Human Occupancy, Standard 55-2013.
- [4] ANSYS, I., 2012. ANSYS FLUENT Theory Guide, Release 14.5.
- [5] ANSYS, I., 2012. ANSYS FLUENT User’s Guide, Release 14.5.
- [6] Arici, O., Yang, S., Huang, D., and Oker, E., 1999. “Computer Model for Automobile Climate Control System Simulation and Application”. *International Journal of Thermodynamics*, 2(2), pp. 59–68. doi: 10.5541/ijot.1034000014.
- [7] Arndt, M., Sauer, M., and Wolz, M., 2007. “Verbrauchssenkung durch verbesserte Klimaanlage-Regelung: Bedarfsgerechte Lüftung mit dem Climate-Control-Sensor”. *ATZ*, 109(5).
- [8] Australian Transport Advisory Council, 1984. Australian Design Rule 15 for Demisting of Windscreens.
- [9] AVL, 2013. AVL FIRE De-icing / De-fogging Module, Version 2013.
- [10] Baehr, H. D., and Stephan, K., 2013. *Wärme- und Stoffübertragung*, 8. ed. Springer, Berlin and Germany. ISBN 9783642365584.
- [11] Bashforth, F., and Adams, J. C., 1883. *An attempt to test the theories of capillary action by comparing the theoretical and measured forms of drops of fluid*. Cambridge University Press.

- [12] Baumgarth, S., Hörner, B., and Reeker, J., 2008. *Handbuch der Klimatechnik*, 5. ed. Müller, Heidelberg. ISBN 3788078200.
- [13] Bernasch, J., Watzenig, D., and Stippel, H., 2010. “Simulationswerkzeuge domänenübergreifend verknüpft”. *ATZextra*, pp. 58–63. doi: 10.1365/s35778-010-0425-x.
- [14] Beysens, D., 1995. “The formation of dew”. *Atmospheric Research*, 39(1-3), pp. 215–237. doi: 10.1016/0169-8095(95)00015-J.
- [15] Beysens, D., Steyer, A., Guenoun, P., Fritter, D., and Knobler, C. M., 1991. “How does dew form?”. *Phase Transitions*, 31(1-4), pp. 219–246. doi: 10.1080/01411599108206932.
- [16] Bharathan, D., Chaney, L., Farrington, R. B., Lustbader, J., Keyser, M., and Rugh, J., 2007. “An Overview of Vehicle Test and Analysis Results from NREL’s A/C Fuel Use Reduction Research”. In 8th Vehicle Thermal Management Systems, Nottingham, UK.
- [17] Birdi, K. S., Vu, D. T., and Winter, A., 1989. “A Study of the Evaporation Rates of Small Water Drops Placed on a Solid Surface”. *The Journal of Physical Chemistry*, 93(9), pp. 3702–3703. doi: 10.1021/j100346a065.
- [18] Bohman, C., Lorenz, M., Hörth, L., Sattelmayer, T., Bouvy, C., Jeck, P., Eckstein, L., and Schüssler, M., 2012. “Thermal Management for EV – Solutions and Implementation within the Research Project ‘E Performance’”. In Aachen Colloquium Automobile and Engine Technology, Germany.
- [19] Böttcher, C., 2006. “Wasserspeicherung in einem Pkw-Klimagerät”. PhD thesis, Technischen Universität Carolo-Wilhelmina zu Braunschweig, Germany.
- [20] Bresenham, J., 1977. “A linear algorithm for Incremental Digital Display of Circular Arcs”. *Communications of the ACM*, 20(2), pp. 100–106. doi: 10.1145/359423.359432.
- [21] Brinkkoetter, C., and Ackermann, J., 2010. “Energiesparendes Wohlfühlklima: Klimakomfort durch insassenselektives Heizen”. *automotion IAV Kundenmagazin*, 2010(03).
- [22] Brunberg, J., and Aspelin, M., 2011. “CFD Modelling of Headlamp Condensation”. Master’s thesis, Chalmers University of Technology, Göteborg.

- [23] Carey, V. P., 2008. *Liquid-vapor phase-change phenomena: An introduction to the thermophysics of vaporization and condensation processes in heat transfer equipment*, 2. ed. Taylor and Francis, New York and NY and USA. ISBN 1591690358.
- [24] CD ADAPCO, 2013. User Guide STAR-CCM+, Version 8.02.
- [25] Chandra, S., Di Marzo, M., Qiao, Y., and Tartarini, P., 1996. “Effect of Liquid-Solid Contact Angle on Droplet Evaporation”. *Fire Safety Journal*, 27(2), pp. 141–158. doi: 10.1016/S0379-7112(96)00040-9.
- [26] Chen, Q., 1995. “Comparison of Different $k-\epsilon$ Models for Indoor Air Flow Computations”. *Numerical Heat Transfer, Part B: Fundamentals*, 28(3), pp. 353–369. doi: 10.1080/10407799508928838.
- [27] Chiou, J. P., 1986. “Application of Solar-Powered Ventilator in Automobiles”. *SAE Technical Paper*, 860585. doi: 10.4271/860585.
- [28] Chung, B.-J., Kim, M. C., and Ahmadinejad, M., 2008. “Film-Wise and Drop-Wise Condensation of Steam on Short Inclined Plates”. *Journal of Mechanical Science and Technology*, 22(1), pp. 127–133. doi: 10.1007/s12206-007-1015-8.
- [29] Croce, G., D’Agaro, P., Angelis, A. d., and Mattiello, F., 2007. “Numerical Simulation of Windshield Defogging Process”. *Proceedings of the Institution of Mechanical Engineers, Part D: Journal of Automobile Engineering*, 221(10), pp. 1241–1250. doi: 10.1243/09544070JAUTO132.
- [30] Croce, G., D’Agaro, P., and Della Mora, F., 2005. “Numerical Simulation of Glass Fogging and Defogging”. *International Journal of Computational Fluid Dynamics*, 19(6), pp. 437–445. doi: 10.1080/10618560500233479.
- [31] Croce, G., D’Agaro, P., Mattiello, F., and Angelis, A. d., 2014. “A Numerical Procedure for Defogging Process Simulation in Automotive Industry”. In *WSEAS International Conference on Heat and Mass Transfer*, Corfu, Greece.
- [32] de Candido, E., Croce, G., and D’Agaro, P., 2012. “Droplet Buildup and Water Retention Prediction in Condensation Processes”. *Heat Transfer Engineering*, 33(13), pp. 1130–1137. doi: 10.1080/01457632.2012.663687.

- [33] Delafosse, A., Collignon, M.-L., Crine, M., and Toye, D., 2011. “Estimation of the Turbulent Kinetic Energy Dissipation Rate from 2D-PIV Measurements in a Vessel Stirred by an Axial Mixel TTP Impeller”. *Chemical Engineering Science*, 66(8), pp. 1728–1737. doi: 10.1016/j.ces.2011.01.011.
- [34] Deutsches Institut für Normung e.V, 1979. Normatmosphäre, DIN ISO 2533.
- [35] Deutsches Institut für Normung e.V, 2006. Ergonomie der thermischen Umgebung – Analytische Bestimmung und Interpretation der thermischen Behaglichkeit durch Berechnung des PMV- und des PPD-Indexes und Kriterien der lokalen thermischen Behaglichkeit (ISO 7730:2005); Deutsche Fassung EN ISO 7730:2005, DIN EN ISO 7730.
- [36] Deutsches Institut für Normung e.V, 2006. Raumluftechnik, Teil 3: Klimatisierung von Personenkraftwagen und Lastkraftwagen, DIN 1946-3.
- [37] Deutsches Institut für Normung e.V, 2007. Ergonomie der thermischen Umgebung – Beurteilung der thermischen Umgebung in Fahrzeugen – Teil 2: Bestimmung der Äquivalenttemperatur, 14505-2.
- [38] Deutsches Institut für Normung e.V, 2011. Glas im Bauwesen – Bestimmung des Wärmedurchgangskoeffizienten (U-Wert) – Berechnungsverfahren, DIN EN 673.
- [39] Dömök, S., 1998. “Klimatisierung Fahrzeuginnenraum mit INKA/TILL unter Berücksichtigung der Behaglichkeit von Insassen”. In *Wärmemanagement des Kraftfahrzeugs*, N. Deußen, ed., Vol. 1. Expert Verlag, Renningen and Germany.
- [40] Doroudian, M., 2004. “Numerical Simulation of Automobile Windshield Defogging”. In ANSYS International Conference, Pittsburgh, PA, USA.
- [41] Drelich, J., Miller, J. D., and Good, R. J., 1996. “The Effect of Drop (Bubble) Size on Advancing and Receding Contact Angles for Heterogeneous and Rough Solid Surfaces as Observed with Sessile-Drop and Captive-Bubble Techniques”. *Journal of Colloid and Interface Science*, 179(1), pp. 37–50. doi: 10.1006/jcis.1996.0186.
- [42] ERGONSIM, 2013. FPC-Model User Manual, Version 2.5.
- [43] Europäische Kommission. Verordnung (EU) Nr. 672/2010 der Kommission vom 27. Juli 2010 über die Typgenehmigung von Entfrostsungs- und

Trocknungsanlagen bestimmter Kraftfahrzeuge und zur Durchführung der Verordnung (EG) Nr. 661/2009 des Europäischen Parlaments und des Rates über die Typgenehmigung von Kraftfahrzeugen, Kraftfahrzeuganhängern und von Systemen, Bauteilen und selbstständigen technischen Einheiten für diese Fahrzeuge hinsichtlich ihrer allgemeinen Sicherheit.

- [44] Family, F., and Meakin, P., 1989. “Kinetics of Droplet Growth Processes: Simulations, Theory, and Experiments”. *Physical Review A*, 40(7), pp. 3836–3854. doi: 10.1103/PhysRevA.40.3836.
- [45] Fanger, P. O., 1970. *Thermal Comfort: Analysis and Applications in Environmental Engineering*. McGraw-Hill, New York and NY and USA. ISBN 0-07-019915-9.
- [46] Fayazbakhsh, M., and Bahrami, M., 2013. “Analytical Modeling of Mist Condensation by Natural Convection Over Inclined Flat Surfaces”. In ASME 2013 Heat Transfer Summer Conference collocated with the ASME 2013 7th International Conference on Energy Sustainability and the ASME 2013 11th International Conference on Fuel Cell Science, Engineering and Technology, Minneapolis, MN, US. ISBN 0791855473.
- [47] Fayazbakhsh, M. A., and Bahrami, M., 2013. “Comprehensive Modeling of Vehicle Air Conditioning Loads Using Heat Balance Method”. *SAE Technical Paper*, 2013-01-1507. doi: 10.4271/2013-01-1507.
- [48] Fiala, D., 1998. “Dynamic Simulation of Human Heat Transfer and Thermal Comfort”. PhD thesis, De Montfort University Leicester, UK.
- [49] Fiala, D., Havenith, G., Bröde, P., Kampmann, B., and Jendritzky, G., 2012. “UTCI-Fiala Multi-Node Model of Human Heat Transfer and Temperature Regulation”. *International Journal of Biometeorology*, 56(3), pp. 429–441. doi: 10.1007/s00484-011-0424-7.
- [50] Fiala, D., Lomas, K. J., and Stohrer, M., 1999. “Computer Prediction of Human Thermoregulatory and Temperature Responses to a Wide Range of Environmental Conditions: The Passive System”. *Journal of Applied Physiology*, 87(5), pp. 1957–1972.
- [51] Fiala, D., Lomas, K. J., and Stohrer Martin, 2001. “Computer Prediction of Human Thermoregulatory and Temperature Responses to a Wide Range of Environmental Conditions”. *International Journal of Biometeorology*, 45(3), pp. 143–159. doi: 10.1007/s004840100099.

- [52] Fiala, D., Lomas, K. J., and Stohrer Martin, 2003. “First Principles Modelling of Thermal Sensation Responses in Steady State and Transient Boundary Conditions”. *ASHRAE Transactions*, 109(1), pp. 179–186.
- [53] Fiala, D., Psikuta, A., Jendritzky, G., Paulke, S., Nelson, D. A., van Marken Lichtenbelt, W. D., and Frijns, A. J., 2010. “Physiological Modelling for Rechnical, Clinical and Research Applications”. *Frontiers in Bioscience*, S2(1), pp. 939–968. doi: 10.2741/S112.
- [54] Flieger, B., 2013. “Innenraummodellierung einer Fahrzeugkabine in der Programmiersprache Modelica”. PhD thesis, RWTH Aachen University, Germany.
- [55] Flieger, B., Streblow, R., and Müller, D., 2012. “Thermisches Pkw-Innenraum-Modell”. In *Wärmemanagement des Kraftfahrzeugs*, P. Steinberg, ed., Vol. 8. Expert Verlag, Renningen and Germany. ISBN 3816931456.
- [56] Frank, W., 1971. “Fragen der Beheizung und Belüftung von Kraftfahrzeugen”. *ATZ*, 73(8), pp. 369–376.
- [57] Frank, W., 1975. *Raumklima und thermische Behaglichkeit: Literaturauswertung durchgeführt im auftrage des Bundesministers für Raumordnung, Bauwesen und Städtebau*, Vol. 104 of *Berichte aus der Bau-forschung*. W. Ernst, Berlin. ISBN 3433007314.
- [58] Fritter, D., Knobler, C. M., Roux, D., and Beysens, D., 1988. “Computer Simulations of the Growth of Breath Figures”. *Journal of Statistical Physics*, 52(5-6), pp. 1447–1459. doi: 10.1007/BF01011659.
- [59] Ganzevles, F., and Geld, C. v. d., 1998. “Heat and Mass Transfer From Internal Flows to Hemispheres and Flat Parts in Between”. *International Journal of Heat and Mass Transfer*, 41(23), pp. 3705–3718. doi: 10.1016/S0017-9310(98)00117-3.
- [60] Garabedian, H., and Heafitz, A., 1997. “State of the Art Electric Vehicle Cold Weather Range”. *SAE Technical Paper*, 971627. doi: 10.4271/971627.
- [61] Gasworth, S., and Tankala, T., 2011. “Reduced Steady State Heating and Air Conditioning Loads via Reduced Glazing Thermal Conductivity”. *SAE Technical Paper*, 2011-01-0126. doi: 10.4271/2011-01-0126.

- [62] Gaydos, J., and Neumann, A., 1987. “The Dependence of Contact Angles on Drop Size and Line Tension”. *Journal of Colloid and Interface Science*, 120(1), pp. 76–86. doi: 10.1016/0021-9797(87)90324-9.
- [63] Gibbs, J. W., 1874-1878. “On the Equilibrium of Heterogeneous Substances”. *Transactions of the Connecticut Academy of Arts and Sciences*, 3, pp. 109–248; 344–524.
- [64] Glühmann, C., and Pahlke, J., 2001. “Verfahren zur Prognose der Wasserdampfkondensation an den Fensterflächen eines Kraftfahrzeuges”. *Technisches Messen*, 68(10), pp. 473–480.
- [65] Gnielinski, V., 2006. “Wärmeübertragung bei der Strömung durch Rohre”. In *VDI-Wärmeatlas*. Springer, Berlin and Germany, p. Ga5. ISBN 3540322183.
- [66] Grigull, U., and Tratz, H., 1965. “Thermischer Einlauf in ausgebildeter laminarer Rohrströmung”. *International Journal of Heat and Mass Transfer*, 8(5), pp. 669–678. doi: 10.1016/0017-9310(65)90016-5.
- [67] Großmann, H., 2010. *Pkw-Klimatisierung: Physikalische Grundlagen und technische Umsetzung*, 1. ed. VDI-Buch. Springer, Berlin and Germany. ISBN 3642054951.
- [68] Hörth, L., Spinnler, M., and Sattelmayer, T., 2011. “Wärmepumpentechnik in Elektrofahrzeugen”. In DKV-Tagung, Aachen, Germany.
- [69] Jung, S., Lee, C., and Jang, K., 2009. “Automatisches Windschutzscheiben-Antibeslagsystem im Hyundai Genesis”. *ATZ*, 111(3), pp. 196–201. doi: 10.1007/BF03222059.
- [70] Käfer, O., 1998. “PKW-Klimatisierung – Umluftautomatik mit Feuchteregelung im Fahrzeugraum”. *ATZ*, 100(6), pp. 436–443.
- [71] Kestin, J., and Richardson, P., 1963. “Heat Transfer Across Turbulent, Incompressible Boundary Layers”. *International Journal of Heat and Mass Transfer*, 6(2), pp. 147–189. doi: 10.1016/0017-9310(63)90035-8.
- [72] Kitada, M., Asano, H., Kataoka, T., Hirayama, S., and Maruta, Y., 2003. “Prediction Technology of Transient Defogging Pattern by CFD”. *Denso Technical Review*, 8(2), pp. 126–130.
- [73] Klan, H., 2006. “Wärmeübergang durch freie Konvektion an umströmten Körpern”. In *VDI-Wärmeatlas*. Springer, Berlin and Germany, p. Fa. ISBN 3540322183.

- [74] Klan, H., 2006. “Wärmeübertragung durch freie Konvektion in geschlossenen Fluidschichten”. In *VDI-Wärmeatlas*. Springer, Berlin and Germany, p. Fc1. ISBN 3540322183.
- [75] Klassen, V., Leder, M., and Hossfeld, J., 2011. “Klimatisierung im Elektrofahrzeug”. *ATZ*, 113(2), pp. 118–123. doi: 10.1365/s35148-011-0029-9.
- [76] Krischer, S., 1970. “Mikroskopische Untersuchung der Tropfenkondensation”. PhD thesis, Technische Universität München, Germany.
- [77] Larson, W. J., and Pranke, L. K., 2007. *Human Spaceflight: Mission Analysis and Design*. Space technology series. McGraw-Hill, New York and NY and USA. ISBN 9780077230289.
- [78] Leach, R. N., Stevens, F., Langford, S. C., and Dickinson, J. T., 2006. “Dropwise condensation: Experiments and Simulations of Nucleation and Growth of Water Drops in a Cooling System”. *Langmuir : the ACS journal of surfaces and colloids*, 22(21), pp. 8864–8872. doi: 10.1021/la061901+.
- [79] Lee, C., Kwon, J., Lee, Y., and Park, J., 2012. “Optimised Air-Conditioning System for Increased Range of Electric Vehicles”. *ATZ*, 114(06), pp. 22–27. doi: 10.1365/s35595-012-0118-8.
- [80] Lee, H., Alcaraz, M. L., Rubner, M. F., and Cohen, R. E., 2013. “Zwitter-Wettability and Antifogging Coatings with Frost-Resisting Capabilities”. *ACS nano*, 7(3), pp. 2172–2185. doi: 10.1021/nn3057966.
- [81] Leipertz, A., 2006. “Tropfenkondensation”. In *VDI-Wärmeatlas*. Springer, Berlin and Germany, p. Jc1. ISBN 3540322183.
- [82] Li, D., 1996. “Drop Size Dependence of Contact Angles and Line Tensions of Solid-Liquid Systems”. *Colloids and Surfaces A: Physicochemical and Engineering Aspects*, 116(1-2), pp. 1–23. doi: 10.1016/0927-7757(96)03582-0.
- [83] LMU Fakultät für Physik, Meteorologie. Meteorologisches Institut Garching, Oskar von Miller Turm. <http://www.meteo.physik.uni-muenchen.de/dokuwiki/doku.php?id=wetter:garching:neu>. Visited at start of experimental runs.
- [84] Lorenz, M., 2011. “Heating and Cooling of Passenger Cabins: An Analysis of the Saving Potential”. In International Conference on Thermal Management for EV/HEV, Darmstadt, Germany.

- [85] Lorenz, M., 2013. *Einfluss der Oberflächenrauigkeit auf den Wärmeübergang und die aerodynamischen Verluste einer Gasturbinenbeschaufelung: Experimentelle Untersuchungen und Entwicklung einer Korrelation für den laminar-turbulenten Umschlag*. Logos Verlag, Berlin and Germany. ISBN 9783832535650.
- [86] Lorenz, M., 2015. Verfahren und Vorrichtung zur Bestimmung einer Eigenschaft eines Objekts, Patent DE 102013111780 A1.
- [87] Lorenz, M., Fiala, D., Spinnler, M., and Sattelmayer, T., 2014. “A Coupled Numerical Model to Predict Heat Transfer and Passenger Thermal Comfort in Vehicle Cabins”. *SAE Technical Paper*, 2014-01-0664. doi: 10.4271/2014-01-0664.
- [88] Lorenz, M., Spinnler M., and Sattelmayer, T., 2012. “Reduzierung des Heizbedarfs von Elektrofahrzeugkabinen durch alternative Scheibentechnik”. In *Wärmemanagement des Kraftfahrzeugs*, P. Steinberg, ed., Vol. 8. Expert Verlag, Renningen and Germany. ISBN 3816931456.
- [89] Marchand, A., Weijs, J. H., Snoeijer, J. H., and Andreotti, B., 2011. “Why is Surface Tension a Force Parallel to the Interface?”. *American Journal of Physics*, 79(10), p. 999. doi: 10.1119/1.3619866.
- [90] Meakin, P., 1992. “Droplet Deposition Growth and Coalescence”. *Reports on Progress in Physics*, 55(2), pp. 157–240. doi: 10.1088/0034-4885/55/2/002.
- [91] Megyesi, P., Roth, M., and Gauterin, F., 2011. “Solar Roof Panel Application to Support the Vehicle Power Supply and Reduce Fuel Consumption”. In International Scientific Conference on Hybrid and Electric Vehicles, Rueil-Malmaison, France.
- [92] Messinger, B., 1953. “Equilibrium Temperature of an Unheated Icing Surface as a Function of Air Speed”. *Journal of the Aeronautical Sciences (Institute of the Aeronautical Sciences)*, 20(1), pp. 29–42. doi: 10.2514/8.2520.
- [93] Mladenov, N., 06.07.2012. Defogging Modell - Fluent 6.3: Personal Communication.
- [94] Mora, L., Gadgil, A. J., and Wurtz, E., 2003. “Comparing Zonal and CFD Model Predictions of Isothermal Indoor Airflows to Experimental Data”. *Indoor Air*, 13(2), pp. 77–85. doi: 10.1034/j.1600-0668.2003.00160.x.

- [95] Morena, M. R., Krah, R., and Kurz, B., 2012. "Nutzerempfinden des Klimakomforts von Fahrzeugsitzen". *ATZ*, 114(6), pp. 478–485. doi: 10.1007/s35148-012-0360-9.
- [96] Nasr, K. J., and AbdulNour, B. S., 2000. "Defrosting of Automotive Windshields: Progress and Challenges". *International Journal of Vehicle Design*, 23(3/4), pp. 360–375.
- [97] Nič, M., Jirát, J., Košata, B., Jenkins, A., and McNaught, A., 2009. *IUPAC Compendium of Chemical Terminology*. IUPAC, Research Triangle Park and NC and USA. ISBN 0-9678550-9-8. doi: 10.1351/goldbook.
- [98] Nie, M., Patel, P., Sun, K., and Meng, D. D., 2009. "Superhydrophilic Anti-Fog Polyester Film by Oxygen Plasma Treatment". In 4th IEEE International Conference on Nano/Micro Engineered and Molecular Systems, Shenzhen, China, pp. 1017–1020. doi: 10.1109/NEMS.2009.5068746.
- [99] Nitz, J., and Hucho, W.-H., 1979. "The Heat Transfer Coefficient of a Passenger Car's Body". *SAE Technical Paper*, 790399. doi: 10.4271/790399.
- [100] Nonoyama, H., Kawai, T., Muraki, T., Takechi, T., Yokoi, J., and Mimoto, M., 2000. Air Conditioning Apparatus for Vehicle with Double Layer Flow Mode, Patent US6135201 A. <http://www.google.com/patents/US6135201>. Last visited 02/18/2015.
- [101] Norin, F., 1989. "Insulating Glazing in Side Windows". *SAE Technical Paper*, 890025. doi: 10.4271/890025.
- [102] Nuraje, N., Asmatulu, R., Cohen, R. E., and Rubner, M. F., 2011. "Durable Antifog Films from Layer-by-Layer Molecularly Blended Hydrophilic Polysaccharides". *Langmuir : the ACS journal of surfaces and colloids*, 27(2), pp. 782–791. doi: 10.1021/la103754a.
- [103] OPEC, 2013. Annual Statistical Bulletin. http://www.opec.org/opec_web/static_files_project/media/downloads/publications/ASB2013.pdf. Last visited 01/28/2015.
- [104] OPEC, 2013. World Oil Outlook. http://www.opec.org/opec_web/static_files_project/media/downloads/publications/WOO_2013.pdf. Last visited 01/28/2015.
- [105] Organization for Economic Co-operation and Development, 2013. *World Energy Outlook 2013*. OECD/IEA, Paris and France. ISBN 9264201300.

- [106] Oxford Dictionaries, 2013. <http://www.oxforddictionaries.com/definition/english/mobility>. Last visited 01/28/2015.
- [107] Pattikonda, R., 2008. Vehicle Shading System and Method Using an Electrically Controlled Transmission Control Material, Patent US2008/0007086 A1.
- [108] Paulke, S., and Kreppold, E., 2008. “The Application of Thermal Simulation Techniques for Seat Comfort Optimizations”. In SIMVEC 14. Konferenz und Fachausstellung Berechnung und Simulation Fahrzeugbau, VDI Berichte 2031, Baden-Baden, Switzerland.
- [109] Pérez-Díaz, J. L., Álvarez-Valenzuela, M. A., and García-Prada, J. C., 2012. “The Effect of the partial pressure of water vapor on the surface tension of the liquid water-air interface”. *Journal of Colloid and Interface Science*, 381(1), pp. 180–182. doi: 10.1016/j.jcis.2012.05.034.
- [110] Peters, A. R., 1972. “Interior Window Fogging – An Analysis of the Parameters Involved”. *SAE Technical Paper*, 720503. doi: 10.4271/720503.
- [111] Pethica, B. A., 1977. “The Contact Angle Equilibrium”. *Journal of Colloid and Interface Science*, 62(3), pp. 567–569. doi: 10.1016/0021-9797(77)90110-2.
- [112] Petr, P., Mustafa, R., and Schulze, M., 2012. “Energieverbrauchs- und Klimakomfortbewertung mittels Gesamtfahrzeugsimulation”. In *Wärme- management des Kraftfahrzeugs*, P. Steinberg, ed., Vol. 8. Expert Verlag, Renningen and Germany. ISBN 3816931456.
- [113] Polifke, W., and Kopitz, J., 2009. *Wärmeübertragung: Grundlagen, analytische und numerische Methoden*, 2. ed. Pearson, Munich and Germany. ISBN 3827373492.
- [114] Präbst, A., Lorenz, M., Hörth, L., Janta, M., Schulze-Ardey, J., Bengler, K., and Sattelmayer, T., 2014. “Forschungsprojekt Visio.M: Thermisches Gesamtkonzept und optimierte Klimaregelung”. *ATZextra*, 19(14), pp. 34–39. doi: 10.1365/s35778-014-1355-9.
- [115] Prandtl, L., 1933. “Neuere Ergebnisse der Turbulenzforschung”. *Zeitschrift des Vereines deutscher Ingenieure*, 7(5), pp. 105–114.
- [116] P+Z ENGINEERING. Theseus FE Product Brochure. http://www.theseus-fe.com/images/downloads/product_flyers/theseusfe_product_brochure.pdf. Last visited 01/28/2015.

- [117] Rat der Europäischen Gemeinschaften, 1978. Richtlinie des Rates vom 21. Dezember 1977 zur Angleichung der Rechtsvorschriften der Mitgliedsstaaten über Entfrostungs- und Trocknungsanlagen für die verglasten Flächen von Kraftfahrzeugen, 78/317/EWG.
- [118] Rauh, H., Krobok, M., and Weiß, M., 2013. Electric Line, Patent US 8456272. <http://www.google.com.ar/patents/US8456272>. Last visited 01/28/2015.
- [119] Recknagel, H., Schramek, E.-R., and Sprenger, E., 2009. *Taschenbuch für Heizung + Klimatechnik 09/10*, 74. ed. Oldenbourg, Munich and Germany. ISBN 9783835631496.
- [120] Richards, T. W., and Carver, E. K., 1921. "A Critical Study of the Capillary Rise Method of Determining Surface Tension with Data for Water, Benzene, Toluene, Chloroform, Carbon Tetrachloride, Ether and Dimethyl Aniline". *Journal of the American Chemical Society*, 43(4), pp. 827–847. doi: 10.1021/ja01437a012.
- [121] Rogers, R. R., and Yau, M. K., 1989. *A Short Course in Cloud Physics*, 3. ed. Pergamon Press, Oxford and UK. ISBN 9780080348636.
- [122] Rotenberg, Y., Boruvka, L., and Neumann, A. W., 1983. "Determination of Surface Tension and Contact Angle from the Shapes of Axisymmetric Fluid Interfaces". *Journal of Colloid and Interface Science*, 93(1), pp. 169–183. doi: 10.1016/0021-9797(83)90396-X.
- [123] Roy, S., Patel, P., and AbdoulNour, B., 2001. "Heat Transfer on a Vehicle Windshield: An Experimental and Numerical Study". In 35th ASME National Heat Transfer Conference, Anaheim, CA, USA.
- [124] Rugh, J., 2002. "Integrated Numerical Modeling Process for Evaluating Automobile Climate Control Systems". *SAE Technical Paper*, 2002-01-1956. doi: 10.4271/2002-01-1956.
- [125] Rugh, J., and Farrington, R. B., 2008. Vehicle Ancillary Load Reduction Project Close-Out Report: An Overview of the Task and a Compilation of the Research Results, Technical Report NREL/TP-540-42454. <http://www.nrel.gov/docs/fy08osti/42454.pdf>. Last visited 01/28/2015.
- [126] Rugh, J. P., Chaney, L., Lustbader, J., and Meyer, J., 2007. "Reduction in Vehicle Temperatures and Fuel Use from Cabin Ventilation, Solar-Reflective Paint, and a New Solar-Reflective Glazing". *SAE Technical Paper*, 2007-01-1194. doi: 10.4271/2007-01-1194.

- [127] Saad, Sameh Mossaad Iskander, 2012. "Axisymmetric Drop Shape Analysis (ADSA) and Lung Surfactant". PhD thesis, University of Toronto, Canada. <http://hdl.handle.net/1807/31927>.
- [128] Sakamoto, H., Watanabe, T., and Taniguchi, F., 1987. "An Analysis of Frost Formation on Vehicle Windows". *SAE Technical Paper*, 870028. doi: 10.4271/870028.
- [129] Schlichting, H., Krause, E., Gersten, K., and Oertel, H., 2006. *Grenzschicht-Theorie*, 10. ed. Springer, Berlin and Germany. ISBN 9783540230045.
- [130] Schmidt, C., Praster, M., Wölki, D., Wolf, S., and Treck, C. v., 2013. Rechnerische und probandengestützte Untersuchung des Einflusses der Kontaktwärmeübertragung in Fahrzeugsitzen auf die thermische Behaglichkeit, 261 in FAT-Schriftenreihe. <https://www.vda.de/de/services/Publikationen/Publikation.~1197~.html>. Last visited 01/28/2015.
- [131] Schmidt, C., Stratbücker, S., Bolineni, S. R., Norrefeldt, V., Wölki, D., Grün, G., and van Treeck, C., 2011. "Skalen-adaptive Simulation zur Innenraumklimatisierung von E-Fahrzeugen". In *PKW-Klimatisierung*, Mager, ed., 7. Expert Verlag, Renningen and Germany, pp. 24–39. ISBN 978-3-8169-3113-3.
- [132] Sevilgen, G., and Kilic, M., 2010. "Transient Numerical Analysis of Airflow and Heat Transfer in a Vehicle Cabin during Heating Period". *International Journal of Vehicle Design*, 52(1/2/3/4), pp. 144–159. doi: 10.1504/IJVD.2010.029641.
- [133] Shikata, K., Uemura, Y., Ichitani, Y., Uchida, G., and Kato, Y., 1999. "Development of Two Layer Flow HVAC Unit". *SAE Technical Paper*, 1999-01-1199. doi: 10.4271/1999-01-1199.
- [134] Shimizu, S., Hara, H., and Asakawa, F., 1983. "Analysis on Air-Conditioning Heat Load of a Passenger Vehicle". *International Journal of Vehicle Design*, 4(3), pp. 292–311.
- [135] Sonntag, D., 1990. "Important new Values of the Physical Constants of 1986, Vapour Pressure Formulations based on ITS-90, and Psychrometer Formulae". *Zeitschrift für Meteorologie*, 40(5), pp. 340–344.
- [136] Szyszka, B., 2002. "Dünne Schichten auf Autoscheiben – heute und morgen". *Journal für Oberflächentechnik*, 42(9), pp. 82–84.

- [137] Tanabe, S.-i., Kobayashi, K., Nakano, J., Ozeki, Y., and Konishi, M., 2002. "Evaluation of Thermal Comfort Using Combined Multi-Node Thermoregulation (65MN) and Radiation Models and Computational Fluid dynamics (CFD)". *Energy and Buildings*, 34(6), pp. 637–646. doi: 10.1016/S0378-7788(02)00014-2.
- [138] Tanemura, M., 1979. "On Random Complete Packing by Discs". *Annals of the Institute of Statistical Mathematics*, 31(2), pp. 351–365.
- [139] Temming, J. Fahrzeugklimatisierung und Verkehrssicherheit: Auswirkungen sommerlichen Klimas in Kfz auf die Leistungsfähigkeit der Fahrer, 177 in FAT-Schriftenreihe. <https://www.vda.de/de/services/Publikationen/Publikation.~868~.html>. Last visited 01/28/2015.
- [140] Urbank, T. M., 2001. "Development and Application of an Integrated Dew Point and Glass Temperature Sensor". *SAE Technical Paper*, 2001-01-0585. doi: 10.4271/2001-01-0585.
- [141] U.S. Department for Transportation, 1996. Laboratory Test Procedure for FMVSS 103 Windshield Defrosting and Defogging Systems.
- [142] Vargaftik, N. B., Volkov, B. N., and Voljak, L. D., 1983. "International Tables of the Surface Tension of Water". *Journal of Physical and Chemical Reference Data*, 12(3), p. 817. doi: 10.1063/1.555688.
- [143] Verein deutscher Ingenieure, 2003. Thermodynamische Stoffwerte von feuchter Luft und Verbrennungsgasen, VDI 4670.
- [144] Verein deutscher Ingenieure, 2004. Hygiene-Anforderungen an die Lüftungstechnik in Fahrzeugen zur Personenbeförderung, VDI 6032.
- [145] Vitali, D., Györög, T., Wleklik, D., Metz, T., and Lorenz, M., 2014. "Enhancing Users Thermal Comfort by Concurrent Engineering on Thermal Systems and Interiors". In 4th International Conference on Car Interiors: Green and Wellness as Challenges of the Future, Torino, Italy.
- [146] Wang, M., Urbank, T. M., and Sangwan, K. V., 2004. "'Clear Vision' Automatic Windshield Defogging System". *SAE Technical Paper*, 2004-01-1373. doi: 10.4271/2004-01-1373.
- [147] Weijs, J. H., Marchand, A., Andreotti, B., Lohse, D., and Snoeijer, J. H., 2011. "Origin of Line Tension for a Lennard-Jones Nanodroplet". *Physics of Fluids*, 23(2), pp. 022001 1–11. doi: 10.1063/1.3546008.

- [148] Wenzel, H., 1969. “Erweiterte Theorie des Wärmeübergangs bei Tropfenkondensation”. *Wärme- und Stoffübertragung*, 2(1), pp. 6–18. doi: 10.1007/BF00749288.
- [149] White, F. M., 1974. *Viscous Fluid Flow*. McGraw-Hill, New York and NY and USA. ISBN 9780070697102.
- [150] Whyman, G., Bormashenko, E., and Stein, T., 2008. “The Rigorous Derivation of Young, Cassie–Baxter and Wenzel Equations and the Analysis of the Contact Angle Hysteresis Phenomenon”. *Chemical Physics Letters*, 450(4-6), pp. 355–359. doi: 10.1016/j.cplett.2007.11.033.
- [151] Yokoyama, S., Tao, M., and Kakuta, N., 2007. “Prediction Computer Program for Whole Body Temperatures and its Application under Various Working Level and Thermal Environmental Condition Combinations”. *Industrial Health*, 45(1), pp. 118–124. doi: 10.2486/indhealth.45.118.
- [152] Young, T., 1805. “An Essay on the Cohesion of Fluids”. *Philosophical Transactions of the Royal Society of London*, 95(0), pp. 65–87. doi: 10.1098/rstl.1805.0005.
- [153] Yuan, Y., and Lee, T. R., 2013. “Contact Angle and Wetting Properties”. In *Surface Science Techniques*, G. Bracco and B. Holst, eds. Springer, Berlin and Germany, pp. 3–34. ISBN 978-3-642-34242-4. doi: 10.1007/978-3-642-34243-1_1.
- [154] Zhai, Z., Chen, Q., Haves, P., and Klems, J. H., 2002. “On Approaches to Couple Energy Simulation and Computational Fluid Dynamics Programs”. *Building and Environment*, 37(8-9), pp. 857–864. doi: 10.1016/S0360-1323(02)00054-9.
- [155] Zhang, H., 2003. “Human Thermal Sensation and Comfort in Transient and Non-Uniform Thermal Environments”. PhD thesis, University of California, Berkeley and USA.
- [156] Zhang, H., Arens, E., Huizenga, C., and Han, T., 2010. “Thermal Sensation and Comfort models for Non-Uniform and Transient Environments, Part I: Local Sensation of Individual Body Parts”. *Building and Environment*, 45(2), pp. 380–388. doi: 10.1016/j.buildenv.2009.06.018.
- [157] Zhang, H., Arens, E., Huizenga, C., and Han, T., 2010. “Thermal Sensation and Comfort models for Non-Uniform and Transient Environments, Part II: Local Comfort of Individual Body Parts”. *Building and Environment*, 45(2), pp. 389–398. doi: 10.1016/j.buildenv.2009.06.015.

- [158] Zhang, H., Arens, E., Huizenga, C., and Han, T., 2010. “Thermal Sensation and Comfort models for Non-Uniform and Transient Environments, Part III: Whole-Body Sensation and Comfort”. *Building and Environment*, 45(2), pp. 399–410. doi: 10.1016/j.buildenv.2009.06.020.
- [159] Zhang, Z., Zhang, W., Zhai, Z., and Chen, Q. Y., 2007. “Evaluation of Various Turbulence Models in Predicting Airflow and Turbulence in Enclosed Environments by CFD: Part 2 - Comparison with Experimental Data from Literature”. *HVAC&R Research*, 13(6), pp. 871–886. doi: 10.1080/10789669.2007.10391460.
- [160] Zhao, H., and Beysens, D., 1995. “From Droplet Growth to Film Growth on a Heterogeneous Surface: Condensation Associated with a Wettability Gradient”. *Langmuir*, 11(2), pp. 627–634. doi: 10.1021/la00002a045.
- [161] Zolet, T. L., Dutra, G. G., de Freitas Maia, G. F., and Pereira, L. V. M., 2011. “CFD and Experimental Correlation of the Defrost Flow and Vehicle’s windshield Defogging”. In 21st Brazilian Congress of Mechanical Engineering, Cobem, ed., Natal, RN, Brazil.

Supervised Theses

There are a number of different student theses (Semesterarbeiten, Diplomarbeiten, bachelor's theses and master's theses) associated with the research of this thesis. These students' contributions were provided to the Lehrstuhl für Thermodynamik in the years 2010 through 2014 under the close supervision of the author of this Ph.D thesis with regard to all academic, professional, and context-related concerns. Various issues were investigated, contributing to automotive technology and fundamental research issues, in particular window fogging phenomena. Results of the supervised theses were partly included in this Ph.D. thesis. The author would like to express his sincere gratitude to all formerly supervised students for their commitment and support of the research project.

Student	Title
Wiedemann, T.	Klimatisierung von Elektrofahrzeugen: Berechnung des stationären Heiz- und Kühlbedarfs und Energieoptimierung der Karosserie, 2010.
Busl, M.	Design of an Energy-Efficient Climate Control Algorithm for Electric Cars, 2011.
Heipl, T.	Konstruktion eines Versuchsstands und experimentelle Untersuchung der Beschlagsneigung und des Wärmedurchgangs verschiedener Verglasungen für Elektrofahrzeuge, 2011.
Dillis, S.	Untersuchung des Potentials einer Wärmerückgewinnungsanlage für den Fahrgastraum von Kraftfahrzeugen, 2011.

Schweizer, F.	Konstruktion und Aufbau eines Zweikammerprüfstands zur Untersuchung des U-Werts und des Scheibenbeschlags von Fahrzeugfenstern, 2011.
Tao, J.	Applikation und Bilanzierung eines Fahrzeuges mit verschiedenen Zuheizmaßnahmen, 2012.
Xu, H.	Numerische Simulation auftriebsinduzierter Strömungen anhand einer vereinfachten Geometrie zur Übertragung auf Strömungsvorgänge im Pkw-Innenraum, 2012.
Ahsbahs, T.	Optimierung und Messungen an einem Scheibenbeschlagsprüfstand zur Reduzierung des Heizbedarfs von E-Fahrzeugen, 2012.
Helmgens, P.	Aufbau und Durchführung einer Sensitivitätsanalyse eines neuartigen Regelalgorithmus zur energieeffizienten Innenraumkonditionierung von Elektro-Fahrzeugen, 2012.
Baskovic Zvar, U.	Turbulence Modeling in a Vehicle Passenger Compartment with the Reference Geometry of the Electric Vehicle Prototype MUTE, 2012.
Gallner, C.	Konstruktion eines Versuchsstands und experimentelle Untersuchung von Tropfenkondensation auf verschiedenen Oberflächen, 2012.
Steinbacher, M.	Experimentelle Bestimmung der Beschlagseigenschaften und des Wärmedurchgangs von Fahrzeugverglasungen, 2012.
Remy, M.	Optimierte Integration von PV-Elementen in E-Fahrzeugen, 2012.
Parada, M.	One - Dimensional Modeling and Control of the Thermal Management System of an Electric Vehicle Prototype, 2013.

Dillis, S.	Abgleich zwischen Simulations- und Versuchsergebnissen von Motorkühlsystemen, 2013.
Rasp, F.	Aufbau und Inbetriebnahme eines Prüfstands zur experimentellen Untersuchung eines neuartigen Thermomanagementsystems für ein Elektro-Kleinstfahrzeug, 2013.
Czingon, M.	Experimentelle Untersuchung von Tropfenkondensation an einem Scheibenbeschlagsprüfstand und Strömungsanalyse mittels PIV, 2013.
Schweizer, F.	Optimierung des Validierungsprozesses der Kühlungssimulation am Beispiel eines Hybrid-Pkw, 2014.
Jain, N.	Computational Fluid Dynamics Investigation of Heat and Mass Transfer of Sessile Droplet Condensation and Evaporation Phenomena, 2014.
Schulze-Ardey, J.	Entwicklung und Implementierung eines Regelalgorithmus für das Thermomanagement des Elektrofahrzeug-Prototyps Visio.M, 2014.
Sickliger, M.	Experimentelle Untersuchung von Beschlag auf der Frontscheibe von Fahrzeugen, 2014.
